

Development of an Incompressible Smoothed
Particle Hydrodynamics Method for
Electrohydrodynamics of Immiscible Fluids and
Rigid Particles

by

Nima Tofighi

Submitted to
the Graduate School of Engineering and Natural Sciences
in partial fulfillment of the requirements for the degree of
Doctor of Philosophy

Sabancı University

March 2016

Development of an Incompressible Smoothed Particle Hydrodynamics Method for
Electrohydrodynamics of Immiscible Fluids and Rigid Particles

Approved by:

Assoc. Prof. Dr. Mehmet Yıldız
(Thesis Supervisor)



Prof. Dr. Ali Koşar



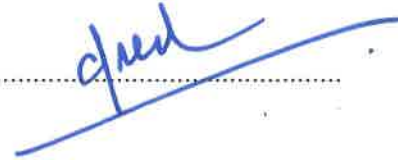
Assoc. Prof. Dr. Burç Mısırlıoğlu



Prof. Dr. James J. Feng
(University of British Columbia)



Prof. Dr. Afzal Suleman
(University of Victoria)



Date of Approval: 21 March 2016

© Nima Tofighi, 2016
All Rights Reserved.

Development of an Incompressible Smoothed Particle Hydrodynamics Method for
Electrohydrodynamics of Immiscible Fluids and Rigid Particles

Nima Tofghi

Ph.D. Dissertation, March 2016

Thesis Supervisor: Assoc. Prof. Dr. Mehmet Yıldız

Abstract

An incompressible smoothed particle hydrodynamics method for modeling immiscible and isothermal flow of two- and three-phase Newtonian fluids and solid particles subject to an external electric field has been developed. Continuum surface force method is used to calculate the surface tension forces on fluid-fluid interfaces. The materials are assumed to be either perfect or leaky dielectrics. Solid particles are modeled using viscous penalty method coupled with rigidity constraints. The equations are discretized using corrected derivatives and artificial particle displacement is used to ensure homogeneous particle distribution. The projection method is used to advance the governing equations of the flow and electric field in time.

The components of the scheme are tested in three stages of two- and three-phase hydrodynamics, multiphase electrohydrodynamics and fluid-structure/solid interaction. The results of each stage is compared to experimental and numerical data available in literature and their validity is established. The combination of the individual elements of the numerical method is used to simulate the motion of rigid particles submerged in Newtonian fluids subject to an external electric field. The behavior of the particles are found to be in agreement with experimental and numerical observations found in the literature. This shows the applicability of the proposed incompressible smoothed particle hydrodynamics scheme in simulating such complex and relatively unexplored phenomena.

Keywords: Incompressible Smoothed Particle Hydrodynamics, Multiphase Flows, Electrohydrodynamics, Fluid-Structure/Solid Interaction.

Development of an Incompressible Smoothed Particle Hydrodynamics Method for Electrohydrodynamics of Immiscible Fluids and Rigid Particles

Nima Tofghi

Ph.D. Dissertation, March 2016

Thesis Supervisor: Assoc. Prof. Dr. Mehmet Yıldız

Özet

Elektrik alan etkisinde olan izotermal ve birbirleri ile karışmayan iki ve üç fazlı Newtonsal akışkan ve katı parçacık akışlarının modellenmesine uygun bir sıkıştırılmaz düzleştirilmiş parçacık hidrodinamiği yöntemi geliştirilmiştir. Akışkanlar arası yüzey geriliminin modellenmesinde süreklilik yüzey kuvveti yöntemi kullanılmıştır. Akışkan ve katı ortamları sızdıran ve tam dielektrik malzeme olarak modellenmiştir. Katı parçacıkları viskoz engel ve rijit cisim hareket koşullarının birarada kullanılması ile modellenmiştir. Denklemler düzeltilmiş türevler ile ayrıklaştırılmış ve yapay parçacık öteleme yöntemi kullanılarak homojen parçacık dağılımı sağlanmıştır. Akım ve elektrik alanının zaman içinde ilerletilebilmesi için projeksiyon yöntemi kullanılmıştır.

Geliştirilen yöntemde kullanılan modellerin performansı ayrı ayrı olarak denenmiş ve doğrulanmıştır. Bu amaçla iki ve üç fazlı hidrodinamik, çok fazlı elektrohidrodinamik ve sıvı-katı etkileşimi konu başlıkları altında farklı simülasyonlar yapılmıştır. Sonuçlar literatürde bulunan deneysel ve sayısal sonuçlar ile karşılaştırılarak doğrulanmıştır. Adı geçen modellerin birleşiminden oluşan sayısal yöntem, Newtonsal akışkanda elektrik alan etkisi altında hareket eden rijit parçacıklarının modellenmesinde kullanılmıştır. Parçacıkların davranışı deneysel ve sayısal yöntemlerle yapılan çalışmalardaki gözlemlerle uyumlu bulunmuştur. Bu sonuçlar geliştirilmiş olan sıkıştırılmaz düzleştirilmiş parçacık hidrodinamiği yönteminin karmaşık ve görece daha az araştırılmış olan bu tarz problemler için uygun bir sayısal yöntem olduğunu göstermektedir.

Anahtar Kelimeler: Sıkıştırılmaz Düzleştirilmiş Parçacık Hidrodinamiği, Çok Fazlı Akım, Elektrohidrodinamik, Sıvı-Katı Etkileşimi.

To my family and friends... yes, that's all.

Acknowledgments

I would like to thank Professor Yıldız for his guidance, dedication, patience and helpful discussions during the course of my studies and research. I would also like to thank Professor Feng for hosting me in UBC and sharing his insights into the art of asking questions and attention to details. Last but not least, I would like to thank the jury members for their time, dedication and helpful comments.

Financial support provided by the Scientific and Technological Research Council of Turkey (TÜBİTAK) and the European Commission Research Directorate General for the following projects is gratefully acknowledged:

- Marie Curie International Reintegration Grant PIRG03-GA-2008-231048: Incompressible single- and multi-phase SPH with improved boundary treatment.
- Project Code 110M547: A smoothed particle hydrodynamics model for the deformation and motion of a bubble in Newtonian and non-Newtonian viscous liquid under the combined effects of gravity and externally applied electric field.
- Project Code 112M721: Modeling of fluid-solid interaction problems by smoothed particle hydrodynamics method.

Contents

1	Introduction	1
1.1	Computational fluid dynamics	1
1.2	Fluid-fluid and fluid-solid interfaces	1
1.3	Electrohydrodynamics: Electrostatics and hydrodynamics	5
1.4	Aims and scope	6
2	Mathematical formulation	8
2.1	Governing equations of the flow	8
2.2	Surface tension	9
2.2.1	Two-phase flows	9
2.2.2	Three-phase flows	11
2.2.3	Interpolation of material properties	12
2.3	Electric field	13
2.3.1	Maxwell stress tensor and electric forces	13
2.3.2	Governing equations	14
2.3.3	General boundary conditions for an interface	16
2.4	Fluid-structure/solid interaction	21
2.5	Dimensionless form of equations	22
3	Smoothed particle hydrodynamics and its numerical implementation	24
3.1	Integral representation	24
3.2	Particle representation	26
3.2.1	Derivatives of variables	26
3.2.2	Homogenization of particle distribution	30
3.3	Neighbor finding	31
3.4	Boundary conditions	32
3.5	Initial particle arrangement	34
3.6	Imposing incompressibility	36
3.6.1	Projection method	36
3.6.2	SPH implementation of projection method	37
3.7	Electrostatic fluid-structure/solid interaction procedure	37

4	Three-phase flows	42
4.1	Introduction	42
4.2	Results	43
4.2.1	Liquid lens	43
4.2.2	Droplet levitation	48
4.2.3	Droplet spreading	52
4.3	Remarks	53
5	Electrohydrodynamics	56
5.1	Introduction	56
5.2	Dimensionless form of the equations	58
5.3	Forces on a flat interface midway of flat electrodes	59
5.4	Contribution of the interfacial forces to the vortex sheet strength	60
5.5	Results	60
5.5.1	Spatial resolution	61
5.5.2	Effects of an external electric field	61
5.5.3	Effects of electrical permittivity and conductivity ratios	64
5.5.4	Effects of electric field intensity	66
5.6	Remarks	71
6	Fluid-structure/solid interaction	72
6.1	Introduction	72
6.2	Dimensionless variables	74
6.3	Results	74
6.3.1	Single disc descent	74
6.3.2	Double disc descent	80
6.3.3	Single disc rotation	86
6.3.4	Single disc migration	89
6.3.5	Single ellipse descent	90
6.4	Remarks	92
7	Electrostatic fluid-structure/solid interaction	95
7.1	Introduction	95
7.2	Migration of a rigid disc in Couette flow	96
7.3	Dielectrophoretic chaining of circular discs	100
7.3.1	Geometric properties, characteristic values and test cases	100
7.3.2	The effect of initial angle	102
7.3.3	The effect of Reynolds number	105
7.3.4	The effect of difference in permittivities	110
7.3.5	The effect of difference in disc diameters	113

7.4	Sedimentation of an elliptic disc in external electrical field	115
7.4.1	Ellipse Alignment in Electric Field	115
7.4.2	Validation of the shifting boundary condition	118
7.4.3	The effect of boundaries on the sedimentation of the elliptic particle subject to an external electric field	120
7.5	Remarks	124
8	Conclusion	126
	Bibliography	128

List of Figures

3.1	Neighboring cells (dark gray) for the cells containing particle of interest i at the bottom-left corner (a), bottom wall (b), left (c) and inside the computational domain and away from the boundaries(d). A dashed cell contains ghost particles.	32
3.2	Arrangement of auxiliary particles in dummy particle method (a,b) and ghost particle method (c,d). Related particles have similar borders. Interpolation sites of dummy particle method are shown with green filling. Neumann and Dirichlet boundaries are shown in the left column while periodic boundary is shown to the right.	33
3.3	Shifting boundary condition: (a) original particle arrangement; (b) particle arrangement after shifting. Red particles are discarded and green particles are added. The area of interest is marked in light gray. Ghost particles are shown with gray fill and are related to particles of similar border within the computational domain.	34
3.4	Particle positions before (a) and after (b) relaxation. Contour shows $\nabla \cdot \mathbf{u}_{\text{apd},i}$	35
4.1	Initial condition for liquid lens simulation shown in the vicinity of the droplet; (a, b) Particle arrangement and 0.5 level contour of color function for first approach. ①, ② and ③ denote phases 1, 2 and 3, respectively; (c, d) Particle arrangement and 0.5 level contour of color function for second approach; (e) Early stage development of non-dimensional lens diameter for first and second approach of initial particle arrangements.	44
4.2	Particle arrangement and 0.5 level contour of color function of two-phase diamond relaxation; (a) Initial diamond arrangement; (b) Intermediate stage; (c) Relaxed circle obtained and used as initial particle arrangement for other test cases.	44
4.3	(a) Effect of resolution on equilibrium shape of test case V_3 (V_3R_1 , V_3R_2 and V_3R_3); (b, c and d) Effect of resolution on equilibrium diameter of lens for cases V_1 , V_3 and V_5 where \blacktriangleright , \blacktriangleleft and \blacktriangle denote R_1 , R_2 and R_3 resolutions, respectively. Straight lines and corresponding markers on vertical axis are time-averaged values, d_f/d_a , shown in table 4.1.	47

4.4	Time snapshots of particle position and droplet boundary (0.5 level contour of color function for droplet, phase 3). Both x and y axes are non-dimensionalized with each test case's respective analytic equilibrium diameter. Only top right quarter has been shown for brevity. left column: case V_1R_3 ; middle column: case V_3R_3 ; right column: case V_5R_3	49
4.5	Time snapshots of all phase boundaries (0.5 level contour of color function of each phase) for case R_3V_3 . Both x and y axes are non-dimensionalized with respective analytic equilibrium diameter. (a) droplet, phase 3; (b) bottom fluid, phase 2; (c) top fluid, phase 1.	50
4.6	Time snapshots of 0.5 level contour for all phases. Top row: case L_1 ; Middle row: case L_2 ; Bottom row: case L_3 ; Column letters a through k are at times 0, 0.03, 0.075, 0.15, 0.3, 0.6, 1.05, 1.5, 2.25, 3.0 and 4.5 seconds. Both x and y axes are non dimensional with respect to d_o and tick marks are spaced 0.82 units apart.	51
4.7	Average vertical velocity of particles in droplet phase versus time for test cases L_1 , L_2 and L_3 . Letters and \times marks on horizontal axes represent the times when snapshots a through h in figure 4.6 are taken.	52
4.8	Equilibrium particle position and droplet boundary (0.5 level contour of color function, phase 2). Only half of the computational domain has been shown for brevity. Solid lines indicate bottom wall (phase 3). (a) $E_o = 0.475$; (b) $E_o = 0.95$; (c) $E_o = 1.9$; (d) $E_o = 3.8$; (e) $E_o = 7.6$; (f) $E_o = 13.3$	54
4.9	Normalized equilibrium droplet height versus E_o . Letters a through f correspond to the droplet shapes shown in figure 4.8.	54
5.1	Spike and bubble tip positions (a) and velocities (b) versus time for different particle spacings; (c) interface profiles at $y_s = 1.7, 1.4, 1.1, 0.8$ and 0.5	62
5.2	Spike and bubble tip positions (a) and velocities (b) for cases NP (red), PN (blue) and NE (green); (c) interface profiles at $y_s = 1.7, 1.4, 1.1, 0.8$ and 0.5	63
5.3	Profiles of normal force magnitudes along the interface for case NP; (a) interface profile; (b) electrical force and its components; (c) electrical force, surface tension and the resultant interfacial force; the cross marks on the interface are placed at 0.1 intervals of normalized interface length. Symbols on the interface and horizontal axes correspond to spike tip (∇), middle point of interface (\circ) and bubble tip (Δ).	63

5.4	Profiles of normal force magnitudes along the interface for case PN; (a) interface profile; (b) electrical force and its components; (c) electrical force, surface tension and the resultant interfacial force; the cross marks on the interface are placed at 0.1 intervals of normalized interface length. Symbols on the interface and horizontal axes correspond to spike tip (∇), middle point of interface (\circ) and bubble tip (Δ).	64
5.5	Spike and bubble tip position (a,b) and velocity (c,d) for $\mathcal{E} = -0.3$ (a,c) and $\mathcal{E} = +0.3$ (b,d); the arrow shows the direction of increasing \mathcal{P}	65
5.6	Spike and bubble tip position (a,b) and velocity (c,d) for $\mathcal{P} = -0.3$ (a,c) and $\mathcal{P} = +0.3$ (b,d); the arrow shows the direction of increasing \mathcal{E}	65
5.7	Magnitude of spike tip forces (left) and bubble tip forces (right) with respect to tip position for $\mathcal{P} = +0.3$	66
5.8	Spike and bubble tip position (a,b) and velocity (c,d) for NP ($\mathcal{P} = -0.3 - \mathcal{E} = +0.3$) (a,c) and PN ($\mathcal{P} = +0.3 - \mathcal{E} = -0.3$) (b,d); the arrows show the direction of increasing E_g (decreasing field intensity).	67
5.9	Interface profiles for $E_g = 5.625$ (blue), 22.5 (cyan), 90 (yellow) and 360 (red); (a) NP ($\mathcal{P} = -0.3 - \mathcal{E} = +0.3$) at spike height $y_s = 1.7, 1.4, 1.1, 0.8$ and 0.5 ; (b) PN ($\mathcal{P} = +0.3 - \mathcal{E} = -0.3$) at bubble height $y_b = 2.1, 2.3, 2.5, 2.7$ and 2.9	68
5.10	Contours of vorticity (fills) and streamlines (lines); the cross marks on the interface are placed at 0.1 intervals of normalized interface length. Symbols on the interface (figure 5.11 on the horizontal axes) correspond to spike tip (∇), middle point of interface (\circ) and bubble tip (Δ). (a,b,c) NP with $E_g = 5.625$ at $y_s = 1.7, 1.1$ and 0.5 (blue contours in figure 5.9-a); (g,h,i) PN with $E_g = 5.625$ at $y_b = 2.1, 2.5$ and 2.9 (blue contours in figure 5.9-b).	69
5.11	Electric force (red), surface tension (blue) and resultant contribution of interfacial forces (black) on vortex sheet strength in right hand side of equation (5.12); symbols on the horizontal axes correspond to spike tip (∇), middle point of interface (\circ) and bubble tip (Δ). These symbols correspond to those in figure 5.10 on the interface. (a,b,c) NP with $E_g = 5.625$ at $y_s = 1.7, 1.1$ and 0.5 ; (d,e,f) PN with $E_g = 5.625$ at $y_b = 2.1, 2.5$ and 2.9	70
6.1	Schematic of all test cases included in this study; (a) CC/SDD; (b) DDD; (c) SDR; (d) SDM; (e) SED.	75
6.2	Closeup view of initial particle distribution at the vicinity of the solid disc. Black points denote solid particles whereas gray points are fluid particles. (a) Initial arrangement; (b) particle positions at $y = 6$	76

6.3	Vertical velocity (a) and vertical position (b) of the solid disc's center of mass versus time for calibration test cases.	77
6.4	Disc position for calibration test cases when CCH5 is at $y = 6$	78
6.5	Velocity and pressure of case CCH5 at $y = 6$; (a) velocity vectors are shown on the left half while the right half plots streamlines. Velocity vectors are drawn at interpolated positions and do not correspond to actual particle locations; (b) left half shows velocity magnitude while right half plots pressure contours. The two halves share the same scale and color bar.	78
6.6	Comparison of simulation results at different spatial resolutions for the rigid disc's center of mass of case SDD/CCH5; (a) vertical position; (b) vertical velocity	80
6.7	Comparison of simulation results with literature data; (a) vertical position; (b) vertical velocity	81
6.8	Repulsive force magnitude with respect to $(c - d) / d$. Legend denotes (n_r, λ) pairs. A negative value indicates crossover of the discs.	83
6.9	Vertical position (a), vertical velocity (c) and force magnitude (e) for cases with $n_r = 2$ and no crossover. Legend denotes (n_r, λ) pairs. Close ups of boxed region are shown on the right column for vertical position (b) and vertical velocity (d).	84
6.10	Snapshots of disc positions for cases without crossover at $t = 0.2, 21, 31.5, 42, 52.5, 63$ and 73.5 . (n_r, λ) pairs are shown at the top of each column: (Yellow) top disc; (Blue) bottom disc. Disc to disc contact or lack thereof is not accurately represented in this figure due to line thicknesses. Refer to table 6.3 for minimum distance between discs during the simulation.	84
6.11	Comparison of simulation results at $Re_p = 56$. (a) vertical position; (b) vertical velocity.	85
6.12	Comparison of simulation results at $Re_p = 391.3$. (a) vertical position; (b) vertical velocity.	86
6.13	Comparison of angular velocity versus particle Re for different aspect ratios. Bulk Re is limited to about 500 in current simulations. Identical colors denote identical aspect ratios.	88
6.14	(a) comparison of streamwise (Blue) and normal (Yellow) velocity profiles at $1.25r$ of the rigid disc's center of mass at Re_p of 20. Refer to [232] for experimental data of Zettner and Yoda. (b) comparison of stagnation point distance from rigid disc's surface with respect to Re_p . Poe and Acrivos utilize an $H/r = 6 \sim 12$ in their experiments.	88

6.15	Streamlines at the vicinity of the disc for $H/r = 4$. Particle positions inside the rigid body (dark) and fluid phase (light) are shown in the background. Rigid body boundary is defined as 0.5 level contour of the color function and is marked by the thicker line. (a) $Re_p = 0.02$; (b) $Re_p = 20$	89
6.16	Comparison of vertical position with respect to time (a) and normal velocity with respect to vertical position (b). (Blue) $h/H = 0.75$; (Yellow) $h/H = 0.25$	90
6.17	(a) horizontal position versus vertical position of the disc; periodic boundary conditions are assumed to imitate a longer channel. The position of the disc starting at the top half is converted to an equivalent of the one starting at the bottom half. The difference between the two curves is reflected on the right axis. (b) horizontal velocity versus time; The difference between absolute values is reflected on the right axis.	91
6.18	Initial particle arrangement inside the rigid elliptic particle	92
6.19	Comparison of horizontal position (a) and angle of the ellipse (b) versus vertical position at high (—) and low (---) Re_t or \mathcal{D}	93
6.20	Comparison of vertical velocities of the ellipse versus time with [231]. (—) $\mathcal{D} = 1.1$; (---) $\mathcal{D} = 1.01$	93
7.1	(a) Schematic of the test case. (b) Closeup view of initial particle distribution at the vicinity of the solid disc. Black points denote solid particles whereas gray points are fluid particles.	97
7.2	Comparison of the vertical position (a) and vertical velocity (b) of the disc's center of mass versus time.	98
7.3	Angular velocity for cases NE (black), (0.2, 5) (red) and (5, 0.2) (blue).	98
7.4	Streamlines (blue) and electric field lines (black) for case NE (a) and permittivity and conductivity pairs of (0.2, 5) (b) and (5, 0.2) (c). Rigid body particles are in darker gray while fluid particles are shown in light gray.	99
7.5	Schematic of the DEP chaining of two circular discs. Discs one and two are colored in white and gray for distinction.	101
7.6	(a) Trajectory of disc one (continuous) and disc two (dashed) with different starting angles; (b) center-to-center separation distance with respect to center-to-center angle with electric field.	102
7.7	Center-to-center (a,c) and rotational (b,d) components of electric forces with respect to angle (a,b) and separation distance (c,d) for different θ_i	104
7.8	Average electric field intensity at the upper wall with respect to angle (a) and separation distance (b) for different θ_i	105
7.9	Dimensionless time for reaching $\theta = 89^\circ$ with respect to Reynolds number for $\theta_i = 45^\circ$ (a) and $\theta_i = 5^\circ$ (b).	106

7.10	(a) Trajectory of disc one (continuous) and disc two (dashed) for $\theta_i = 45^\circ$ starting angle at different Reynolds numbers; (b) center-to-center separation distance with respect to angle.	107
7.11	(a) Trajectory of disc one (continuous) and disc two (dashed) for $\theta_i = 5^\circ$ starting angle at different Reynolds numbers; (b) center-to-center separation distance with respect to angle.	107
7.12	Center-to-center (a,c) and rotational (b,d) components of electric forces with respect to angle (a,b) and separation distance (c,d) for different Reynolds numbers at $\theta_i = 45^\circ$	108
7.13	Center-to-center (a,c) and rotational (b,d) components of electric forces with respect to angle (a,b) and separation distance (c,d) for different Reynolds numbers at $\theta_i = 5^\circ$	109
7.14	(a) Trajectory of disc one (continuous) and disc two (dashed) for $\theta_i = 45^\circ$ with different disc-to-disc permittivity ratios; (b) center-to-center separation distance with respect to angle.	111
7.15	(a) Trajectory of disc one (continuous) and disc two (dashed) for $\theta_i = 5^\circ$ degrees starting angle with different disc-to-disc permittivity ratios; (b) center-to-center separation distance with respect to angle.	111
7.16	Center-to-center (a) and rotational (b) components of electric forces with respect to angle for different disc-to-disc permittivity ratios at $\theta_i = 45^\circ$	112
7.17	Center-to-center (a) and rotational (b) components of electric forces with respect to angle for different disc-to-disc permittivity ratios at $\theta_i = 5^\circ$	113
7.18	(a) Trajectory of disc one (continuous) and disc two (dashed) for $\theta_i = 45^\circ$ with different radii; (b) center-to-center separation distance with respect to angle.	114
7.19	(a) Trajectory of disc one (continuous) and disc two (dashed) for $\theta_i = 5^\circ$ with different radii; (b) center-to-center separation distance with respect to angle.	115
7.20	Center-to-center (a) and rotational (b) components of electric forces with respect to angle for different disc radii at $\theta_i = 45^\circ$	116
7.21	Center-to-center (a) and rotational (b) components of electric forces with respect to angle for different disc radii at $\theta_i = 5^\circ$	116
7.22	Center-to-center (a) and rotational (b) components of velocity with respect to angle for different disc radii at $\theta_i = 45^\circ$	117
7.23	Center-to-center (a) and rotational (b) components of velocity with respect to angle for different disc radii at $\theta_i = 5^\circ$	117
7.24	Orientation of the elliptic disc with different initial starting angles while aligning with the electric field for case S (a) and case U (b). The electric field is oriented at 90° (vertical).	119

7.25	Horizontal position (a) and orientation (b) of the elliptic disc while sedimenting.	120
7.26	Horizontal position (a) and orientation (b) of the elliptic disc of case S while sedimenting in an external electric field.	122
7.27	Horizontal position (a) and orientation (b) of the elliptic disc of case U while sedimenting in an external electric field.	122
7.28	Hydrodynamic torque (blue), electric torque (red) and resultant torque applied to the ellipse of case U with boundary configurations of A (a), B (b), C (c) and D (d) while sedimenting in an external electric field. A positive value induces a counter-clockwise rotation.	124
7.29	Horizontal component of hydrodynamic force (blue), electric force (red) and resultant force applied to the ellipse of case U with boundary configurations of A (a), B (b), C (c) and D (d) while sedimenting in an external electric field. A positive value moves the ellipse to the right.	125

List of Tables

4.1	Simulation parameters and results for liquid lens elongation test case . . .	43
4.2	Simulation parameters and results for droplet levitation test case	50
6.1	Viscosity ratio and interpolation scheme for calibration purpose; C stands for calibration test cases.	76
6.2	Time and vertical velocity of rigid disc's center of mass at $y = 6$ for calibration test cases	77
6.3	Force parameter pairs and minimum distance between disc surfaces during the simulation for DDD cases. Negative values denote crossover. dimensionless particle spacing is approximately 0.0625.	83
6.4	Dimensionless parameters for DDD cases compared to literature data. . .	85
6.5	Simulation parameters and Re_t for SED and numerical simulations of Xia <i>et al.</i> [231] and Suzuki and Inamuro [152].	92
7.1	Time until the disc reaches one radius distance of channel center (regular) or bottom wall (bold). An underline shows that all conditions for Quincke rotation are satisfied. The disc reaches channel center at $t^*G = 25.94$ when no electric field is applied.	99
7.2	Configurations for testing the shifting boundary condition.	119
7.3	Terminal Reynolds number Re_t for cases S and U for different boundary configurations. When no electric field is applied $Re_t = 13.5$ (<i>cf.</i> table 6.5).	121

Nomenclature

Abbreviations

AC	Alternating Current
ALE	Arbitrary Lagrangian-Eulerian
APD	Artificial Particle Displacement
CFD	Computational Fluid Dynamics
CFL	Courant-Friedrichs-Lewy
CSF	Continuum Surface Force
CSS	Continuum Surface Stress
DC	Direct Current
DEP	Dielectrophoresis
DKT	Drafting-Kissing-Tumbling
DLM	Distributed Lagrange Multiplier
DNS	Direct Numerical Simulation
EFSI	Electrostatic Fluid-Structure/Solid Interaction
EHD	Electrohydrodynamics
FD	Fictitious Domain
FDM	Finite Difference Method
FEM	Finite Element Method
FSI	Fluid-Structure/Solid Interaction
FT	Front Tracking

FVM	Finite Volume Method
IB	Immersed Boundary
ISPH	Incompressible Smoothed Particle Hydrodynamics
LS	Level Set
MBT	Multiple Boundary Tangent
MPS	Moving Particle Semi-implicit
PF	Phase Field
PFEM	Particle Finite Element Method
RKPM	Reproducing Kernel Particle Method
RTI	Rayleigh-Taylor Instability
SPH	Smoothed Particle Hydrodynamics
VOF	Volume of Fluid
VP	Viscous Penalty
WAM	Weighted Arithmetic Mean
WCSPH	Weakly Compressible Smoothed Particle Hydrodynamics
WHM	Weighted Harmonic Mean

Dimensionless numbers

\mathcal{A}	Atwood number
Bo	Bond number
Ei	Electro-inertial number
Eg	Electro-gravitational number
Eo	Eotvos number
Eu	Euler number
Fr	Froude number
Re	Reynolds number

We Weber number

Ratios

\mathcal{E} Electrical conductivity ratio

\mathcal{D} Density ratio

\mathcal{V} Viscosity ratio

\mathcal{P} Electrical permittivity ratio

\mathcal{P}_r Disc-to-disc electric permittivity ratio

\mathcal{R} Diameter ratio

\mathcal{R}_r Disc-to-disc diameter ratio

Greek symbols

δ Dirac delta function

δ^{ij} Kronecker delta

δ_p Particle spacing

γ Surface tension coefficient

κ Surface curvature

μ Viscosity

ϕ Electrical potential

ψ Particle number density

ρ Density

σ Electrical conductivity

τ Timescale

θ Angle

$\delta\mathbf{r}$ Artificial particle displacement vector

$\boldsymbol{\tau}$ Viscous stress

ε Electrical permittivity

Latin symbols

\hat{c}	Color function
\mathbf{T}	Stress tensor
\mathbf{a}	Correction factor
\mathbf{D}	Electric displacement vector
\mathbf{E}	Electric field vector
\mathbf{f}	Force vector, generic vector
\mathbf{g}	Gravitational acceleration vector
\mathbf{J}	Electric current
\mathbf{n}	Interface normal
\mathbf{r}	Distance vector
\mathbf{u}	Velocity vector
\mathbf{x}	Position vector
c	Smoothed color function
f	Generic scalar
h	Smoothing length
I	Identity matrix
I_s	Inertia of the solid object
J_d	Number of particles within the computational domain
J_n	Number of neighboring particles
J_s	Number of solid particles
M_s	Mass of the solid object
p	Pressure
q	Electrical charge density
T	Torque

t	Time
w	Kernel function

Superscripts

(i)	i th component, explicitly (1) or (2)
(n)	Timestep
$+$	Intermediate values
$*$	Dimensionless variable
i	i th component
j	j th component

Subscripts

(α)	Phase α
$(\alpha\beta)$	Between phases α and β
(β)	Phase β
(b)	Body force
(c)	Capillary component
(e)	Electrical force
(h)	Hydrodynamic component
(s)	Surface tension force
i	Particle i
ij	Difference between particles i and j
j	Particle j
ji	Difference between particles j and i
c	Characteristic value

Chapter 1

Introduction

1.1 Computational fluid dynamics

There are three approaches to studying fluid flows: analytical, experimental and numerical. Analytical solutions are limited to particular geometrical configurations and have been a major research topic for centuries. In regards to more complex phenomena, experimental methods have been the single source of information until the advent of computers which made numerical methods viable. The numerical method of investigating fluid flow, commonly known as Computational Fluid Dynamics (CFD), is the process of predicting fluid flow, heat transfer, mass transfer, chemical reactions, electrical and magnetic influence and related phenomena by solving the mathematical equations which govern these processes using a numerical method.

Experiments provide quantitative description of flow using measurements for one variable at a time, at a limited number of points and time instants. The results are limited to laboratory-scale models for a limited range of problems and operating conditions subject to measurement errors and unintended perturbations. While numerical simulations alleviate some of the shortcomings of the experiments, CFD is very much limited by the mathematical models, discretization methods and implementation of the computational code. For complex problems with refined solutions the computational costs, in terms of time and energy, may very well surpass that of an equivalent experiment. In other cases, such as very small or very large scale phenomena, experimental procedures may be difficult, expensive or impossible. As a result, experiments, numerical methods and to a lesser extent analytical solutions go hand in hand to help understand a variety of flow configurations.

1.2 Fluid-fluid and fluid-solid interfaces

Fluid flows encountered daily include, but are not limited to, meteorological and environmental phenomena such as rain, wind and particulate transport in atmosphere, heating,

cooling and ventilation of buildings and electronic devices and interaction of various solid bodies with the surrounding medium. All of the aforementioned flows involve interfacial interactions, be it between multiple fluid layers or between a fluid and a solid surface (moving or stationary). As a result there is a large amount of research dedicated to the study of the interfacial phenomena. A variety of numerical methods are formulated to simulate the dynamics of the interfaces. While the boundaries between the basic elements of the numerical methods dealing with interfaces may not be as clear in every implementation, it is possible to put the essential steps into three categories. Assuming rigid behavior for solid components of a simple system, the three elements are fluid solver, interface handler and coupling scheme.

Continuum level (macro-scale) fluid solvers may be categorized into Eulerian, Lagrangian and Eulerian-Lagrangian. In Eulerian fluid solvers, the coordinate system is stationary in reference frame while fluid parcels travel through the computational domain. In Lagrangian point of view, the coordinate system follows fluid parcels and is mobile with respect to the reference frame. Eulerian-Lagrangian methods, as the name implies, are a mix of the two approaches where some elements are calculated in Eulerian fashion while other features are followed in a Lagrangian manner. The evolution of the interface may be handled via two different approaches: interface-tracking and interface-capturing. The former uses an explicit (or implicit) representation of the interface in a Lagrangian fashion and tracks its evolution across the fluid background. The latter follows the interface in an implicit fashion via evolving a representative function or variable and reconstructing the interface to apply its effects on the flow field. Interface-capturing methods are generally coupled to an Eulerian representation of the flow field while interface-tracking methods may use either Eulerian or Lagrangian representation. In the simplest form of coupling, either fluid solver or interface handling procedure may take precedence, that is either the fluid affects the interface position or interface position affects the fluid flow and the reciprocated effects are resolved in the next time instance. In fully coupled model the interface and fluid flow are evolved simultaneously which generally involves higher computational cost.

Among Eulerian approaches coupled with interface-capturing methods, Volume of Fluid (VOF) and Level Set (LS) are the more widespread variants. VOF method was proposed by Hirt and Nichols [1] and uses a function with a sharp jump to distinguish the interface which is advected by the fluid velocity. The method generally involves a reconstruction of the interface after every advection step to compute the curvature, surface tension, viscous forces and any additional interface related variables. Advecting a step function and reconstruction step require sophisticated methods that have resulted in several variants [2–14]. Despite the difficulties, the method is able to handle large topological changes and preserves mass naturally. In LS, pioneered by the work by Osher and Sethian [15], the interface is defined as the zero-level of a smooth function. This provides a

straightforward method of calculating the interface normal, curvature and other interface-related properties. The smoothness of the function facilitates its convection and it may be reinitialized to maintain its smoothness. However, the smoothness of the function means that interface location may be inaccurate and the information is diffused across the interface, causing worse mass conservation in comparison with VOF. Some examples of LS method may be found in [15–33]. Spatial discretization in Eulerian interface-capturing methods are usually carried out using Finite Difference Method (FDM) and Finite Volume Method (FVM) and occasionally Finite Element Methods (FEM).

As an alternative to interface-capturing, interface-tracking method is also coupled with Eulerian representation of the fluid to solve interfacial problems. In a variation introduced by Glimm and co-workers [34] and aptly named Front Tracking (FT), additional computational elements are introduced explicitly to keep track of the front. The underlying fluid mesh may be adapted to the interface [35, 36] or remain intact [37–39]. The main advantage of the method lies in its ability to avoid numerical diffusion and maintain a sharp interface, resulting in several publications [40–46]. On the other hand this raises the complexity of the method and handling of large topological changes becomes difficult. Additionally, the interface elements may accumulate in one segment of the interface while leaving other parts less resolved which requires further manipulation of the distribution of interface elements. Spatial discretization in the aforementioned methods are usually carried out using FDM and FVM and occasionally FEM. A different implementation of the interface-capturing scheme, which is mostly associated with FEM, uses a fluid solver that resides between Eulerian and Lagrangian representation. Pioneered by Hirt *et al.* [47, 48], Arbitrary Lagrangian-Eulerian (ALE) method uses a fluid mesh that moves according to a set law. In its extremes the mesh is either stationary (Eulerian) or moves with the fluid (Lagrangian). Being similar to FT in its interface representation, ALE suffers the same problem of limited topological changes while the necessity of the occasional remeshing of the fluid domain adds to the complexity of the algorithm. However, the flexibility of the ALE in small interface deformations resulted in its widespread adoption [49–55]

Since including solid bodies, Fluid-Structure/Solid Interaction (FSI) problems have some inherent Lagrangian nature to them. In this case, the interface tracking may be either implicit or explicit. A family of FSI methods, collectively known as Fictitious Domain (FD) approaches [56–59], use an implicit representation of the moving boundaries. These methods apply a specific constraint to the rigid area and the solid body is represented by a smooth or sharp function on the flow field. In this sense the methods bear some resemblance to LS methods. On the other hand Immersed Boundary Method (IB) [60, 61] is closely related to FT in the way the solid body is followed explicitly. On the other hand, the effects of the presence of the solid body are distributed on the fluid in a manner which may be classified closer to LS methods. ALE method is directly applicable to interfaces with moving boundaries with minimal modification compared to its fluid-fluid counterpart.

FDM, FVM and FEM are equally used in FSI problems.

Lagrangian interface-tracking, as a natural representation of the moving interface, may be coupled with a Lagrangian representation of the fluid flow to alleviate the shortcomings mentioned above. To this end, several methods have been developed which allow for material interface to be specifically defined and followed. Boundary conditions on the interface are easy to enforce while complicated treatments for non-linear convective terms are circumvented. These advantages come at the cost of higher computational overhead, additional procedures to maintain a homogeneous discretization and a general lack of control over local resolution. One such Lagrangian method rooted in FEM is called Particle Finite Element Method (PFEM) [62, 63] which treats mesh nodes as free particles that move with the fluid. The domain is continuously remeshed according to the positioning of the nodes and governing equations are solved using the FEM. PFEM has been used for several problems [64–71].

The above mentioned Lagrangian method is still dependent on a form of mesh generation which adds to its computational overhead. Mesh-free Lagrangian methods alleviate this problem by using flexible connectivity and relying on kernel approximation of variables. Two such methods are Moving Particle Semi-implicit (MPS) method [72] and Smoothed Particle Hydrodynamics (SPH) method [73, 74]. In the context of fluid dynamics, SPH was initially applied to free surface flow employing an explicit approach using a pseudo compressible state equation [75]. Later on, MPS method [72] was proposed employing a projection scheme [76] followed by a similar approach for SPH [77, 78]. The two variants of the SPH were distinguished later as Weakly Compressible SPH (WCSPH) for the pseudo-compressible variant and Incompressible SPH (ISPH) for the projection-based SPH. MPS and ISPH have been developed independently and applied to many problems [79–81]. Recently it has been shown that the difference between the two methods lies in the specific kernel used and an equivalence between MPS weighting function and ISPH kernel is established [79, 82]. A MPS weighting function translates into two ISPH kernel functions, one for gradient and one for Laplacian. Similarly, an ISPH kernel translates into two distinct MPS weighting functions. MPS has been used to simulate free surface flows [83–86], droplet dynamics [81, 87, 88] and FSI [72].

Having been developed earlier, use of SPH (both variants) is much more prevalent than MPS. Some of the applications of SPH include multi-phase flows [89–93], free-surface flows such as wave impact, dam break and sloshing [75, 90, 94–97] as well as river dynamics, flow in fractures and porous media and soil mechanics [98–100] and fluid-structure interaction such as impact, particle dynamics and elastic bodies [101–106].

1.3 Electrohydrodynamics: Electrostatics and hydrodynamics

Electrohydrodynamics (EHD) refers to the hydrodynamics coupled with electrostatics. Electrical forces are generated at the interface between materials of different electrical properties when an external electrical field is applied to the system. These forces may have significant effects on the behavior of the interface and could serve as a control mechanism by affecting its stability, motion and evolution. The earliest record of an electrohydrodynamic experiment dates back to seventeenth century describing the formation of conical shapes upon bringing a charged rod above sessile drops [107, 108]. Some applications of the electrical field in manipulation of fluid-fluid interfaces include mixing of fluids [109–111], coalescence and breakup of bubbles [112–114], generating droplets and bubbles [115–117] and controlling their sizes [118–120]. As for fluid-solid interfaces and mainly considering solid bodies suspended in a background fluid, assembly of colloidal particles is one example [121, 122]. Two dimensional crystals [123–125] and functional microwires have been fabricated using this method [126]. Electrorheological fluids where viscosity is controlled via electrical field intensity is another example [127–129]. Some biological applications include cell manipulation [130, 131], DNA stretching [132, 133], patterning biomolecules and biopolymers [134, 135] and tissue engineering and biosensing [136, 137].

Early models describing the behavior of interfaces subject to an external electric field focused on perfect conductors or perfect dielectrics. These models were not adequate in explaining instabilities observed in poorly conducting liquids. To alleviate the shortcomings, the leaky dielectric model was proposed [138, 139]. The model assumes infinitesimal amount of free charge confined to a thin interface while the bulk of the fluid is free of charge. Electric forces are perpendicular to the interface in perfect conductors and perfect dielectrics and balance with the changes in the interface profile and surface tension. The free charge accumulated on the interface of leaky dielectric materials modifies the electric field resulting in tangential force which in turn is balanced by viscous stresses due to flow field. such that viscous flow develops in response to tangential forces created on the interface. In reality free charges will diffuse away from the interface, resulting in a layer of counterions of finite thickness called electric double layer [140]. Nevertheless, the leaky dielectric model is found to be adequate when electric double layer is thin compared to the particle size, avoiding additional complexity of modeling the diffuse layer [108, 121].

As for numerical modeling, the approaches are similar to that of a regular fluid-fluid or fluid-solid interface with governing equations of electric field solved in conjunction with the flow field. The solution of electric and flow fields may be partially or fully coupled. The flow field is directly affected by the electric field through electric forces while the flow field affects the electric field through displacement of the interface in an indirect fashion.

1.4 Aims and scope

Smoothed particle hydrodynamics is one of the more prevalent Lagrangian mesh-less methods which relies on moving particles as spatial discretization points. The particles are mostly advected by the flow while minor modifications are introduced to ensure proper resolution in the computational domain. This gives the method a natural tendency to adapt to the interfaces and as such, it is widely used in flows involving free surfaces such as wave generation, dam break, sloshing motion, and impact. However, the use of SPH is less frequent in subjects such as three-phase flows where more than two phases are in contact simultaneously, electrostatic manipulation of interfaces or passive movement of fully submerged solid bodies. This study aims to explore these very subjects with the aim to spread the use of SPH beyond its classical fluid mechanics territory.

The structure of the rest of this writing is as follows:

- The governing equations for a multiphase incompressible, immiscible, isothermal system is described in chapter 2. Handling surface tension for two- and three-phase flows using continuum surface force model is described in detail. The final piece of the mathematical model, *i.e.* electrostatics, is explained as well and two different approaches are described.
- The details of the numerical implementation are presented in chapter 3. Basic elements and operations such as convolution filtering, neighbor finding and implementing boundary conditions are described in detail. SPH spatial derivatives and time marching scheme are provided for electrostatic fluid-structure/solid interaction, the most complex case studied here.
- Chapter 4 explores the accuracy of the two- and three-phase implementation via several test cases and validations with literature data. Liquid lens, droplet levitation and droplet spreading are chosen due to their well known behavior.
- In chapter 5, the electrohydrodynamic component of the ISPH scheme is used to investigate the effects of the electric field for the simplest model configuration combining surface tension, viscous, gravitational and electrical forces, Rayleigh-Taylor instability.
- Chapter 6 validates the fluid-structure/solid interaction scheme implemented. To this end, the linear motion of a single circular disc and a pair of discs sedimenting in quiescent fluid is investigated. Then the rotational motion of a circular disc in simple shear is validated against literature data. The combined linear and rotational motion is tested by simulating the migration of circular disc in simple shear as well as the sedimentation of an elliptic disc in quiescent fluid.

- All the previous elements tested in chapters 4 to 6 are combined in chapter 7 to simulate the electrostatic fluid-structure/solid interaction. Three cases are considered and the effects of the electric field on the behavior of the solid particles is compared with the non-electrified counterparts. The first case is the migration of a circular disc in simple shear subject to an external electric field. The interactions of a pair of circular discs suspended in quiescent fluid is investigated as the second case. The third case covers the effects of boundary configurations on the sedimentation trajectory of an elliptical particle.
- Finally, the concluding remarks are drawn in chapter 8.

Chapter 2

Mathematical formulation

2.1 Governing equations of the flow

In all studies conducted here, the fluids are assumed to be incompressible, immiscible and isothermal, flowing in a two-dimensional domain possibly influenced by an external electric field.

The equations describing the evolution of the flow field may be written as [141, 142]

$$\nabla \cdot \mathbf{u} = 0, \quad (2.1)$$

$$\rho \frac{D\mathbf{u}}{Dt} = \nabla \cdot \mathbb{T}_{(h)} + \mathbf{f}_{(b)} + \mathbf{f}_{(s)} + \mathbf{f}_{(e)}, \quad (2.2)$$

where \mathbf{u} is the velocity vector, t is time, ρ is density and

$$\frac{D}{Dt} = \frac{\partial}{\partial t} + \mathbf{u} \cdot \nabla, \quad (2.3)$$

represents the material time derivative. For a Newtonian fluid the stress tensor $\mathbb{T}_{(h)}$ may be written as

$$\mathbb{T}_{(h)} = -pI + \boldsymbol{\tau}. \quad (2.4)$$

Here p denotes pressure and $\boldsymbol{\tau}$ is the viscous stress tensor defined as

$$\boldsymbol{\tau} = \mu [\nabla \mathbf{u} + (\nabla \mathbf{u})^\dagger], \quad (2.5)$$

where μ is fluid viscosity and superscript \square^\dagger denotes the transpose operation. Modifying equation (2.2) for an incompressible Newtonian fluid results in the following relation

$$\rho \frac{D\mathbf{u}}{Dt} = -\nabla p + \nabla \cdot \boldsymbol{\tau} + \mathbf{f}_{(b)} + \mathbf{f}_{(s)} + \mathbf{f}_{(e)}, \quad (2.6)$$

where $\mathbf{f}_{(b)}$, $\mathbf{f}_{(s)}$ and $\mathbf{f}_{(e)}$ are gravity, surface tension and electrical forces. Being a body

force, gravity is treated directly as

$$\mathbf{f}_{(b)} = \rho \mathbf{g}, \quad (2.7)$$

where \mathbf{g} is the gravitational acceleration vector. Further details about $\mathbf{f}_{(s)}$ and $\mathbf{f}_{(e)}$ will be given in the following sections.

2.2 Surface tension

Surface tension is the tendency of the liquids to obtain the least surface area possible. It occurs due to abrupt changes in molecular forces when fluid properties change in a discontinuous fashion. It is an inherent phenomena to the flow of multiphase immiscible fluids.

Within this study, a VOF like color function is used to distinguish the individual phases of the flow. This function, also referred to as ‘‘color function’’, is defined as

$$\hat{c}_{(\alpha)}(\mathbf{x}) = \begin{cases} 1, & \text{if phase } \alpha \text{ is present at } \mathbf{x}, \\ 0, & \text{otherwise,} \end{cases} \quad (2.8)$$

for each phase α of the flow for the whole domain. As an example a three-phase flow will have three color functions of $\hat{c}_{(1)}$, $\hat{c}_{(2)}$ and $\hat{c}_{(3)}$ such that $\sum_{\alpha=1}^3 \hat{c}_{(\alpha)}(\mathbf{x}) = 1$.

There are two common methods to account for surface tension force in literature: Continuum Surface Force (CSF) and Continuum Surface Stress (CSS). In CSF, the surface tension force is transformed into a volumetric local force. In CSS, the surface tension force is specified via divergence of a stress tensor to recover a volumetric representation of the surface tension. The main difference between the two methods is in explicit calculation of surface curvature in CSF while this step is implicit in CSS. Both methods suffer from parasitic currents in under-resolved regions due to imbalance between surface tension and pressure.

2.2.1 Two-phase flows

Assuming an infinitesimally thin surface element of area dA at an arbitrary position on the interface between two immiscible fluids, it is possible to define the boundary conditions at the interface as

$$\|\mathbb{T}_{(h)}^{ij}\| n^j = f_{(sa)}^i \quad (2.9)$$

where $\|\square\| = \square_{(1)} - \square_{(2)}$ represents the discontinuity at the interface of phases 1 and 2 while n^i is surface normal. The $\mathbf{f}_{(sa)}$ defined above is the surface tension force per unit interfacial area,

$$\mathbf{f}_{(sa)} = \gamma \kappa \mathbf{n} - \gamma \mathbf{i}, \quad (2.10)$$

where γ is surface tension coefficient and κ is surface curvature. For constant surface tension coefficient, $\mathbf{f}_{(sa)}$ reduces to

$$\mathbf{f}_{(sa)} = \gamma \kappa \mathbf{n}^i, \quad (2.11)$$

which is always normal to the interface.

To arrive at the formulation used in CSF proposed by Brackbill *et al.* [143], Consider a volume force $\mathbf{f}_{(s)}$ that gives the correct surface tension force per unit interfacial area $\mathbf{f}_{(sa)}$ as interface thickness H approaches the limit of infinitesimally thin interface,

$$\lim_{H \rightarrow 0} \int_{\Delta V} \mathbf{f}_{(s)} d^3x = \int_{\Delta A} \mathbf{f}_{(sa)} dA. \quad (2.12)$$

Here ΔV is a volume encompassing the area ΔA of the interface and thickness H perpendicular to the interface. $\mathbf{f}_{(sa)}$ is defined on the interface and $\mathbf{f}_{(s)}$ is zero out of ΔV . Using a one-dimensional Dirac delta $\delta = \delta[\mathbf{n}(\mathbf{x}_s) \cdot (\mathbf{x} - \mathbf{x}_s)]$ as a function of distance from point \mathbf{x}_s on the interface, the right hand side of equation (2.12) may be rewritten as

$$\begin{aligned} \int_{\Delta A} \mathbf{f}_{(sa)} dA &= \int_{\Delta V} \mathbf{f}_{(s)} d^3x \\ &= \int_{\Delta V} \gamma \kappa \mathbf{n} \delta d^3x, \end{aligned} \quad (2.13)$$

which upon comparing with equation (2.12) results in the following relation for volumetric representation of the surface tension force

$$\mathbf{f}_{(s)} = \gamma \kappa \mathbf{n} \delta. \quad (2.14)$$

To relate $\mathbf{f}_{(s)}$ in equation (2.14) to the color function, κ , \mathbf{n} and δ must be represented in terms of \hat{c} . Since the color function contains a sharp change of value at the interface, it must be smoothed out before it can be used. This is possible by convolving \hat{c} with an interpolation kernel. It is natural for this interpolation kernel to be the SPH kernel function w which will be discussed in the following section. The SPH interpolation kernel has a compact support of h and integrates to unity within its support domain. As such a smoothed color function may be defined as

$$c(\mathbf{x}) = \int_V \hat{c}(\mathbf{x}') w(\mathbf{x}' - \mathbf{x}; h) d^3x'. \quad (2.15)$$

The smoothed color function will approach the color function at the limit of infinitesimal interface thickness. It is also shown that the gradient of the smoothed color function approaches the behavior of a Dirac delta at the limit of infinitesimal interface thickness [143], *i.e.*

$$\lim_{H \rightarrow 0} \nabla c = \mathbf{n} \delta = \nabla \hat{c}. \quad (2.16)$$

This leads to the following formulation for the Dirac delta function

$$\delta = |\nabla c|. \quad (2.17)$$

Similarly, surface normal and surface curvature may also be defined using the smoothed color function as

$$\mathbf{n} = \frac{\nabla c}{|\nabla c|}, \quad (2.18)$$

$$\kappa = -\nabla \cdot \mathbf{n} = -\nabla \cdot \left(\frac{\nabla c}{|\nabla c|} \right), \quad (2.19)$$

respectively, leading to

$$\mathbf{f}_{(s)} = \gamma \nabla \cdot \left(\frac{\nabla c}{|\nabla c|} \right) \nabla c \quad (2.20)$$

for volumetric representation of the surface tension force.

The CSS method proposed by Lafaurie *et al.* [144] is based on defining a capillary pressure tensor as

$$\mathbb{T}_{(c)}^{ij} = -\gamma (\delta^{ij} - n^i n^j) \delta \quad (2.21)$$

with δ_{ij} denoting Kronecker delta. It is shown that

$$\mathbf{f}_{(s)} = \gamma \kappa \mathbf{n} \delta = -\nabla \cdot \mathbb{T}_{(c)}, \quad (2.22)$$

which relates CSF and CSS method. As a result, the main difference between the two methods lies in the numerical implementation rather than mathematical representation [145].

In all cases studied here, CSF method is used to calculate the surface tension forces.

2.2.2 Three-phase flows

Surface tension force given in equation (2.20) is valid for an interface between two fluids. Modifications have to be made to resolve a three-phase flow and especially a situation where all of the three phases meet at a single point, also known as a triple-junction. Assuming a finite interface thickness, as it is the case for CSF method, a triple junction will pose a problem when a point in space is influenced by interface between two sets of different fluids, their respective curvature and binary surface tension coefficients. In order to circumvent this difficulty, Smith *et al.* [146] have proposed decomposing the surface tension coefficient into phase specific surface tension coefficients such that $\gamma_{(\alpha\beta)} = \gamma_{(\alpha)} + \gamma_{(\beta)}$. Here, $\gamma_{(\alpha\beta)}$ is the binary surface tension coefficient between phases α and β while $\gamma_{(\alpha)}$ and $\gamma_{(\beta)}$ are phase-specific surface tension coefficients for phases α and β , respectively. Considering a three phase flow, the aforementioned decomposition will lead to following

relations for phase specific surface tension coefficients,

$$\begin{cases} \gamma_{(1)} = \frac{1}{2} (+\gamma_{(12)} + \gamma_{(13)} - \gamma_{(23)}), \\ \gamma_{(2)} = \frac{1}{2} (+\gamma_{(12)} - \gamma_{(13)} + \gamma_{(23)}), \\ \gamma_{(3)} = \frac{1}{2} (-\gamma_{(12)} + \gamma_{(13)} + \gamma_{(23)}). \end{cases} \quad (2.23)$$

In the same spirit, each surface is assigned a phase-specific normal, curvature and Dirac delta function, $\mathbf{n}_{(\alpha)} = \nabla c_{(\alpha)} / |\nabla c_{(\alpha)}|$, $\kappa_{(\alpha)} = -\nabla \cdot \mathbf{n}_{(\alpha)}$ and $\delta_{(\alpha)} = |\nabla c_{(\alpha)}|$, respectively. Combining phase specific surface tension coefficients, curvature, normal and Dirac delta function with (2.14), the resultant volumetric surface tension force may be rewritten as a sum of three force components as

$$\mathbf{f}_{(s)} = \sum_{\alpha=1}^3 (\gamma \kappa \mathbf{n} \delta)_{(\alpha)}. \quad (2.24)$$

In terms of the smoothed color function equation 2.20 may be reinterpreted as

$$\mathbf{f}_{(s)} = \sum_{\alpha=1}^3 \left(\gamma \nabla \cdot \left(\frac{\nabla c}{|\nabla c|} \right) \nabla c \right)_{(\alpha)}. \quad (2.25)$$

The model provided in equations (2.23) and (2.25) is able to capture both two-phase and three-phase behavior. For example, assuming a two-phase flow with fluids 1 and 2 with a binary surface tension coefficient of γ , one may revert to a standard two-phase CSF model by either setting $\gamma_{(12)} = \gamma_{(13)} = \gamma$ and $\gamma_{(23)} = 0$ or simply $\gamma_{(12)} = \gamma$ and $\gamma_{(13)} = \gamma_{(23)} = 0$ since phase 3 does not exist.

As pointed out in [147], a constraint has to be enforced to keep the erroneous normals that may occur at the outer edges of interface from contaminating the computed surface tension force. In this study, only gradient values exceeding a certain threshold, $|\nabla c| > \epsilon/h$, are used in surface tension force calculations. An ϵ value of 0.08 has been found to provide accurate results without removing too much detail [148].

2.2.3 Interpolation of material properties

Since calculation of derivatives across a sharp jump in material properties is not possible, a similar smoothing procedure to that of the color function is employed to generate a transition region across the interface. Among different interpolation methods, Weighted Arithmetic Mean (WAM) and Weighted Harmonic Mean (WHM) are chosen for this study. The intermediate value of any property $\hat{f}_{(\alpha)}$ with a discontinuity across the interface may be written as

$$f = \sum_{\alpha=1}^n c_{(\alpha)} \hat{f}_{(\alpha)}, \quad n = 2 \text{ or } 3 \quad (2.26)$$

$$\frac{1}{f} = \sum_{\alpha=1}^n \frac{c_{(\alpha)}}{\hat{f}_{(\alpha)}}, \quad n = 2 \text{ or } 3 \quad (2.27)$$

for WAM and WHM, respectively.

2.3 Electric field

2.3.1 Maxwell stress tensor and electric forces

Under static conditions, electric and magnetic phenomena are independent since their fields are uncoupled. If characteristic time scale of the electrostatic process is larger than that of the magnetic phenomena, the electrostatic equations provide a good approximation [108]. When considering electrohydrodynamics, dynamic currents are small and magnetic induction effects may be neglected. As such, the coupling between hydrodynamics described by equations (2.1) and (2.6) and electrostatics is through Maxwell stress tensor [108, 149, 150],

$$\mathbb{T}_{(e)} = \varepsilon^* \varepsilon_0 \mathbf{E} \mathbf{E} - \frac{1}{2} \varepsilon^* \varepsilon_0 \mathbf{E} \cdot \mathbf{E}, \quad (2.28)$$

which excludes magnetic phenomena. Here \mathbf{E} denotes the electric field vector, ε_0 is the electric permittivity of the vacuum and ε_r is the relative permittivity of the fluid. Absolute permittivity, $\varepsilon = \varepsilon^* \varepsilon_0$, will be referred to as permittivity for simplicity.

The electric force $\mathbf{f}_{(e)}$ of equation (2.6) is calculated by taking the divergence of the Maxwell stress tensor. This results in

$$\mathbf{f}_{(e)} = \mathbf{V} \cdot \mathbb{T}_{(e)} = -\frac{1}{2} \mathbf{E} \cdot \mathbf{E} \mathbf{V} \varepsilon + q^v \mathbf{E} + \mathbf{V} \left(\frac{1}{2} \mathbf{E} \cdot \mathbf{E} \frac{\partial \varepsilon}{\partial \rho} \rho \right). \quad (2.29)$$

Here q^v is the volume charge density near the interface.

The first term on the right hand side of equation (2.29), called the polarization force (dielectric force),

$$\mathbf{f}_{(ep)} = -\frac{1}{2} \mathbf{E} \cdot \mathbf{E} \mathbf{V} \varepsilon, \quad (2.30)$$

will always act in a direction normal to the interface, pointing from higher permittivity medium to the lower permittivity medium, due to negative permittivity gradient while its magnitude is mostly dependent on field intensity. The second term, called Coulomb force,

$$\mathbf{f}_{(eq)} = q^v \mathbf{E}, \quad (2.31)$$

is a result of interactions between electric field and electric charges and will be oriented

in the direction of the electric field. The third term, called electrorestriction, represents the effects of changes in permittivity due to variations in fluid density. This term has no contribution in an incompressible and isothermal fluid. The resultant electric force has a complex behavior which will be discussed further in upcoming sections.

2.3.2 Governing equations

In order to calculate the electric force of equation (2.29), the electric field vector and volumetric charge have to be known. As mentioned before, magnetic effects are negligible in electrohydrodynamics and this results in an irrotational electric field [108]

$$\nabla \times \mathbf{E} = 0, \quad (2.32)$$

which in turn allows for defining the electric field as the gradient of an electric potential as

$$\mathbf{E} = -\nabla \phi. \quad (2.33)$$

Volumetric charge may be defined according to Gauss's law as the divergence of electric displacement, εE , in differential form

$$q^v = \nabla \cdot (\varepsilon \mathbf{E}). \quad (2.34)$$

The volumetric charge behaves according to a diffusion-advection equation of the form

$$\frac{Dq^v}{Dt} = \nabla \cdot (\sigma \mathbf{E}), \quad (2.35)$$

where σ is electric conductivity. Combining equations (2.34) and (2.35), it is possible to obtain the following relation

$$q^v = q_0^v e^{-\frac{\sigma}{\varepsilon} t}, \quad (2.36)$$

for charge relaxation in a homogeneous incompressible fluid [111]. This gives an electrical timescale of $\tau_e = \varepsilon/\sigma$ for the relaxation of an initial charge of q_0^v . Comparing τ_e with viscous timescale of the flow given by $\tau_h = \rho l^2/\mu$ where l is an appropriate length scale, it is possible to define two distinctive regimes for slightly conducting fluids. To narrow down the scope of discussion, it is assumed that no free charges present in the system. If $\tau_e \gg \tau_h$ the fluid will behave like a perfect dielectric as charge accumulation takes much longer than the flow process, effectively acting like no free charge is present on the interface. On the other hand, if $\tau_e \ll \tau_h$, the charge relaxation is instantaneous when compared to flow phenomena, meaning that charge accumulation process at the interface is unaffected by the flow. The former situation is the basis of perfect dielectric model while the latter leads to leaky dielectric model.

Perfect dielectric model

As mentioned before, when $\tau_e \gg \tau_h$ the fluids may be considered as perfect dielectric material. In this situation, the external electric field polarizes the molecules of the material and subsequently these newly formed molecular dipoles affect the electric field. The ensuing electric field may be calculated directly by solving for the electric potential using equation (2.34). As no free charge is present in the medium, the governing equation for the electric potential may be written as

$$\nabla \cdot (\varepsilon \nabla \phi) = 0. \quad (2.37)$$

Subsequently, the electric field is determined using equation (2.33) and substituted in equation (2.29) where q^v is zero to calculate $\mathbf{f}_{(e)}$.

As there is no free charge at the interface between the two fluids of different permittivities, continuity of the normal component of electric displacement and continuity of the electric potential

$$\|\phi\| = 0, \quad (2.38)$$

$$\|\varepsilon \nabla \phi\| \cdot \mathbf{n} = 0, \quad (2.39)$$

are applicable. In a similar approach to that of the CSF method, the above boundary conditions are implicitly incorporated in equation (2.37) when permittivity is smoothed across the interface using either of the equations (2.26) or (2.27).

Equations (2.29), (2.33) and (2.37) provide the complete description of the perfect dielectric model and its coupling to the momentum equation (2.6). It is worth noting that electric conductivity has no role in perfect dielectric model.

Leaky dielectric model

When $\tau_e \ll \tau_h$, the charge density at the interface of the multi-phase medium reaches a steady state much faster than the timescale of the flow. Equation (2.35) may be cast into dimensionless form

$$\frac{\tau_h}{\tau_e} \left(\frac{Dq^*}{Dt^*} \right) = \nabla^* \cdot (\sigma^* \mathbf{E}^*), \quad (2.40)$$

where asterisks denote dimensionless variables. At the limit of leaky dielectric fluids the left hand side of the equation (2.40) vanishes leading to static charge conservation expressed by the divergence of the current density, $\sigma \mathbf{E}$, due to the electrical conduction. This gives the following relation

$$\nabla \cdot (\sigma \nabla \phi) = 0, \quad (2.41)$$

for the electric potential of a leaky dielectric material.

At the interface between two leaky dielectric materials, electric potential and electric current remain continuous. This results in the following boundary conditions

$$\|\phi\| = 0, \quad (2.42)$$

$$\|\sigma \nabla \phi\| \cdot \mathbf{n} = 0. \quad (2.43)$$

As discussed before in perfect dielectric model, the above boundary conditions are implicitly incorporated in equation (2.37) when conductivity is smoothed across the interface using either of the equations (2.26) or (2.27).

Equations (2.29), (2.33) and (2.41) provide the complete description of the leaky dielectric model and its coupling to the momentum equation (2.6). It is worth noting that electric conductivity's only role is in determination of electric field and it has no direct role in calculation of $\mathbf{f}_{(e)}$. As long as the condition $\tau_e \ll \tau_h$ is satisfied, only the conductivity ratio of the two materials affects the electric field.

2.3.3 General boundary conditions for an interface

The form of $\mathbf{f}_{(e)}$ derived in equation (2.29) is analogous to the CSS treatment of the surface tension forces. An alternative form of equation (2.29) resembling the CSF method may be derived by modifying the boundary conditions at the interface.

Continuity of a material interface dictates that

$$\begin{cases} \|u^i n^i\| = 0, \\ \|u^i s^i\| = 0. \end{cases} \quad (2.44)$$

The stress tensor, including electrical and viscous components, may be written as [151]

$$\mathbb{T}^{ij} = - \left\{ p + \frac{E^2}{2} \left[\varepsilon - \rho \left(\frac{\partial \varepsilon}{\partial \rho} \right) \right] \right\} \delta^{ij} + E^i D^j + \mu (u^{i,j} + u^{j,i}), \quad (2.45)$$

where $\mathbf{D} = \varepsilon \mathbf{E}$ is electric displacement vector. As such, the stress balance across the interface is [143]

$$\|\mathbb{T}^{ij}\| n^j = \gamma \kappa n^i - \gamma^{,i}, \quad (2.46)$$

which is essentially a combination of equations (2.9) and (2.10) with the electrical effects included.

The above stress tensor of equation (2.45) may be multiplied with surface normal to find the in-plane stress or traction vector,

$$\mathbb{T}^{ij} n^j = - \left\{ p + \frac{E^2}{2} \left[\varepsilon - \rho \left(\frac{\partial \varepsilon}{\partial \rho} \right) \right] \right\} n^i + E^i D^j n^j + \mu (u^{i,j} + u^{j,i}) n^j. \quad (2.47)$$

Further multiplication with interface normal vector n^i gives normal stresses as

$$\begin{aligned}
\mathbb{T}^{ij}n^jn^i &= - \left\{ p + \frac{E^2}{2} \left[\varepsilon - \rho \left(\frac{\partial \varepsilon}{\partial \rho} \right) \right] \right\} \delta^{ii} + E^i D^j n^j n^i + \mu (u^{ij} + u^{ji}) n^j n^i \\
&= -p - \frac{E^2}{2} \left[\varepsilon - \rho \left(\frac{\partial \varepsilon}{\partial \rho} \right)_T \right] + E_{(n)} D_{(n)} + \mu \left(n^i \frac{\partial u^i}{\partial n} + n^j \frac{\partial u^j}{\partial n} \right) \\
&= -p - \frac{\varepsilon}{2} (E_{(n)}^2 + E_{(s)}^2) + \frac{\rho E^2}{2} \left(\frac{\partial \varepsilon}{\partial \rho} \right) + \varepsilon E_{(n)} E_{(n)} + \mu \left(n^i \frac{\partial u^i}{\partial n} + n^j \frac{\partial u^j}{\partial n} \right) \\
&= -p - \frac{\varepsilon}{2} (E_{(n)}^2 - E_{(s)}^2) + \frac{\rho E^2}{2} \left(\frac{\partial \varepsilon}{\partial \rho} \right) + 2\mu n^i \frac{\partial u^i}{\partial n}, \tag{2.48}
\end{aligned}$$

where $\square_{(n)}$ and $\square_{(s)}$ denoted normal and tangential components. Multiplication of traction with interface tangent vector s^i results in the tangential component of the stress as

$$\begin{aligned}
\mathbb{T}^{ij}n^js^i &= - \left\{ p + \frac{E^2}{2} \left[\varepsilon - \rho \left(\frac{\partial \varepsilon}{\partial \rho} \right) \right] \right\} n^i s^i + E^i D^j n^j s^i + \mu (u^{ij} + u^{ji}) n^j s^i \\
&= E_{(s)} D_{(n)} + \mu \left(s^i \frac{\partial u^i}{\partial n} + n^j \frac{\partial u^j}{\partial s} \right) \\
&= \varepsilon E_{(s)} E_{(n)} + \mu \left(s^i \frac{\partial u^i}{\partial n} + n^j \frac{\partial u^j}{\partial s} \right). \tag{2.49}
\end{aligned}$$

Replacing equations (2.48) and (2.49) in equation (2.46) and assuming $\partial \varepsilon / \partial \rho = 0$, the stress balance across the interface may be written as

$$\begin{cases} \left\| -p - \frac{\varepsilon}{2} (E_{(n)}^2 - E_{(s)}^2) + \frac{\rho E^2}{2} \left(\frac{\partial \varepsilon}{\partial \rho} \right)_T + 2\mu n^i \frac{\partial u^i}{\partial n} \right\| = \gamma \kappa, \\ \left\| \varepsilon E_{(s)} E_{(n)} + \mu \left(s^i \frac{\partial u^i}{\partial n} + n^j \frac{\partial u^j}{\partial s} \right) \right\| = -\frac{\partial \gamma}{\partial s}, \end{cases} \tag{2.50}$$

where $\square_{(\alpha n)}$ and $\square_{(\alpha s)}$ denote normal and tangent in fluid α . Rearranging with respect to pressure for normal direction and surface gradient of surface tension coefficient in the tangential direction, one may write

$$\begin{cases} \|p\| = \left\{ \frac{\varepsilon^{(1)}}{2} (E_{(1n)}^2 - E_{(1s)}^2) - \frac{\varepsilon^{(2)}}{2} (E_{(2n)}^2 - E_{(2s)}^2) \right\} \\ \quad + \left\{ 2\mu_{(1)} n^i \left(\frac{\partial u^i}{\partial n} \right)_{(1)} - 2\mu_{(2)} n^i \left(\frac{\partial u^i}{\partial n} \right)_{(2)} \right\} + \gamma \kappa, \\ -\frac{\partial \gamma}{\partial s} = \left\{ E_{(1s)} D_{(1n)} - E_{(2s)} D_{(2n)} \right\} \\ \quad + \left\{ \mu_{(1)} \left(s^i \frac{\partial u^i}{\partial n} + n^j \frac{\partial u^j}{\partial s} \right)_{(1)} - \mu_{(2)} \left(s^i \frac{\partial u^i}{\partial n} + n^j \frac{\partial u^j}{\partial s} \right)_{(2)} \right\}. \end{cases} \tag{2.51}$$

One may identify force components analogous to CSF representation, including the sur-

face tension itself, as

$$\left\{ \begin{array}{l} f_{(sn)} = \gamma \kappa, \\ f_{(vn)} = 2\mu_{(1)} n^i \left(\frac{\partial u^i}{\partial n} \right)_{(1)} - 2\mu_{(2)} n^i \left(\frac{\partial u^i}{\partial n} \right)_{(2)}, \\ f_{(en)} = \frac{\varepsilon_{(1)}}{2} (E_{(1n)}^2 - E_{(1s)}^2) - \frac{\varepsilon_{(2)}}{2} (E_{(2n)}^2 - E_{(2s)}^2), \\ f_{(ss)} = -\frac{\partial \gamma}{\partial s}, \\ f_{(vs)} = \mu_{(1)} \left(s^i \frac{\partial u^i}{\partial n} + n^i \frac{\partial u^i}{\partial s} \right)_{(1)} - \mu_{(2)} \left(s^i \frac{\partial u^i}{\partial n} + n^i \frac{\partial u^i}{\partial s} \right)_{(2)}, \\ f_{(es)} = E_{(1s)} D_{(1n)} - E_{(2s)} D_{(2n)}. \end{array} \right. \quad (2.52)$$

Perfect dielectric model

The electrical components of the forces give in equation (2.52) may be further simplified depending on the chosen electrical model. For a perfect dielectric model, the continuity of tangential field and electrical displacement, $\mathbf{D} = \varepsilon \mathbf{E}$, across the interface may be expressed as

$$\left\{ \begin{array}{l} \|\epsilon^{ijk} n^j E^k\| = 0, \\ \|D^i n^i\| = 0, \end{array} \right. \quad (2.53)$$

where ϵ^{ijk} is the Levi-Civita symbol.

There are two approaches to simplifying (2.52) using the boundary conditions given in equation (2.53). The normal component of the first approach relies only on the electric field and may be derived as

$$\begin{aligned} f_{(en)} &= \frac{\varepsilon_{(1)}}{2} (E_{(1n)}^2 - E_{(1s)}^2) - \frac{\varepsilon_{(2)}}{2} (E_{(2n)}^2 - E_{(2s)}^2) \\ &= \frac{\varepsilon_{(1)}}{2} \left[\left(\frac{\varepsilon_{(2)} E_{(2n)}}{\varepsilon_{(1)}} \right)^2 - E_{(2s)}^2 \right] - \frac{\varepsilon_{(2)}}{2} (E_{(2n)}^2 - E_{(2s)}^2) \\ &= E_{(2s)}^2 \left(\frac{\varepsilon_{(2)}}{2} - \frac{\varepsilon_{(1)}}{2} \right) + E_{(2n)}^2 \left(\frac{\varepsilon_{(2)}^2}{2\varepsilon_{(1)}} - \frac{\varepsilon_{(2)}}{2} \right) \\ &= \frac{\varepsilon_{(2)} - \varepsilon_{(1)}}{2} \left(\frac{\varepsilon_{(2)}}{\varepsilon_{(1)}} E_{(2n)}^2 + E_{(2s)}^2 \right). \end{aligned} \quad (2.54)$$

The above result is similar to the one presented in [151] and gives the final result in terms of tangential and normal field intensities. The normal component using the second approach

may be written as

$$\begin{aligned}
f_{(en)} &= \frac{\varepsilon_{(1)}}{2} (E_{(1n)}^2 - E_{(1s)}^2) - \frac{\varepsilon_{(2)}}{2} (E_{(2n)}^2 - E_{(2s)}^2) \\
&= E_{(2s)}^2 \left(\frac{\varepsilon_{(2)}}{2} - \frac{\varepsilon_{(1)}}{2} \right) + E_{(2n)}^2 \left(\frac{\varepsilon_{(2)}}{2\varepsilon_{(1)}} - \frac{\varepsilon_{(2)}}{2} \right) \\
&= D_{(2n)}^2 \left(\frac{1}{2\varepsilon_{(1)}} - \frac{1}{2\varepsilon_{(2)}} \right) + E_{(2s)}^2 \left(\frac{\varepsilon_{(2)}}{2} - \frac{\varepsilon_{(1)}}{2} \right) \\
&= \frac{D_{(n)}^2}{2} \left(\frac{1}{\varepsilon_{(1)}} - \frac{1}{\varepsilon_{(2)}} \right) + \frac{E_{(s)}^2}{2} (\varepsilon_{(2)} - \varepsilon_{(1)}), \tag{2.55}
\end{aligned}$$

which represents the results in terms of tangential electric field and normal electrical displacement. This form is identical to the one obtained in [149]. Regardless of the approach taken, the tangential components cancel out across the interface,

$$f_{(es)} = E_{(1s)}D_{(1n)} - E_{(2s)}D_{(2n)} = 0, \tag{2.56}$$

which is in agreement with the observation made for the polarization component of the electrical forces.

Using the second approach, the stress balance across the interface for perfect dielectric fluids may be written as

$$\left\{ \begin{aligned}
\|p\| &= \left\{ \frac{D_{(n)}^2}{2} \left(\frac{1}{\varepsilon_{(1)}} - \frac{1}{\varepsilon_{(2)}} \right) + \frac{E_{(s)}^2}{2} (\varepsilon_{(2)} - \varepsilon_{(1)}) \right\} \\
&+ \left\{ 2\mu_{(1)}n^i \left(\frac{\partial u^i}{\partial n} \right)_{(1)} - 2\mu_{(2)}n^i \left(\frac{\partial u^i}{\partial n} \right)_{(2)} \right\} + \gamma\kappa, \\
-\frac{\partial\gamma}{\partial s} &= \left\{ \mu_{(1)} \left(s^i \frac{\partial u^i}{\partial n} + n^i \frac{\partial u^i}{\partial s} \right)_{(1)} - \mu_{(2)} \left(s^i \frac{\partial u^i}{\partial n} + n^i \frac{\partial u^i}{\partial s} \right)_{(2)} \right\},
\end{aligned} \right. \tag{2.57}$$

Leaky dielectric model

The simplifications applied to equation (2.52) for a leaky dielectric model relies on continuity of tangential electric field and normal current, $\mathbf{J} = \sigma\mathbf{E}$, given by

$$\left\{ \begin{aligned}
\|\epsilon^{ijk}n^jE^k\| &= 0, \\
\|J^in^i\| &= 0.
\end{aligned} \right. \tag{2.58}$$

The normal electric force may be written in terms of electrical properties of both fluids

and electric field intensity in one fluids, *e.g.* fluid two, as

$$\begin{aligned}
f_{(en)} &= \frac{\varepsilon_{(1)}}{2} (E_{(1n)}^2 - E_{(1s)}^2) - \frac{\varepsilon_{(2)}}{2} (E_{(2n)}^2 - E_{(2s)}^2) \\
&= \frac{\varepsilon_{(1)}}{2} \left[\left(\frac{\sigma_{(2)} E_{(2n)}}{\sigma_{(1)}} \right)^2 - E_{(2s)}^2 \right] - \frac{\varepsilon_{(2)}}{2} (E_{(2n)}^2 - E_{(2s)}^2) \\
&= \frac{E_{(2n)}^2}{2} \left[\left(\frac{\sigma_{(2)}}{\sigma_{(1)}} \right)^2 \varepsilon_{(1)} - \varepsilon_{(2)} \right] + \frac{E_{(2s)}^2}{2} (\varepsilon_{(2)} - \varepsilon_{(1)}), \tag{2.59}
\end{aligned}$$

which is similar to the formulation provided in [151].

A more compact form may be obtained by writing in terms of tangential electric field and normal current. The normal component of the electric force in this approach may be written as

$$\begin{aligned}
f_{(en)} &= \frac{\varepsilon_{(1)}}{2} (E_{(1n)}^2 - E_{(1s)}^2) - \frac{\varepsilon_{(2)}}{2} (E_{(2n)}^2 - E_{(2s)}^2) \\
&= E_{(2n)}^2 \left[\left(\frac{\sigma_{(2)}}{\sigma_{(1)}} \right)^2 \frac{\varepsilon_{(1)}}{2} - \frac{\varepsilon_{(2)}}{2} \right] + E_{(2s)}^2 \left(\frac{\varepsilon_{(2)}}{2} - \frac{\varepsilon_{(1)}}{2} \right) \\
&= J_{(2n)}^2 \left[\frac{\varepsilon_{(1)}}{2\sigma_{(1)}^2} - \frac{\varepsilon_{(2)}}{2\sigma_{(2)}^2} \right] + E_{(2s)}^2 \left(\frac{\varepsilon_{(2)}}{2} - \frac{\varepsilon_{(1)}}{2} \right) \\
&= \frac{J_{(n)}^2}{2} \left[\frac{\varepsilon_{(1)}}{\sigma_{(1)}^2} - \frac{\varepsilon_{(2)}}{\sigma_{(2)}^2} \right] + \frac{E_{(s)}^2}{2} (\varepsilon_{(2)} - \varepsilon_{(1)}), \tag{2.60}
\end{aligned}$$

while the tangential component is

$$\begin{aligned}
f_{(es)} &= E_{(1s)} D_{(1n)} - E_{(2s)} D_{(2n)} \\
&= \varepsilon_{(1)} E_{(1s)} E_{(1n)} - \varepsilon_{(2)} E_{(2s)} E_{(2n)} \\
&= \frac{\varepsilon_{(1)}}{\sigma_{(1)}} E_{(1s)} J_{(1n)} - \frac{\varepsilon_{(2)}}{\sigma_{(2)}} E_{(2s)} J_{(2n)} \\
&= E_{(s)} J_{(n)} \left(\frac{\varepsilon_{(1)}}{\sigma_{(1)}} - \frac{\varepsilon_{(2)}}{\sigma_{(2)}} \right). \tag{2.61}
\end{aligned}$$

The above formulation is identical to the one derived by Tomar *et al.* [149] who modified equation (2.29) directly to obtain equations (2.60) and (2.61). Similar to the difference between CSF and CSS for calculating surface tension forces, the difference between (2.29) and (2.60-2.61) lies mostly in the numerical implementation. The representation given in (2.60) and (2.61) satisfies the conditions put forward by Brackbill *et al.* [143], provided that the boundary conditions given in equation (2.58) are satisfied. On the other hand, equation (2.29) contains divergence of electric field in q^v which does not approach a δ function as interface width becomes infinitesimally small, thus violating the conditions set forth in [143]. However, in a numerical implementation of (2.60-2.61), the boundary conditions given in (2.58) are not completely satisfied and this negates advantage of this method over (2.29).

Using both $E_{(s)}$ and $J_{(n)}$, the stress balance across the interface may be rewritten as

$$\left\{ \begin{aligned} \|p\| &= \left\{ \frac{J_{(n)}^2}{2} \left(\frac{\varepsilon_{(1)}}{\sigma_{(1)}^2} - \frac{\varepsilon_{(2)}}{\sigma_{(2)}^2} \right) + \frac{E_{(s)}^2}{2} (\varepsilon_{(2)} - \varepsilon_{(1)}) \right\} \\ &+ \left\{ 2\mu_{(1)} n^i \left(\frac{\partial u^i}{\partial n} \right)_{(1)} - 2\mu_{(2)} n^i \left(\frac{\partial u^i}{\partial n} \right)_{(2)} \right\} + \gamma \kappa, \\ -\frac{\partial \gamma}{\partial s} &= \left\{ E_{(s)} J_{(n)} \left(\frac{\varepsilon_{(1)}}{\sigma_{(1)}} - \frac{\varepsilon_{(2)}}{\sigma_{(2)}} \right) \right\} \\ &+ \left\{ \mu_{(1)} \left(s^i \frac{\partial u^i}{\partial n} + n^i \frac{\partial u^i}{\partial s} \right)_{(1)} - \mu_{(2)} \left(s^i \frac{\partial u^i}{\partial n} + n^i \frac{\partial u^i}{\partial s} \right)_{(2)} \right\}. \end{aligned} \right. \quad (2.62)$$

2.4 Fluid-structure/solid interaction

In its classic form, the two-dimensional equations governing the motion of a rigid body may be written as

$$\frac{d\mathbf{x}_s}{dt} = \mathbf{u}_s^t, \quad (2.63)$$

$$\frac{d\theta_s}{dt} = u_s^r, \quad (2.64)$$

$$M_s \frac{d\mathbf{u}_s^t}{dt} = \mathbf{f}_{(h)} + \mathbf{f}_{(b)} + \mathbf{f}_{(e)}, \quad (2.65)$$

$$I_s \frac{du_s^r}{dt} = T_{(h)} + T_{(e)}, \quad (2.66)$$

where \mathbf{x}_s and \mathbf{u}_s^t are the linear position and velocity, θ_s and u_s^r are the angle and angular velocity, T is the torque exerted on the body and M_s and I_s denote mass and inertia, respectively. Except for

$$\mathbf{f}_{(b)} = M_s \mathbf{g}, \quad (2.67)$$

the method of coupling equations (2.65) and (2.66) to the fluid, *i.e.* calculating forces and torques, is dependent on the FSI scheme.

In methods with explicit boundaries and conforming meshes, such as ALE and SPH, it is possible to express the forces and torques through the stress applied at the interface as

$$\mathbf{f}_{(\square)} = \int_{\partial B} \mathbf{n} \cdot \mathbb{T}_{(\square)} d\mathbf{l}, \quad (2.68)$$

$$T_{(\square)} = \int_{\partial B} \mathbf{r}_s \times \mathbf{n} \cdot \mathbb{T}_{(\square)} d\mathbf{l}, \quad (2.69)$$

where \square stands for either of hydrodynamic or Maxwell stress tensor and \mathbf{r}_s is the vector connecting the body's center of mass to the point where $\mathbb{T}_{(\square)}$ is applied. In this case the fluid has to match a boundary velocity of

$$\mathbf{u} = \mathbf{u}_s^t + u_s^r \times \mathbf{r}_s, \quad (2.70)$$

to impose the no-slip boundary condition

In an approach such as IB method, the coupling is achieved via a body force rather than stress transfer at the interface. In IB, the mesh is fixed and the interface travels over the fluid mesh. As the rigid body moves due to gravity and electrical forces, the hydrodynamic body force, calculated at the interface, is applied to the fluid to ensure the no-slip condition. It adjusts the velocity difference between the rigid body and fluid by accelerating or decelerating the fluid [61, 152].

On the other hand FD methods assume both fluid and solid to behave as fluids of different characteristics. Distributed Lagrange Multiplier (DLM) method uses Lagrange multipliers to impose rigid body-like stress distribution within the fluid region representing the solid body [57]. Viscous Penalty (VP) method achieves the same goal by increasing the viscosity of the fluid region representing the solid body [59, 153]. An explicit interface propagation is used in DLM while a color function is used in VP.

A similar approach to that of the VP method is taken in this study. An increased viscosity is used to mimic a solid body while the boundaries are moved in a Lagrangian fashion [59, 153]. Additionally, rigidity constraints for linear and angular motion are applied to the bodies [72, 154]. Assuming a rigid body discretized by J_s particles, the rigidity constraints may be interpreted as

$$\mathbf{u}_s^t = \frac{1}{M_s} \sum_{j=1}^{J_s} \mathbf{u}_j, \quad (2.71)$$

$$u_s^r = \frac{1}{I_s} \sum_{j=1}^{J_s} \mathbf{u}_j \times \mathbf{r}_{js}. \quad (2.72)$$

Further details about the method will be provided in subsequent sections.

2.5 Dimensionless form of equations

A general form of the dimensionless equations may be obtained by using characteristic scales. Since each case has its own characteristic values, the relevant dimensionless numbers will be provided in that case's respective section. Characteristic scales used are defined as

$$\begin{aligned} \mathbf{x}^* &= \frac{\mathbf{x}}{l_c}, & \mathbf{u}^* &= \frac{\mathbf{u}}{u_c}, & p^* &= \frac{p}{p_c}, & \mathbf{E}^* &= \frac{\mathbf{E}}{E_c}, & t^* &= t \left(\frac{u_c}{l_c} \right), \\ \rho^* &= \frac{\rho}{\rho_c}, & \mu^* &= \frac{\mu}{\mu_c}, & \gamma^* &= \frac{\gamma}{\gamma_c}, & g^* &= \frac{g}{g_c}, & \varepsilon^* &= \frac{\varepsilon}{\varepsilon_c}, \end{aligned} \quad (2.73)$$

leading to the following dimensionless form

$$\rho^* \frac{D^* \mathbf{u}^*}{D^* t^*} = -Eu \nabla^* p^* + \frac{1}{Re} \nabla^* \cdot \boldsymbol{\tau}^* + \frac{1}{Fr_{(b)}} \mathbf{f}_{(b)}^* + \frac{1}{We_{(s)}} \mathbf{f}_{(s)}^* + \frac{1}{Ei_{(e)}} \mathbf{f}_{(e)}^*, \quad (2.74)$$

where

$$\text{Eu} = \frac{p_c}{\rho_c u_c^2}, \quad (2.75)$$

$$\text{Re} = \frac{\rho_c u_c l_c}{\mu_c}, \quad (2.76)$$

$$\text{Fr} = \frac{u_c^2}{g_c l_c}, \quad (2.77)$$

$$\text{We} = \frac{\rho_c l_c u_c^2}{\gamma_c}, \quad (2.78)$$

$$\text{Ei} = \frac{\rho_c u_c^2}{\varepsilon_c E_c^2}, \quad (2.79)$$

are Euler, Reynolds, Froude, Weber and Electroinertial numbers. Equations (2.1), (2.37) and (2.41) remain unchanged in their dimensionless forms.

Due to different nature of the cases studied here, the relevant scales and dimensionless values will be provided in respective sections.

Chapter 3

Smoothed particle hydrodynamics and its numerical implementation

3.1 Integral representation

An exact representation of any function of the form $f(\mathbf{r})$ at point \mathbf{r}_i in volume V , encompassing the whole computational domain, may be obtained by its convolution with Dirac delta function as

$$f(\mathbf{r}_i) = \int_V f(\mathbf{r}') \delta(|\mathbf{r}_i - \mathbf{r}'|) d\mathbf{r}', \quad (3.1)$$

where Dirac delta function is

$$\delta(|\mathbf{r}_i - \mathbf{r}|) = \begin{cases} \infty, & \mathbf{r} = \mathbf{r}_i, \\ 0, & \text{otherwise.} \end{cases} \quad (3.2)$$

While $\int_V \delta d\mathbf{r} = 1$ is bounded, δ is not suitable for numerical applications due to its infinite peak since every variable has a finite representation in computational hardware. To provide a practical integral representation of the function at a specific point in continuum space, δ is replaced by a weighting function, hereby referred to as the kernel function, resulting in the following relation

$$\langle f(\mathbf{r}_i) \rangle = \int_{\Omega} f(\mathbf{r}') w(|\mathbf{r}_i - \mathbf{r}'|; h) d\mathbf{r}'. \quad (3.3)$$

Here, angled brackets represent a kernel approximation operation for the original function. The kernel has the same normalization property as δ ,

$$\int_{\Omega} w(|\mathbf{r}_i - \mathbf{r}|; h) d\mathbf{r} = 1, \quad (3.4)$$

within its bounded domain of Ω , also known as compact support, such that $w = 0$ if $\mathbf{r} \notin \Omega$. For a kernel function with a cylindrical (or spherical in three dimensions) support domain

this reduces to

$$w(|\mathbf{r}_i - \mathbf{r}|; h) = 0 \quad \text{if } |\mathbf{r}_i - \mathbf{r}| > nh, \quad (3.5)$$

where h is called the smoothing length and n is usually a constant depending on the kernel type. For infinitesimally small h , w must converge to δ to recover equation (3.2). A Taylor series expansion of equation (3.3) shows the approximation is second order accurate as long as w is an even function [155].

In a similar fashion, the divergence operation may be formulated as

$$\langle \nabla \cdot \mathbf{f}(\mathbf{r}_i) \rangle = - \int_{\Omega} \mathbf{f}(\mathbf{r}') \cdot \nabla w(|\mathbf{r}_i - \mathbf{r}'|; h) d\mathbf{r}'. \quad (3.6)$$

This shows an important property of the SPH where derivative of a variable manifested itself as a kernel derivative. This shows the importance of the kernel function in SPH approximations, especially in discrete space.

Besides the above mentioned conditions, kernels have to satisfy several other criteria to ensure stability, accuracy and consistency of the integral representation [155, 156]. Some of the kernels used are Gaussian [74], Wendall [157], quadratic [158], quartic [73], cubic [159] and quintic [160]. In this work two dimensional forms of both cubic spline kernel,

$$w(|\mathbf{r}_i - \mathbf{r}|; h) = \frac{15}{7\pi h^2} \begin{cases} \frac{2}{3} - q^2 + \frac{1}{2}q^3, & 0 \leq q < 1, \\ \frac{1}{6}(2 - q)^3, & 1 \leq q < 2, \\ 0, & 2 \leq q, \end{cases} \quad (3.7)$$

and quintic spline kernel,

$$w(|\mathbf{r}_i - \mathbf{r}|; h) = \frac{7}{478\pi h^2} \begin{cases} (3 - q)^5 - 6(2 - q)^5 + 15(1 - q)^5, & 0 \leq q < 1, \\ (3 - q)^5 - 6(2 - q)^5, & 1 \leq q < 2, \\ (3 - q)^5, & 2 \leq q < 3, \\ 0, & 3 \leq q, \end{cases} \quad (3.8)$$

are used where $q = |\mathbf{r}_i - \mathbf{r}|/h$. It is notable that kernels have a dimension of inverse of length squared which helps define an area in two dimensions.

As mentioned in section 2.2, the kernel functions are used to smooth the color function before calculating the surface tension and interpolating material properties. For the same smoothing length, cubic spline has a smaller support domain and higher peak when compared to quintic spline. For this reason, cubic spline kernel is used to calculate the smoothed color function resulting in a thinner interface. On the other hand, quintic spline kernel is used to calculate the derivatives which increases the stability and accuracy of the method [148].

3.2 Particle representation

In SPH, the computation domain is discretized using a finite number of particles. Integral representations given in section 3.1 are converted to summations over all neighboring particles j within the compact support of the particle of interest at \mathbf{r}_i . Equation (3.3) may be approximated further as

$$\langle \mathbf{f}(\mathbf{r}_i) \rangle = \sum_{j=1}^{J_n} \frac{1}{\psi_j} \mathbf{f}(\mathbf{r}_j) w(r_{ij}; h), \quad (3.9)$$

where J_n is the number of neighboring particles, $\mathbf{r}_{ij} = \mathbf{r}_i - \mathbf{r}_j$, $r_{ij} = |\mathbf{r}_{ij}|$ and ψ_i is the number density defined as

$$\psi_i = \sum_{j=1}^{J_n} w(r_{ij}; h), \quad (3.10)$$

which represents the inverse of particle volume. From this point forward $w(r_{ij}; h)$ will be referred to as w_{ij} and the angled brackets will be dropped for brevity.

3.2.1 Derivatives of variables

There are two approximations in the particle representation given in equation (3.9). The first one is due to the difference between the kernel and delta functions. The second one is due to the fact that a discrete representation of the kernel does not have the normalization property. In the simple case of interpolation at a certain point in space, ψ acts as a renormalization coefficient. It represents the discrete volume of the particle rather than its intended continuum value, thus resolving the normalization problem. However, the situation is more complicated for derivatives of the function. There are two approaches to remedy the errors due to discrete kernel representation. The first one is to correct the kernel to mimic the properties of the continuous counterpart while another approach is to correct the derivative itself.

The first approach falls under the Reproducing Kernel Particle Method (RKPM) where a correction function is multiplied with the kernel function producing the corrected kernel. The correction function is calculated by setting the higher moments of the corrected kernel to zero [161]. For an n th order accurate reconstruction, all higher moments up to n th moment should be set to zero. The method has been used by many authors [162–170]. Linear reproduction condition for the kernel is equivalent to constant reproduction condition for the gradient of the kernel. One such correction function in two dimensions given in [171]

is

$$\mathbf{C}_i = \begin{bmatrix} \sum_{j=1}^{J_n} \frac{1}{\psi_j} x_{ji}^{(1)} \frac{\partial w_{ij}}{\partial x_{ij}^{(1)}} & \sum_{j=1}^{J_n} \frac{1}{\psi_j} x_{ji}^{(1)} \frac{\partial w_{ij}}{\partial x_{ij}^{(2)}} \\ \sum_{j=1}^{J_n} \frac{1}{\psi_j} x_{ji}^{(2)} \frac{\partial w_{ij}}{\partial x_{ij}^{(1)}} & \sum_{j=1}^{J_n} \frac{1}{\psi_j} x_{ji}^{(2)} \frac{\partial w_{ij}}{\partial x_{ij}^{(2)}} \end{bmatrix}^{-1}, \quad (3.11)$$

which modifies the kernel gradient as $\mathbf{C}_i \nabla w_{ij}$ and corrects the first derivative. Here a numeric superscript in parentheses is used to show the components of a vector.

The correction method used here is based on the second approach where the derivative of the variable is corrected directly [148]. The procedure of deriving the first derivative and Laplacian operator for a vector in Cartesian coordinates is given in the following sections.

First derivative

The approximation for the gradient starts with Taylor series expansion of $f^p(\mathbf{r}_j)$, *i.e.* p th component of function f at point \mathbf{r}_j where particle j resides. The expansion up to second derivative with respect to particle i may be written as

$$f^p(\mathbf{r}_j) = f^p(\mathbf{r}_i) + r_{ji}^l \frac{\partial f^p(\mathbf{r}_i)}{\partial x_i^l} \Big|_{\mathbf{r}_j=\mathbf{r}_i} + \frac{1}{2} r_{ji}^l r_{ji}^k \frac{\partial^2 f^p(\mathbf{r}_i)}{\partial x_i^l \partial x_i^k} \Big|_{\mathbf{r}_j=\mathbf{r}_i} + \mathcal{O}(\mathbf{r}^3) \quad (3.12)$$

Upon multiplying equation (3.12) by $\partial w_{ij} / \partial x_j^s$ and integrating over the compact support one may write

$$\begin{aligned} \int_{\Omega} (f^p(\mathbf{r}_j) - f^p(\mathbf{r}_i)) \frac{\partial w_{ij}}{\partial x_j^s} d^2 \mathbf{r}_j &= \frac{\partial f^p(\mathbf{r}_i)}{\partial x_i^l} \underbrace{\int_{\Omega} r_{ji}^l \frac{\partial w_{ij}}{\partial x_j^s} d^2 \mathbf{r}_j}_{I^{ls}} \\ &+ \frac{1}{2} \frac{\partial^2 f^p(\mathbf{r}_i)}{\partial x_i^l \partial x_i^k} \underbrace{\int_{\Omega} r_{ji}^l r_{ji}^k \frac{\partial w_{ij}}{\partial x_j^s} d^2 \mathbf{r}_j}_{I^{lks}} \end{aligned} \quad (3.13)$$

The first and second integrals on the right hand side of equation (3.13) are tensors of rank two and three, respectively. Considering that the kernel has symmetric compact support, integrating the third-rank tensor by parts and employing Green-Gauss theorem results in

$$I^{lks} = - \int_{\Omega} w_{ij} \frac{\partial r_{ji}^l r_{ji}^k}{\partial r_j^s} d^2 \mathbf{r}_j = - \int_{\Omega} w_{ij} (r_{ji}^l \delta^{sk} + r_{ji}^k \delta^{ls}) d^2 \mathbf{r}_j. \quad (3.14)$$

Further simplifying the above integral by bringing the Kronecker deltas out of the integrand one may show that

$$I^{lks} = -\delta^{sk} \int_{\Omega} r_{ij}^l w_{ij} d^2 \mathbf{r}_j - \delta^{ls} \int_{\Omega} r_{ji}^k w_{ij} = 0 d^2 \mathbf{r}_j, \quad (3.15)$$

since kernel is a symmetric even function and multiplication of an even function by an odd

function produces an odd function. Similarly, the second rank tensor may be simplified as

$$I^{ls} = -\delta^{ls} \int_{\Omega} w_{ij} d^2 \mathbf{r}_j = -\delta^{ls}, \quad (3.16)$$

provided that the normalization condition holds. Substituting equations (3.15) and (3.16) in equation (3.13) and considering that $\partial w_{ij}/x_j^s = -\partial w_{ij}/x_i^s$, one may write the integral representation of the first derivative as

$$\frac{\partial f^p(\mathbf{r}_i)}{\partial x_i^s} = \int_{\Omega} (f^p(\mathbf{r}_j) - f^p(\mathbf{r}_i)) \frac{\partial w_{ij}}{\partial x_i^s} d^2 \mathbf{r}_j. \quad (3.17)$$

When transforming equation (3.17) into particle representation, I^{ls} is no longer equal to Kronecker delta and its contribution has to be accounted for. As a result equation (3.17) is modified to

$$\int_{\Omega} (f^p(\mathbf{r}_j) - f^p(\mathbf{r}_i)) \frac{\partial w_{ij}}{\partial x_i^s} d^2 \mathbf{r}_j = \frac{\partial f^p(\mathbf{r}_i)}{\partial x_i^l} \int_{\Omega} r_{ji}^l \frac{\partial w_{ij}}{\partial x_i^s} d^2 \mathbf{r}_j. \quad (3.18)$$

Replacing the integration operation with summation on the neighbors of particle i , equation (3.18) may be rewritten in particle representation as

$$\sum_{j=1}^{J_n} \frac{1}{\psi_j} (f^p(\mathbf{r}_j) - f^p(\mathbf{r}_i)) \frac{\partial w_{ij}}{\partial x_i^s} = \frac{\partial f^p(\mathbf{r}_i)}{\partial x_i^l} a_i^{ls}, \quad (3.19)$$

where

$$a_i^{ls} = \sum_{j=1}^{J_n} \frac{r_{ji}^l}{\psi_j} \frac{\partial w_{ij}}{\partial x_i^s}. \quad (3.20)$$

Equation (3.19) may also be written in matrix form as

$$\begin{bmatrix} \sum_{j=1}^{J_n} f_{ji}^{(1)} a_{ij}^{(1)} \\ \sum_{j=1}^{J_n} f_{ji}^{(1)} a_{ij}^{(2)} \end{bmatrix} = \begin{bmatrix} \sum_{j=1}^{J_n} r_{ji}^{(1)} a_{ij}^{(1)} & \sum_{j=1}^{J_n} r_{ji}^{(2)} a_{ij}^{(1)} \\ \sum_{j=1}^{J_n} r_{ji}^{(1)} a_{ij}^{(2)} & \sum_{j=1}^{J_n} r_{ji}^{(2)} a_{ij}^{(2)} \end{bmatrix} \begin{bmatrix} \frac{\partial f_i^{(1)}}{\partial x_i^{(1)}} \\ \frac{\partial f_i^{(1)}}{\partial x_i^{(2)}} \end{bmatrix}, \quad (3.21)$$

where

$$a_{ij}^s = \frac{1}{\psi_j} \frac{\partial w_{ij}}{\partial x_i^s}. \quad (3.22)$$

The correction function given in equation (3.11) was tested and the results were on par with those of equation (3.19) used throughout this study.

Laplacian operator

The two-dimensional relation for the second derivative in integral form may be given as [172]

$$2 \int_{\Omega} (f^p(\mathbf{r}_i) - f^p(\mathbf{r}_j)) \frac{r_{ij}^s}{r_{ij}^2} \frac{\partial w_{ij}}{\partial x_i^m} d^2 \mathbf{r}_j = \frac{1}{2} \frac{\partial^2 f^p(\mathbf{r}_i)}{\partial x_i^s \partial x_i^m} + \frac{1}{4} \frac{\partial^2 f^p(\mathbf{r}_i)}{\partial x_i^k \partial x_i^k} \delta^{sm}. \quad (3.23)$$

Equation (3.23) may be modified for a divergence free field such as velocity, by contracting p and s indices as

$$2 \int_{\Omega} (f^p(\mathbf{r}_i) - f^p(\mathbf{r}_j)) \frac{r_{ij}^p}{r_{ij}^2} \frac{\partial w_{ij}}{\partial x_i^m} d^2 \mathbf{r}_j = \frac{1}{4} \frac{\partial^2 f^p(\mathbf{r}_i)}{\partial x_i^k \partial x_i^k} \delta^{pm}. \quad (3.24)$$

Similar to the treatment given to equation (3.18), equation (3.24) may be rewritten as

$$8 \int_{\Omega} (f^p(\mathbf{r}_i) - f^p(\mathbf{r}_j)) \frac{r_{ij}^p}{r_{ij}^2} \frac{\partial w_{ij}}{\partial x_i^m} d^2 \mathbf{r}_j = \frac{\partial^2 f^p(\mathbf{r}_i)}{\partial x_i^k \partial x_i^k} \int_{\Omega} r_{ij}^p \frac{\partial w_{ij}}{\partial x_i^m} d^2 \mathbf{r}_j, \quad (3.25)$$

to enable its transformation into particle representation. It can be written in matrix form as

$$8 \sum_{j=1}^{J_n} (f_{ji}^{(1)} r_{ji}^{(1)} + f_{ji}^{(2)} r_{ji}^{(2)}) \begin{bmatrix} a_{ij}^{(1)} \\ a_{ij}^{(2)} \end{bmatrix} = \begin{bmatrix} \sum_{j=1}^{J_n} r_{ji}^{(1)} a_{ij}^{(1)} & \sum_{j=1}^{J_n} r_{ji}^{(2)} a_{ij}^{(1)} \\ \sum_{j=1}^{J_n} r_{ji}^{(1)} a_{ij}^{(2)} & \sum_{j=1}^{J_n} r_{ji}^{(2)} a_{ij}^{(2)} \end{bmatrix} \begin{bmatrix} \frac{\partial^2 f_i^{(1)}}{\partial x_i^k \partial x_i^k} \\ \frac{\partial^2 f_i^{(2)}}{\partial x_i^k \partial x_i^k} \end{bmatrix}, \quad (3.26)$$

or in index form as

$$8 \sum_{j=1}^{J_n} \frac{1}{\psi_j} (f^p(\mathbf{r}_i) - f^p(\mathbf{r}_j)) \frac{r_{ij}^p}{r_{ij}^2} \frac{\partial w_{ij}}{\partial x_i^m} = \frac{\partial^2 f^p(\mathbf{r}_i)}{\partial x_i^k \partial x_i^k} a_i^{pm}. \quad (3.27)$$

Upon contracting indices s and m in equation (3.23), an alternative form of Laplacian for a vector field may be obtained as

$$8 \int_{\Omega} (f^p(\mathbf{r}_i) - f^p(\mathbf{r}_j)) \frac{r_{ij}^s}{r_{ij}^2} \frac{\partial w_{ij}}{\partial x_i^s} d^2 \mathbf{r}_j = (2 + \delta^{mm}) \frac{\partial^2 f^p(\mathbf{r}_i)}{\partial x_i^k \partial x_i^k}, \quad (3.28)$$

which is also suitable for scalar variables such as pressure and electric potential. Casting into particle representation and considering the discrete form of δ^{mm} , equation (3.28) may be written as

$$8 \sum_{j=1}^{J_n} \frac{1}{\psi_j} (f^p(\mathbf{r}_i) - f^p(\mathbf{r}_j)) \frac{r_{ij}^s}{r_{ij}^2} \frac{\partial w_{ij}}{\partial x_i^s} = (2 + a_i^{mm}) \frac{\partial^2 f^p(\mathbf{r}_i)}{\partial x_i^k \partial x_i^k}. \quad (3.29)$$

3.2.2 Homogenization of particle distribution

Adapting the derivative formula for a discretized environment is the first step in maintaining the accuracy of the particle representation. However, ensuring the homogeneity of the discretized environment, *i.e.* particle distribution, is another step in helping the accuracy of a particle method. Two examples are the method called XSPH [164, 173] and Artificial Particle Displacement (APD) [174, 175]. These methods modify the trajectory of the particles to avoid local increase or decrease in their numbers, regarding them as computational nodes rather than fluid parcels.

In XSPH, particle velocity is relaxed over their neighbors, giving them a more consistent motion and subsequently avoiding excessive change in particle distribution. To put it into mathematical terms

$$\frac{d\mathbf{x}_i}{dt} = \mathbf{u}_i - \zeta \sum_{j=1}^{J_n} \frac{1}{\psi_j} \mathbf{u}_{ij} w_{ij}, \quad (3.30)$$

where the second term on the right hand side is the XSPH velocity while ζ is a relaxation factor between zero and one. A higher relaxation factor gives more uniform motion but detracts from the accuracy of the solution while a low relaxation factor may not be effective.

In APD, the particle positions are slightly modified based on directional emptiness, *i.e.* particles are shifted to fill the empty spaces within the computational domain. This is achieved by adding a slight perturbation to particle position via

$$\delta\mathbf{r}_i = \zeta \sum_{j=1}^{J_n} \frac{\mathbf{r}_{ij}}{r_{ij}^3} r_{\text{avg},i}^2 u_{\text{apd},i} \Delta t, \quad (3.31)$$

where $r_{\text{avg},i} = \sum_{j=1}^{J_n} r_{ij}/J_n$ is the average particle spacing, Δt is the computational time step length, $u_{\text{apd},i}$ is a representative velocity and ζ is the APD coefficient. Since equation (3.31) is an odd function, $\delta\mathbf{r}_i$ will be close to zero for near homogeneous distributions. When there is significant particle accumulation in a region, the perturbation vector will point away from the clustered region and toward the less populated parts of the particle neighborhood.

The value of the APD coefficient depends on the choice of the $u_{\text{apd},i}$. A common choice in previous studies of the group for $u_{\text{apd},i}$ has been the maximum velocity within the computational domain [148, 176]. In this case an APD coefficient of $\zeta = 0.06$ is found to provide satisfactory balance between accuracy and homogeneous particle distribution. Another choice for the $u_{\text{apd},i}$ is the local maximum within the neighborhood of particle i . A similar value of $\zeta = 0.06$ is acceptable for this case as well. Inspired by XSPH, one

may use an average local velocity difference of the form

$$u_{\text{apd},i} = \sum_{j=1}^{J_n} \frac{1}{\psi_j} |\mathbf{u}_{ij}| w_{ij}. \quad (3.32)$$

In this case, particles away from the main features of the flow are not affected and an APD coefficient of unity has been found to provide acceptable results.

3.3 Neighbor finding

All discrete operations carried out for the particle of interest i require the information on neighboring particles j within the compact support of the kernel function. The neighbor information has to be updated each time the particles move and this step takes up considerable computational resources.

The most straightforward method of finding the neighbors is direct-search algorithm where the distance between particle i and all other particles within the computational domain is calculated and those satisfying the condition $r_{ij} \leq nh$ are considered as neighbors of particle i . The number of operations required for this method is of order $\mathcal{O}(J_d^2)$, where J_d is the total number of particles within the computational domain. An improvement of the method stores the neighborhood relationship recursively, *i.e.* if particle j is a neighbor of particle i , both particles will store the relationship. This reduces the number of operations to $\mathcal{O}(J_d^2/2)$.

An improved version of the direct-search algorithm is the linked-list algorithm which is suitable for simulations with constant smoothing length, as is the case in this study. In this method, an overlaying mesh is used to classify the particles into neighboring regions. The number of the overlaying mesh cells is chosen such that all rectangles are uniform and side length is never smaller than nh . After associating each particle with its corresponding cell, a direct-search is performed within that cell and its neighboring eight cells. This reduces the number of operations required to $\mathcal{O}(J_d)$ [155]. Similar to the improvement made in direct-search algorithm, it is possible to consider only half of the neighboring cells while searching for particle neighbors. This reduces the number of cells traversed while searching for neighbors to five per particle.

Figure 3.1 shows a schematic of the neighboring cells used in this study. Here, particles used for imposing boundary conditions are included in neighbor searching procedure and may become a neighbor of a particle within the computational domain. These particles reside outside of the computational domain and are assigned to their respective cells marked with dashed lines in figure 3.1. In the particular implementation used here, the neighbor finding procedure starts from the lower-left boundary of the computational domain and sweeps toward the upper-right boundary. As shown in figure 3.1-d, five cells

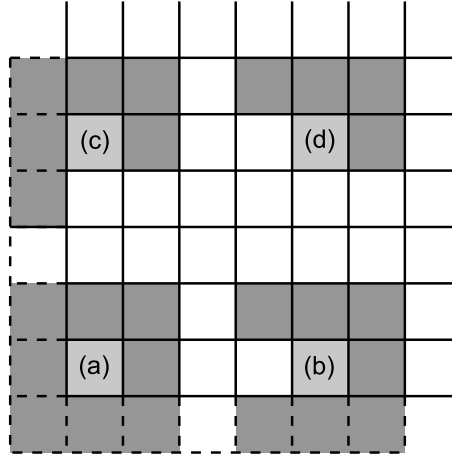


Figure 3.1: Neighboring cells (dark gray) for the cells containing particle of interest i at the bottom-left corner (a), bottom wall (b), left (c) and inside the computational domain and away from the boundaries(d). A dashed cell contains ghost particles.

are searched for each particle of interest i . If the cell containing particle i is adjacent to a boundary, all neighboring ghost cells are also included in the search.

3.4 Boundary conditions

Like other spatial discretization methods such as FDM and FVM, a common method of imposing boundary conditions in SPH is by placing auxiliary computational elements outside of the computational domain. Another function of such elements or particles in SPH is to fill the compact support of the kernel function and avoid misleading particles when APD is used. These particles may be allocated statically or dynamically. The former will be referred to as dummy particle method while the latter will be called ghost particle method.

In dummy particle method shown in figure 3.2-a and b, auxiliary particles are arranged in layers outside of the boundary in a uniform fashion with the same separation distance as the main particles. The number of layers is chosen to cover the full compact support of the particles inside the computational domain. Dummy particles remain stationary during the simulation while their properties are interpolated from the values inside the computational domain. The interpolation sites, shown in green filling for respective dummy particles, are the mirror of the dummy particle with respect to the boundary for non-periodic (figure 3.2-a). The interpolation sites for periodic boundaries are found by shifting the position of the respective dummy particles inside of the computational domain (figure 3.2-b). Two issues with this simplistic method is that the interpolation point is not necessarily occupied by a main particle and a particle on the boundary does not see a symmetric distribution.

Ghost particle method used in this study alleviates the problems of dummy particle method by actively allocating auxiliary particles based on the location of the main par-

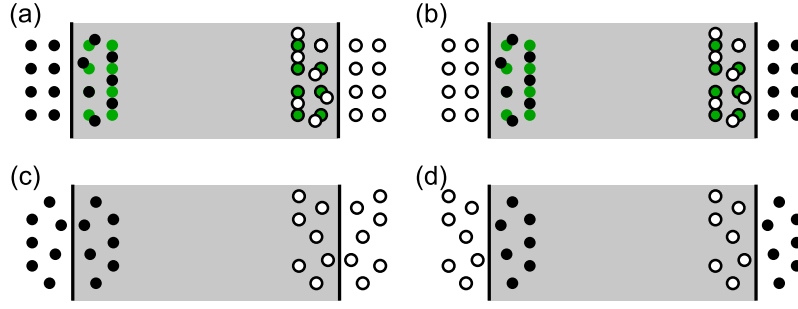


Figure 3.2: Arrangement of auxiliary particles in dummy particle method (a,b) and ghost particle method (c,d). Related particles have similar borders. Interpolation sites of dummy particle method are shown with green filling. Neumann and Dirichlet boundaries are shown in the left column while periodic boundary is shown to the right.

ticles. As shown in figure 3.2-c, a Ghost particle is positioned to mirror the associated main particle with respect to the boundary for non-periodic boundary conditions. For a periodic boundary condition, the ghost positions are found by shifting the position of the particles adjacent to the opposite boundary (figure 3.2-d). This provides a clear source for the properties of the ghost particle (phase, viscosity, density, electric permittivity and electric conductivity) and results in a symmetric distribution with respect to boundaries. It is worth mentioning that in this study, no particles reside on the boundaries. This reduces the variety of the particles inside the domain, facilitating numerical solution and matrix forming by reducing exceptions. It also helps in establishing boundary conditions, especially the periodic boundary condition.

The aforementioned ghost particle method is only suitable for straight boundaries with right corners. An adaptation of the ghost particle approach to arbitrary boundaries, dubbed Multiple Boundary Tangent (MBT) method, is presented in [172]. The method presented here is a subset of MBT and will be simply referred to as such.

The properties of the ghost particles in relation to their main particles depend on the type of the boundary conditions. The common boundary conditions employed in this study are constant zero (Dirichlet or first-type), zero gradient (Neumann or second-type) and periodic. Denoting velocity, pressure or electric potential by f , ghost values for constant zero boundary condition are set according to $f_g = -f_m$ while both zero gradient and periodic ghost values are set according to $f_g = f_m$. An additional feature of the periodic condition is that a main particle passing through boundary will be transferred to the computational cell adjacent to the opposite boundary. A schematic of the ghost-main particle relationship is provided in figure 3.2.

An additional form of boundary condition, dubbed shifting boundary, is used in this study. It allows for infinite motion of a flow feature (descending rigid body or ascending bubble) in quiescent background fluid in a bounded computational domain. Use of periodic boundary condition is not suitable in this case as such a treatment will cause the feature to interact with its own wake. An inlet-outlet pair will be complicated to implement

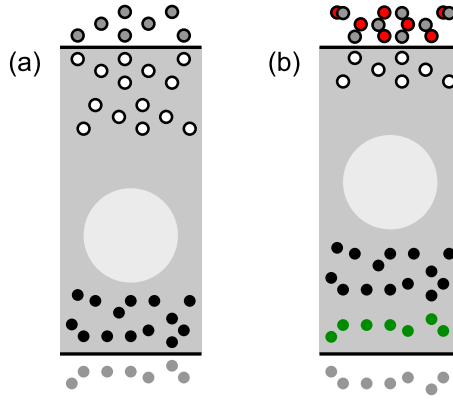


Figure 3.3: Shifting boundary condition: (a) original particle arrangement; (b) particle arrangement after shifting. Red particles are discarded and green particles are added. The area of interest is marked in light gray. Ghost particles are shown with gray fill and are related to particles of similar border within the computational domain.

if the system is to be solved in a spatial representation. The shifting condition allows for unlimited simulation of the evolution of the feature of interest in a bounded domain. It is based on no-penetration and no-slip conditions for velocity and known electric potential. Zero pressure gradient is also required due to the numerical method used. Figure 3.3 provides a schematic of the boundary condition. The feature of interest is placed at the center of the computational domain (shown in light gray). As its center of mass changes position up to one particle spacing in any direction (up or down), all particles are shifted so that the feature is centered again (figure 3.3-b). Any particles transferred out of computational domain are discarded (red particles) and the first level ghosts of the opposite boundary are transformed into main particles (ghost particles). To avoid possible disturbances near the boundaries, a hard damping function based on hyperbolic tangent profile is applied to the velocities near the boundaries. If the computational domain is large enough, the feature of interest will not sense the changes in position and simulations may continue without adverse effects of the boundaries.

3.5 Initial particle arrangement

The constantly updated neighborhood information of SPH particles negates the need for keep strict positioning and connectivity information during the simulation. However, depending on the nature of the cases at hand, some consideration has to be given to the initial positioning of the particles. The arrangement of the solid body particles should conform to the boundaries of the object. The same is correct for flows where the final outcome is at a stationary state such as hydrostatic equilibrium [177]. The initial position of the particles may be arranged through specialized methods such as meshing [155] or particle packing algorithms [177]. Another method is to run a modified simulation for obtaining an initial

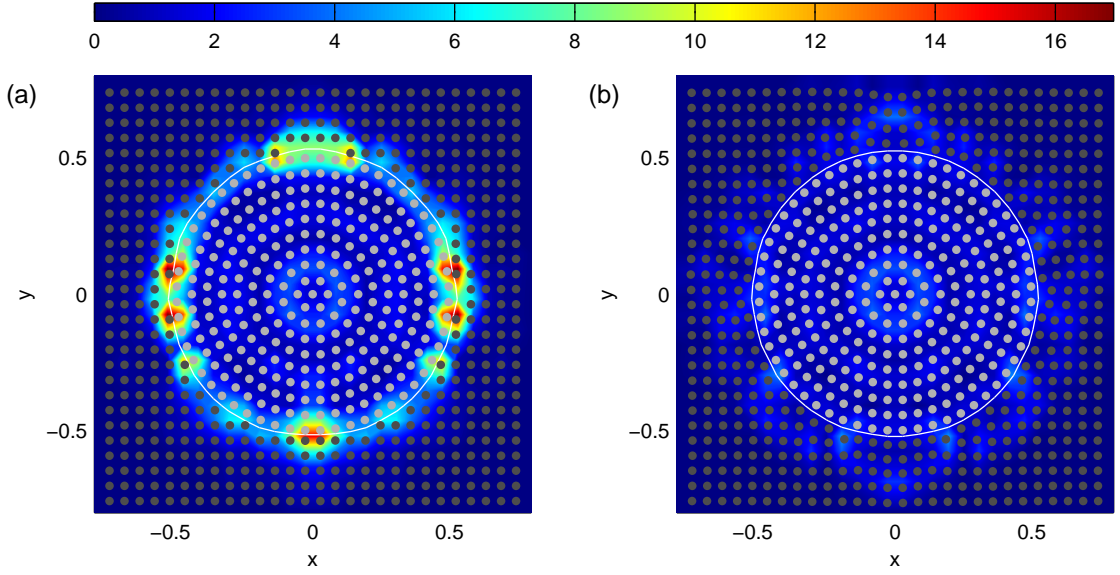


Figure 3.4: Particle positions before (a) and after (b) relaxation. Contour shows $\nabla \cdot \mathbf{u}_{\text{apd},i}$.

arrangement compatible with the code. The second method, while more time consuming than the first, has the benefit of being fully compatible with code responsible for the simulation since positioning errors are already accounted for. It is also easier to implement through minor modifications. Two cases were tested in this study using the second method.

The first case is to prepare an initial droplet arrangement for liquid lens simulation which will be elaborated further in section 4.2. The initial particle arrangement had considerable effect since the final result of this case was of a quiescent nature. The relaxation procedure here was based on using a physical phenomena, *i.e.* the tendency of a suspended droplet to become circular. A similar test was carried out for rising bubbles, but those cases showed no major difference between relaxed and non-relaxed arrangements. This is expected since the bubble does not come to rest during the simulation.

The second case where a conforming particle arrangement is tested was in descent of a circular disk in quiescent medium in section 6.3.1. The results showed no considerable difference when fluid particles were cut from an initially Cartesian arrangement compared to when the particles were relaxed into a boundary conforming shape. The relaxation process in this case was based on a modified form of APD whereby a small portion of the gradient of $r_{\text{avg},i}$ was used as $u_{\text{apd},i}$ to modulate velocity in addition to position in the fluid phase. The particle arrangement before and after applying the relaxation procedure is shown in figure 3.4.

In this study, all particles are arranged in a uniform Cartesian arrangement, except for rigid bodies, liquid lens and droplet levitation test cases. Further details are provided in respective sections.

3.6 Imposing incompressibility

There are two common ways to impose incompressibility in SPH. The original SPH implementation proposed for hydrodynamic simulations of incompressible flows by Monaghan [75] used a pseudo state equation. The state equation has taken many forms in literature, however, its general form may be written as

$$p = f(\rho; u_s), \quad (3.33)$$

where f is a function of density ρ and a representative speed of sound u_s . This variant, known as WCSPH, is fast and easy to implement, however, suffers from arbitrary pressure oscillation and small time step. Many treatments and improvements are proposed to alleviate the initial shortcomings, however, the most important problem resides with the use of the artificial equation of state itself.

Cummins and Rudmann [77] developed an alternative form of SPH to address the shortcomings of WCSPH. The method, widely known as ISPH, is based on Chorin's projection method [76] and relies on a predictor-corrector approach. While ISPH is computationally more expensive, the pressure field is smoother than that of WCSPH and it allows for larger time steps. ISPH method is used in all simulations carried out in this study.

3.6.1 Projection method

The projection method relies on Helmholtz-Hodge decomposition of a vector field \mathbf{f} defined on a simply connected domain. This means that the vector field may be written as the summation of solenoidal \mathbf{f}_{sol} and irrotational \mathbf{f}_{irr} parts. The following relations apply to such a field

$$\nabla \cdot \mathbf{f} = \nabla^2 \Phi, \quad (3.34)$$

$$\mathbf{f}_{\text{sol}} = \mathbf{f} - \nabla \Phi, \quad (3.35)$$

where the irrotational part is shown as the gradient of the potential field Φ .

Applying this concept to equation (2.6), the projection method may be described as follows. The procedure starts by calculating a prediction of the velocity, known as intermediate velocity, by excluding pressure gradient. The pressure is then calculated by replacing \mathbf{f} with intermediate velocity and Φ with pressure in equation (3.34). The final step is to correct the velocity by using the calculated pressure. This step is carried out using equation (3.35) where \mathbf{f}_{sol} is the divergence free velocity.

3.6.2 SPH implementation of projection method

Since ISPH is a Lagrangian method, an additional particle movement step has to be added to the projection method described in section 3.6.1. Knowing position and velocity of the particles at n th timestep and marking intermediate values with a plus, the original method proposed in [77] for ISPH of simple flows may be summarized as

1. $\mathbf{r}^+ = \mathbf{r}^{(n)} + \Delta t \mathbf{u}^{(n)}$,
2. $\mathbf{u}^+ = \mathbf{u}^{(n)} + \Delta t \nabla \cdot (\mu \nabla \mathbf{u}^{(n)}) / \rho$,
3. $\nabla \cdot (\nabla p / \rho) = \nabla \cdot \mathbf{u}^+ / \Delta t$,
4. $\mathbf{u}^{(n+1)} = \mathbf{u}^+ - \Delta t (\nabla p / \rho)$,
5. $\mathbf{r}^{(n+1)} = \mathbf{r}^{(n)} + \Delta t (\mathbf{u}^{(n)} + \mathbf{u}^{(n+1)}) / 2$.

3.7 Electrostatic fluid-structure/solid interaction procedure

In its most complex form, the study conducted here includes the effects of gravity, surface tension, electric field and rigid bodies inside the fluid environment. The full description of the numerical method, electrohydrodynamic fluid-structure/solid interaction, is provided here. Any repeated equations are marked with a prime. All cases with lesser amount of complexity follow the same solution, provided that only relevant stages are maintained.

The projection scheme is advanced in time using a first-order Euler approach. The Courant-Friedrichs-Lewy (CFL) condition [178],

$$\Delta t = \eta \min_{1 \leq j \leq J_d} \left[\frac{h}{u_j}, \frac{\rho_j h^2}{2\mu_j}, \left(\frac{\rho_j h^3}{\max_{(\alpha)} \gamma_{(\alpha)}} \right)^{\frac{1}{2}}, \left(\frac{\rho_j h^3}{\epsilon_j E_j^2} \right)^{\frac{1}{2}} \right], \quad (3.36)$$

is used to determine the timestep of the simulation where η is taken to be equal to 0.25 [148]. Initial number density and particle mass are computed via

$$\psi_i = \sum_{j=1}^{J_n} w_{ij}, \quad (3.10')$$

$$m_i = \frac{\rho_i}{\psi_i}. \quad (3.37)$$

Prior to the movement of particles in the predictor step, APD vector is calculated through

$$\delta \mathbf{r}_i^{(n)} = \zeta \left(\sum_{j=1}^{J_n} \frac{\mathbf{r}_{ij}}{r_{ij}^3} r_{\text{avg},i}^2 u_{\text{apd},i} \right)^{(n)} \Delta t, \quad (3.31')$$

after which particles are displaced to their intermediate positions using

$$\mathbf{r}_i^+ = \mathbf{r}_i^{(n)} + \mathbf{u}_i^{(n)} \Delta t + \delta \mathbf{r}_i^{(n)}. \quad (3.38)$$

Since particles have moved, neighborhood relationships are reestablished. Particle number densities and fluid density may be update now as

$$\psi_i^+ = \sum_{j=1}^{J_n} w_{ij}^+, \quad (3.10')$$

$$\rho_i^+ = m_i \psi_i^+, \quad (3.39)$$

or postponed after intermediate velocity is calculated in equations (3.42) and (3.39'). The color function is smoothed through

$$c_{(\alpha)i} = \frac{1}{\psi_i} \sum_{j=1}^{J_n} \hat{c}_{(\alpha)j} w_{ij}, \quad (3.40)$$

and all material properties are updated using either WAM or WHM methods via

$$f_i = \sum_{\alpha=1}^3 c_{(\alpha)i} \hat{f}_{(\alpha)}, \quad (2.26')$$

$$\frac{1}{f_i} = \sum_{\alpha=1}^3 \frac{c_{(\alpha)i}}{\hat{f}_{(\alpha)}}. \quad (2.27')$$

After updating color and material properties, surface tension and electrical forces are computed at the intermediate particle positions. Surface tension is calculated in several stages. First, color gradient is computed using the following discretized form

$$\frac{\partial f_j^p}{\partial x_i^l} = (a_i^{ls})^{-1} \sum_{j=1}^{J_n} \frac{f_{ji}^p}{\psi_j} \frac{\partial w_{ij}}{\partial x_i^s}, \quad (3.19')$$

and delta function is found. Then surface normals are calculated through

$$\mathbf{n}_{(\alpha)i} = \left(\frac{\nabla c_i}{|\nabla c_i|} \right)_{(\alpha)}. \quad (2.18')$$

Valid normals are then smoothed in a way similar to the color function and then used to compute the curvature via

$$\kappa_{(\alpha)i} = -\nabla \cdot \mathbf{n}_{(\alpha)i}, \quad (2.19')$$

using equation (3.19'). Putting all components together, surface tension is calculated as

$$\mathbf{f}_{(s)i} = \sum_{\alpha=1}^3 (\gamma \kappa_i \mathbf{n}_i \delta_i)_{(\alpha)}. \quad (2.24')$$

In the next stage of the simulation, electrical potential of the system is found by solving

$$\nabla \cdot (\varepsilon_i \nabla \phi_i) = 0, \quad (2.37')$$

$$\nabla \cdot (\sigma_i \nabla \phi_i) = 0, \quad (2.41')$$

subject to relevant boundary conditions for perfect dielectric and leaky dielectric models, respectively, using the following discretized form

$$\frac{\partial}{\partial x_i^k} \left(\varphi_i \frac{\partial f_i^p}{\partial x_i^k} \right) = \frac{8}{2 + a_i^{mm}} \sum_{j=1}^{J_n} \frac{2\varphi_i \varphi_j}{\varphi_i + \varphi_j} \frac{f_{ij}^p}{\psi_j} \frac{r_{ij}^s}{r_{ij}^2} \frac{\partial w_{ij}}{\partial x_i^s}. \quad (3.29')$$

Electric field is then computed from the electric potential by

$$\mathbf{E}_i = -\nabla \phi_i, \quad (2.33')$$

discretized by equation (3.19'). Permittivity gradient is calculated in a similar fashion and used along with electric field to calculate polarization force,

$$\mathbf{f}_{(ep)i} = -\frac{1}{2} \mathbf{E}_i \cdot \mathbf{E}_i \nabla \varepsilon_i. \quad (2.30')$$

Coulomb force is found through

$$\mathbf{f}_{(eq)i} = q_i^v \mathbf{E}_i, \quad (2.31')$$

where electric potential is used to directly compute the volumetric charge,

$$q_i^v = \nabla \cdot (\varepsilon_i \nabla \phi_i), \quad (2.34')$$

using equation (3.29'). The electric force components are limited to regions with acceptable permittivity and conductivity gradients, similar to the measures taken for acceptable normals. Accepted components are added to form the resultant electric force,

$$\mathbf{f}_{(e)i} = \mathbf{f}_{(ep)i} + \mathbf{f}_{(eq)i}. \quad (2.29')$$

After all interfacial forces are accounted for, the intermediate velocity is computed through

$$\mathbf{u}_i^+ = \mathbf{u}_i^{(n)} + \frac{\Delta t}{\rho^{(n)}} (\nabla \cdot \boldsymbol{\tau}_i + \mathbf{f}_{(b)i} + \mathbf{f}_{(s)i} + \mathbf{f}_{(e)i})^{(n)}, \quad (3.41)$$

where viscous dissipation $\nabla \cdot \tau_i$ is discretized using

$$\frac{\partial}{\partial x_i^k} \left(\varphi_i \frac{\partial f_i^p}{\partial x_i^k} \right) = 8 (a_i^{pm})^{-1} \sum_{j=1}^{J_n} \frac{2\varphi_i \varphi_j}{\varphi_i + \varphi_j} \frac{f_{ij}^p}{\psi_j} \frac{r_{ij}^p}{r_{ij}^2} \frac{\partial w_{ij}}{\partial x_i^m}. \quad (3.27')$$

If not updated after initial movement in equation (3.10'), the intermediate number density is calculated employing the following relation

$$\psi_i^+ = \psi_i^{(n)} - \Delta t \psi_i^{(n)} (\nabla \cdot \mathbf{u}_i^+), \quad (3.42)$$

subject to appropriate boundary conditions, which is then used to compute intermediate density,

$$\rho_i^+ = m_i \psi_i^+. \quad (3.39')$$

To impose rigid motion, the current velocity of the solid particles is used to compute a center-of-mass velocity and an angular velocity for the solid object through

$$\mathbf{u}_s^{t+} = \frac{1}{M_s^+} \sum_{j=1}^{J_s} \frac{\mathbf{u}_j^+}{\psi_j^+}, \quad (2.71')$$

$$\mathbf{u}_s^{r+} = \frac{1}{I_s^+} \sum_{j=1}^{J_s} \frac{\mathbf{u}_j^+ \times \mathbf{r}_{js}}{\psi_j^+}, \quad (2.72')$$

and then assign an individual velocity to each solid particle according to rigid body motion as

$$\mathbf{u}_i^+ = \mathbf{u}_s^{t+} + \mathbf{u}_s^{r+} \times \mathbf{r}_{is}. \quad (2.70')$$

As density remains constant for particles of the solid phase, M_s and I_s represent the rigid body's volume and moment of inertia about its center of mass as

$$M_s^+ = \sum_{j=1}^{J_s} \frac{1}{\psi_j^+}, \quad I_s^+ = \sum_{j=1}^{J_s} \frac{\mathbf{r}_{js}^+ \cdot \mathbf{r}_{js}^+}{\psi_j^+}. \quad (3.43)$$

In the corrector step, pressure at the next timestep is found by solving Poisson equation subject to relevant boundary conditions using intermediate values,

$$\nabla \cdot \left(\frac{1}{\rho_i^+} \nabla p_i^{(n+1)} \right) = \frac{\nabla \cdot \mathbf{u}_i^+}{\Delta t}. \quad (3.44)$$

The left hand side is discretized using equation (3.29') while the right hand side is discretized following equation (3.19'). The calculated pressure is then employed to correct the velocity of the particles, hence advancing them to next timestep using the following relation,

$$\mathbf{u}_i^{(n+1)} = \mathbf{u}_i^+ - \frac{1}{\rho_i^+} \nabla p_i^{(n+1)} \Delta t. \quad (3.45)$$

In order to handle larger density ratios between different phases of the flow, $\nabla p/\rho$ is replaced with its equivalent form, $\nabla(p/\rho) - p\nabla(1/\rho)$, which is discretized as

$$\begin{aligned} \frac{1}{\rho} \frac{\partial p_i}{\partial x_i^k} a_i^{kl} &= \sum_{j=1}^{J_n} \frac{1}{\psi_j} \left[\left(\frac{p_j}{\rho_j} - \frac{p_i}{\rho_i} \right) - \left(\frac{p_i}{\rho_j} - \frac{p_i}{\rho_i} \right) \right] \frac{\partial w_{ij}}{\partial x_i^l} \\ &= \sum_{j=1}^{J_n} \frac{1}{\rho_j \psi_j} (p_j - p_i) \frac{\partial w_{ij}}{\partial x_i^l}. \end{aligned} \quad (3.46)$$

This form, also referred to as non-conservative form, ensures zero pressure gradient when particle of interest and its neighbors are of identical pressure. At this point, rigidity constraints of equations (2.71'-2.70') are imposed on the velocity vector values at the next time step. Finally, particles are moved to their corrected positions using the following relation

$$\mathbf{r}_i^{(n+1)} = \mathbf{r}_i^{(n)} + \frac{1}{2} (\mathbf{u}_i^{(n)} + \mathbf{u}_i^{(n+1)}) \Delta t + \delta \mathbf{r}_i^{(n)}. \quad (3.47)$$

The final step involves reestablishment of neighborhood information. If number density was calculated using equation (3.42), the number density and particle mass are restored to their original values. If equation (3.10') and (3.39) were used, number density and particle masses will be recalculated via the same equations based on the new neighborhood information.

Chapter 4

Three-phase flows*

4.1 Introduction

Multiphase flows where two or more fluids have interfacial contact surfaces are one of the most common features observed in many engineering and natural processes and have been a subject of interest for modeling in many studies. It is a challenging problem as the evolution of the interface is a crucial step in modeling of multiphase flows which needs to be handled delicately to result in reliable simulations.

In their simplest form, multiphase flows are composed of two immiscible fluid streams. Many studies have been performed on two-phase flows using mesh dependent, meshless and hybrid approaches. Mesh dependent methods include VOF [1, 179, 180], LS methods [15, 28, 181] and Phase Field (PF) methods [182, 183] which are purely Eulerian where interface is captured implicitly through use of a scalar function. Hybrid Eulerian-Lagrangian approaches, such as Front Tracking method [39, 184], provide a sharper interface representation by employing markers to track the interface explicitly which adds to their accuracy at the cost of extra complexity and computational expense. In this regard, the Lagrangian nature of meshless methods is an inherent advantage of this kind of approach as it facilitates the tracking of interfaces with large deformations. Among all different variants of meshless methods, SPH has received a great deal of attention in modeling multiphase flows [75, 89–92, 94–96].

Despite the large pool of research available in two-phase flows, there have been relatively fewer studies carried out on flows containing three different fluids, partly due to complexities inherent in phase interactions and possible triple-junctions present in these flows. A few examples include level set studies of triple junctions [146, 185] and droplet spreading [186], droplet impact simulation using front tracking [187], phase field simulations of several three-phase flows [188, 189] and weakly compressible smoothed particle hydrodynamics simulations of two and three-phase flows [93].

*Appears in: N. Tofighi and M. Yildiz, Numerical simulation of single droplet dynamics in three-phase flows using ISPH, *Comput. Math. Appl.* (2013). doi:10.1016/j.camwa.2013.05.012

Table 4.1: Simulation parameters and results for liquid lens elongation test case

	$\gamma_{(13)}/\gamma_{(12)}$ ($\gamma_{(13)} = \gamma_{(23)}$)	d_a			d_o/d_a	d_f/d_a		
		R_1	R_2	R_3		R_1	R_2	R_3
V_1	0.8	0.4771	0.4830	0.4601	0.6527	0.9687	0.9827	0.9939
V_2	0.9	0.4501	0.4556	0.4340	0.6919	0.9702	0.9827	0.9881
V_3	1.0	0.4313	0.4366	0.4159	0.7220	0.9684	0.9785	0.9856
V_4	1.1	0.4173	0.4224	0.4024	0.7463	0.9647	0.9783	0.9819
V_5	1.2	0.4064	0.4114	0.3919	0.7663	0.9602	0.9786	0.9865

A number of test cases have been simulated to test the capabilities of the proposed three-phase ISPH scheme. First, elongation of a circular droplet encompassed between two immiscible fluid layers have been studied and compared to analytic values in section 4.2.1. Extending this test case towards a more dynamic one, levitation of a circular droplet initially at rest between two layers of immiscible fluids have been simulated in section 4.2.2. Finally to demonstrate flexibility of the method in handling moving contact lines involving density and viscosity differences, simulations of droplet spreading on a solid surface are conveyed and compared against analytical results available in literature in section 4.2.3.

4.2 Results

4.2.1 Liquid lens

In this section, simulation results for liquid lens test case are presented and compared against analytical equilibrium lens diameter. Having an analytical solution, this test case is very well suited for testing the accuracy of proposed scheme for modeling three-phase flows. Computational domain for every simulation is taken to be a square with a side length of l . Three different particle resolutions of R_1 , R_2 and R_3 have been used in simulations which have 50×50 , 100×100 and 200×200 particles, respectively. The initial particle arrangement scheme along with its relation to l will be elaborated further in the following paragraphs. All fluid properties are set to unity for every phase involved in simulations while binary surface tension coefficients assume different values depending on the test cases considered. Table 4.1 summarizes the important simulation parameters and results obtained for surface tension coefficient ratios of V_1 through V_5 at each of the resolutions R_1 , R_2 and R_3 . Different phases are ordered as shown in figures 4.1-b and 4.1-d. No slip and zero pressure gradient boundary conditions are applied to all boundaries.

Effect of initial particle arrangement

It is observed that initial particle arrangement has profound effect on results obtained from SPH simulations [177]. Two different approaches were used to arrange initial particle po-

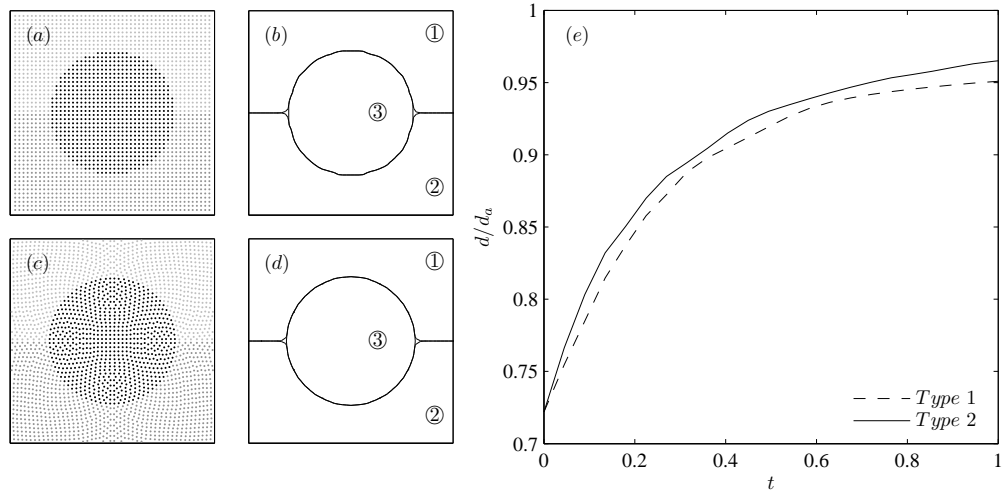


Figure 4.1: Initial condition for liquid lens simulation shown in the vicinity of the droplet; (a, b) Particle arrangement and 0.5 level contour of color function for first approach. ①, ② and ③ denote phases 1, 2 and 3, respectively; (c, d) Particle arrangement and 0.5 level contour of color function for second approach; (e) Early stage development of non-dimensional lens diameter for first and second approach of initial particle arrangements.

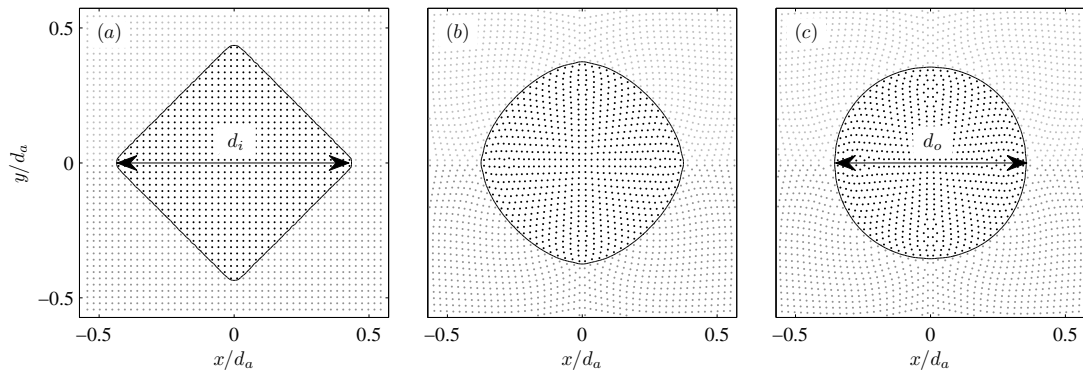


Figure 4.2: Particle arrangement and 0.5 level contour of color function of two-phase diamond relaxation; (a) Initial diamond arrangement; (b) Intermediate stage; (c) Relaxed circle obtained and used as initial particle arrangement for other test cases.

sitions in following simulations. The first approach, being the most straightforward one, consists of arranging the particles on an equally spaced formation in both dimensions. Particles within an “intended” radius of $0.5d'_o$ from the center of computational domain are marked as phase 3 and considered to be belonging to the droplet of interest, while remaining particles are divided into top and bottom portions, phase 1 and phase 2 respectively (figure 4.1-a). This method results in a rough surface pattern with an approximate initial “acquired” diameter of d_o for the encompassed droplet.

The second method involves allowing a diamond (45° tilted square) droplet of known area to deform into a circular droplet of an intended diameter of d'_o under the effect of surface tension forces in a two-phase system, hence two-phase diamond droplet relaxation shown in figure 4.2. To achieve this end within the scope of proposed three-phase model, a particle arrangement with uniform spacing in both dimensions is used and particles within a diamond of intended diagonal d'_i are considered as the droplet of interest, phase 3 (figure 4.2-a), while remaining top and bottom portions are marked as phases 1 and 2, respectively. It is notable that due to finite spacing between particles, actual diagonal of the diamond is d_i , which is slightly smaller than d'_i . Computational domain length is chosen such that $l = 2.6d'_i$ and diamond is relaxed in two-phase mode by setting $\gamma_{(12)} = 0$. The resulting circular droplet has an acquired diameter of d_o and is used as an initial condition for particle arrangement (figures 4.1-c and 4.2-c).

In both cases, initial velocities are set to zero. These initial configurations are tested against analytical equilibrium lens diameter. Assuming that equilibrium contact angle is defined by

$$\frac{\sin \theta_{(1)}}{\gamma_{(23)}} = \frac{\sin \theta_{(2)}}{\gamma_{(13)}} = \frac{\sin \theta_{(3)}}{\gamma_{(12)}} \quad (4.1)$$

and $\theta_{(1)} = \theta_{(2)}$, equilibrium lens diameter is found using the following relation [189, 190],

$$d_a = \left(\frac{2(\pi - \theta_{(1)}) - \sin(2(\pi - \theta_{(1)}))}{4A_o^2 \sin^2(\pi - \theta_{(1)})} \right)^{-1/2}. \quad (4.2)$$

This defines the distance between two triple junctions and is based on Young’s law where A_o represents initial droplet area and $\theta_{(\alpha)}$ is the contact angle of phase α with two other phases. Figure 4.1-e shows non-dimensional lens diameter versus time at early stages of simulation for both initial conditions at resolution R_2 where all binary surface tension coefficients are equal to 1. It is observable that results obtained using the first initial condition type start to fall behind those of the second type at early stages of simulation. This trend continues at later simulation times yielding an equilibrium diameter, d_f/d_a , of 0.9519 for the first method against 0.9785 for the second method of initial condition generation. This is mainly due to inaccurate measurement of initial condition acquired diameter, d_o , in the first method of initial condition generation as well as intermittent surface tension force observed when using a circular arrangement carved out of a Cartesian initial position.

Therefore, all the simulation results presented hereafter are initialized using the second method.

Effect of resolution and surface tension coefficient ratio

In this section, effects of resolution and surface tension coefficients on the evolution of liquid lens are studied. It is worthwhile to note that different resolutions have different initial acquired diameter, d_o , because of the relaxation process involved in initial condition generation. It is not possible to create diamonds with the same acquired diagonal, d_i , using equally spaced particles at different resolutions for the same computational domain size as only multiples of the finite particle spacing is accessible. This results in different final acquired diameters, d_o , for initial diamond droplets of different resolution. However, once divided by the analytic equilibrium diameter, the resulting non-dimensional initial diameters will have the same value for each surface tension ratio group, V_1 through V_5 , which is shown in table 4.1 as d_o/d_a . This ensures that when presented in non dimensional form, the results will not be affected by the relaxation process.

Figure 4.3-a shows near tip droplet profile for the three resolutions considered in this study while figures 4.3-b, c and d are non-dimensional lens diameter versus time plots for cases V_1 , V_3 and V_5 . It is observed that as the droplet lengthens under the effect of surface tension forces exerted, an equilibrium diameter is obtained. At this stage, the droplet starts to exhibit oscillations in diameter which is an expected behavior, providing that these oscillations will die out eventually. However, as the approximated differentiation and numerical implementation have small inherent round off errors affecting surface tension force which drives the lengthening phenomenon, the oscillations are not quite regular and are not damped out during the simulation times considered here. To circumvent this shortcoming, the lens diameter is time averaged after a certain threshold. Here, the averaging process starts as soon as the non-dimensional lens diameter reaches 95% of the analytic diameter. The time averaged equilibrium lens diameter is shown as a straight line for each resolution on figures 4.3-b, c and d and also in table 4.1 under d_f/d_a . The result of this simple averaging criteria is not quite informative for cases with lower resolution as it disregards the transitional behavior and focuses on equilibrium diameter. This may result in over predicting the performance, as it is the case for $R_1 V_1$ where time averaged equilibrium diameter is satisfactory despite abnormally long transitional period. However, combining it with timed plots of non-dimensional diameter, which reveal irregular behavior such as slow lengthening observed in case $R_1 V_1$, renders it a sufficient criteria for assessing the performance of the proposed method.

Comparing the time averaged values shown in table 4.1, it is seen that better steady state results are obtained at higher resolutions. The effect of higher resolution is to make the triple junction slimmer, observable in figure 4.3-a as sharper lens tip and less abrupt cut, so that the remaining portion of droplet has a smoother shape thus allowing it to extend

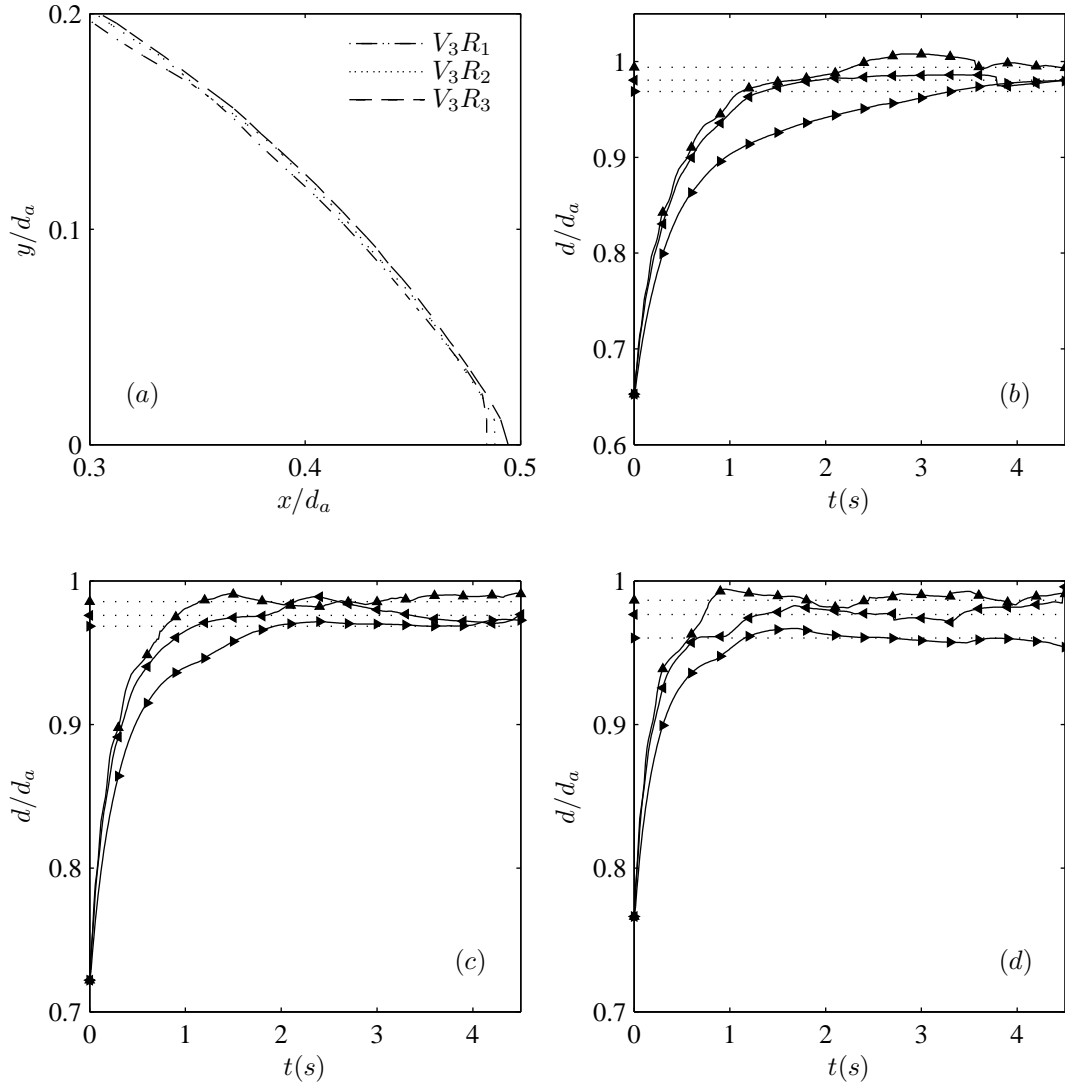


Figure 4.3: (a) Effect of resolution on equilibrium shape of test case V_3 (V_3R_1 , V_3R_2 and V_3R_3); (b, c and d) Effect of resolution on equilibrium diameter of lens for cases V_1 , V_3 and V_5 where \blacktriangleright , \blacktriangleleft and \blacktriangle denote R_1 , R_2 and R_3 resolutions, respectively. Straight lines and corresponding markers on vertical axis are time-averaged values, d_f/d_a , shown in table 4.1.

furthermore toward the equilibrium diameter. Conducting a similar analysis on transient characteristics of the simulations (figures 4.3-b, c and d), it is possible to observe that the test case with lowest resolution, R_1 , has the lowest rate of lengthening among all resolutions while higher resolutions considered here, R_2 and R_3 , exhibit the same characteristic initial lengthening rate. Slow lengthening is augmented for R_1 cases as the final lens diameter becomes larger (more slender lens shape), which occurs as the ratio of surface tension coefficients, $\gamma_{(13)}/\gamma_{(12)}$, has a lower value. The reason for this effect may also be seen in figure 4.3-a. As the resolution is reduced, it is possible to identify an abrupt cut near the tip of the lens which affects the accuracy of the computed surface curvature and subsequently surface tension force. At higher surface tension coefficient values, more slender equilibrium shapes occur which in turn should have sharper (smaller $\theta_{(3)}$) three-phase junctions. This demands a higher resolution to be fully captured which results in worse performance for lower resolution test case and signifies the importance of higher resolution requirements for higher surface tension coefficient ratios.

Figure 4.4 shows time snapshots of 0.5 level contour of color function of droplet, phase 3, along with particle positions for test cases V_1R_3 , V_3R_3 and V_5R_3 . As both dimensions are non-dimensionalized using analytic equilibrium lens diameter, final length of the droplet will be equal to 0.5 while it's height would be different. It is possible to observe that in all test cases shown, particles are spread fairly evenly across the computational domain, a desired property in SPH simulations which is a result of artificial particle displacement method employed here.

Figure 4.5 shows time snapshots of 0.5 level of color function contour at different time steps for all three-phases of case V_3R_3 . Each phase is actually treated as a separate entity when calculating surface tension forces using phase specific surface tension coefficients.

4.2.2 Droplet levitation

In this section, results of the levitation of a circular droplet, initially at rest between two layers of immiscible fluids, are presented (figures 4.1-c and 4.1-d). Droplet levitation presents a more challenging and dynamic problem to test the capabilities of the proposed three-phase formulation as the droplet breaks free of the bottom surface and rises in top fluid solely because of surface tension forces as no other body forces are present. Here initial particle arrangement is obtained by relaxing a diamond shaped two-phase droplet consisting of 200×200 particles into a circle of diameter d_o . Particle velocities in both directions are set to zero. All fluid properties except for surface tension coefficients are set to unity. As indicated in table 4.2, surface tension coefficients between phases 1 and 2 ($\gamma_{(12)}$, top fluid and bottom fluid) and between phases 1 and 3 ($\gamma_{(13)}$, top fluid and droplet) are set to unity while the surface tension coefficient between droplet and bottom fluid varies for different test cases. No slip and zero pressure gradient boundary conditions

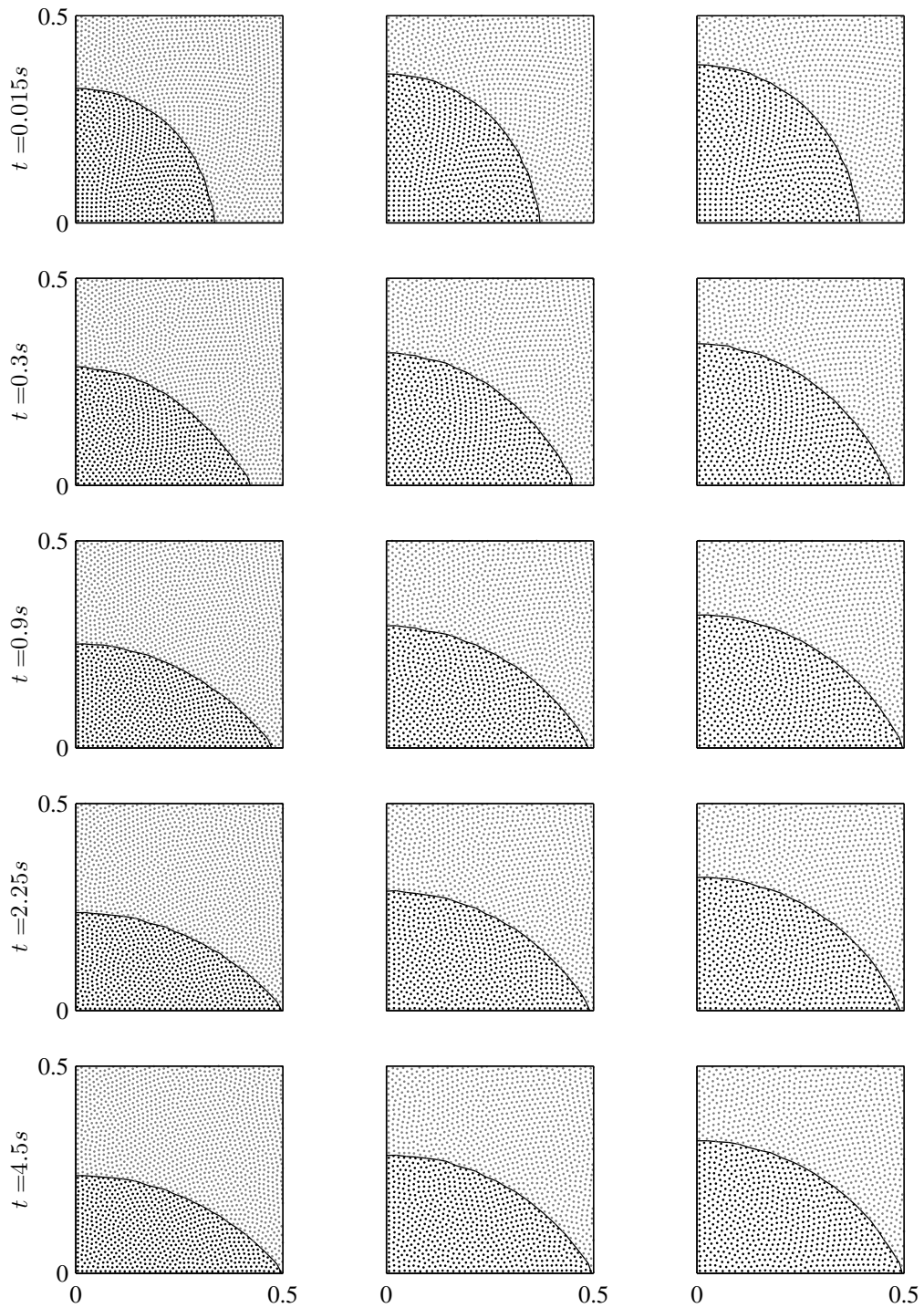


Figure 4.4: Time snapshots of particle position and droplet boundary (0.5 level contour of color function for droplet, phase 3). Both x and y axes are non-dimensionalized with each test case's respective analytic equilibrium diameter. Only top right quarter has been shown for brevity. left column: case V_1R_3 ; middle column: case V_3R_3 ; right column: case V_5R_3 .

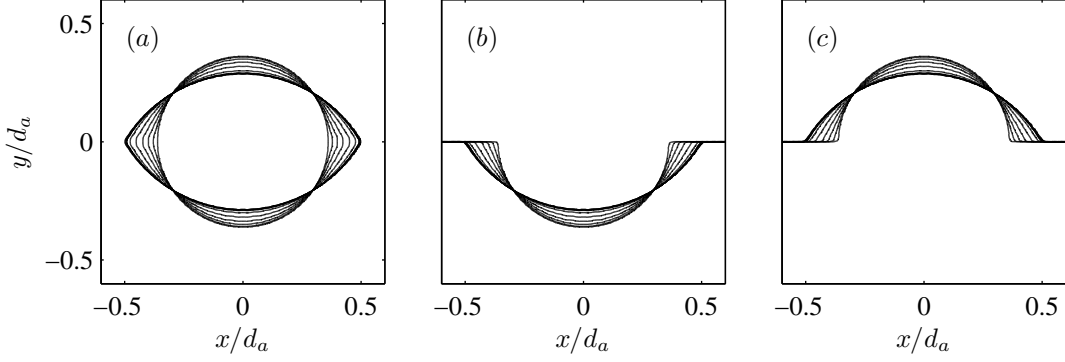


Figure 4.5: Time snapshots of all phase boundaries (0.5 level contour of color function of each phase) for case R_3V_3 . Both x and y axes are non-dimensionalized with respective analytic equilibrium diameter. (a) droplet, phase 3; (b) bottom fluid, phase 2; (c) top fluid, phase 1.

Table 4.2: Simulation parameters and results for droplet levitation test case

Test Case	$\gamma_{(23)}/\gamma_{(13)}$ ($\gamma_{(12)} = \gamma_{(13)}$)	Maximum $u_{av,y}$
L_1	2.5	0.1730
L_2	5	0.4186
L_3	10	0.8541

are applied to all the walls encompassing the computational domain, a square of $3.3d_o$ side length.

Figure 4.6 provides time snapshots of droplet levitation for all three test cases considered here. As the droplet starts to break off from the bottom surface, it experiences a deformation as a result of surface tension force exerted. The ratio of $\gamma_{(23)}/\gamma_{(13)}$ has an important implication here as it directly influences the initial amount of the force exerted. This is better observable if the average velocity, $\mathbf{u}_{av} = \sum_{j=1}^{J_{(3)}} (\hat{c}_{(3)} \mathbf{u}_j / J_{(3)})$, of all particles belonging to phase 3, $J_{(3)}$, is investigated. Figure 4.7 shows average vertical velocity, $u_{av,y}$, of the droplet for all the test cases. Times when snapshots in figure 4.6 have been taken are marked on figure 4.7 by identical letters. It is evident that larger surface tension ratios give rise to larger initial vertical velocity values. Table 4.2 summarizes maximum average vertical velocity for all cases studied here. Another impact of larger $\gamma_{(23)}/\gamma_{(13)}$ is smaller $\theta_{(1)}$ (angle between droplet and bottom fluid) at the time when droplet barely touches the bottom fluid. After separation is completed and droplet is free of the bottom fluid, droplet and top fluid pair are expected to act as a two-phase flow. This would result in a circular shape for the droplet after it comes to rest. All test cases studied here comply with this expectation although minor penetrations happen at the trailing edge of the droplet as it separates from bottom fluid. The position where the droplet comes to rest is also affected by the value of $\gamma_{(23)}/\gamma_{(13)}$. Larger values results in a higher final position for the droplet.

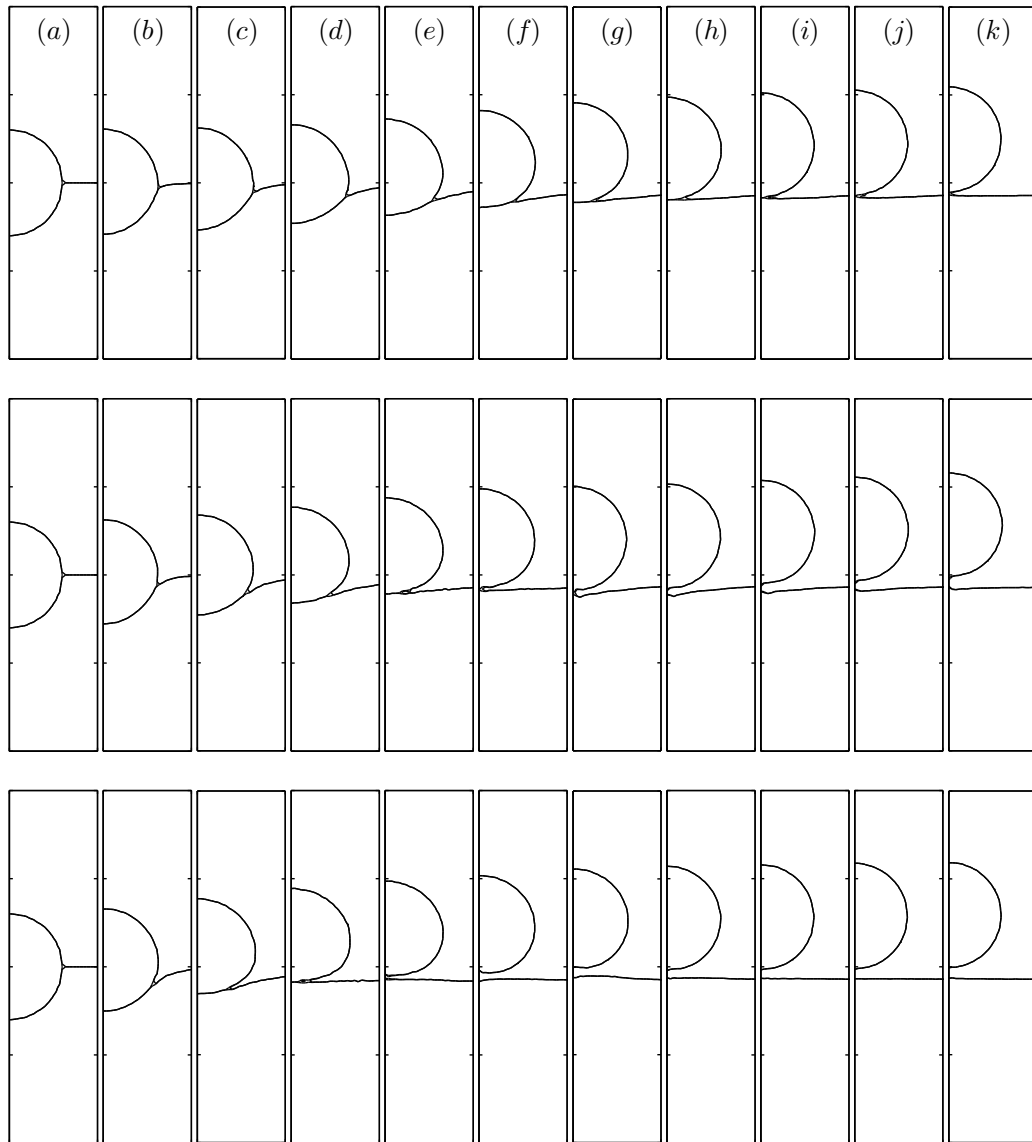


Figure 4.6: Time snapshots of 0.5 level contour for all phases. Top row: case L_1 ; Middle row: case L_2 ; Bottom row: case L_3 ; Column letters a through k are at times 0, 0.03, 0.075, 0.15, 0.3, 0.6, 1.05, 1.5, 2.25, 3.0 and 4.5 seconds. Both x and y axes are non dimensional with respect to d_o and tick marks are spaced 0.82 units apart.

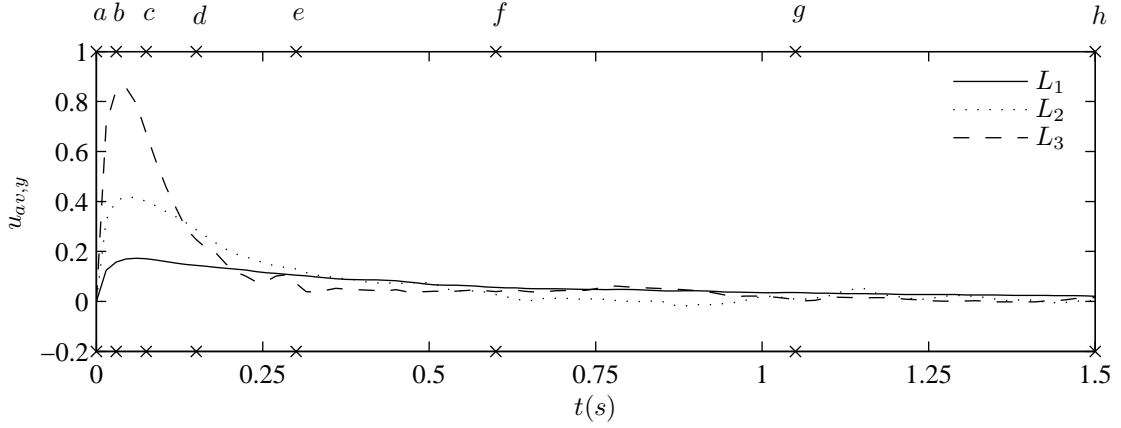


Figure 4.7: Average vertical velocity of particles in droplet phase versus time for test cases L_1 , L_2 and L_3 . Letters and \times marks on horizontal axes represent the times when snapshots a through h in figure 4.6 are taken.

4.2.3 Droplet spreading

In order to demonstrate the capability of the proposed interface treatment scheme in handling moving contact line problems, droplet spreading simulations involving different Eotvos numbers are conveyed and results are compared to analytical solutions. The problem of interest is treated as a three-phase system where each of the fluid and solid phases have a distinct smoothed color function, $c_{(\alpha)}$, associated with them. Here, phases 1, 2 and 3 indicate surrounding fluid, droplet and solid bottom surface, respectively. A half circle droplet having a radius of R_0 is positioned on the bottom surface centered at the origin. The computational domain has a non dimensional size of 3×10 and is discretized by 60×200 of equally spaced particles in a Cartesian initial positioning. In addition to the particles within the computational domain, four rows of immovable particles are also appended to phase 3. These particles are lined up below the solid surface boundary with the same spacing as of the particles above the boundary. The motivation behind using this method is to have an accurate value for the smoothed color function, $c_{(\alpha)}$, unit normal, $\mathbf{n}_{(\alpha)}$, and curvature, $\kappa_{(\alpha)}$. These particles are neither included in calculation of other field variables nor in maintaining boundary conditions on the bottom surface.

Initially, all particles are assumed to be motionless. No slip and zero pressure gradient boundary conditions are enforced on all bounding walls, however, in order to circumvent shear stress singularity arising near contact line, no slip condition is relaxed to a local free slip at the vicinity of triple junction. Hence horizontal velocity is found using $u_x = \zeta (\partial u_x / \partial y)_{wall}$, where slip length, ζ , is assumed to be infinite for particles having non zero $c_{(\alpha)}$ for all phases. Accounting for the interface thickness, at most four boundary particles in the vicinity of the contact line are subject to this condition.

Under combined effects of surface tension and gravitational forces, the droplet deforms until reaching its equilibrium shape. The steady state shape obtained by the droplet is

dependent on the equilibrium contact angle, θ_e , and Eotvos number,

$$\text{Eo} = \frac{\rho_{(2)} - \rho_{(1)}}{\gamma_{(12)}} g R_0^2, \quad (4.3)$$

where $\rho_{(1)}$ and $\rho_{(2)}$ are densities of droplet and surrounding fluid, respectively, and g is the gravitational acceleration acting downward. In all cases, $\rho_{(2)}/\rho_{(1)}$ is assumed to be equal to 20. Contact angle between droplet and solid surface is determined by the equilibrium of surface tension forces on the triple junction as indicated by (classical argument by Young,) $\gamma_{(23)} + \gamma_{(12)} \cos \theta_e - \gamma_{(13)} = 0$, which upon incorporating the definition of phase specific surface tension coefficients (2.23) may be rewritten as

$$\theta_e = \cos^{-1} \left(\frac{\gamma_{(1)} - \gamma_{(2)}}{\gamma_{(1)} + \gamma_{(2)}} \right). \quad (4.4)$$

In all test cases considered here, $\gamma_{(1)}$ is set equal to $\gamma_{(2)}$, resulting in an equilibrium angle of 90° .

A high Eo (*i.e.* $\text{Eo} \gg 1$) implies that droplet shape is governed by gravitational forces whereas a low Eo (*i.e.* $\text{Eo} \ll 1$) indicates a surface tension dominated shape at steady state. Flows with intermediate values of Eo feature a non-trivial competition between these two effects. For $\text{Eo} \gg 1$, the analytical solution for the maximum height of the droplet is given by $H = R_0 (1 - \cos \theta_e) \sqrt{\pi (2\theta_e - 2 \cos \theta_e \sin \theta_e)}$. As for $\text{Eo} \ll 1$, the analytical solution indicates that the maximum height of the deformed droplet is proportional to Eo as $H = 2R_0 \text{Eo}^{-1/2} \sin(\theta_e/2)$. A set of simulations for $0.1 \leq \text{Eo} \leq 13.3$ are performed and the results are compared with the aforementioned asymptotic analytical solutions.

Figure 4.8 provides plots of 0.5 level contour of color function as well as particle placements at equilibrium for different Eo while figure 4.9 provides normalized steady state droplet height for $0.1 \leq \text{Eo} \leq 13.3$. As the difference between initial and final shapes of droplet for case $\text{Eo} = 0.1$ is negligible, its contour plot is not shown here. It is observable that the computed normalized droplet height agrees well with the asymptotic solutions given for $\text{Eo} \gg 1$ and $\text{Eo} \ll 1$. As for the intermediate values of Eo, a transition between spherical cap and puddle shape occurs. At higher Eo, the difference between asymptotic solution and numerical results decreases.

4.3 Remarks

In this chapter, the proposed ISPH method for modeling incompressible, immiscible three-phase fluid flows has been tested. Surface tension coefficients are decomposed into phase specific coefficients and surface tension force is exerted by implementing CSF model. To complement this, a unique color function is associated with each phase and then smoothed out to improve the robustness of the method while a threshold has been implemented for

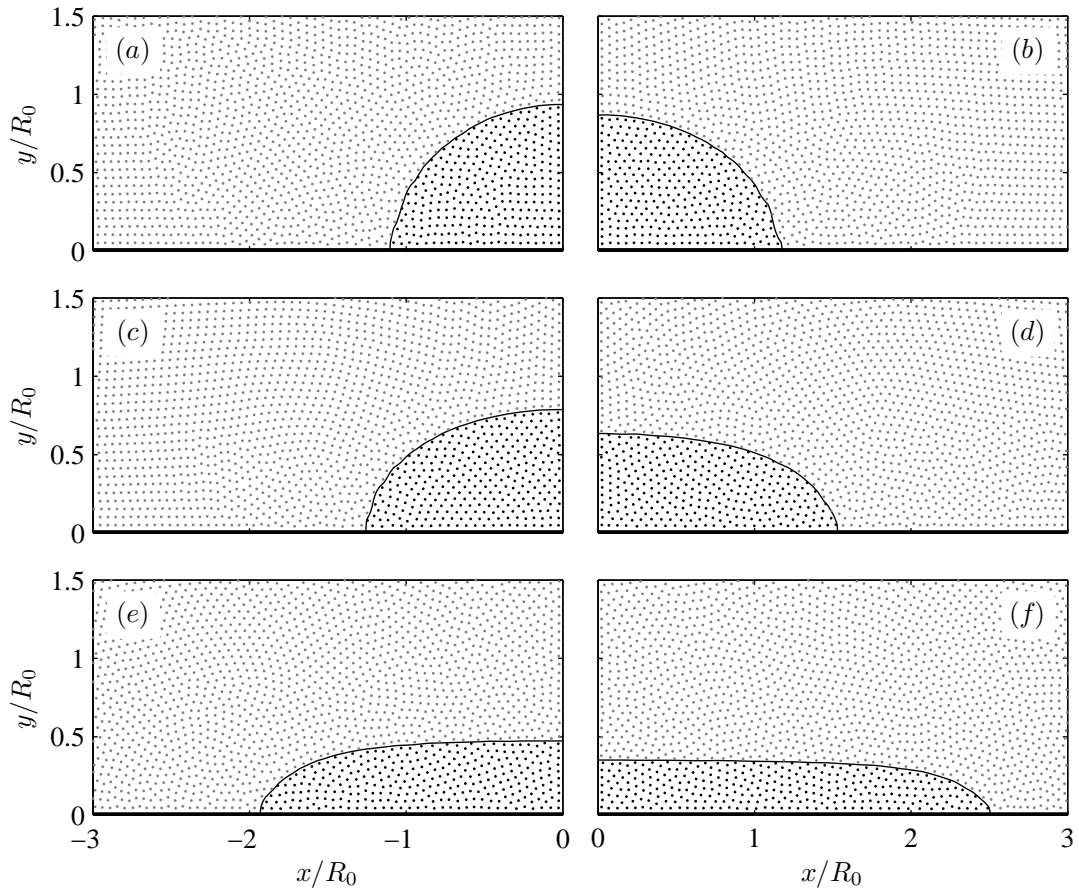


Figure 4.8: Equilibrium particle position and droplet boundary (0.5 level contour of color function, phas 2). Only half of the computational domain has been shown for brevity. Solid lines indicate bottom wall (phase 3). (a) $Eo = 0.475$; (b) $Eo = 0.95$; (c) $Eo = 1.9$; (d) $Eo = 3.8$; (e) $Eo = 7.6$; (f) $Eo = 13.3$

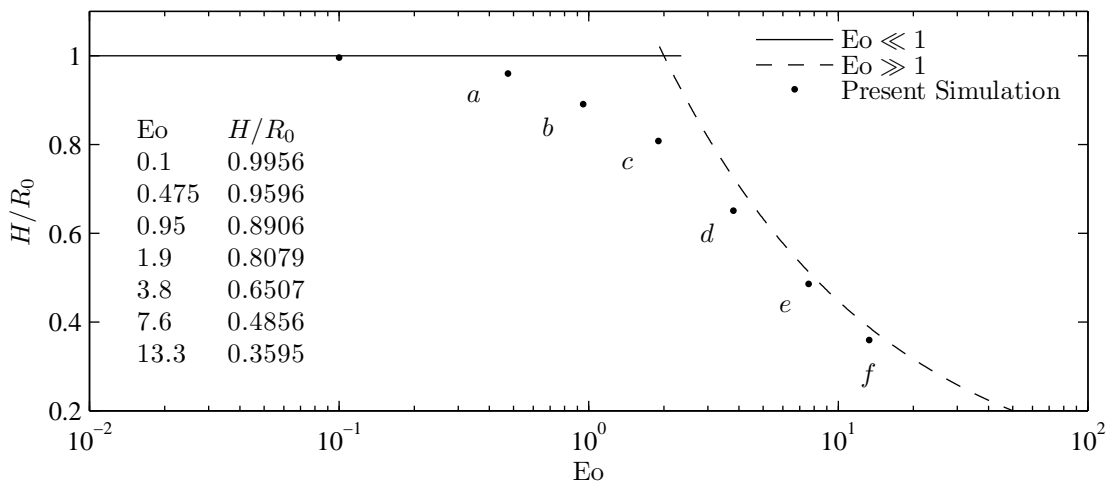


Figure 4.9: Normalized equilibrium droplet height versus Eo . Letters a through f correspond to the droplet shapes shown in figure 4.8.

choosing reliable normals to increase the accuracy of computed surface tension force. Furthermore, artificial particle displacement has been employed to ensure uniform spread of particles throughout the computational domain. Several test cases have been simulated to ensure the capability of the method in handling various three-phase flow combinations.

Having an analytical solution, formation of a lens shape from a circular droplet under surface tension forces have been studied to facilitate testing the accuracy of the proposed method. Results show that this test case is highly sensitive to initial particle positioning, favoring an arrangement obtained from two-phase diamond droplet relaxation over a droplet simply carved out of an equally spaced particle arrangement. Simulations have been carried out in three different resolutions, revealing that an abrupt cut at the tip of the lens is responsible for the inaccuracies incurred at low resolutions. The results obtained from high resolution simulations at different surface tension ratios using improved initial condition are found to be compatible with analytical solution of the equilibrium lens length. To further test the capabilities of the proposed method in handling dynamic problems, a droplet levitation test case has been simulated for different surface tension ratios. It is observed that, higher surface tension ratios result in faster break up from surface due to larger force exerted at triple junction. Furthermore, higher surface tension ratio resulted in larger maximum droplet velocity and higher stopping height. As the last test case, droplet spreading with a contact angle of 90° has been considered. With minor modifications, the method has been able to simulate contact line dynamics for a variety of Eotvos numbers, demonstrating the flexibility of the method and its capability in handling density and viscosity differences between phases. Results obtained for $Eo \gg 1$ and $Eo \ll 1$ are compatible with analytical results available for these two extremes while a transition from spherical cap to puddle shape occurs for Eo values in between.

The simulations conducted here and the comparison of the results show that the proposed ISPH scheme is capable of handling flows with up to three unique phases. This proves it as a suitable basis for the addition of the electrostatic and fluid-structure/solid interaction components which will be tested further in chapters 5, 6 and 7.

Chapter 5

Electrohydrodynamics*

5.1 Introduction

An interface between two immiscible fluids may be subject to capillary, viscous and gravitational forces, depending on the flow configuration. Manipulation of this interface by introducing an external electric field has been of great interest. Earlier works on this subject have been carried out by Taylor [138], who proposed the leaky dielectric model. Melcher conducted further studies on the effects of tangential and perpendicular fields on the interface [139, 191]. A review of several flow configurations are provided by Saville [108]. Some examples of the applications of electrically manipulated interfaces are found in spraying [192, 193], flow focusing [194], dispersion [195], micromixing [196–198] and pattern formation [199, 200], to name a few.

The manipulation of the interface with the electric field is highly dependent upon the orientation of the electric field with respect to the interface and the electrical properties of the fluids in question. The electric field may be parallel or perpendicular to the initially undisturbed interface while the fluids may be either perfect or leaky dielectrics. Pease and Russel [201] investigated the pattern formation in leaky and perfect dielectric fluids using linear stability analysis, pointing out the importance of conductivity in the liquid. Shankar and Sharma [202] conducted a similar study for leaky dielectric fluids using lubrication theory. Craster and Matar [200] investigated the instabilities in thin films in the non-linear regime and reported the effects of fluid properties on the formation of instabilities. In these studies the electric field direction is perpendicular to the interface. Tilley *et al.* [203] investigated small-amplitude capillary waves on a non-conducting (perfect dielectric) liquid sheet subject to a parallel electric field, and showed that the electrical force delays rupture in the sheet. Further extension to arbitrary amplitudes was carried out by Papageorgiou and Vanden-Broeck [204]. The effects of parallel and perpendicular electric fields on the

*Appears in: N. Tofighi, M. Ozbulut, J.J. Feng and M. Yildiz, The effect of normal electric field on the evolution of immiscible Rayleigh-Taylor instability, *Theor. Comput. Fluid Dyn.* (2016). doi:10.1007/s00162-016-0390-0

evolution of the interface in (pressure driven) channel flows were studied by Uguz and Aubry [205]. Their results show that both parallel and perpendicular electric fields may be used to stabilize or destabilize the interface.

The studies mentioned above disregarded gravity because of the dominating role of electrical and capillary forces. One configuration where gravity plays an important role in driving the flow is Rayleigh-Taylor Instability (RTI). First observed by Lord Rayleigh [206] and Taylor [207], the instability happens when a heavier fluid sits atop a lighter one. The effects of an external electric field on the RTI have been well studied [198, 208–212]. Mohamed and Shehawy [208] investigated the effects of a perpendicular electric field for perfect dielectric fluids using the method of multiple-scale perturbations. Their results show that the electric field may stabilize or destabilize the interface depending on the electric permittivity and density ratios. Elbade [210] studied the effects of parallel electric field and identified a stabilizing regime for RTI of inviscid perfect dielectric fluids. Barannyk *et al.* [212] further investigated this case for the limit of thin upper layer and reported a periodic motion at the interface for large enough electric fields. Joshi *et al.* [211] derived the dispersion relation for perturbation at the interface, emphasizing the viscous and leaky dielectric nature of the fluids. Most of the studies on electrohydrodynamic RTI are limited to the linear regime, and little has been done on the nonlinear development on longer time scales. To author's knowledge, the only exception is Cimpanu *et al.* [198], who performed Direct Numerical Simulation (DNS) of RTI in perfect dielectric medium subject to parallel electric field and found the results in the linear regime to be in agreement with their linear stability analysis. They further investigated the non-linear regime using DNS and proposed a method for modulating the interface using timed electric field application.

Another limitation of the prior studies is their use of the perfect dielectric model. In reality, conductivity plays an important role in the evolution of interfacial forces in most fluids of interest [211, 213, 214]. The evolution of RTI in viscous leaky dielectric fluids in the presence of an external field involves complex interaction of surface and body forces. In this regard, a close observation of the interfacial forces and vorticity generation may provide valuable information regarding the later stages of the RTI evolution. To this end, RTI perturbed by a small-amplitude cosine wave subject to a perpendicular electric field is simulated. Unlike a parallel field, a perpendicular electric field does not result in suppression of the instability, allowing us to study the effects at later stages of the evolution.

The current method has been used successfully to simulate Rayleigh-Taylor instability [215] and deformation of a neutrally buoyant droplet suspended in an external electric field [216]. As RTI in the presence of an external field is a combination of the aforementioned cases, no further validation studies are conducted and electrohydrodynamic RTI is simulated directly. The results obtained here show that within the range of the parameters covered, the surface charges play an important role in shaping the interface. The

electrical forces are concentrated on either of the bubble or the spike tips, depending on the parameters, and compete with the surface tension forces. The dominant mechanism in vorticity generation is found to be the surface tension force. However, the electric forces show comparable role at later stages of the simulation for higher field strengths.

5.2 Dimensionless form of the equations

The governing equations are made dimensionless assuming the following characteristic scales

$$\begin{aligned} \mathbf{x}^* &= \frac{\mathbf{x}}{W}, & t^* &= \frac{t}{\sqrt{W/g}}, & \mathbf{u}^* &= \frac{\mathbf{u}}{\sqrt{gW}}, & \kappa^* &= \kappa W, \\ p^* &= \frac{p - \rho \mathbf{g} \cdot \mathbf{x}}{\bar{\rho} g W}, & \rho^* &= \frac{\rho}{\bar{\rho}}, & \mathbf{g}^* &= \frac{\mathbf{g}}{g}, \\ \mathbf{E}^* &= \frac{\mathbf{E}}{E_\infty}, & \phi^* &= \frac{\phi}{E_\infty W}, & q^* &= \frac{q^v}{\bar{\epsilon} E_\infty / W}, \end{aligned} \quad (5.1)$$

where $\bar{\square}$ denotes arithmetic average between heavier and lighter fluid values. W is the width of the computational domain while E_∞ and g_∞ denote undisturbed electric field strength and gravitational acceleration, respectively. In addition, ratios of heavy to light fluid values are defined as

$$\mathcal{A} = \frac{\rho_h - \rho_l}{2\bar{\rho}}, \quad \mathcal{V} = \frac{\mu_h - \mu_l}{2\bar{\mu}}, \quad \mathcal{P} = \frac{\epsilon_h - \epsilon_l}{2\bar{\epsilon}}, \quad \mathcal{C} = \frac{\sigma_h - \sigma_l}{2\bar{\sigma}}. \quad (5.2)$$

where subscripts \square_h and \square_l denote heavy and light fluids, respectively. Implementing these scales, the dimensionless numbers may be rewritten as

$$\text{Re} = \frac{\bar{\rho} \sqrt{g_\infty} W^3}{\bar{\mu}}, \quad \text{Bo} = \frac{\bar{\rho} g_\infty W^2}{\gamma}, \quad \text{Eg} = \frac{\bar{\rho} g_\infty W}{\bar{\epsilon} E_\infty^2}, \quad (5.3)$$

where Re, Bo and Eg are Reynolds, Bond and Electro-gravitational numbers [217], respectively. Taking Re, Bo, \mathcal{A} and \mathcal{V} constant, the remaining effective parameters are Eg, \mathcal{P} and \mathcal{C} , allowing this study to assess the effects of electrical properties and electric field intensity on the evolution of the instability. The motivation behind choosing \mathcal{P} and \mathcal{C} in their current form is to determine the force directions by observing the sign of these parameters.

To maintain the relative magnitude of the interfacial forces when comparing them, $\mathbf{f}_{(s)}$ and $\mathbf{f}_{(e)}$ are normalized with $\bar{\rho} g_\infty$.

5.3 Forces on a flat interface midway of flat electrodes

To demonstrate the underlying relation between \mathcal{P} , \mathcal{C} and $\mathbf{f}_{(e)}$, a simplification for flat regions is derived here. As bubble and spike tips have relatively flat surfaces, this will provide further insight about the behavior of these structures with respect to \mathcal{P} and \mathcal{C} . Using dimensional form of the variables and starting with the definition of a divergence free electric field (equation (2.41)), it is possible to approximate the divergence of the electric field across the interface as

$$\nabla \cdot \mathbf{E} \approx -\bar{\mathbf{E}} \cdot \frac{\nabla \sigma}{\bar{\sigma}}. \quad (5.4)$$

It is notable that the strength of electric field due to finite potential $\Delta\phi$ on a flat interface depends on its position with respect to the electrodes and \mathcal{C} as

$$\bar{\mathbf{E}} \approx \frac{\Delta\phi}{(H-y)(1-\mathcal{C}) + y(1+\mathcal{C})} \mathbf{n}. \quad (5.5)$$

Without a loss in generality, it is assumed that $\bar{\sigma} = \bar{\varepsilon}$ and test cases are set according to this assumption. Upon setting $\nabla f = -\delta \mathbf{n} \Delta f$, where $\Delta f = f_h - f_l$ represents permittivity or conductivity difference between heavy and light fluids, one may rewrite equation (2.35) as

$$q^v \approx -2\bar{\varepsilon}\delta \bar{\mathbf{E}} \cdot \mathbf{n} (\mathcal{P} - \mathcal{C}). \quad (5.6)$$

As noted before, positive normal vector points from heavier fluid to the lighter one in this study. This means that surface normal and electric field vector point in the same direction on the flat portions of the interface. Consequently, approximations of $\mathbf{f}_{(eq)}$ and $\mathbf{f}_{(ep)}$ follow as

$$\mathbf{f}_{(eq)} \approx -2\bar{\varepsilon}\delta (\mathcal{P} - \mathcal{C}) \bar{\mathbf{E}}^2 \mathbf{n}, \quad \mathbf{f}_{(ep)} \approx \bar{\varepsilon}\delta \mathcal{P} \bar{\mathbf{E}}^2 \mathbf{n}, \quad (5.7)$$

while $\mathbf{f}_{(e)}$ may be approximated as

$$\mathbf{f}_{(e)} \approx -\bar{\varepsilon}\delta (\mathcal{P} - 2\mathcal{C}) \bar{\mathbf{E}}^2 \mathbf{n}. \quad (5.8)$$

Equations (5.5), (5.7) and (5.8) provide a coarse approximation to the electric field and the electric force applied to the bubble and the spike tip regions, facilitating a general observation of the trends.

5.4 Contribution of the interfacial forces to the vortex sheet strength

Following Dopazo *et al.* [218] and Wu [219], the vortex sheet strength on an infinitesimal path of length δ_ω perpendicular to the interface may be written as

$$\Gamma = \int_{-\delta_\omega/2}^0 \omega_l dn + \int_0^{\delta_\omega/2} \omega_h dn. \quad (5.9)$$

The contribution of pressure to $D\Gamma/Dt$ may be written as

$$\mathbf{n} \times \left\| \frac{1}{\rho} \nabla p \right\| = \mathbf{n} \times \nabla \left\| \frac{p}{\rho} \right\|, \quad (5.10)$$

where $\|f\| = f_h - f_l$. Rearranging $\|p/\rho\|$ into

$$\left\| \frac{p}{\rho} \right\| = \frac{\|p\|}{\rho_h} - \left(\frac{1}{\rho_l} - \frac{1}{\rho_h} \right) p_l \quad (5.11)$$

and considering the stress balance on the interface [216], one may rewrite the left hand side of equation (5.10) as

$$\mathbf{n} \times \left\| \frac{1}{\rho} \nabla p \right\| = -\mathbf{n} \times \frac{\nabla (\mathbf{n} \cdot \mathbf{f}_{(e)} + \mathbf{n} \cdot \mathbf{f}_{(s)})}{\bar{\rho} (1 + \mathcal{A})} - \mathbf{n} \times \frac{2\mathcal{A}}{\bar{\rho} (1 - \mathcal{A}^2)} \nabla p_l, \quad (5.12)$$

where both fluids have identical viscosities while \mathcal{A} and $\bar{\rho}$ denote Atwood number and average density, respectively. The first term on the right hand side of the above equation will be computed to study the effects of the interfacial forces on vortex sheet strength. Although the above definition assumes an infinitesimally thin interface, the forces used to evolve a diffuse representation of the interface in the simulations are employed here. As such, the forces are interpolated at the nominal location of the interface (0.5 level contour of color function) before calculating equation (5.12).

5.5 Results

In this study Re , Bo , \mathcal{A} and \mathcal{V} are assumed to be constants and equal to 225, 150, 1/3 and 0 while \mathcal{P} , \mathcal{E} and Eg are varied to study the effects of electrical forces. The computational domain consists of a rectangle of size 1×4 discretized by 80×320 particles arranged on a Cartesian grid. This corresponds to a uniform particle spacing of 1/80 for the base resolution. Top and bottom walls obey the no-slip condition and have a constant potential difference. Side walls allow slip but prohibit penetration. The electric field direction is fixed pointing downward and parallel to the side walls. To define heavier and lighter fluid

regions, an initial interfacial perturbation according to

$$\hat{c}(x, y) = \begin{cases} 0, & y > 2 + 0.025 \cos(2\pi x), \\ 1, & y < 2 + 0.025 \cos(2\pi x), \end{cases} \quad (5.13)$$

is used. Two sets of parameters, PN (Positive permittivity ratio $\mathcal{P} = 0.3$, Negative conductivity ratio $\mathcal{C} = -0.3$, $E_g = 90$) and NP (Negative permittivity ratio $\mathcal{P} = -0.3$, Positive conductivity ratio $\mathcal{C} = 0.3$, $E_g = 90$), are referred to as baseline cases. When studying the effects of each parameter, the other parameters are kept constant at the baseline values. First the convergence of the numerical results with respect to spatial resolution is established. Then the baseline cases are compared to RTI with no electric field and the general behavior of the interfacial forces are presented. The effects of the electrical properties of the fluids are investigated by simulating RTI at different \mathcal{P} and \mathcal{C} . Finally, by varying E_g , the effects of electric field intensity on the evolution of instability is studied.

5.5.1 Spatial resolution

As the particles are initially arranged in an equally spaced Cartesian grid, equation (5.13) results in an interface with a resolution-dependent step-like pattern. While the computational method is extensively tested for RTI without an external electric field [215], addition of electric forces necessitates further confirmation of proper resolution. To test the effects of the resolution on the results, case NP with particle spacings of 1/40, 1/60, 1/80, 1/100 and 1/120 is simulated and the results are compared.

Figure 5.1 plots the simulation results where the lowest point of the heavier fluid is called the ‘‘spike tip’’ (\square_s) and the highest point of the lighter fluid is referred to as the ‘‘bubble tip’’ (\square_b). Interface profiles are taken at moments when the spike reaches the following positions: $y_s = 1.7, 1.4, 1.1, 0.8$ and 0.5 . Due to its initial step-like nature, the interface retains a slightly sinuous profile during the simulation. This results in a wavy pattern in surface tension force as it depends on the second derivative of the color function (*cf.* figures 5.3 and 5.4). However, as it is seen in figure 5.1-a and 5.1-b, position and velocity profiles are quite similar for 1/80 and finer particle spacings. The interface profiles in the vicinity of the spike and bubble (figure 5.1-c) have similar structures as well. Based on these observations and considering that this study focuses mostly on the behavior of the spike and bubble regions, the base resolution is found adequate.

5.5.2 Effects of an external electric field

In order to identify the effects of the electric field on Rayleigh-Taylor instability, the evolution of baseline cases are compared to that of a case with No Electric field, NE. Figure 5.2 provides spike and bubble tip positions and velocities along with snapshots of interface

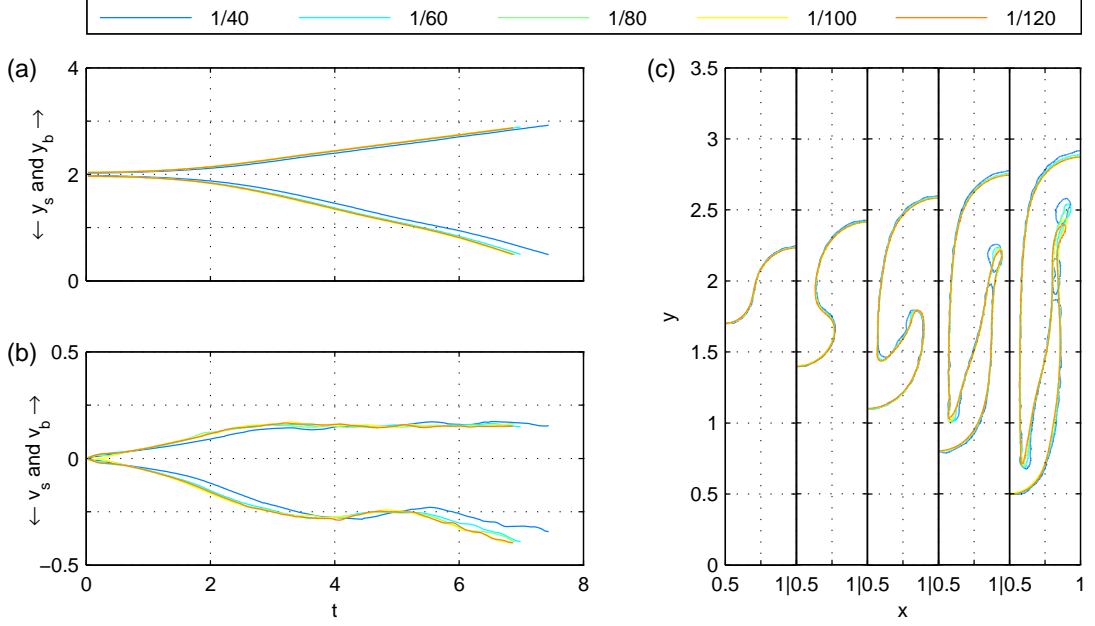


Figure 5.1: Spike and bubble tip positions (a) and velocities (b) versus time for different particle spacings; (c) interface profiles at $y_s = 1.7, 1.4, 1.1, 0.8$ and 0.5 .

profiles at $y_s = 1.7, 1.4, 1.1, 0.8$ and 0.5 . For case NP, the electric field affects the position of the spike tip much more than the bubble tip. The spike moves faster while the bubble is slightly slower. The opposite is true for case PN where the bubble is the faster feature. When compared at similar spike tip position, the longer side tails of case PN may also be attributed to its faster bubble ascent.

To better demonstrate the force composition (and analyze its effects) along the interface, figures 5.3 and 5.4 provide the force components perpendicular to the interface versus normalized interface length at spike tip position $y_s = 1.4$. A superscript \square^n is used to denote the normal component when necessary. A positive value indicates a force pointing from heavier fluid to the lighter one. The only tangential component (not shown) applied to the interface is due to $\mathbf{f}_{(eq)}$ which is an order of magnitude smaller than its normal component and two orders of magnitude smaller than the surface tension force.

Figures 5.3-b and 5.4-b show the normal electric force $\mathbf{f}_{(e)}^n$ and its components, $\mathbf{f}_{(ep)}$ and $\mathbf{f}_{(eq)}^n$, as defined in equation (2.29). The polarization force $\mathbf{f}_{(ep)}$ always points in the opposite direction of the permittivity gradient, *i.e.* toward the heavier fluid for case NP and in reverse direction for case PN. The Coulomb force $\mathbf{f}_{(eq)}$ is only parallel to the electric field and its direction is dependent on q . At this stage of the simulation, the extrema of $\mathbf{f}_{(eq)}^n$ occur at the spike tip, bubble tip and the relatively flat region between the two inflection points along the interface. $\mathbf{f}_{(ep)}$ has a smaller and relatively uniform magnitude along the interface when compared to $\mathbf{f}_{(eq)}^n$.

Figures 5.3-c and 5.4-c plot the electric force $\mathbf{f}_{(e)}^n$, surface tension $\mathbf{f}_{(s)}$ and their sum-

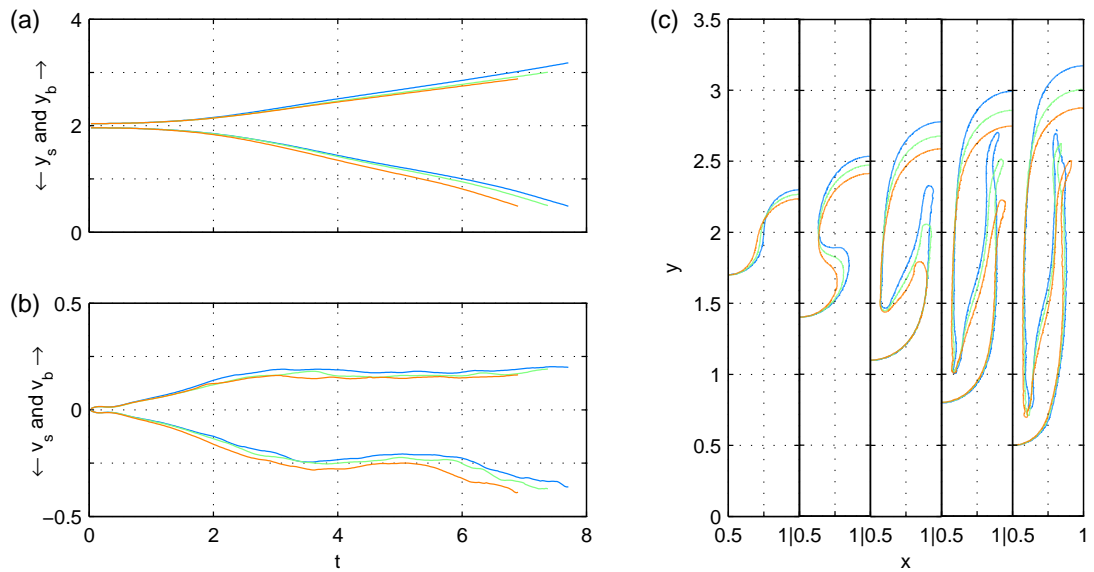


Figure 5.2: Spike and bubble tip positions (a) and velocities (b) for cases NP (red), PN (blue) and NE (green); (c) interface profiles at $y_s = 1.7, 1.4, 1.1, 0.8$ and 0.5 .

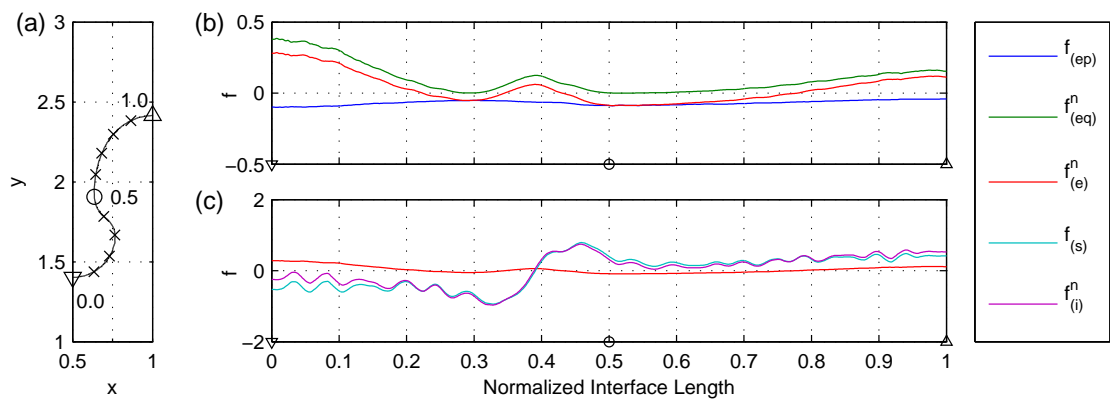


Figure 5.3: Profiles of normal force magnitudes along the interface for case NP; (a) interface profile; (b) electrical force and its components; (c) electrical force, surface tension and the resultant interfacial force; the cross marks on the interface are placed at 0.1 intervals of normalized interface length. Symbols on the interface and horizontal axes correspond to spike tip (∇), middle point of interface (\circ) and bubble tip (Δ).

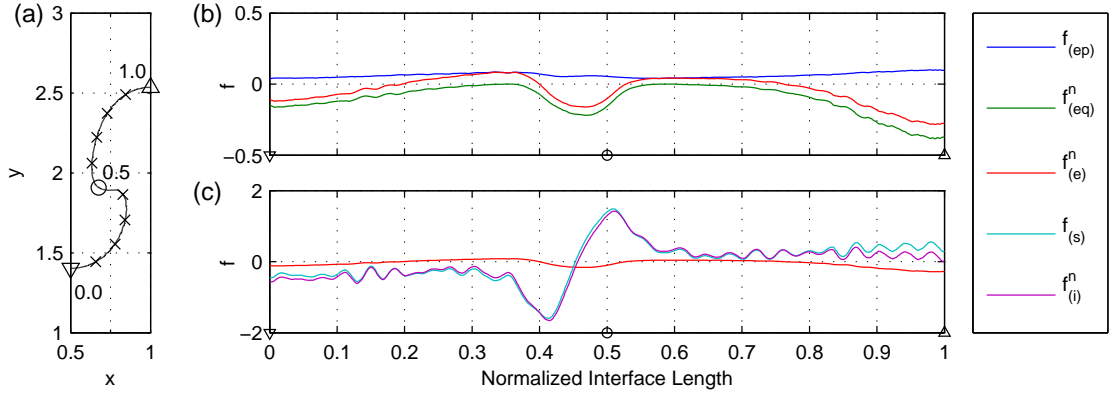


Figure 5.4: Profiles of normal force magnitudes along the interface for case PN; (a) interface profile; (b) electrical force and its components; (c) electrical force, surface tension and the resultant interfacial force; the cross marks on the interface are placed at 0.1 intervals of normalized interface length. Symbols on the interface and horizontal axes correspond to spike tip (∇), middle point of interface (\circ) and bubble tip (Δ).

mation $\mathbf{f}_{(i)}^n$. Compared to the surface tension, which is larger at sharper corners of the interface, the electric force is almost negligible except at bubble tip (case PN) or spike tip (case NP). The role of the resultant electric force in these cases may be described as that of countering the hindrance of surface tension force which tends to minimize the surface energy by reducing the curvature. In case NP, the total force on the spike region is reduced due to the presence of the external electric field while the impeding force on the bubble is slightly increased. Having the inverse force configuration, case PN experiences the opposite situation where bubble ascent is less prohibited and spike descent is slightly more hindered. This results in faster bubble ascent for case PN and faster spike descent for case NP, as observed in figure 5.2.

5.5.3 Effects of electrical permittivity and conductivity ratios

To study the effects of the permittivity ratio, the conductivity ratio is kept constant at $\mathcal{C} = \pm 0.3$ while \mathcal{P} is varied from -0.9 to $+0.9$ in steps of 0.2. As for the effects of the conductivity ratio, $\mathcal{P} = \pm 0.3$ while \mathcal{C} is varied from -0.5 to $+0.5$ in steps of 0.2.

Figure 5.5 shows spike and bubble positions and velocities with respect to time for constant \mathcal{C} . The arrows show the direction of increasing permittivity ratio \mathcal{P} . The effect of increase in \mathcal{P} is identical for both $\mathcal{C} = \pm 0.3$, resulting in an increase in bubble ascent velocity while hindering the spike descent. Comparing the two cases, it is notable that the effects are more pronounced in the spike for $\mathcal{C} = +0.3$ while the bubble is more affected in $\mathcal{C} = -0.3$. Assuming that the bubble or the spike tip of different cases passing through the same height experience the same electric field, it is seen that $\mathbf{f}_{(e)}$ and its components $\mathbf{f}_{(ep)}$ and $\mathbf{f}_{(eq)}$ have a linear relationship with \mathcal{P} (*cf.* Appendix). Increasing \mathcal{P} at constant

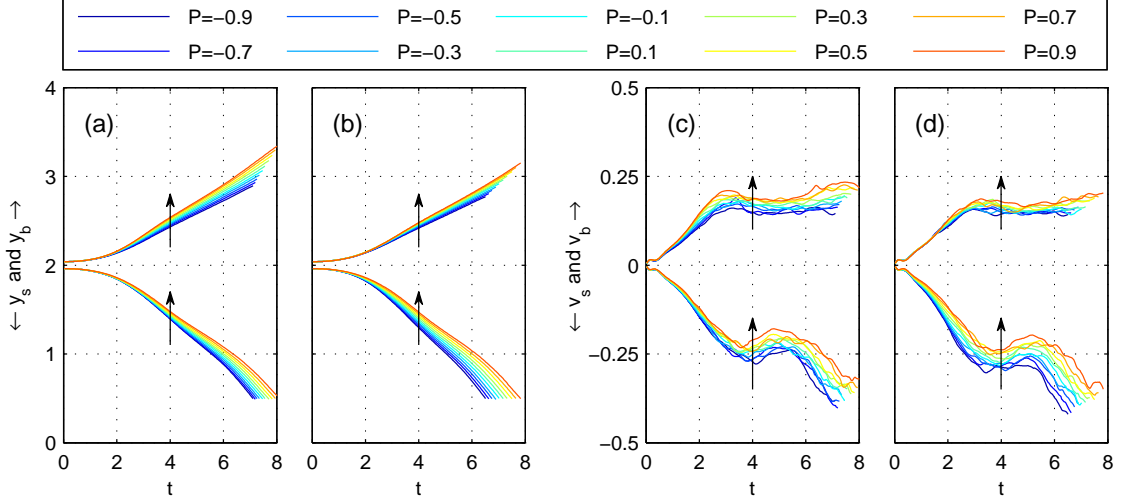


Figure 5.5: Spike and bubble tip position (a,b) and velocity (c,d) for $\mathcal{E} = -0.3$ (a,c) and $\mathcal{E} = +0.3$ (b,d); the arrow shows the direction of increasing \mathcal{P} .

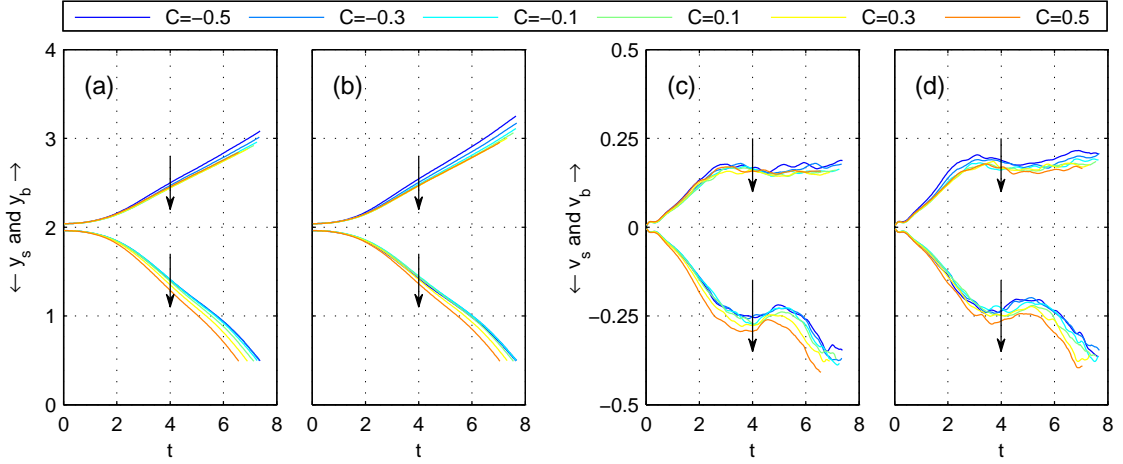


Figure 5.6: Spike and bubble tip position (a,b) and velocity (c,d) for $\mathcal{P} = -0.3$ (a,c) and $\mathcal{P} = +0.3$ (b,d); the arrow shows the direction of increasing \mathcal{C} .

\mathcal{C} increases $\mathbf{f}_{(e)}$ which in turn reduces the spike descent velocity and increases the bubble ascent velocity. For $\mathcal{C} < 0$, the electric field is stronger at larger y thus having greater effect on the bubble while $\mathcal{C} > 0$ has a similar effect on the spike (*cf.* equation (5.5) in Appendix).

Figure 5.6 provides spike and bubble tip positions and velocities with respect to time for different \mathcal{C} at constant \mathcal{P} . Increasing \mathcal{C} reduces the ascent velocity of the bubble while increasing the descent velocity of the spike. For the range of parameters studied here, the bubble tip position tends to converge to a similar profile for $\mathcal{C} > 0$ whereas such convergence for the spike happens for $\mathcal{C} < 0$. A similar observation is valid for the tip velocities as well. The reason behind this behavior lies in the relation between electric field intensity and \mathcal{C} (*cf.* equation (5.5) in Appendix). At $\mathcal{C} = 0$ the electric field intensity

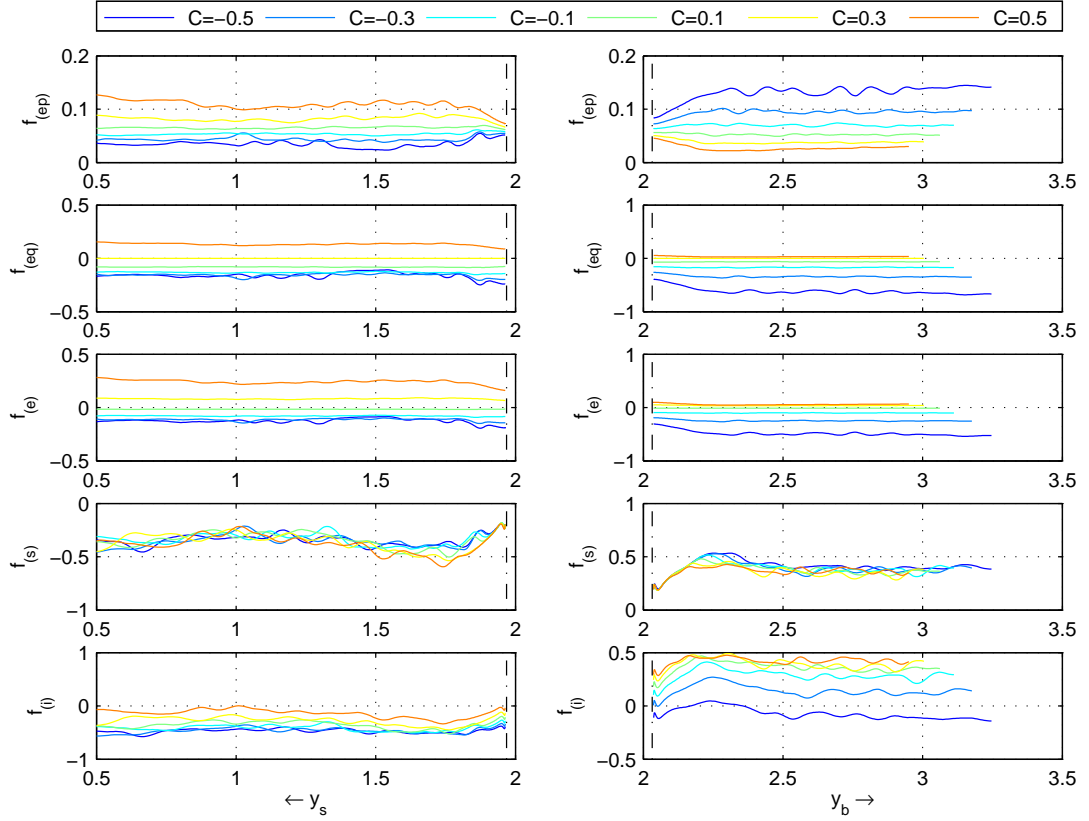


Figure 5.7: Magnitude of spike tip forces (left) and bubble tip forces (right) with respect to tip position for $\mathcal{P} = +0.3$.

is uniform and equal to E_∞ . Further increase in \mathcal{C} results in a reduction in electric field intensity at the bubble region. The difference in electric field intensity between consecutive levels of \mathcal{C} is also reduced for larger \mathcal{C} . As a result, the electric force magnitude tends to converge to a minimum value at larger \mathcal{C} , as seen in figure 5.7-right for $\mathcal{P} = +0.3$. The reverse is true for the spike region where the electric force profiles converge for $\mathcal{C} < 0$ (figure 5.7-left). Figure 5.7 also shows surface tension and resultant interfacial force for bubble and spike tips with respect to the related feature's position. Surface tension is mostly insensitive to changes in electrical properties. As expected, surface tension is the dominant interfacial force where electrical force has the smallest magnitude, *i.e.* for $\mathcal{C} < 0$ on the spike and for $\mathcal{C} > 0$ on the bubble. As a result, a converging profile is observed for each feature in its respective interval of \mathcal{C} . Similar observations are valid when $\mathcal{P} = -0.3$.

5.5.4 Effects of electric field intensity

Positions, velocities and interface profiles

To investigate the effects of the electric field intensity, the electro-gravitational number is started from 5.625 and multiplied by two for consecutive cases until $Eg = 360$ where a lower Eg denotes larger electric field intensity. The permittivity and conductivity ratio are

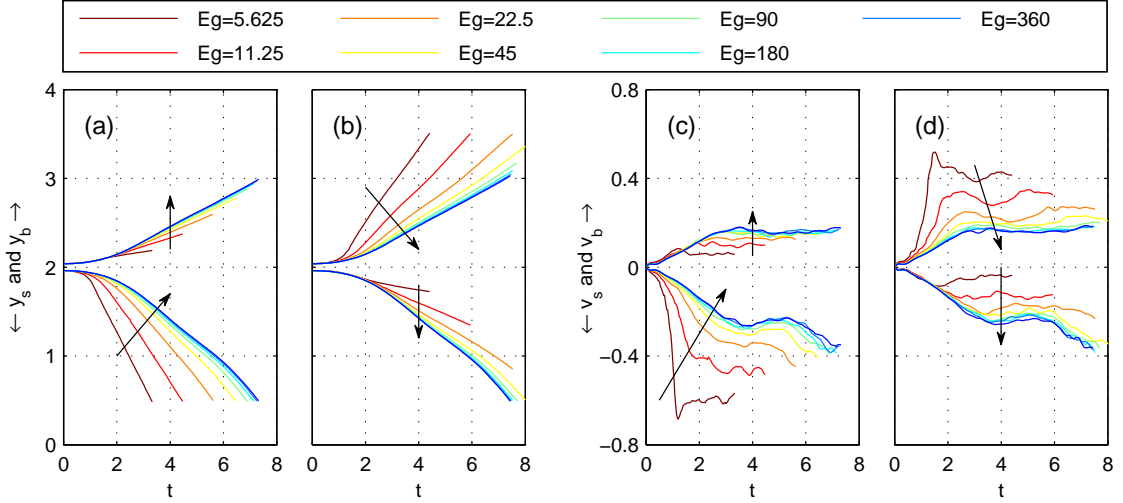


Figure 5.8: Spike and bubble tip position (a,b) and velocity (c,d) for NP ($\mathcal{P} = -0.3 - \mathcal{C} = +0.3$) (a,c) and PN ($\mathcal{P} = +0.3 - \mathcal{C} = -0.3$) (b,d); the arrows show the direction of increasing E_g (decreasing field intensity).

kept at baseline values of NP and PN.

Figure 5.8 provides spike and bubble tip positions and velocities for both NP and PN baselines. Larger electric field intensities augment the effects observed in section 5.5.2, *i.e.* an increase in the spike velocity and a decrease in the bubble velocity for NP. For PN, the reverse is true. The effects are more pronounced in the spike tip for NP and in the bubble tip for PN. After an initial movement at $E_g = 5.625$, the bubble and spike tips are almost stationary for cases NP and PN, respectively. Combined with the fast motion of the opposite feature, this results in significant deviations from the interface profiles for RTI at $\mathcal{A} = 1/3$ in the absence of the electric field which will be discussed further in the following paragraphs. The potential flow region (constant velocity movement) of evolution is reached earlier at smaller E_g while reacceleration of spike does not appear during the simulation times considered here.

Figure 5.9 plots interface profiles at $E_g = 5.625, 22.5, 90$ and 360 . The interface profiles are shown at identical spike tip positions for NP. Fast spike motion and nearly stagnant bubble at $E_g = 5.625$ result in a lack of heavy fluid at the spike region. This in turn leads to a very small spike and thin stem with completely suppressed side tails. This behavior resembles that of very high \mathcal{A} RTI. Increasing E_g results in thicker stem and well developed side tails. As for PN, the interface profiles are plotted at identical bubble tip heights. At $E_g = 5.625$, the spike tip moves much slower than the bubble tip. This leads to a thick spike with a small structure rising at its side. This structure resembles bubbles rising in quiescent fluid at high Bo numbers (small surface tension). At $E_g = 22.5$, the spike and the bubble cover similar distances with respect to time, which is a feature of very low \mathcal{A} RTI. By further increasing E_g , the profiles approach those in the absence of the electric field.

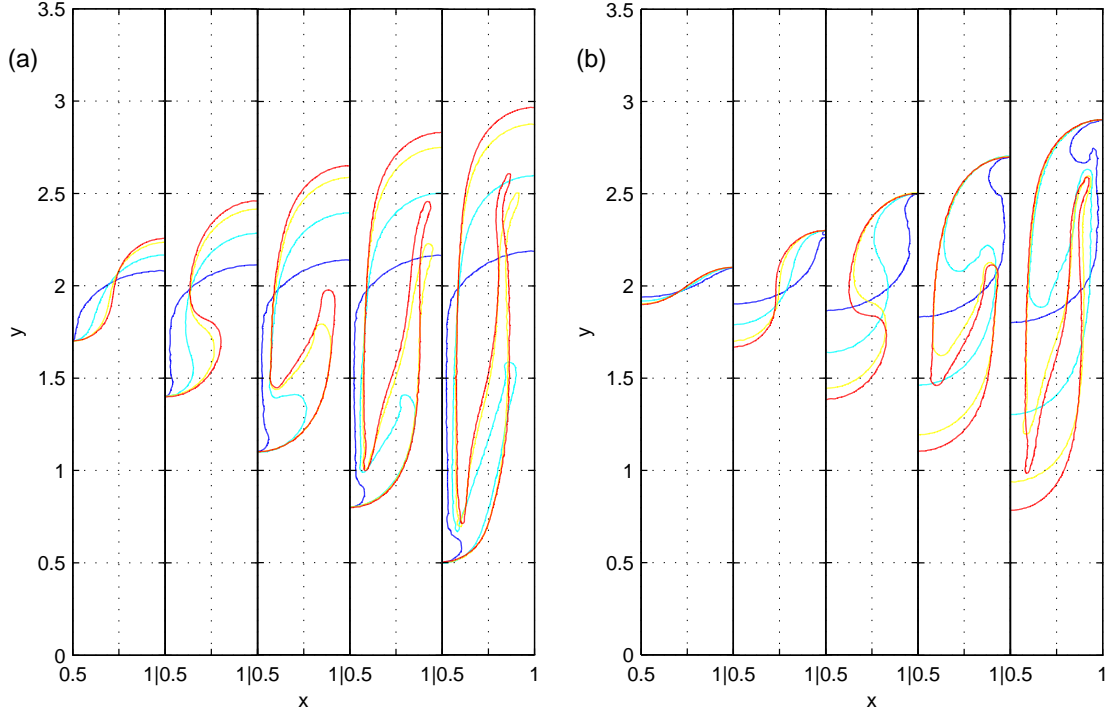


Figure 5.9: Interface profiles for $E_g = 5.625$ (blue), 22.5 (cyan), 90 (yellow) and 360 (red); (a) NP ($\mathcal{P} = -0.3 - \mathcal{C} = +0.3$) at spike height $y_s = 1.7, 1.4, 1.1, 0.8$ and 0.5 ; (b) PN ($\mathcal{P} = +0.3 - \mathcal{C} = -0.3$) at bubble height $y_b = 2.1, 2.3, 2.5, 2.7$ and 2.9 .

Vortical structures

To investigate the effects of the electric field intensity on the vortical structures, figure 5.10 shows vorticity contours and streamlines near the interface drawn in red at $E_g = 5.625$. The figure shows case NP at $y_s = 1.7, 1.1$ and 0.5 and case PN at $y_b = 2.1, 2.5$ and 2.9 . These six panels correspond to those of figure 5.11 which depicts $\mathbf{n} \times \nabla (\mathbf{n} \cdot \mathbf{f}_{(e)})$, $\mathbf{n} \times \nabla (\mathbf{n} \cdot \mathbf{f}_{(s)})$ and their summation as a measure of the first term on the right hand side of equation (5.12) along the interface. The interface is marked at 0.1 intervals of the normalized interface length on the contour lines of figure 5.10 and horizontal axes of figure 5.11, where symbols ∇ , \circ and \triangle correspond to the spike tip, middle point of the interface and the bubble tip, respectively.

In figure 5.10, the single vortex generated at early stages of the simulation is highly skewed toward the heavier fluid for case NP and toward the lighter fluid for case PN. This structure, which rotates counter-clockwise, encompasses large regions of one fluid while leaving the other fluid almost stagnant, except near the interface (figure 5.10-a,d). Vorticity generation sites are clearly observable near the tip of the preferred structure (spike for NP and bubble for PN) in figure 5.10-b,e. Occasionally, counter-rotating vortices may emerge near the main vortex in the lighter fluid for case NP and in heavier fluid for case PN (not shown here). A co-rotating vortical structure emerges at the later stages shown in figure 5.10-c,f. Such co-rotating vortices are not observed in the NE simulation. The co-rotating

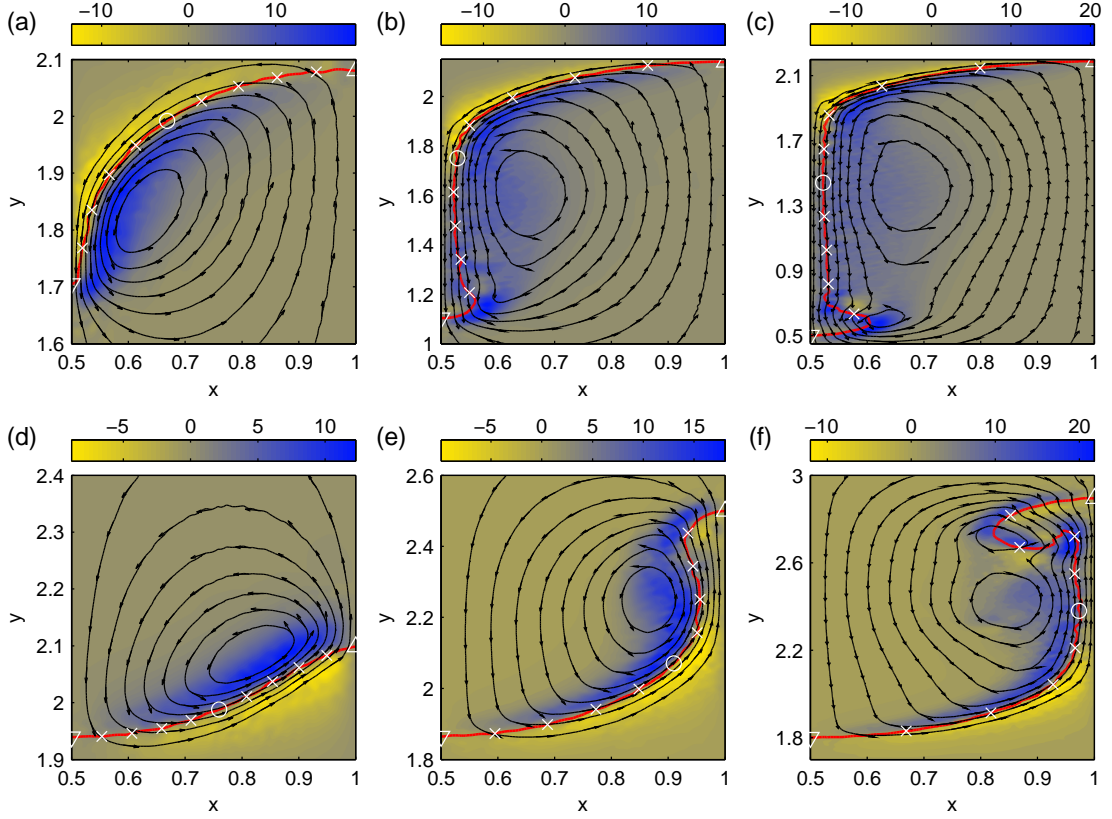


Figure 5.10: Contours of vorticity (fills) and streamlines (lines); the cross marks on the interface are placed at 0.1 intervals of normalized interface length. Symbols on the interface (figure 5.11 on the horizontal axes) correspond to spike tip (∇), middle point of interface (\circ) and bubble tip (\triangle). (a,b,c) NP with $E_g = 5.625$ at $y_s = 1.7, 1.1$ and 0.5 (blue contours in figure 5.9-a); (g,h,i) PN with $E_g = 5.625$ at $y_b = 2.1, 2.5$ and 2.9 (blue contours in figure 5.9-b).

vortices of case PN merge as the bubble rises to $y_b = 3.8$ while the co-rotating vortices in case NP persist during the simulation time (until $y_s = 0.2$).

Figure 5.11 provides a measure of the role of the electric forces in generation of the observed vortical structures. The very early stages involving generation of small co-rotating vortices are similar to that of the case NE (*cf.* section 5.5.1). However, the rest of the evolution is different when large electric field values are used. As is seen in figure 5.11-a,d, the dominant vorticity generation mechanism is through electric forces near the tip of the preferred structure (spike for NP and bubble for PN). As the features start to extend (5.11-b,e), additional sites are introduced where surface tension is the dominant generation mechanism. The sites dominated by the electric force also start to move away from the tips (5.11-c,f) which results in the generation of the smaller co-rotating vortex observed in 5.10-c,f. At later stages of the simulation, both surface tension and electric forces play an equal role in vorticity generation.

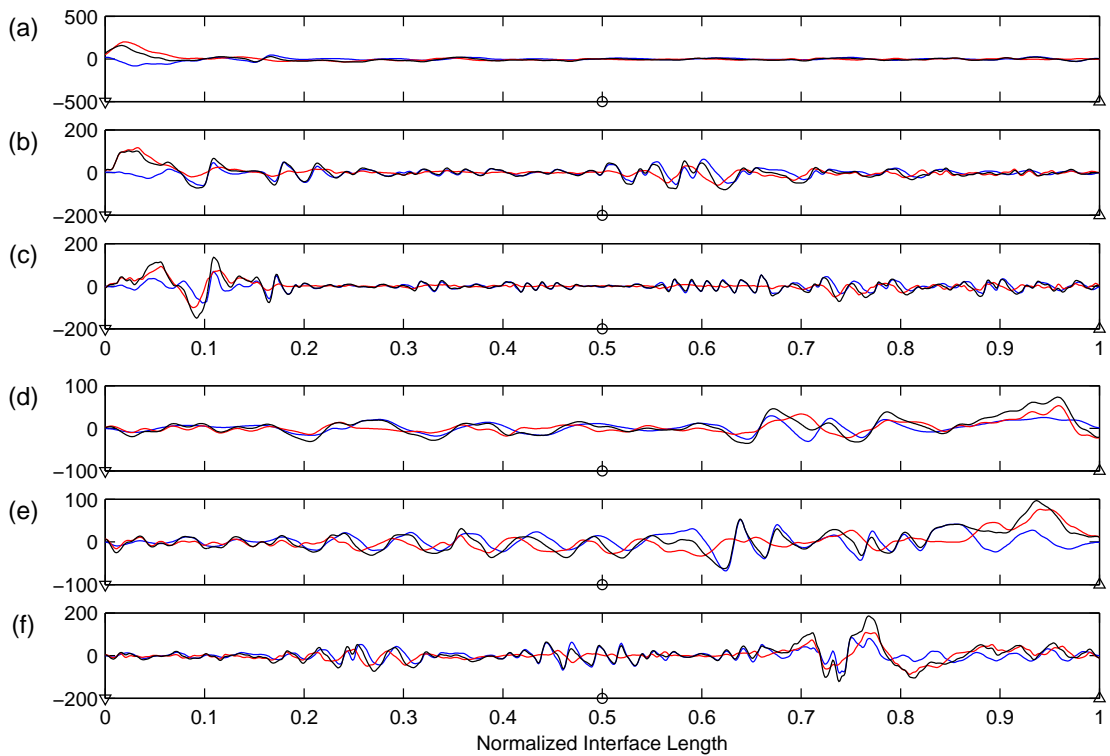


Figure 5.11: Electric force (red), surface tension (blue) and resultant contribution of interfacial forces (black) on vortex sheet strength in right hand side of equation (5.12); symbols on the horizontal axes correspond to spike tip (∇), middle point of interface (\circ) and bubble tip (Δ). These symbols correspond to those in figure 5.10 on the interface. (a,b,c) NP with $E_g = 5.625$ at $y_s = 1.7, 1.1$ and 0.5 ; (d,e,f) PN with $E_g = 5.625$ at $y_b = 2.1, 2.5$ and 2.9 .

5.6 Remarks

Rayleigh-Taylor instability appears when a heavier fluid lies on a lighter one in a gravitational field and serves as one of the basic test cases where interfacial effects may be investigated. Manipulation of this instability using electric fields has been the subject of many studies. Most of these studies, however, are based on linearized or simplified models. In this study, incompressible immiscible RTI of leaky dielectric fluids is simulated until its late stages using Smoothed Particle Hydrodynamics method at $Re = 225$, $Bo = 150$, $\mathcal{A} = 1/3$ and $\mathcal{V} = 0$. The electric field is taken to be perpendicular to the initial interface so as to maintain the unstable evolution. Interfacial forces and vortex generation are studied to explain how the interfacial evolution is affected by the permittivity ratio, the conductivity ratio and the electric field intensity.

The results show that increasing the top-to-bottom permittivity ratio augments the rise of the bubble while hindering the descent of the spike. On the other hand, increasing the conductivity ratio results in a decrease in the bubble velocity while augmenting the spike movement. At large conductivity ratios, the bubble is more affected when the permittivity ratio is positive whereas the spike is more affected when permittivity ratio is negative. Increasing the electric field intensity has different effects depending on the combination of the permittivity and conductivity ratios. Applying larger field intensities results in narrower structures. At higher field intensities, electric forces dominate vorticity generation at early stages of the simulation. However, the role of surface tension and electric forces become comparable at later stages of the evolution.

To summarize, it is shown that manipulating the electric field intensity in conjunction with electrical properties of the fluids allow for control of the interfacial morphology by suppressing certain features while augmenting others in a fluid-fluid interface. Further effects on fluid-solid interfaces and particle trajectories will be investigated in section 7, after the fluid-structure/solid interaction scheme is validated in section 6.

Chapter 6

Fluid-structure/solid interaction*

6.1 Introduction

The interaction of a solid structure with a fluid is one of the most common features observed in nature and industry. These phenomena cover a wide spectrum of objects interacting with a fluid environment such as airfoils and hydrofoils [220], flexible bodies [221, 222], impacting solids [103–105], sedimentation and motion of rigid and deformable particles [57, 59, 102, 223, 224] and blood cells [225–227] to fluid interacting with moving boundaries such as flow in biological systems [60, 228] and motion in containers [101, 106, 229]. When considered individually, computational fluid dynamic methods have conventionally embedded an Eulerian perspective while computational solid mechanics are generally described in a Lagrangian framework. The Coupling schemes may be loosely grouped as those that introduce external terms into Navier-Stokes equations and those that rely on specific boundary conditions [230]. The combination of discretization scheme and coupling method has resulted in the emergence of a number of prevalent modeling schemes for numerical simulation of fully resolved fluid-structure interaction. In this study, only the motion of particles conforming to the rigid body movement constraints have been considered.

The most straightforward modeling scheme in simulation of fluid flow around solid bodies is to assume the object as a moving wall while imposing relevant boundary conditions [102, 220, 231, 232]. These methods do not bring any external terms in Navier-Stokes equations. One such scheme used to capture the interaction of a solid object and fluid body is known as ALE method which relies on body fitted mesh. The mesh then is convected with respect to the frame of reference [47, 53]. As the fluid boundary mesh moves in tandem with the body in a Lagrangian manner, it may deform and distort at large translational or rotational motion. Different strategies have been employed to alleviate such a problem,

*Appears in: N. Tofighi, M. Ozbulut, A. Rahmat, J.J. Feng and M. Yildiz, An incompressible smoothed particle hydrodynamics method for the motion of rigid bodies in fluids, *J. Comput. Phys.* (2015). doi:10.1016/j.jcp.2015.05.015

the most common being remeshing approach where the computational domain is spatially discretised. Depending on the implementation, such operations may incur substantial computational time. The ALE scheme is used extensively to simulate a variety of FSI problems [223, 228, 233].

Another class of modeling schemes are those that impose boundary conditions or solid behavior via external terms while using fixed grids. One of the most prevalent methods in this category is the IB method [60, 61] which introduces a forcing term in the governing equations of the flow to impose the boundary conditions. This force term, locally effective around boundary regions and applied via a pseudo delta function, allows for simulation of the interactions between fluid and solid without a need for movement of fluid mesh. Several variations of the method have been proposed and employed to simulate complex flows involving passive and active solid objects in two and three-dimensions [152, 234, 235]. An extensive review of IB method has been provided in [236].

A closely related scheme used on fixed meshes is the FD method. While IB method generally focuses on boundary regions, most FD methods impose rigidity constraints to recover rigid-like behavior within the entire fluid region intersecting with solid objects. One such scheme is the DLM method, generally used in conjunction with FEM discretization techniques [57, 237]. Governing equations of fluid and solid are solved and coupled via distributed Lagrange multipliers (acting as external forcing in governing equations) to mimic rigid body motion. DLM has been successfully applied to several problems such as particle sedimentation and movement of flexible bodies in fluid [221, 222, 237, 238]. Another class of FD uses a penalization term, several orders of magnitude larger than the prevalent terms in governing equations of the flow, to induce rigid motion [239]. Such terms may be external to NS equations, such as Brinkman type penalization [240, 241], or internal such as VP method which employs the dissipation within the NS equations [58, 59, 153].

In terms of spatial discretization, a solid body may be meshed and followed in a Lagrangian fashion (interface tracking) or evolved via LS, VOF or PF methods (interface capturing) [224]. On the other hand, fluid may be discretized by moving (body fitted) or stationary Eulerian mesh, possibly featuring local refinement, or resolved by Lagrangian discretization points. There is an inherent advantage in discretizing both fluid and solid phases in a Lagrangian fashion, using particle methods. By proper initialization of particle positions, it is possible to trace all the moving boundaries without additional treatment [242]. A review of different particle methods has been provided in [243]. SPH has been successfully used to simulate sloshing motion [101], sedimentation and particle dynamics [102], rigid body impact problems [103–105] and elastic bodies [106].

The ISPH scheme described in section 2 is extensively tested in five cases involving the linear motion, rotational motion and their combinations for one or two particles in two dimensions. First, the linear motion is validated against literature data. To this end,

sedimentation of a single circular disc is tested in section 6.3.1 and the interaction of two discs descending in quiescent fluid is investigated in section 6.3.2. Then, the rotational motion of circular disc in simple shear is validated in section 6.3.3. Finally, migration of a circular disc in shear flow and sedimentation of an elliptic particle in quiescent fluid are used to test the scheme for combined linear and rotational motions in sections 6.3.4 and 6.3.5. These problems are chosen because of comparable results in the literature. However, the scheme may be generalized in a straightforward way to a multiphase SPH solver for many embedded solid particles.

6.2 Dimensionless variables

Dimensionless values of this chapter are formed using the following scales

$$\begin{aligned} \mathbf{x} &= \mathbf{x}^*/l_c, & \rho &= \rho^*/\rho_f, & \mathbf{u} &= \mathbf{u}^*/u_c, & t &= t^*(u_c/l_c), \\ p &= (p^* - \rho \mathbf{g} \cdot \mathbf{x}) / (0.5 \rho u_c^2), & \mathcal{D} &= \rho_s/\rho_f, & \mathcal{V} &= \mu_s/\mu_f, \end{aligned} \quad (6.1)$$

leading to a Reynolds number defined as

$$\text{Re} = \frac{\rho_f u_c l_c}{\mu_f}, \quad (6.2)$$

where \mathbf{x} is the position vector, \mathbf{g} is the constant gravitational acceleration vector and l_c and u_c denote characteristic length and velocity, respectively.

6.3 Results

In this section, the results of the simulations carried out during this study are presented. Each of the test case groups are assigned an abbreviation to facilitate further reference. These are CC (Calibration Cases), SDD (Single Disc Descent), DDD (Double Disc Descent), SDR (Single Disc Rotation), SDM (Single Disc Migration) and SED (Single Ellipse Descent). Schematics for all cases are presented in figure 6.1 for brevity. Unless otherwise noted, all results are presented in dimensionless forms obtained from characteristic variables provided in the respective section.

6.3.1 Single disc descent

Calibration of model parameters

The proposed scheme for simulation of passive rigid bodies treats all phases as liquids of different viscosities initially, only to differentiate the solid phase by the rigidity constraints (2.70-2.72) afterwards. As such, the viscosity ratio between the phases and the way the

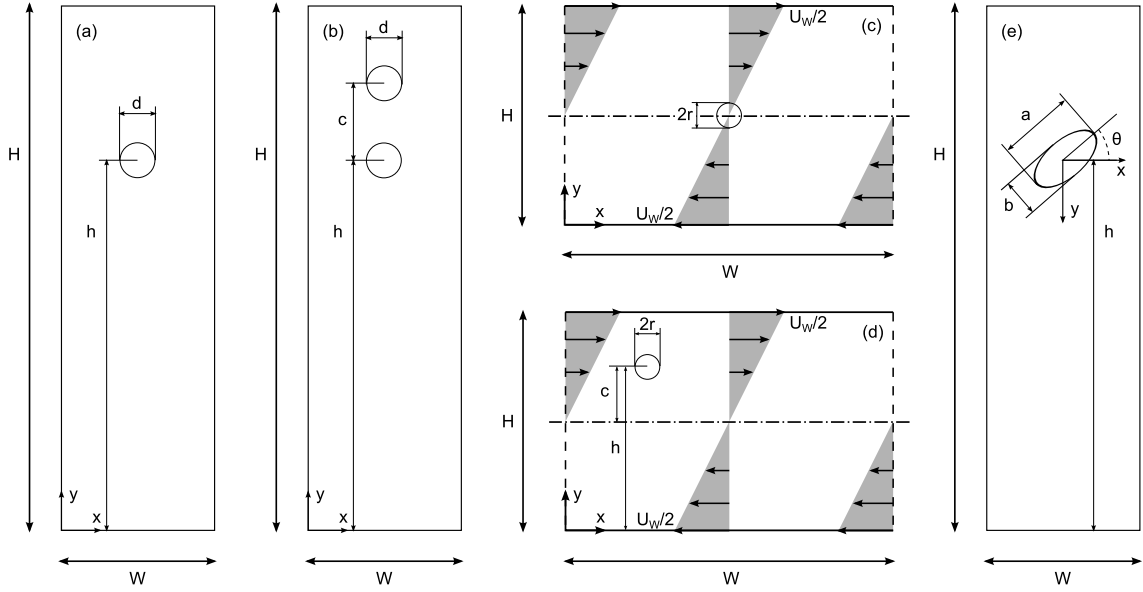


Figure 6.1: Schematic of all test cases included in this study; (a) CC/SDD; (b) DDD; (c) SDR; (d) SDM; (e) SED.

phase transitions are carried out have significant effects on the results obtained [59, 153]. To identify a suitable range for \mathcal{V} and choose the appropriate interpolation scheme, several simulations of a rigid disc descending from rest under gravity in quiescent fluid have been conducted. Characteristic length and velocity are chosen as $l_c = d$ and $u_c = \sqrt{gd}$ (cf. figure 6.1-a) while dimensionless numbers governing this case are $Re_p = \rho_f \sqrt{gd^3} / \mu_f$, h/d , \mathcal{D} and \mathcal{V} . Reynolds number is set to 39.1, h/d is equal to 16 and a density ratio of 1.25 is chosen while \mathcal{V} and interpolation scheme vary as noted in table 6.1. No-slip, no penetration and zero gradient pressure boundary conditions are applied at bounding walls.

The computational domain consists of an 8×24 rectangle discretized by 62300 particles arranged with respect to their phase for easier setup. Particles within the rigid body conform to the boundaries and are positioned along concentric circles at uniform radial spacing around the rigid disc's center. The radial spacing is chosen such that 10 circles fit inside the disc while the number of particles along each of these circles vary to keep the overall inter-particle spacing as uniform as possible. Fluid particles are arranged on a uniformly spaced Cartesian grid where particles coinciding with the rigid body are removed. As seen in figure 6.2-a, the particle spacing in the vicinity of the rigid body is not uniform and has a step-like pattern. However, figure 6.2-b shows that this is not permanent and the particles are adapted to the boundaries as the disc starts to descend. This uniform distribution is due to the APD which comes into effect as the disc starts to move [174].

As the proposed scheme treats all phases as liquids and applies rigidity constraints afterwards, the velocities obtained by individual solid particles during liquid phase treatment affects the overall motion of the solid after the constraints are applied. It is expected to achieve a solid-like behavior at large enough viscosities. However, a threshold has to be

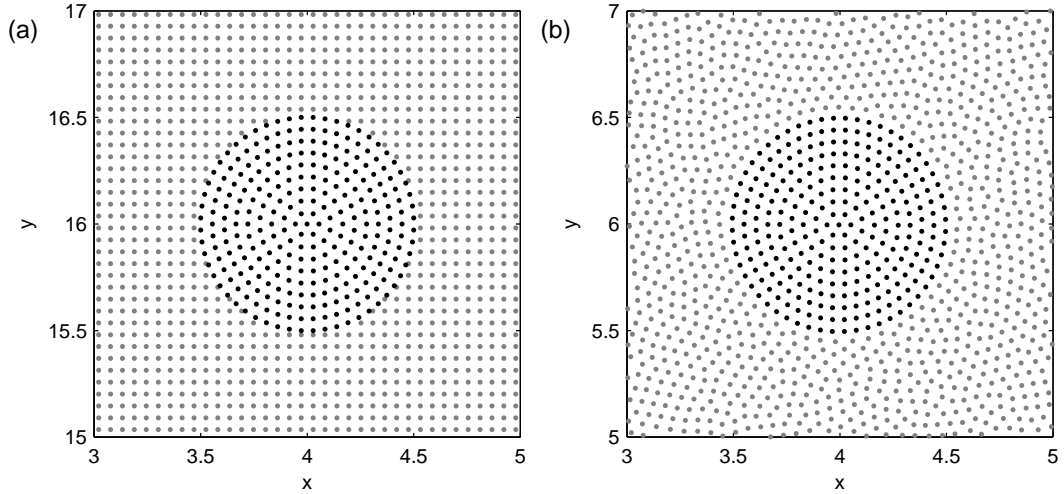


Figure 6.2: Closeup view of initial particle distribution at the vicinity of the solid disc. Black points denote solid particles whereas gray points are fluid particles. (a) Initial arrangement; (b) particle positions at $y = 6$

Table 6.1: Viscosity ratio and interpolation scheme for calibration purpose; C stands for calibration test cases.

Case	CCH1	CCH2	CCH3	CCH4	CCH5	CCH6	CCH7	CCA5
\mathcal{V}	1	3	10	30	100	300	1000	100
Interp. Sch.	WHM	WAM						

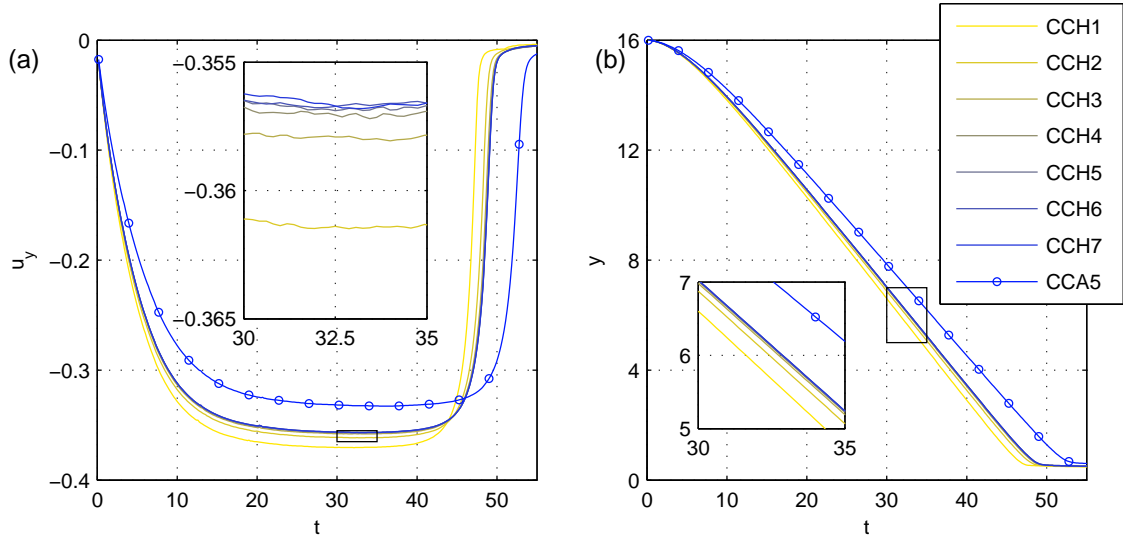


Figure 6.3: Vertical velocity (a) and vertical position (b) of the solid disc's center of mass versus time for calibration test cases.

Table 6.2: Time and vertical velocity of rigid disc's center of mass at $y = 6$ for calibration test cases

Case	CCH1	CCH2	CCH3	CCH4
t	31.6301	32.4237	32.7429	32.8264
u_y	-0.3703	-0.3614	-0.3579	-0.3571
Case	CCH5	CCH6	CCH7	CCA5
t	32.8634	32.8760	32.8780	35.5742
u_y	-0.3568	-0.3567	-0.3568	-0.3327

set as larger viscosity ratios may destabilize the simulation. To this end, viscosity ratios of 1 through 1000 are tested (table 6.1). Figure 6.3 presents vertical velocity and vertical position of the rigid disc's center of mass versus time. Focusing on cases with WHM interpolation, it appears that the profiles converge at about a viscosity ratio of $\mathcal{V} = 100$. To demonstrate the difference between disc positions better, figure 6.4 provides contours of the solid disc when case CCH5 is at $y = 6$, during its descent at terminal velocity. The differences between profiles become negligible for viscosity ratios above 100. Time until the disc reach $y = 6$ and their terminal velocity at the same height are provided for all test cases in table 6.2.

In conjunction with the viscosity ratio, the interpolation scheme used to transition through phase boundaries affects the outcome of the simulation as well. To demonstrate this effect, WAM scheme is compared to WHM scheme. In WAM, the transition occurs at equal distances at both sides of the phase boundaries whereas in WHM the transition is skewed toward the higher-valued material property. Specifically in these test cases, the effective transition region is 4 particle-spacing wide, covering two rows of particles on each side of the interface. In WAM, both sides are involved in transition whereas in WHM, the viscous diffuse interface is effectively limited to particles inside the rigid body. As higher

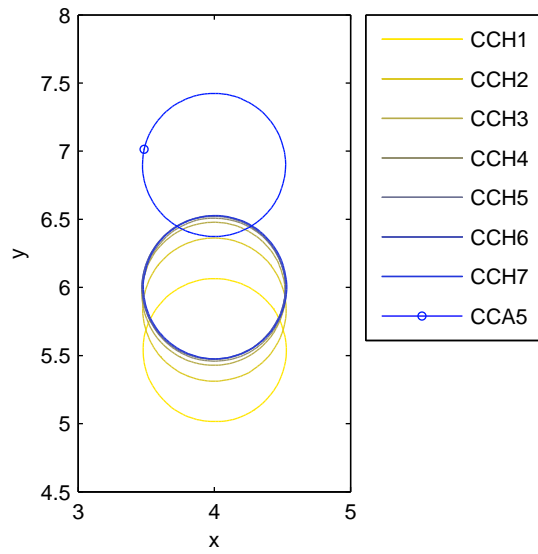


Figure 6.4: Disc position for calibration test cases when CCH5 is at $y = 6$.

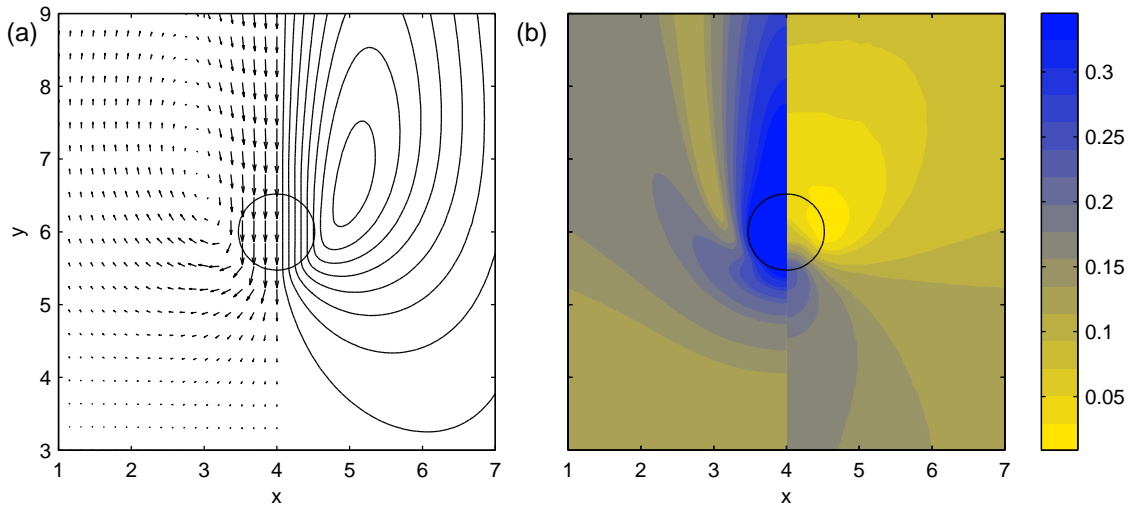


Figure 6.5: Velocity and pressure of case CCH5 at $y = 6$; (a) velocity vectors are shown on the left half while the right half plots streamlines. Velocity vectors are drawn at interpolated positions and do not correspond to actual particle locations; (b) left half shows velocity magnitude while right half plots pressure contours. The two halves share the same scale and color bar.

viscosity generates larger skin friction, it is desired to avoid transition in fluid domain as much as possible. In this sense the use of WAM, which generates a thicker region of higher viscosity inside the fluid domain than WHM, hinders the descent of the disc. Simulation results presented in figures 6.3, 6.4 (bearing the marker “o”) and table 6.2 confirm this observation as WAM case lags behind the respective WHM case. Compared to WHM, a substantially weaker convergence rate has been observed when similar viscosity ratios are tested for WAM cases up to $\mathcal{V} = 100$ (not shown here).

Figure 6.5 provides pressure and velocity plots of case CCH5 at $y = 6$. Left figure provides velocity vectors and streamlines while right figure shows velocity magnitude and pressure contours. Rigid disc’s boundary is visualized as 0.5 level contour of the color function. Velocity vectors within the disc are parallel and equal in length following the linear rigid body motion while two vortices are observed to the sides of the body. It is notable that while pressure solution extends inside the body, contours passing through the interface are relatively perpendicular to the perceived boundary of the object.

Based on the simulation results presented here, it may be inferred that a viscosity ratio of $\mathcal{V} = 100$ along with WHM interpolation scheme produces consistent results. These values along with the initial particle arrangement method are maintained throughout the simulations conducted in this study, unless noted otherwise.

Comparison of results

In order to test the ability of the proposed method in capturing linear motion in the absence of angular motion, descent of a rigid disc in quiescent fluid under gravitational acceleration is simulated. Geometry is presented in figure 6.1-a and particle arrangement scheme and simulation parameters are identical to those of the calibration case CCH5. To summarize, dimensionless parameters are set as $\text{Re}_p = 39.1$, $\mathcal{D} = 1.25$ and $\mathcal{V} = 100$.

Figure 6.6 provides simulation results at three resolutions with total number of particles of 37650, 62230 and 119986. When released from rest, all cases undergo an acceleration, descent at semi-constant velocity and deceleration stage when approaching the bottom boundary. As it is seen in the figure, while the difference in position increases at later stages of the simulation, it is almost negligible for two higher resolution cases. The case with lower resolution accelerates faster than the others, has larger terminal velocity and experiences the effects of the bottom boundary earlier. The cases with higher resolution experience nearly identical acceleration while the case with higher resolution descends slower during the constant velocity stage which spans about 30 percent of the evolution.

Based on the differences observed for the resolutions tested above, the middle case is chosen for comparison with WCSPH results of Hashemi *et al.* [102] and DLM simulations of Glowinski *et al.* [57]. The results for vertical position and vertical velocity are presented in figure 6.7. The current method overestimates the vertical position of the disc during the simulation, however, the trend in vertical velocity is not as straightforward. Simulations by

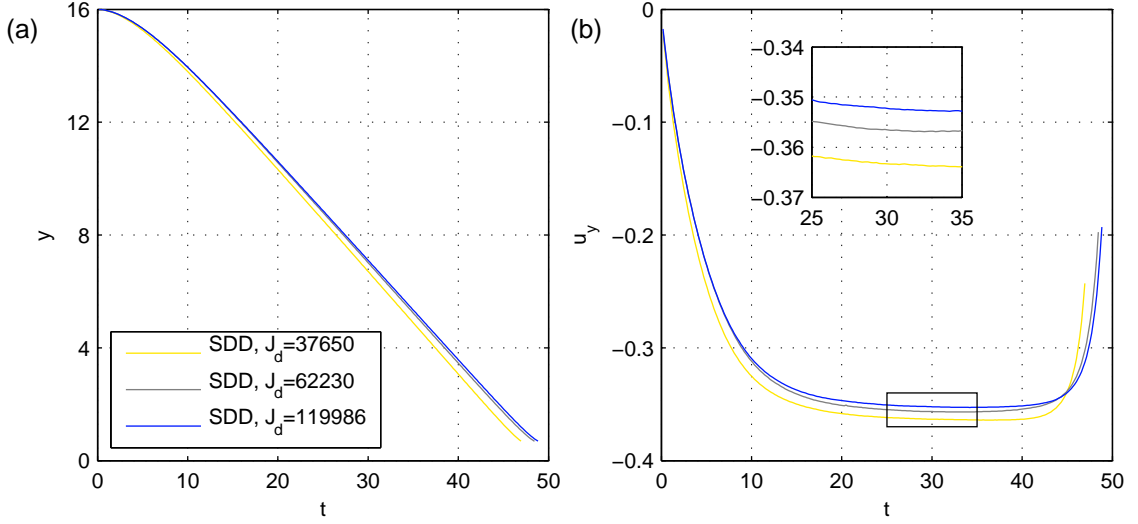


Figure 6.6: Comparison of simulation results at different spatial resolutions for the rigid disc's center of mass of case SDD/CCH5; (a) vertical position; (b) vertical velocity

Hashemi *et al.* and Glowinski *et al.* agree better during the acceleration stage while SDD predicts a slower descent. However, the terminal velocities predicted by SDD are in better agreement with DLM results while WCSPH overestimates the terminal velocity. The final deceleration stage is the most varied stage as DLM starts to experience boundary effects before others while SDD shows such effects the last. Based on these results, it is possible to infer that the proposed method shows quantitative agreement with the numerical results provided by [57, 102] for the overall duration of the simulation.

6.3.2 Double disc descent

Definition of spring-type repulsive forces

In this section, the interaction between two rigid discs descending in quiescent fluid is studied. This test case will help in measuring the success of the proposed method in handling multiple bodies and the interaction of interpolation regions. To this end, two rigid discs with equal diameter are placed such that the line connecting the centers of the discs is parallel to vertical walls and has a length c . A schematic of the test case is shown in figure 6.1-b while initial particle positions follow the scheme presented in figure 6.2-a. Characteristic parameters are identical to SDD and the problem is fully described by specifying domain size, h/d , Re , \mathcal{D} , \mathcal{V} and an additional parameter, c/d .

It is known that when released from rest, such configuration of discs will undergo drafting-kissing-tumbling (DKT) [244] stages. In other words, the following disc catches up with the leading counterpart where they descend at constant terminal velocity while at near contact configuration. However, this configuration is unstable and a rotational motion will ensue which results in discs breaking off and drifting apart. Due to its uniform spatial

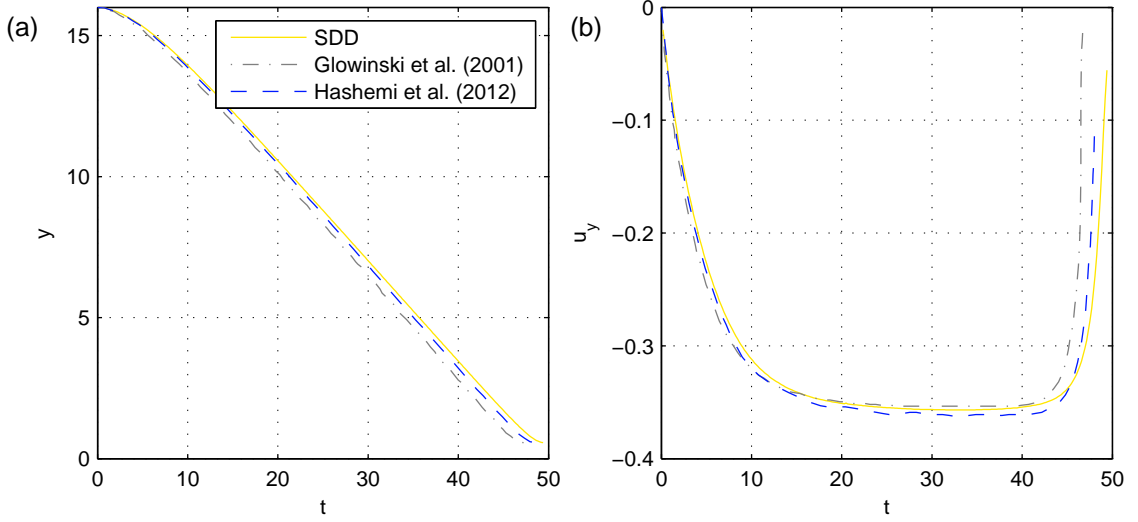


Figure 6.7: Comparison of simulation results with literature data; (a) vertical position; (b) vertical velocity

resolution, the method proposed here is not suitable for resolving near-contact situations that happen during DKT. As a result a repulsive force is required to ensure a minimum distance of one particle-spacing is maintained between the rigid bodies. Such repulsive forces have been extensively used in literature and take different forms such as lubrication force [231, 245] and spring force [57, 231, 246]. The general composition of a spring force may be broken down to three components, a measure of center-to-center distance, a direction vector and a constant coefficient representing the force magnitude (*cf.* [57] for a detailed discussion). In this study, the spring force is formulated to benefit from the information available to individual particles during the simulation. As such, the center-to-center distance is replaced by the value of opposing rigid body particles' smoothed color function at rigid body particle of interest. Similarly, the average distance vector between particle of interest and all particles of opposing rigid body within its support domain is used to determine the direction of repelling force. Denoting c_r as the constant coefficient, the repulsive force applied to rigid body α due to its proximity with rigid body β may be formulated as

$$\mathbf{f}_{(ar)i} = \frac{c_r}{\lambda} \left(\frac{c_{(\beta)i}}{c_{(\alpha)i}} \right)^{n_r} \sum_{j=1}^{J_n} \frac{\mathbf{r}_{ij} \hat{c}_{(\beta)j}}{\delta_p}, \quad (6.3)$$

which will be added to the right hand side of equation (3.41) as $\mathbf{f}_{(ar)i} \Delta t / \rho_s$. In above formulation, n_r is a value to manipulate the sharpness of the curve with respect to color, λ is a parameter to manipulate the maximum force value at a certain color threshold and δ_p represents the particle spacing. Although this study does not deal with rigid objects of arbitrary shapes, dividing $c_{(\beta)i}$ by $c_{(\alpha)i}$ increases the repulsive force at sharp corners as particles at these positions have lower $c_{(\alpha)i}$. The repulsive force defined here is applied to individual particles, resulting in higher c_r than full body repulsive forces. A spring force

benefiting from LS function has been derived in [247].

The spring force noted above is formulated in terms of color function and its spatial magnitude relies on the particle distribution. To demonstrate the effectiveness of the formulation, it is tested by simulating DDD with $Re_p = 56$, $\mathcal{D} = 1.1$, $h/d = 25$, $c/d = 2$ in a 30×10 computational domain discretized by 62226 particles. Table 6.3 provides spring force parameter pairs used in the simulations. It is worth noting that only drafting and kissing stages were observed when particles were initially arranged in a symmetric layout. To destabilize the solution, particles belonging to both rigid discs were rotated by 10 degrees from the initial configuration shown in figure 6.2-a. While generating asymmetry in fluid field solutions, such perturbation has a side effect on the spring force formulation which will be elaborated in the following paragraphs.

Figure 6.8 shows force magnitude versus the distance between disc surfaces for different (n_r, λ) pairs. Minimum values of this distance are presented in table 6.3 as well. The negative values observed for $(2, 5)$, $(2, 10)$ and $(2, 100)$ denote a crossover between the discs during the simulation. It is notable that the numerical method is able to handle such crossovers, however, the results are devoid of physical meaning. A look at the overall shapes of the forces reveals that crossover changes the force profile in a substantial manner. This is an expected outcome as the direction vector and distance measures rely on the smoothed color function which no longer represents the transition surfaces during a crossover. Excluding cases with crossover, it is possible to observe the actual effect of parameter pairs in spatial domain. While profile change is negligible for $(0.5, 0.25)$, $(1, 0.25)$ and $(2, 0.25)$, increasing n_r delays the onset of force application. On the other hand, increasing λ reduces the minimum distance between the discs for a given n_r , as larger force magnitudes are shifted toward shorter distances (larger color function) while the onset of force application remains unchanged.

To further assess the effects of parameter pairs on the evolution of DDD in time, figure 6.9 provides vertical position, vertical velocity and total force magnitude between discs with respect to time for cases without crossover. Considering the vertical position, it is possible to say that the parameter pairs have negligible effect in drafting and kissing stages while a lower λ expedites the tumbling stage. As noted before, rigid particle positions are not symmetric and this results in a moment due to repulsive spring force. When λ is reduced, spring force is larger at a further distance, resulting in greater moments and subsequently an earlier tumbling motion. The effects of earlier tumbling motion is also visible in vertical velocity as disc velocities diverge. However, reduction in λ has a distinct effect in vertical velocity when repulsive forces are activated. In particular, a bouncing motion is observed when $\lambda = 0.1$, while the corresponding oscillation is reflected in the force profile as well. Such behavior is not present at higher values of λ and a smooth transition is observed in both velocity and force magnitude. It is worth noting that kissing stage remains mostly unaltered for all parameter pairs.

Table 6.3: Force parameter pairs and minimum distance between disc surfaces during the simulation for DDD cases. Negative values denote crossover. dimensionless particle spacing is approximately 0.0625.

Case	R1	R2	R3	R4	R5
n_r	0.5	1	2	2	2
λ	0.25	0.25	0.1	0.25	0.5
$\min(\frac{c-d}{d})$	0.0999	0.0796	0.0659	0.0524	0.0408
Case	R6	R7	R8	R9	R10
n_r	2	2	2	2	2
λ	0.75	1	5	10	100
$\min(\frac{c-d}{d})$	0.0321	0.0254	-0.0253	-0.0449	-0.656

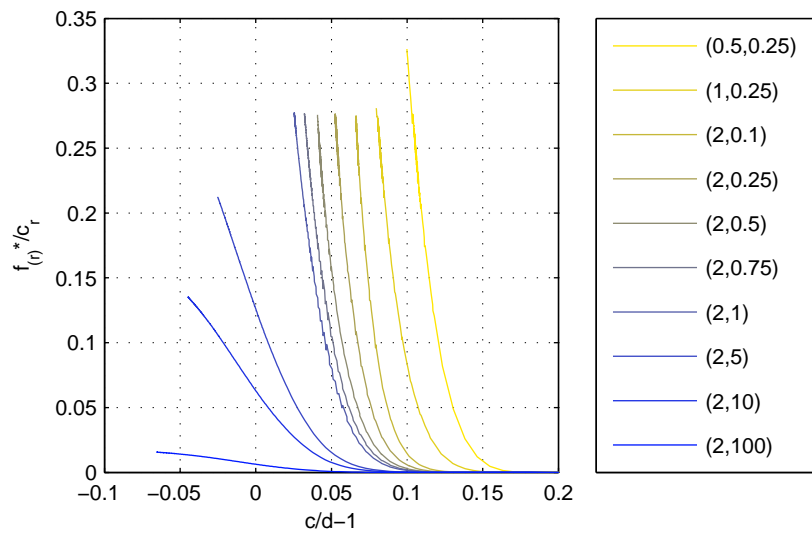


Figure 6.8: Repulsive force magnitude with respect to $(c - d) / d$. Legend denotes (n_r, λ) pairs. A negative value indicates crossover of the discs.

Figure 6.10 provides the relative positions of discs during DKT motion. In accordance with previous observations, the final distance between discs is the most affected stage of the simulation. Cases with smaller λ rotate further during tumbling stage before drifting apart and tend to depart faster. As explained before, this is a side effect of the asymmetric repulsive force acting at farther distances, generating larger moments.

Comparison of results

In this section the results of case DDD at two different Re_p is compared to numerical results provided in [57, 102]. Spring force parameters are set to (2, 0.25) for both cases while dimensionless parameters governing the cases are presented in table 6.4.

Figure 6.11 provides vertical position and vertical velocity of DDD1 compared to WC-SPH results of [102]. Positions appear to be identical until tumbling stage while a slight difference in vertical velocities is observed upon kissing stage. Tumbling stage shows no-

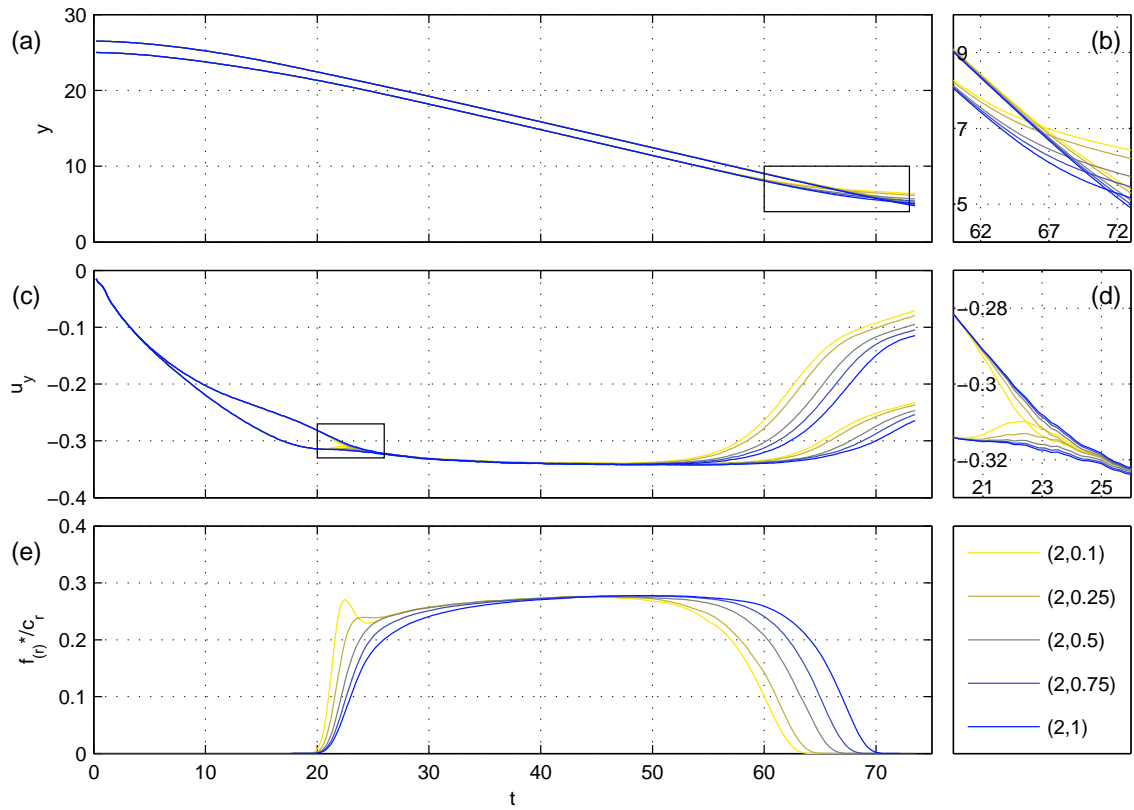


Figure 6.9: Vertical position (a), vertical velocity (c) and force magnitude (e) for cases with $n_r = 2$ and no crossover. Legend denotes (n_r, λ) pairs. Close ups of boxed region are shown on the right column for vertical position (b) and vertical velocity (d).

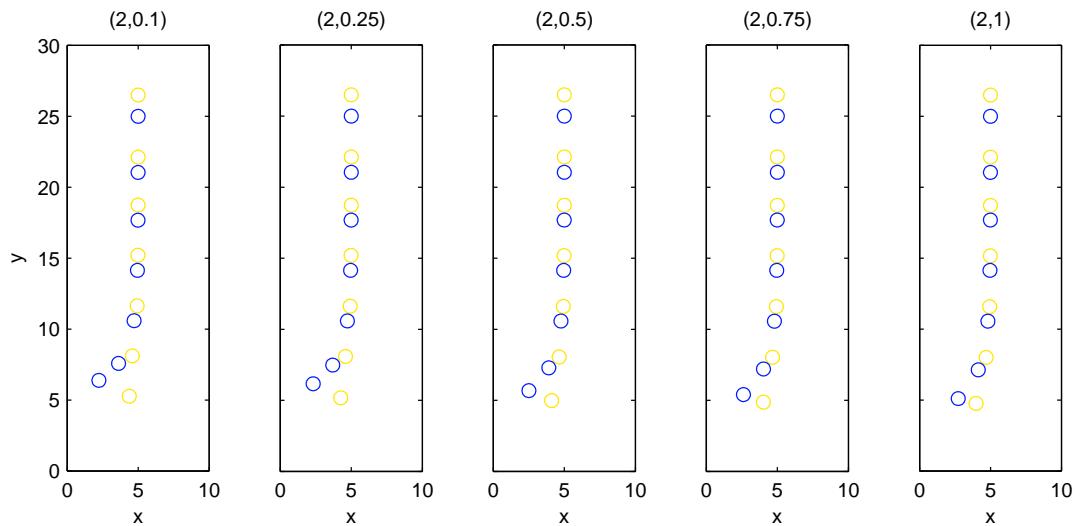


Figure 6.10: Snapshots of disc positions for cases without crossover at $t = 0.2, 21, 31.5, 42, 52.5, 63$ and 73.5 . (n_r, λ) pairs are shown at the top of each column: (Yellow) top disc; (Blue) bottom disc. Disc to disc contact or lack thereof is not accurately represented in this figure due to line thicknesses. Refer to table 6.3 for minimum distance between discs during the simulation.

Table 6.4: Dimensionless parameters for DDD cases compared to literature data.

Case	Re_p	\mathcal{D}	J_d	$H \times W$	c/d	h/d
DDD1	56	1.1	62226	30×10	2	25
DDD2	391.3	1.5	74846	24×8	2	18

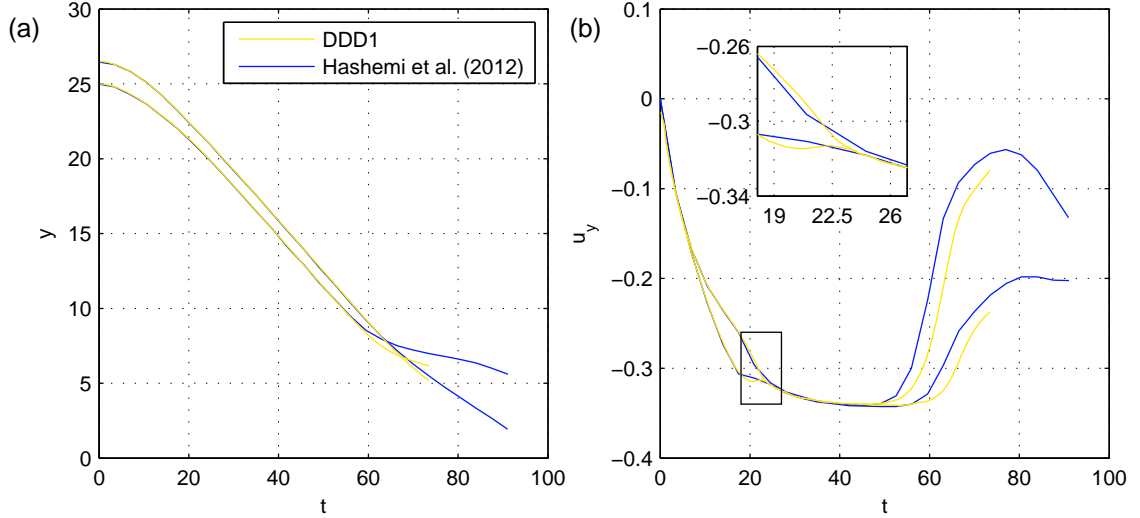


Figure 6.11: Comparison of simulation results at $Re_p = 56$. (a) vertical position; (b) vertical velocity.

ticeable difference between the two cases as DDD1 delays in its initiation, however, barring the delay the velocity curves appear to be identical to those of [102]. It should be noted that in these simulations DKT is a result of numerical instabilities and highly dependent on the repulsive force employed, whereas the physical counterpart is due to imperfections in particle surface [248]. As such, it may be deduced that the current method agrees with the results of [102] at low Re_p .

To assess the performance the proposed scheme at higher Re_p , simulation results of DDD2 are compared to those of [57] in figure 6.12. DDD2 overestimates vertical position and has significant delay in tumbling stage when compared to [57]. Vertical velocity is underestimated during drafting stage, however, the shapes of the curves follow that of [57] closely, featuring the crossover between velocity curves of top and bottom discs at about $t = 6$. While similar bouncing motion is observed during the kissing stage in both cases, Glowinski's case tumbles almost immediately at $t \approx 10$ whereas DDD2 delays kissing until $t \approx 11$, remains in contact and tumbles later at $t \approx 13$. Considering the discrepancies in repulsive force application and noting higher Re_p of this test case, it is possible to assess that the current method has been able to capture the essential characteristics of DKT up to the Re_p tested here.

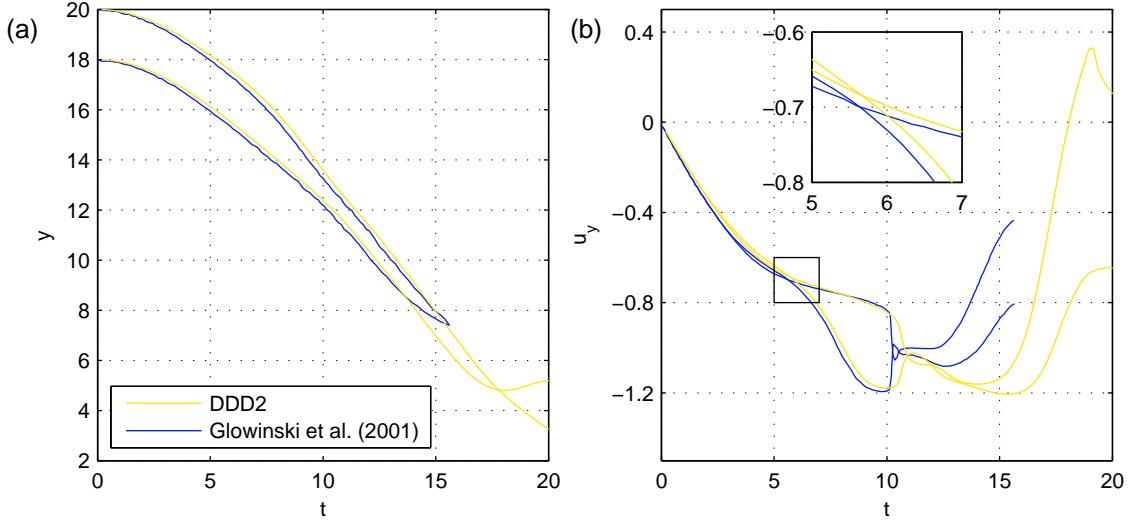


Figure 6.12: Comparison of simulation results at $Re_p = 391.3$. (a) vertical position; (b) vertical velocity.

6.3.3 Single disc rotation

In order to isolate the angular motion and assess the performance of the proposed method in the absence of linear motion, rotation of a neutrally buoyant, single rigid disc suspended in Couette flow is simulated and the results are compared with the data available in literature. This test case has been subject to extensive experimental and numerical investigation, spanning a wide range of Reynolds numbers [232, 238, 249]. Dimensionless numbers governing this case are bulk Reynolds number $Re_b = \rho_f GH^2 / \mu_f$, particle Reynolds number $Re_p = \rho_f Gr^2 / \mu_f$ and confinement ratio H/r . G is the shear rate of the undisturbed flow where $U_w = GH$.

A series of simulations with increasing Re_p have been conducted for three H/r values while Re_b is limited to 500. A channel flow with no disturbance may remain stable until $Re_b \approx 1500$ [250]. However, the presence of the disc within the channel causes considerable disturbance, lowering the threshold substantially [249, 251]. The rigid disc is placed at the center of the computational domain at rest while fluid particles are initialized with the analytical velocity of a Couette flow with respect to their initial position. A schematic of the computational domain is provided in figure 6.1-c while initial particle arrangement is set similar to case SDD such that 15 layers of particles fit inside the rigid disc. Total number of particles used are 14385, 28769 and 57566 for $H/r = 4, 8, 16$, respectively. Horizontal walls are set to move at $U_w/2$ in opposite directions while no slip and zero pressure gradient conditions are applied. Computational domain is stretched up to $8r$ on both sides of the disc in streamwise direction ending in periodic boundaries.

When suspended in unbound linear shear, the disc is known to attain a dimensionless angular velocity of $\omega/G = 0.5$. At higher values of Re_p , the angular velocity is reduced in a linear fashion with a slope of -0.5 [232, 252]. This trend is extended to finite confine-

ment ratios where the general behavior of the angular velocity consists of an initial plateau followed by a linear reduction in logarithmic scale at higher Re_p . A reduction in plateau and slope values have been reported in both experimental and numerical investigations [232, 238, 249, 253]. Despite the agreement in characteristics of the flow, discrepancies are observed at higher Re_h values among literature data. As current discretization scheme is not suitable for direct simulation of turbulent bounded flows, Re_b is limited to 500 to avoid explicit turbulence models. Figure 6.13 provides dimensionless angular velocity versus Re_p for the confinement ratios considered here. As it is seen in the figure, excellent agreement is achieved in the plateau region, however, the current method overestimates the angular velocity in the linear region. It is possible to observe that the onset of linear region is shifted to lower Re_p at higher H/r in current simulations, a characteristic in agreement with the numerical observations of [238].

Figure 6.14-a provides streamwise and normal components of the velocities for $H/r = 4$ at $Re_p = 20$. Streamwise velocity is skewed toward $y > 2$ where the flow accelerates as it leaves the vicinity of while a slow down is observed when the flow approaches the rotating disc for $y < 2$. Normal component of the velocity is relatively symmetric with respect to the center line of the channel and represents a reverse flow compared to the linear velocity of the disc. Both profiles are in good agreement with numerical and experimental data provided by [232]. Figure 6.14-b the distance from stagnation point to disc surface at $H/r = 8$ for Re_p up to 4. The stagnation point gets closer to the surface as Re_p number increases, a trend followed by numerical [232] and experimental [254] results. Stagnation distances obtained with the current method are in quantitative agreement with those of Ding and Aidun [232].

Figure 6.15 provides streamlines inside and outside of the solid objects for Re_p of 0.02 and 20. Particle positions are shown in the background while perceived boundary of the rigid body is shown by 0.5 level contour of the color function. The streamlines present may be categorized into three types. Those that travel across the periodic boundaries contribute a positive torque to rotate the disc by passing between the moving wall and rigid body. Reversing streamlines change direction in the vicinity of the disc and oppose its rotation. Closed streamlines move around the disc due to the viscous penalty mimicking the no-slip condition on the disc surface. As Re_p increases the streamlines become skewed in the direction of rotation and reversing and closing streamlines draw closer to one another. Similar patterns have been observed in numerical and experimental results as well [232, 249, 253]

Based on the results presented in this section, it is possible to infer that the proposed method is able to capture the isolated rotational motion up to Re_p and Re_b studied here.

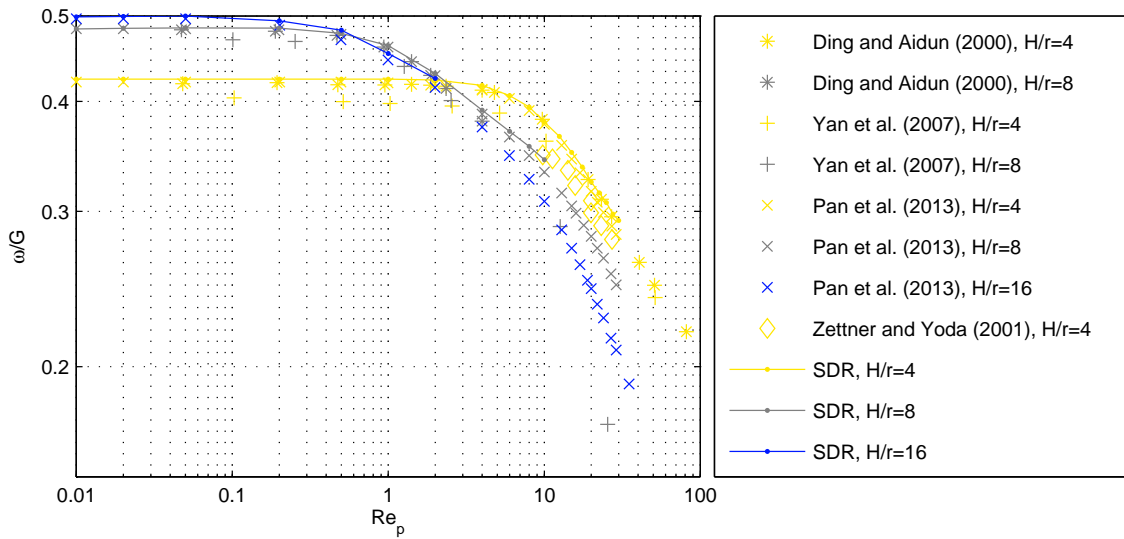


Figure 6.13: Comparison of angular velocity versus particle Re for different aspect ratios. Bulk Re is limited to about 500 in current simulations. Identical colors denote identical aspect ratios.

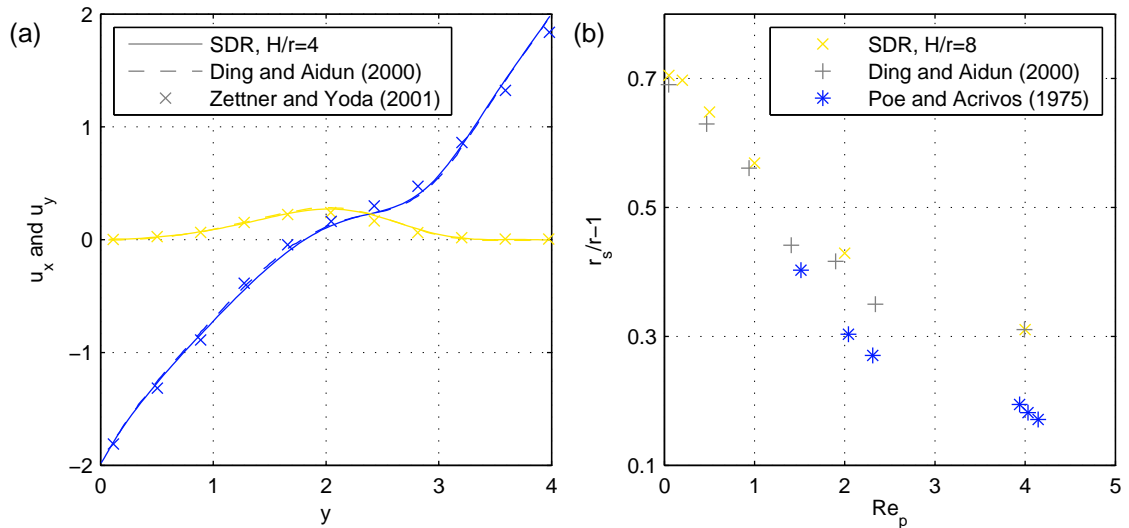


Figure 6.14: (a) comparison of streamwise (Blue) and normal (Yellow) velocity profiles at $1.25r$ of the rigid disc's center of mass at Re_p of 20. Refer to [232] for experimental data of Zettner and Yoda. (b) comparison of stagnation point distance from rigid disc's surface with respect to Re_p . Poe and Acrivos utilize an $H/r = 6 \sim 12$ in their experiments.

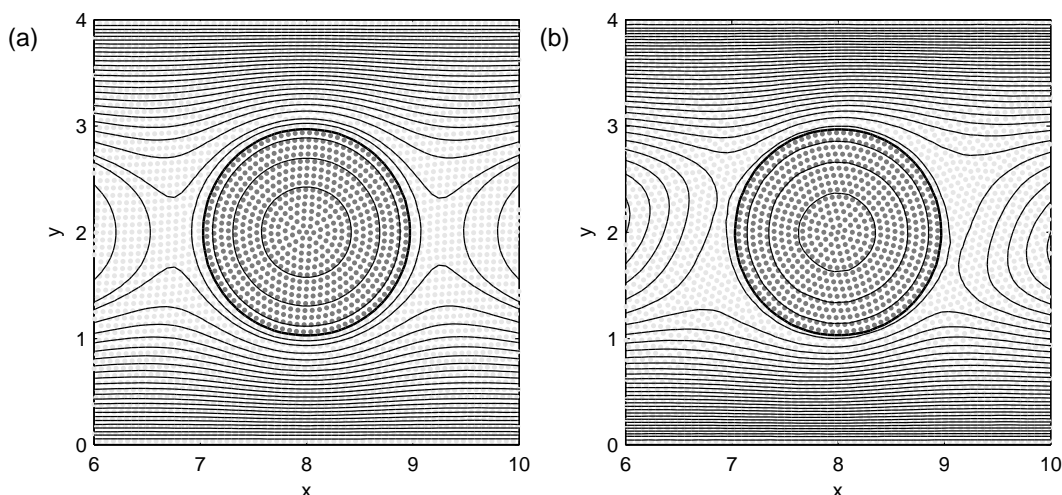


Figure 6.15: Streamlines at the vicinity of the disc for $H/r = 4$. Particle positions inside the rigid body (dark) and fluid phase (light) are shown in the background. Rigid body boundary is defined as 0.5 level contour of the color function and is marked by the thicker line. (a) $Re_p = 0.02$; (b) $Re_p = 20$.

6.3.4 Single disc migration

To assess the interaction of combined linear and angular motion in the absence of any body force, migration of a neutrally buoyant rigid disc in plane Couette flow is simulated. When released from rest (or any other streamwise velocity) at a distance c from the middle of the channel, it is expected that the disc will migrate toward the centerline while moving with the flow. Dimensionless numbers governing this test case are similar to those of case SDR with an additional distance to radius ratio of $c/r = 2$. Computational domain consists of an 8×32 rectangle discretized by 14402 particles initially arranged similar to the case SDD such that 9 concentric circles cover inside the rigid disc. Boundary and initial conditions are similar to case SDR. A schematic of this case is provided in 6.1-d.

In order to compare the results with numerical data provided in [223, 246, 249], Re_p and Re_b are set equal to 0.625 and 40, respectively. The changes in the evolution of the disc due to initial slip velocity of the rigid body has not been substantial and only those starting from rest at $h/H = 0.25$ and 0.75 , cases SDM1 and SDM2, are presented here. Figure 6.16 provides normal position and normal velocity of the disc during its migration toward the center of the channel. The positions are in excellent agreement with literature data. Normal velocity versus normal position shows an oscillatory behavior observed by [244] and bound in a similar range while [246] presents a smooth curve with slightly larger magnitude. It is notable the current method predicts similar range for both SDM1 and SDM2 whereas vertical velocity of [244] is smaller when $h/H = 0.25$.

Figure 6.17 provides streamwise position and streamwise velocity for both cases. As

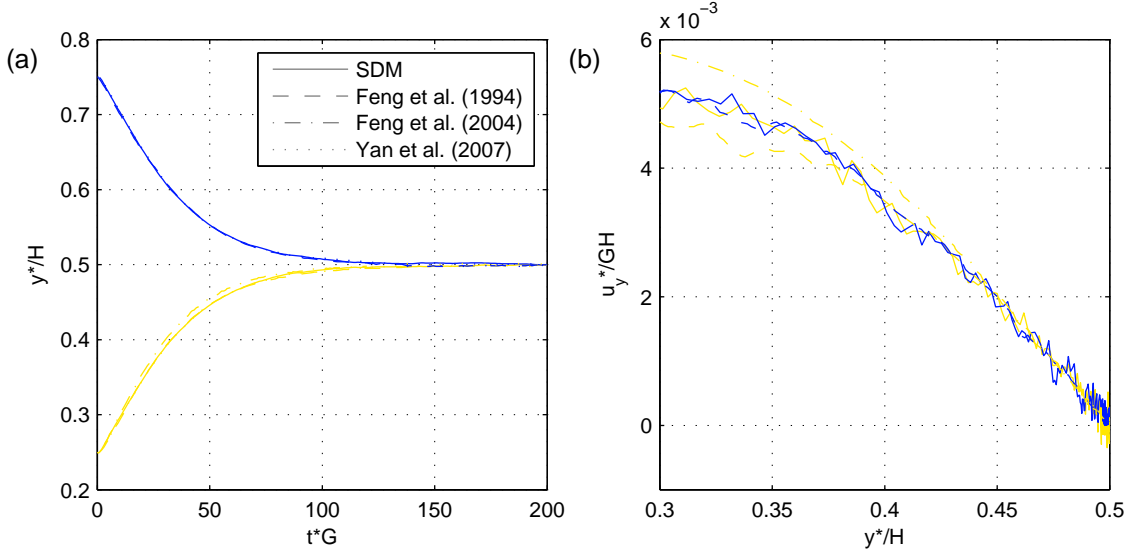


Figure 6.16: Comparison of vertical position with respect to time (a) and normal velocity with respect to vertical position (b). (Blue) $h/H = 0.75$; (Yellow) $h/H = 0.25$.

the behavior of the rigid body in SDM1 and SDM2 should be identical, the difference between the streamwise values may serve as a test of accuracy and symmetry of the simulations carried out here. As it is observed, the position and velocity differences are maintained to $\mathcal{O}(-3)$. While the error in velocity is consistent throughout the simulation, position difference becomes noticeable when the discs reach steady state in the middle of the channel and start to oscillate around the point of equilibrium.

6.3.5 Single ellipse descent

To combine the effects of linear and angular motion in the presence of an external body force, sedimentation of a rigid ellipse in quiescent fluid is simulated. It is known that drastically different motion patterns may ensue depending on the channel width, initial angle and positioning of the elliptic particle [231, 244]. In this study, two cases at moderate and low Re are simulated and compared to the results provided by Xia *et al.* [231] and Suzuki and Inamuro [152]. Dimensionless parameters governing this test case are Re , \mathcal{D} , aspect ratio a/b , blockage ratio W/a and h/d . Characteristic length and velocity scales are defined as $l_c = d = \sqrt{ab}$ and $u_c = \sqrt{gd}$, resulting in a Reynolds number defined as $Re_p = \rho_f \sqrt{gd^3} / \mu$. Alternatively, using major axis length, a , as length scale and terminal velocity, u_t , as the velocity scale, one may rewrite Reynolds number as $Re_t = \rho_f u_t a / \mu$. A schematic view of the test case is provided in figure 6.1-e. Computational domain consists of a 45.25×5.65 rectangle discretized by 80035 particles while the center of ellipse is placed at $h/d = 34$ with an angle of $\theta = \pi/4$. Aspect ratio and blockage ratio are set to 2 and 4, respectively. Boundary conditions are similar to that of case SDD. Other important parameters are included in table 6.5.

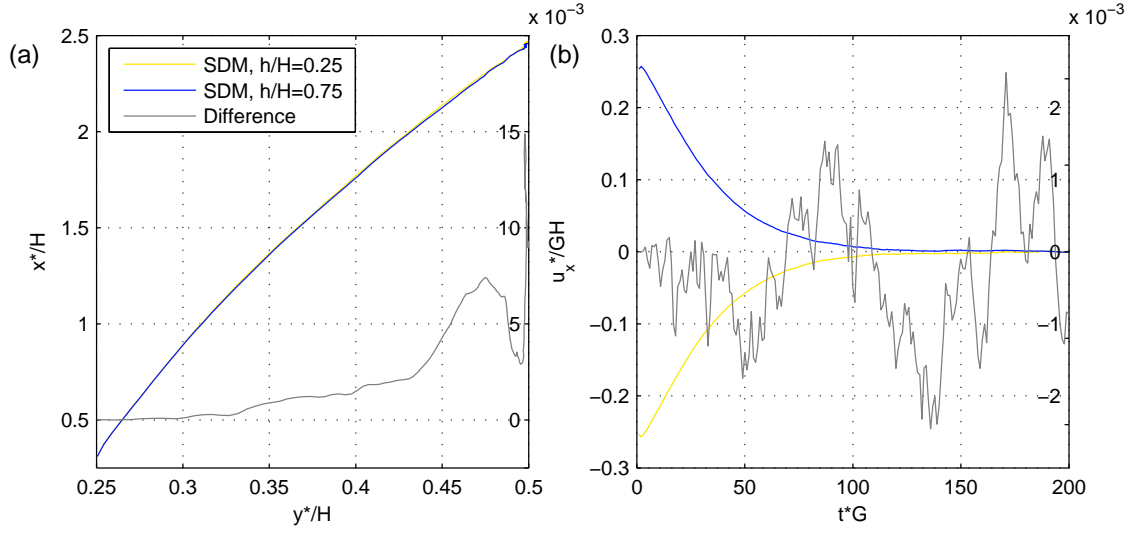


Figure 6.17: (a) horizontal position versus vertical position of the disc; periodic boundary conditions are assumed to imitate a longer channel. The position of the disc starting at the top half is converted to an equivalent of the one starting at the bottom half. The difference between the two curves is reflected on the right axis. (b) horizontal velocity versus time; The difference between absolute values is reflected on the right axis.

The elliptic disc is discretized such that a relatively uniform particle distribution is achieved in the transition region where the solid particles are within the support domain of the fluid particles. To this end, the rigid body is divided into concentric ellipses, each obtained by shrinking the major and minor axes of the ellipse by one particle spacing. Denoting major and minor axes of the outermost ellipse by a and b respectively, the j th layer has its axes set to $a_j = a - (j - 1) \delta_p$ and $b_j = b - (j - 1) \delta_p$, where δ_p is the particle spacing. The following equations are used to arrange the particles on the first quadrant of the j th ellipse:

$$x_{i+1} = x_i + \frac{\delta_p}{\sqrt{1 + \frac{b_j^2 x_i^2}{a_j^2 (a_j^2 - x_i^2)}}}, \quad (6.4)$$

$$y_{i+1} = b_j \sqrt{1 - \frac{x_{i+1}^2}{a_j^2}}. \quad (6.5)$$

The remaining quadrants are arranged by mirroring the first quadrant. If two particles are placed closer than one particle spacing, they are combined into a single particle placed midway between the original particles. Figure 6.18 shows the particle arrangement of the elliptic disc used in this study. Particle spacing is chosen such that particles are arranged in 7 concentric ellipses. The rest of the particles (fluid region) are arranged in a Cartesian formation with uniform spacing and particles overlapping with solid region are removed.

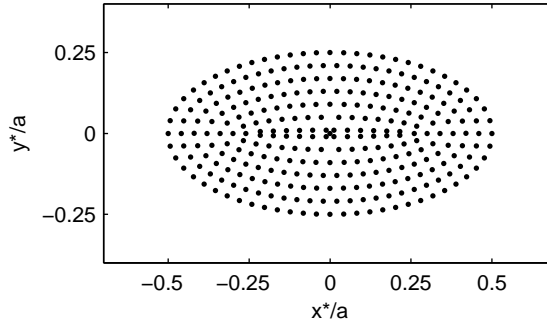


Figure 6.18: Initial particle arrangement inside the rigid elliptic particle

Table 6.5: Simulation parameters and Re_t for SED and numerical simulations of Xia *et al.* [231] and Suzuki and Inamuro [152].

Case	\mathcal{D}	SED		[231]	[152]
		Re_p	Re_t	Re_t	Re_t
1	1.1	58.8	13.5	12.9	12.6
2	1.01	58.8	2.15	2.08	1.92

Figure 6.19 provides horizontal position and angle of the ellipse versus vertical position of its center of mass. At $\mathcal{D} = 1.1$, the ellipse tends to have an oscillatory motion that damps out at later stages, leaving the ellipse in a horizontal position at the center of the channel descending at constant velocity. In this configuration, the results of [231] and [152] are in complete agreement while SED1 tends to miss the points where the ellipse changes its movement direction. It is possible to identify the reason for such behavior by examining the vertical velocity of the ellipse provided in figure 6.20. Since SED1 descends faster, it is expected that changes in direction occur in consecutively further points compared to [231]. Due to oscillatory nature of the flow, the error is compounded at each extrema until the motion damps out. Despite this, the characteristic behavior and final configuration of the ellipse are captured accurately. At $\mathcal{D} = 1.01$, the prediction of position by each of the numerical simulations shown in figure 6.19 is equally accurate and comparable. In terms of angle and vertical velocity, SED2 is in good agreement with results of Xia *et al.* [231] while [152] predicts a slightly larger angle. All cases end up at the middle of the channel in a horizontal position. Table 6.5 provides Re_t for SED and reference simulations. In both \mathcal{D} , SED predicts the largest Re_t while [152] assumes the smallest.

6.4 Remarks

The proposed two dimensional smoothed particle hydrodynamics method has been tested for moving rigid discs in Newtonian fluids. The method treats all phases as liquids of different viscosity while applying rigidity constraints to particles within the solid region. As a result, the method of transitioning between fluid viscosities representing solid and

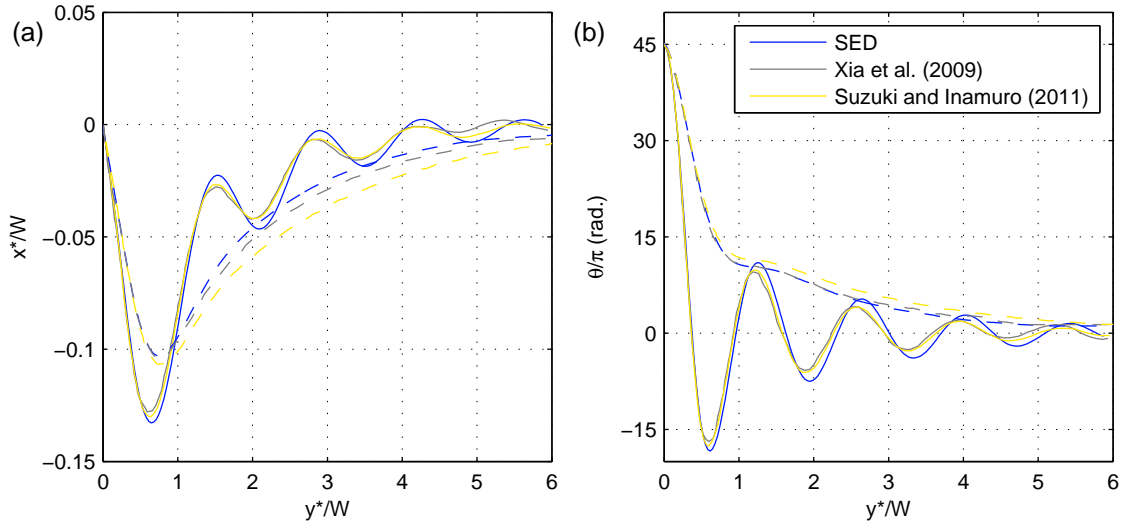


Figure 6.19: Comparison of horizontal position (a) and angle of the ellipse (b) versus vertical position at high (—) and low (--) Re_t or \mathcal{D} .

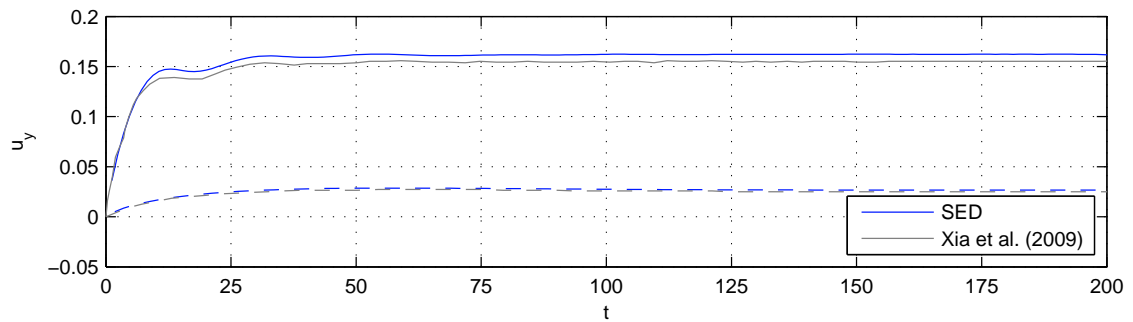


Figure 6.20: Comparison of vertical velocities of the ellipse versus time with [231]. (—) $\mathcal{D} = 1.1$; (--) $\mathcal{D} = 1.01$.

fluid regions and the ratio between these viscosities play an important role in the accuracy and robustness of the scheme. To calibrate these parameters, descent of a rigid disc in quiescent medium is simulated and weighed harmonic interpolation in conjunction with a viscosity ratio of 100 is found to provide consistent results.

In order to fully measure the performance of the proposed method in capturing isolated and combined linear and rotational motion, a series of test cases are simulated. Single and double disc descending in quiescent medium are used to measure the performance of the method in simulating linear motion and near contact situations where interpolation regions overlap. A repulsive force benefiting from color information available to SPH particles is developed and successfully tested. Rotation of a neutrally buoyant single disc in Couette flow is tested to measure the performance of the method in rotational motion. The results within the test range are in quantitative agreement with literature data. Combined linear and angular motion is tested by simulating the migration of a neutrally buoyant circular disc placed off center in Couette flow and sedimentation of an elliptic disc in quiescent medium under gravity. Results of both cases are found to be in agreement with literature data.

The tests carried out in this chapter show the suitability of the proposed FSI scheme in capturing the behavior of rigid bodies in Newtonian flow. This concludes the separate testing of all the required elements of the scheme, *i.e.* two- and three-phase flows, EHD and FSI. The next chapter combines all these elements for numerical simulation of electrostatic fluid-structure/solid interaction.

Chapter 7

Electrostatic fluid-structure/solid interaction

7.1 Introduction

External electric field, as a means of manipulation of particle position in quiescent fluid, is of great importance in micro- and nano-fluidics for assembly of colloidal particles or biological entities [121, 255]. In particular, dielectrophoresis (DEP) has become one of the more popular methods for characterization, manipulation and actuation of particles [256, 257]. This is due to better control and faster response when compared to other methods such as capillary [258], sedimentation [123] and chemical [259]. DEP has been used to trap [260–264], separate [265–271] and concentrate [264, 272, 273] particles and biological entities, assembly of colloidal particles into two-dimensional crystals [274] and nanowires [123] as well as formation of tissues using biological cells [136, 275, 276].

The process of DEP, caused by spatial non-uniformities in electric field, is studied numerically for both AC [122, 255, 277, 278] and DC [121, 256, 257, 279, 280] electric fields. When compared to its surrounding fluid, a more polarizable particle migrates toward higher electric field gradients while a less polarizable particle drifts away from regions with high electric field gradients [255]. The non-uniformities in the electric field may be due to electrode placement, proximity of the particles to one-another or to the electrodes which creates asymmetric force distribution on particle surface. The non-uniformity due to electrode placement results in particle movement while proximity of the particles leads to particle attraction to or repulsion from the electrode surface. Two particles suspended in a quiescent medium is the basic configuration for study of the DEP assembly. The presence of particles distorts the local electric field, causing a force imbalance which in turn results in relative motion between the particles [137, 281]. Ai and Qian [121], Hossan *et al.* [256], Kang [279] and Xie *et al.* [280] investigate the interaction of a pair of neutrally buoyant particles suspended in uniform DC electric field for various sets of

electrical properties. They use fully resolved numerical simulations where electric stresses are defined through Maxwell stress tensor [139]. Their results show that a pair of particles with similar electrical properties tend to align with the electric field while dissimilar particles position such that their center-to-center line is perpendicular to the electric field direction.

A series of studies of particle motion subject to an external electrical field is presented in this chapter. First, the motion of a single circular disc suspended in uniform shear flow is investigated in section 7.2. The particle is affected by the proximity of the electrodes and shows different behavior depending on material properties. The second case of section 7.3 investigates the chaining behavior of a pair of particles suspended in quiescent fluid under different material properties and geometrical configurations. As the third case, sedimentation of an elliptical particle within a constrained or infinitely large environments is examined in section 7.4.

7.2 Migration of a rigid disc in Couette flow

In this section, migration of a neutrally buoyant rigid disc in plane Couette flow subject to an external electric field is simulated. When no electric field is present, a circular disc released at a distance h from the middle of the channel is expected to migrate toward the centerline while moving with the flow for $Re \leq 2$ [223, 238]. When exposed to an external electric field, the motion of the disc may be altered depending on the properties of the fluid, solid and their proximity. A schematic of this case is provided in figure 7.1-a. Similar to the case without electrical field of section 6.3, the computational domain consists of an 8×32 rectangle discretized by 13806 particles initially arranged in a Cartesian grid for fluid and concentric circles for the solid. A close-up view of the particle arrangement at the vicinity of the solid disc is provided in figure 7.1-b. The confinement ratio is $\mathcal{D} = 0.125$ while the disc is placed at $h/H = 0.25$ below the centerline. To investigate the effects of electric field, Ei is set to $Re/4$ to provide a large enough electric force while Re is equal to 0.625. Top and bottom walls abide by no-slip condition and are moving in opposite directions at a velocity of $U_w/2$ where $U_w = GH$. A constant electric potential difference of $\Delta\phi = E_\infty H$ is imposed between the moving walls, resulting in an electric field perpendicular to the flow. Periodic boundary condition is imposed in streamwise direction for all variables. Permittivity and conductivity ratios are individually varied as 0.2, 0.5, 2 and 5 (table 7.1). When $\mathcal{P} = \mathcal{C}$, $\mathbf{f}_{(eq)}$ vanishes. This leads to electric forces that are perpendicular to the disc's surface, in-plane with the flow. This force configuration does not contribute to the disc's rotation, although it affects its translational motion due to its proximity to channel walls in the particular setup used here. Equal permittivity and conductivity ratios are avoided here.

There are two primary reasons for different behavior of the electrified cases compared

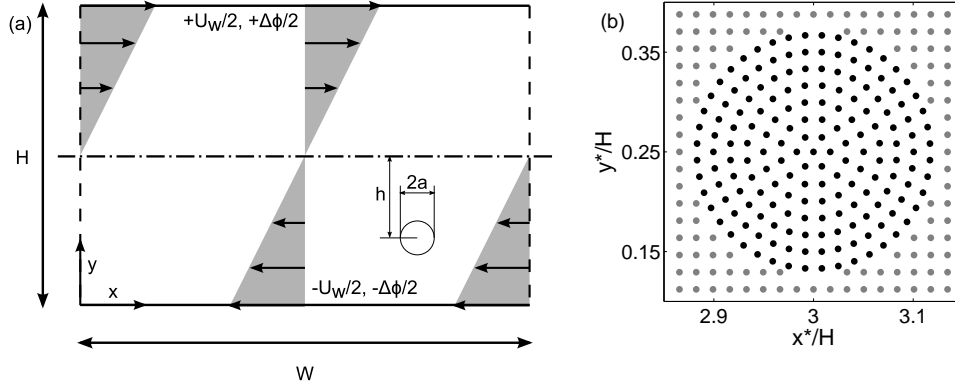


Figure 7.1: (a) Schematic of the test case. (b) Closeup view of initial particle distribution at the vicinity of the solid disc. Black points denote solid particles whereas gray points are fluid particles.

to the case with no external electric field present. The first one is the DEP due to proximity of electrodes and the other is the tendency of electrical forces in changing the angular velocity of the disc. If the electrical timescale of the solid is larger than that of the fluid, $\tau_s/\tau_f > 1$, the rigid body will migrate to regions of lower electric field gradient, *i.e.* toward the electrodes in this case. The reverse is true for $\tau_s/\tau_f < 1$ where the body favors regions of higher electric field gradient [255]. The effects on angular rotation are also tied to the relationship between electrical timescales of the fluid and solid. When $\tau_s/\tau_f > 1$, the electrical forces point from fluid toward solid, resulting in an electrical torque that is unstable and tends to rotate the disc. Given large enough electric field and a preferred direction, a spontaneous rotation called Quincke rotation may ensue [282, 283]. If $\tau_s/\tau_f < 1$, the electrical torque will resist the rotation of the disc. In this study, the linear shear dictates the preferred direction, however, the electric field intensity is not enough to generate Quincke rotation all cases that satisfy $\tau_s/\tau_f > 1$ (table 7.1). Regardless, the torque generated by the electric forces is enough to affect the rotational motion of the disc.

Figure 7.2 plots the trajectory and velocity of the disc for the case without electric field (NE) and for $(\mathcal{P}, \mathcal{E})$ pairs of (0.2, 5) and (5, 0.2). The disc in case (0.2, 5) is accelerated toward the centerline while in case (5, 0.2), it is moved toward the wall. Case (5, 0.2) is solved until the disc touches the bottom wall. Noting that $\tau_s/\tau_f = \mathcal{P}/\mathcal{E}$, case (0.2, 5) is more polarizable and migrates toward larger electric gradient. In this case, both hydrodynamic and electrical forces lead the particle away from the channel wall, resulting in faster migration toward channel center when compared to NE. The difference between normal velocities of (0.2, 5) and NE becomes smaller as the disc moves away from the wall and the gradient of electric field becomes more symmetric. On the other hand, (5, 0.2) is less polarizable and this results in its attraction to smaller electric field gradient. In this case, electrical forces act against the hydrodynamic forces and bring the disc toward the wall. The normal motion of the disc comes to a stop when it reaches the bottom wall. Figure

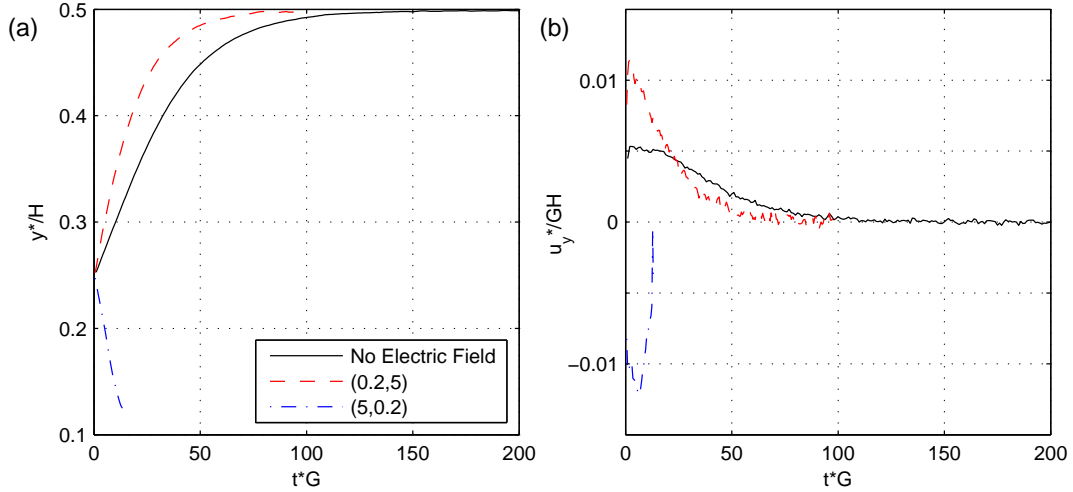


Figure 7.2: Comparison of the vertical position (a) and vertical velocity (b) of the disc's center of mass versus time.

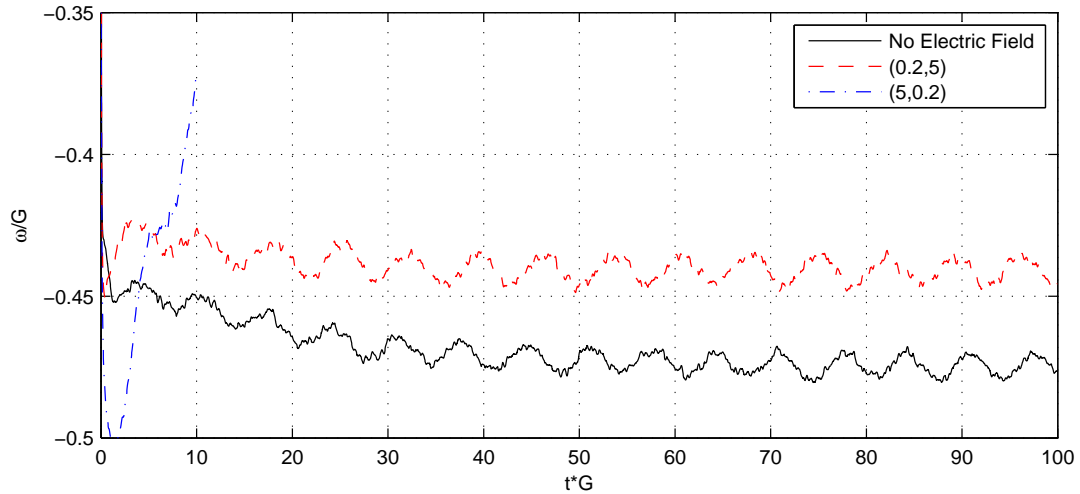


Figure 7.3: Angular velocity for cases NE (black), (0.2, 5) (red) and (5, 0.2) (blue).

7.3 shows the angular velocity of the aforementioned cases. The configuration of electric forces in case (5, 0.2) is such that the condition for Quincke rotation is satisfied. This results in an electric torque that assists the rotation of the disc in the flow, resulting in faster angular velocity compared to case NE. On the other hand, the electrical torque applied to (0.2, 5) resists the rotation and this results in reduced angular velocity compared to case NE.

Figure 7.4 shows streamlines and electric field lines for cases NE, (0.2, 5) and (5, 0.2) at steady state. The electric field lines are attracted to the solid body when $\mathcal{C} > 1$ and avoid the body as much as possible when $\mathcal{C} < 1$. As expected for $Re = 0.625$, the streamlines are fairly symmetric for case NE. While case (0.2, 5) reaches a steady state in the middle of the channel, its streamline pattern is different from NE. As shown in figure 7.3, the

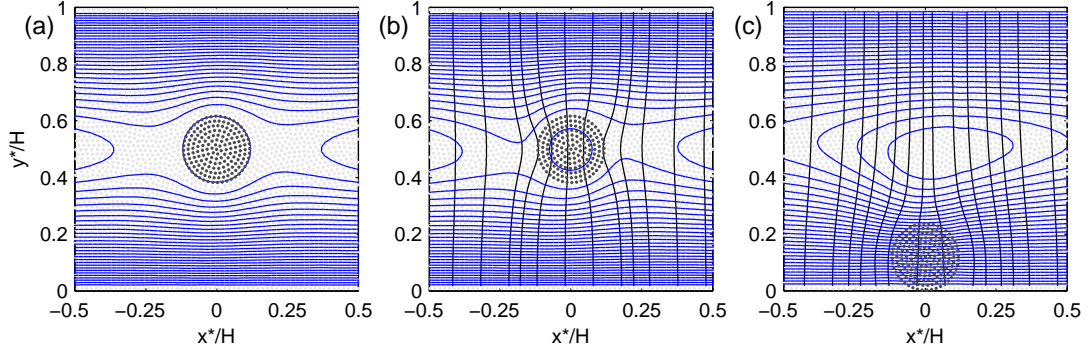


Figure 7.4: Streamlines (blue) and electric field lines (black) for case NE (a) and permittivity and conductivity pairs of (0.2, 5) (b) and (5, 0.2) (c). Rigid body particles are in darker gray while fluid particles are shown in light gray.

Table 7.1: Time until the disc reaches one radius distance of channel center (regular) or bottom wall (bold). An underline shows that all conditions for Quincke rotation are satisfied. The disc reaches channel center at $t^*G = 25.94$ when no electric field is applied.

\mathcal{P}	0.2	0.5	2	5	
\mathcal{C}	0.2	-	80.05	<u>19.18</u> <u>13.34</u>	
	0.5	17.79	-	<u>44.89</u> <u>29.37</u>	
	2	13.49	17.18	-	<u>33.59</u>
	5	13.81	16.89	24.07	-

disc rotates in clockwise direction. However, since the disc's rotation is hampered, the streamlines are skewed in counter-clockwise direction to satisfy the no-slip behavior. In case (5, 0.2), the disc ends up at the channel wall, resulting in a large vortical structure in the middle of the channel directly above it. The structure is leaning in the direction of the flow at the upper half of the channel which is not obstructed by the disc.

Table 7.1 provides the time until the disc comes to one radius distance of the bottom wall or the channel center. Bold numbers show that the disc approaches the bottom wall while an underline indicates that conditions for Quincke rotation are satisfied. The disc reaches the channel center at $t^*G = 25.94$ when no electric field is applied. When $\tau_f > \tau_s$ (lower triangle), the disc travels faster toward the channel center while when $\tau_f < \tau_s$ (upper triangle) the disc travels slower toward the channel center or moves toward the channel wall. Such observations are reported in experiments as well [284]. As it is seen, increasing the permittivity ratio at a constant conductivity ratio results in a gradual increase in the time needed for the disc to reach the channel center. At large enough permittivity ratios the trajectory is reversed and the disc migrates toward the channel wall. At this point, further increase of the permittivity ratio results in a faster migration toward the channel wall. The inverse of this trend is observed when the permittivity ratio is kept constant and the conductivity ratio is increased.

7.3 Dielectrophoretic chaining of circular discs

7.3.1 Geometric properties, characteristic values and test cases

In this section, dielectrophoretic interaction of two neutrally buoyant circular discs suspended in quiescent background fluid is examined. The pair of discs begin to move and eventually chain together when an external field is applied. Their trajectory depends on the electrical properties of the materials as well as the initial orientation of the discs. The behavior is observed in both perfect dielectric [121, 280] and leaky dielectric [256, 279] models as well as experiments [123, 137, 285]. Discs with identical polarizability, compared to the background fluid, tend to chain such that the line connecting the centers of both discs is parallel to the electric field. When one disc is more polarizable than the fluid and the other is less polarizable, the final orientation is such that the center-to-center line lies perpendicular to the electric field. The perfect dielectric model is used here and the parameters are chosen such that the results are valid for micro-scale particles [121, 280].

Figure 7.5 provides a schematic of the problem considered here. Two circular discs with radii of r_1 and r_2 are suspended in a square cavity of side length $H = 20r_1$. For better distinction, disc one is shown in white while disc two is in gray. The distance between disc centers is referred to as L_c here while a surface-to-surface distance of $L_s = L_c - r_1 - r_2$ is also defined. Since in its most general form discs one and two may not have identical radius, L_s provides a better measure of the distance and facilitates comparison. The discs are positioned at an angle of θ with horizontal line at a distance $L_s/2 = r_1/2$ from the center of the computational domain. A constant potential difference of $\Delta\phi$ is applied between horizontal walls, shown as continuous lines, resulting in an undisturbed electric field in vertical direction. This means that the center-to-center line is at $\pi/2 - \theta$ with the electric field and when aligned with the field, θ is equal to $\pi/2$. Defining θ as shown in figure 7.5 facilitates the presentation of the results as θ increases with time. Side walls, shown in dashed lines, are insulated and electric field lines are parallel to these walls. All bounding walls are subject to no-slip condition.

Since no mechanical input is applied to the system, characteristic velocity is based on dielectrophoretic velocity scale. According to Saville [108],

$$u_c = \frac{\varepsilon_c l_c E_c^2}{\mu_c}. \quad (7.1)$$

All other characteristic values are chosen as

$$\begin{aligned} \rho_c &= \rho_f, & \mu_c &= \mu_f, & \varepsilon_c &= \varepsilon_f, \\ l_c &= r_1, & E_c &= E_\infty = \Delta\phi/H, & p_c &= \rho_c u_c^2, \end{aligned} \quad (7.2)$$

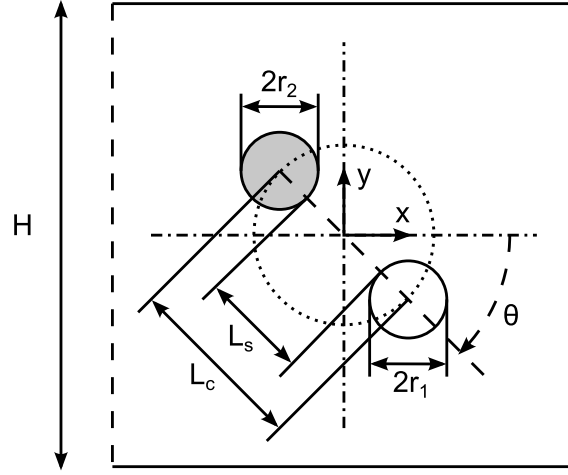


Figure 7.5: Schematic of the DEP chaining of two circular discs. Discs one and two are colored in white and gray for distinction.

leading to the following dimensionless numbers

$$\text{Re} = \rho_f \varepsilon_f \left(\frac{r_1 E_\infty}{\mu_f} \right)^2, \quad (7.3)$$

$$\text{Ei} = \rho_f \varepsilon_f \left(\frac{r_1 E_\infty}{\mu_f} \right)^2, \quad (7.4)$$

$$\begin{aligned} \mathcal{R} &= \frac{r_1}{H}, & \mathcal{R}_r &= \frac{r_2}{r_1}, \\ \mathcal{P} &= \frac{\varepsilon_1}{\varepsilon_f}, & \mathcal{P}_r &= \frac{\varepsilon_2}{\varepsilon_1}. \end{aligned} \quad (7.5)$$

As it is seen, Reynolds and Electro-inertial numbers are identical which means the characteristic velocity of equation (7.1) may be obtained if the equality $\text{Re} = \text{Ei}$ in characteristic form is solved for u_c .

Several parameters affect the trajectory followed by each of the discs. Kang [279] and Hossan *et al.* [256] discuss the behavior of leaky dielectric discs with similar and dissimilar electrical properties. Xie *et al.* [280] examine the effects of different size on the motion of the discs. However, all the above cases are limited to low Re since they discard the convective terms of the momentum equation (2.6). SPH handles the convective terms naturally and allows for seamless extension to larger Re numbers. The studies conducted here are confined to discs that have larger permittivities than the surrounding fluid and a permittivity ratio of $\mathcal{P} = 40$ is chosen to match the studies made in [121, 280]. Four cases will be considered here. First, the effect of initial angle with the electric field is inspected. Then the effect of Re on the behavior of the discs will be examined. Specifically, the cases examined by Ai and Qian [121] and Xie [280] concentrate on $\text{Re} = 0.007$. Here, Re values up to 116 are simulated to provide a better understanding of the chaining behavior,

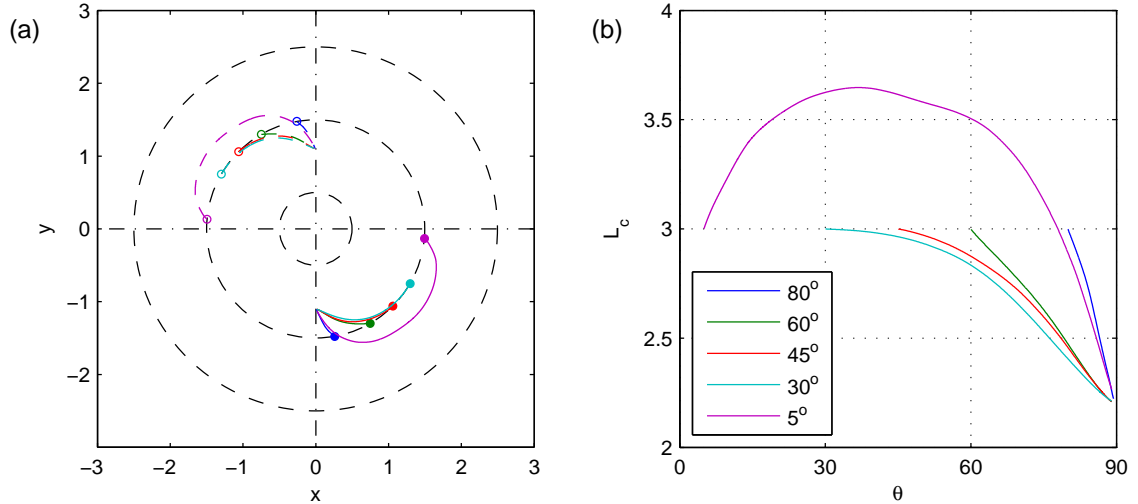


Figure 7.6: (a) Trajectory of disc one (continuous) and disc two (dashed) with different starting angles; (b) center-to-center separation distance with respect to center-to-center angle with electric field.

especially since the chaining happens faster at higher Re and is of practical interest. The third case investigates the effects of dissimilarities in electrical properties. The difference between permittivities of the discs is gradually increased to range from a simple defect to different materials. The final case considers the behavior of discs with different radii.

7.3.2 The effect of initial angle

In this section, the behavior of the discs at five starting angles of $\theta_i = 80, 60, 45, 30$ and 5 degrees, corresponding to $10, 30, 45, 60$ and 85 degrees with the electric field, is considered. Since the positioning of the discs results in slightly different particle arrangements, each case is discretized by different number of particles. The number of particles for each case in the order mentioned above are 22514, 22498, 22506, 22498 and 22512. The discs are identical and have a permittivity ratio of $\mathcal{P} = 40$ while $Re = Ei = 0.007$. All simulations are carried out until $\theta = 89^\circ$ and the corresponding dimensionless times for each case are 8.13, 8.62, 10.94, 12.22 and 37.08.

Figure 7.6 provides trajectories of the discs as well as the center-to-center distance L_c with respect to θ . A circle marker shows the initial position of the discs. As expected from identical discs, all cases rotate and align with the electric field. In all cases, with the exception of 5° , the distance between the discs decreases during their travel. For $\theta_i = 5^\circ$, the distance between the discs increases until $\theta = 37^\circ$ reaching a maximum of $L_c = 3.65$ before dropping to $L_c = 2.25$ at $\theta = 89^\circ$. This also explains the big jump in time required for reaching $\theta = 89^\circ$ when starting from an initial angle of 5 degrees.

A better understanding of the effect of angle on the behavior of the discs may be obtained by observing the changes of electrical forces with respect to θ and L_c . Figure 7.7

plots the electric force component in the center-to-center direction $f_{(en)}$ where a positive value indicates an attractive force as well as the electric force component normal to the center-to-center direction $f_{(es)}$, which results in a clockwise rotation if its value is positive. It is expected that as the discs align with the electric field, the center-to-center force reaches a maximum while the component causing the rotation vanishes. Figure 7.7-a shows that center-to-center component remains attractive throughout the trajectory for cases with $\theta_i \leq 45^\circ$. Cases starting at 30 and 5 degrees experience an initially repulsive $f_{(en)}$. The angular span of the repulsive force is rather short in case $\theta_i = 30^\circ$ and is not enough to cause an increase in the initial separation between the discs. On the other hand, approximately one third of the travel angle in case $\theta_i = 5^\circ$ is spent in repulsive region and this results in significant increase in separation distance as shown in figure 7.6-b. It is worth noting that in both 30° and 5° cases the repulsive force changes to an attractive one at about $\theta = 37^\circ$, which also corresponds to the angle when the trajectory of case $\theta_i = 5^\circ$ changes from a diverging path to a converging one (figure 7.6-b). The maximum value of $f_{(en)}$ is comparable for all cases, regardless of the starting angle and resides in the final portions of the travel. Unlike $f_{(en)}$, the magnitude of the $f_{(es)}$ is dependent on the starting angle of the discs and the largest magnitude among all cases belongs to $\theta_i = 45^\circ$. If the case in question does not pass $\theta = 45^\circ$ during its travel, *i.e.* $\theta_i = 80^\circ$ and 60° , then the maximum $f_{(es)}$ is achieved at the initial stages of the travel. However, if the discs pass through the 45 degrees point, the maximum of $f_{(es)}$ lies slightly after 45° mark. The relation between disc separation and $f_{(en)}$ and $f_{(es)}$ is provided in figure 7.7-c and d, respectively. The shift in $f_{(en)}$ from repulsion to attraction at maximum separation distance is clearly visible for case $\theta_i = 5^\circ$ in figure 7.7-c. As the discs become closer, the differences between $f_{(en)}$ becomes smaller and all cases reach a maximum at $L_c = 2.25$. The reason for reaching maximum center-to-center force prior to chaining may be attributed to a shortage of particles resolving the electric field between the discs. As the discs get closer than the compact support range of the kernel, the number of fluid particles between the discs becomes smaller and the particles belonging to the solid phase start to interact with one another across the discs. This results in a reduction in gradients across different phases and reduces the electrical forces. As for $f_{(es)}$ for cases with $\theta_i \leq 60^\circ$, there is a direct relationship between the rotational component and separation distance as the maximum value lies slightly below $L_c = 3$. In case $\theta_i = 5^\circ$, there is an increase in $f_{(es)}$ for $3 < L_c < 3.5$ followed by a decrease as the discs converge.

Due to the electrostatic model used here, all changes in the geometrical configuration of the components affect the electrical properties of the computational domain and in turn have immediate effects on the field intensity observed at the walls. Figure 7.8 provides average electric field intensity \bar{E} taken at the upper wall of the computational domain. Since the discs have larger permittivity than the fluid, the overall permittivity of the computational domain is larger than that of the fluid only system. This results in a slightly

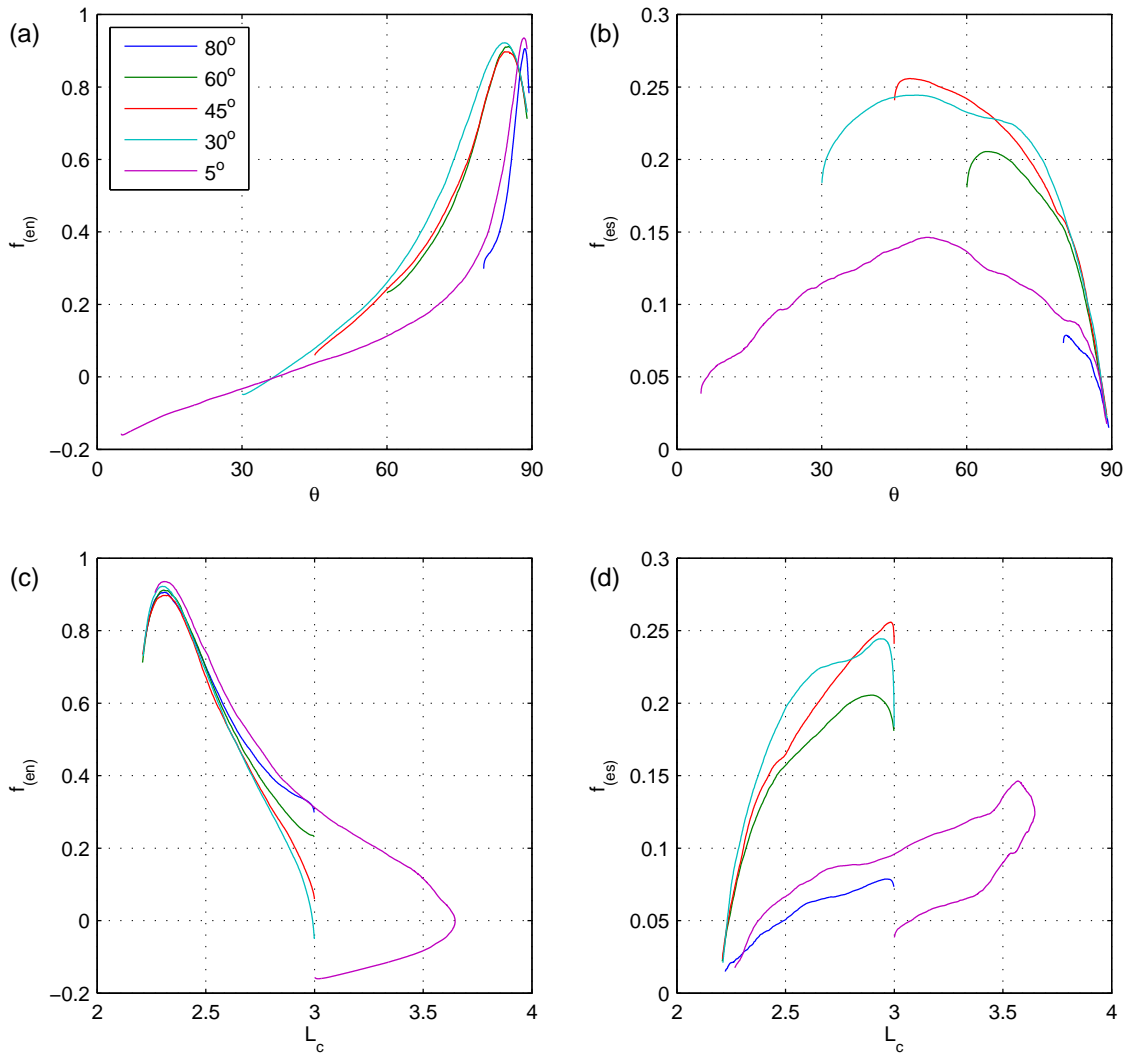


Figure 7.7: Center-to-center (a,c) and rotational (b,d) components of electric forces with respect to angle (a,b) and separation distance (c,d) for different θ_i .

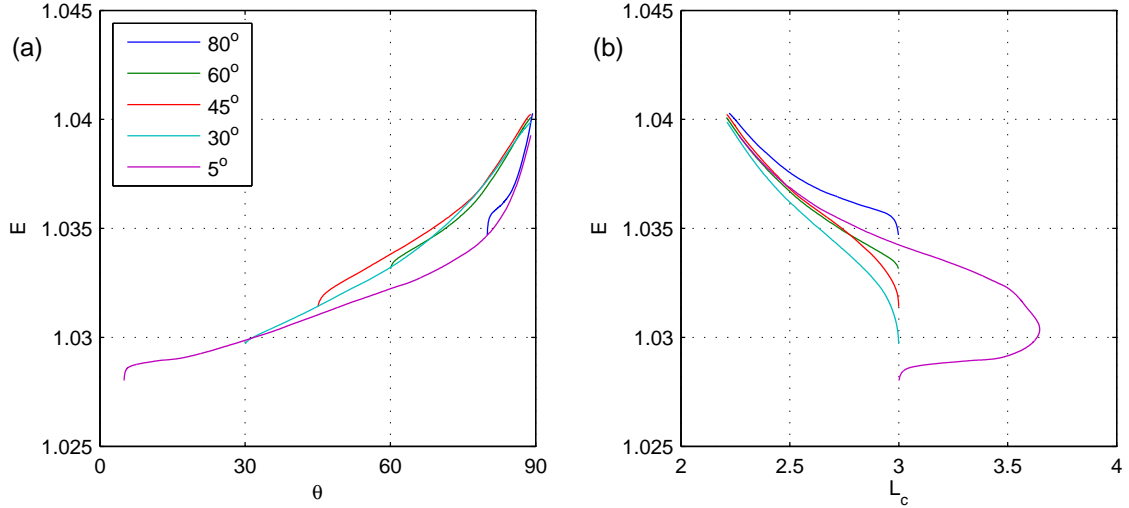


Figure 7.8: Average electric field intensity at the upper wall with respect to angle (a) and separation distance (b) for different θ_i .

larger field intensity than E_∞ . While the initial average intensity is different for different starting angles, all cases approach the same value of \bar{E} toward the end of the simulation. This observation may be used to approximate the orientation of the discs without visual confirmation. A comparison with figure 7.7-a,c also shows that \bar{E} has similar behavior to $f_{(en)}$.

7.3.3 The effect of Reynolds number

In this section, the effects of Reynolds and Electro-inertial numbers on the behavior of the discs is studied. Reynolds and Electro-inertial numbers are identical in this case and electric field intensity is used to change their value. From a practical standpoint, changing the field intensity is one of the control parameters in the chaining phenomenon and has a parabolic relationship with characteristic velocity, as seen in equation (7.1). This means that using larger electric field will expedite the chaining process. Based on the observations made in previous section, two initial angles of 45 and 5 degrees are chosen for these tests. The number of particles discretizing the domain is identical to the values given in the previous section for respective starting angles. Electric field is doubled in successive cases resulting in Reynolds numbers of 0.007, 0.028, 0.113, 0.453, 1.813, 7.253, 29.01 and 116.1. Figure 7.9-a and b provides times t_f until a stable $\theta = 89^\circ$ is achieved with respect to Reynolds number. A stable $\theta = 89^\circ$ is assumed to be a situation where the discs will align with the electric field in their next approach to a 90 degrees angle. As seen in figure 7.9, the time remains relatively constant for $Re < 1$ for both cases and increase rapidly for $Re > 1$. This means that while the dimensional time of the process drops continuously as long as chaining occurs, the time gained by increasing Reynolds number is much smaller for $Re > 1$. As such, it may be inferred that it is best to carry out the chaining process

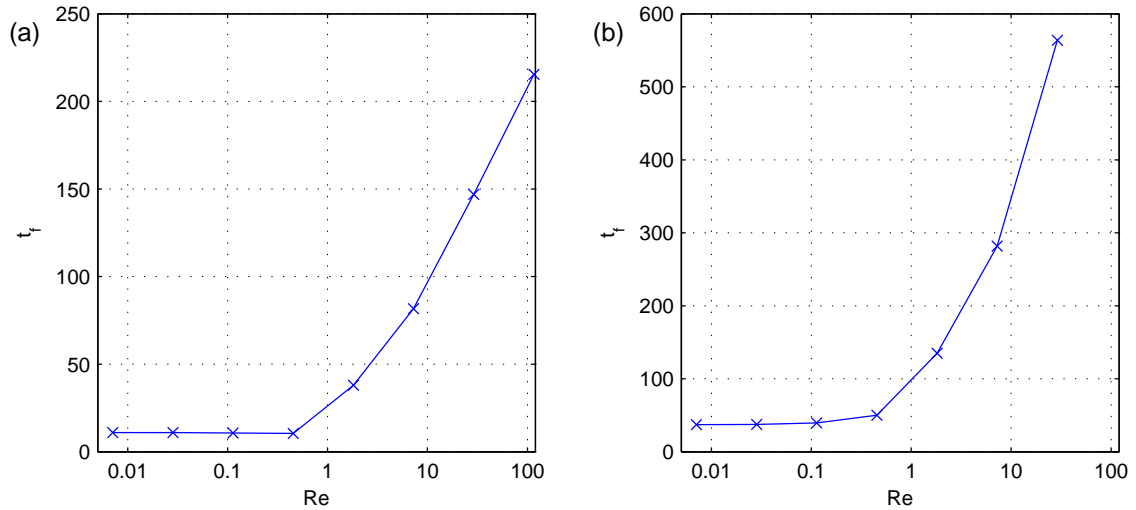


Figure 7.9: Dimensionless time for reaching $\theta = 89^\circ$ with respect to Reynolds number for $\theta_i = 45^\circ$ (a) and $\theta_i = 5^\circ$ (b).

close to unit Reynolds number.

Figures 7.10 and 7.11 provide trajectories and separation distances for starting angles of 45 and 5 degrees, respectively. As expected, the difference in trajectories for cases with $Re \leq 0.113$ is negligible. Cases with Reynolds numbers about unity, *i.e.* $Re = 0.113$ and 1.813 , have insignificant overshoot from the 90° mark where the center-to-center line of the discs becomes aligned with the electric field. At higher Re numbers the discs pass the 90° and travel further before aligning with the electric field. This reduces the effectiveness of the chaining procedure at higher Re , as observed in figure 7.9. For the highest Reynolds number studied here at $\theta_i = 45^\circ$, the discs make multiple passes at the 90° mark. At $\theta_i = 5^\circ$, the separation becomes so large that the discs no longer interact with one another and no chaining occurs. A comparison of separation distance between $\theta_i = 45^\circ$ and 5° shows that the effects of the increase in Re is much more pronounced at smaller initial angle. The reason for this is the increase in separation distance between the discs for $\theta_i = 5^\circ$ at the initial stages of the simulation which has significant effects on the interactions of the discs.

To better demonstrate the reason behind the effects of the Reynolds number on the chaining behavior, electrical forces are shown in figures 7.12 and 7.13. Regardless of the Reynolds number, both $f_{(en)}$ and $f_{(es)}$ are comparable in scale. The observations regarding the similarity in trajectories for cases with $Re \leq 0.113$ holds for center-to-center and rotational forces as well. For cases with a starting angle of 45 degrees, the force remains attractive for all Re while the maximum shifts to larger angles at higher Re . A comparison of figures 7.12-a and c shows that the reason is due to the fact that cases with larger Re achieve smaller L_c at larger θ . Since $f_{(en)}$ is directly related to L_c , this delays the angle where maximum attraction is achieved. The rotational force of cases with $\theta_i = 45^\circ$ scales

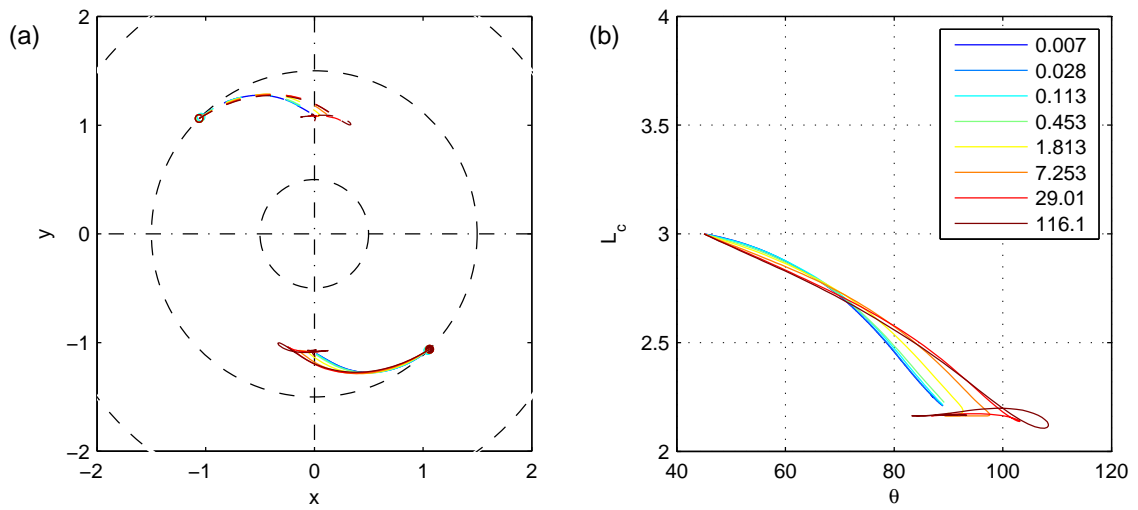


Figure 7.10: (a) Trajectory of disc one (continuous) and disc two (dashed) for $\theta_i = 45^\circ$ starting angle at different Reynolds numbers; (b) center-to-center separation distance with respect to angle.

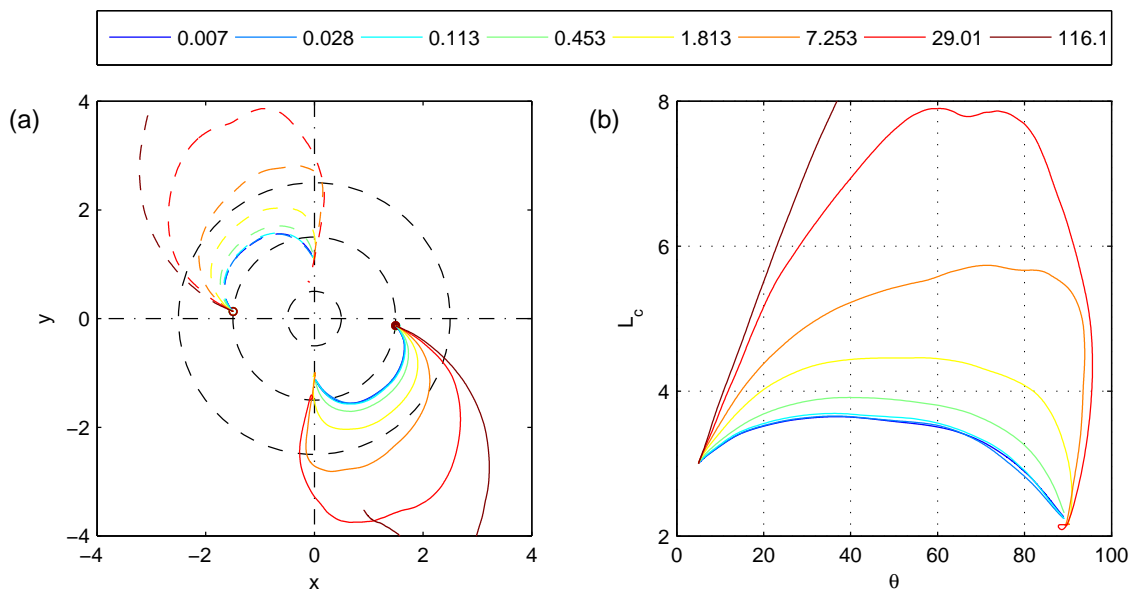


Figure 7.11: (a) Trajectory of disc one (continuous) and disc two (dashed) for $\theta_i = 5^\circ$ starting angle at different Reynolds numbers; (b) center-to-center separation distance with respect to angle.

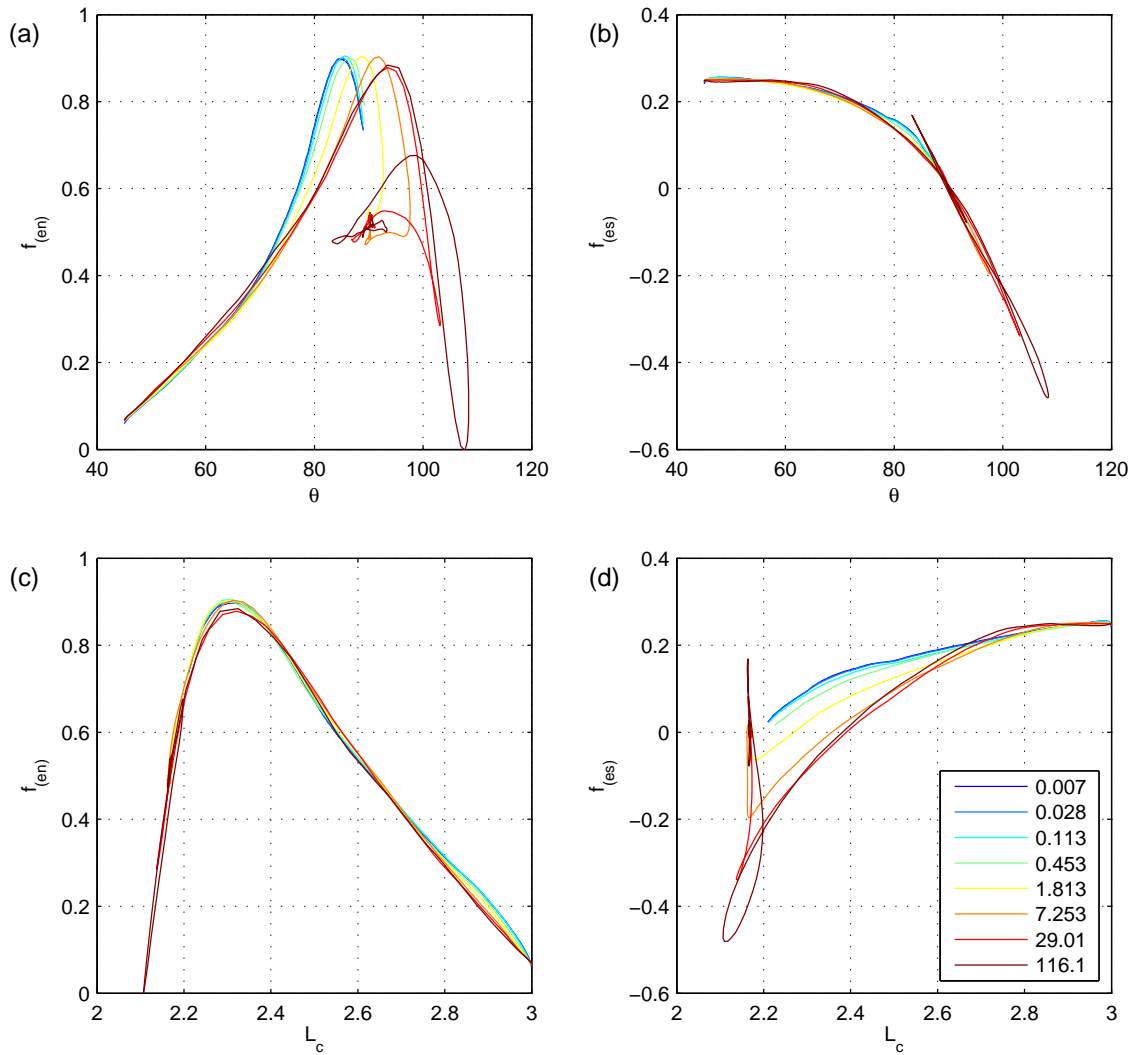


Figure 7.12: Center-to-center (a,c) and rotational (b,d) components of electric forces with respect to angle (a,b) and separation distance (c,d) for different Reynolds numbers at $\theta_i = 45^\circ$.

well with angle and the difference between different Re is quite small. As expected, the rotational force is zero when discs are aligned with the electric field. The cases passing 90° experience a negative rotational force which causes counter-clockwise rotation, returning them toward an aligned position. The effects of increasing Re is more dramatic for $\theta_i = 85^\circ$. The effects of increase in separation distance is evident in figures 7.13-a and c. The increase in attractive force with respect to θ is much slower for larger Re while the change from repulsion to attraction happens at greater distance. The initial increase in separation distance affects the rotational force as well where it decreases significantly at larger Reynolds numbers.

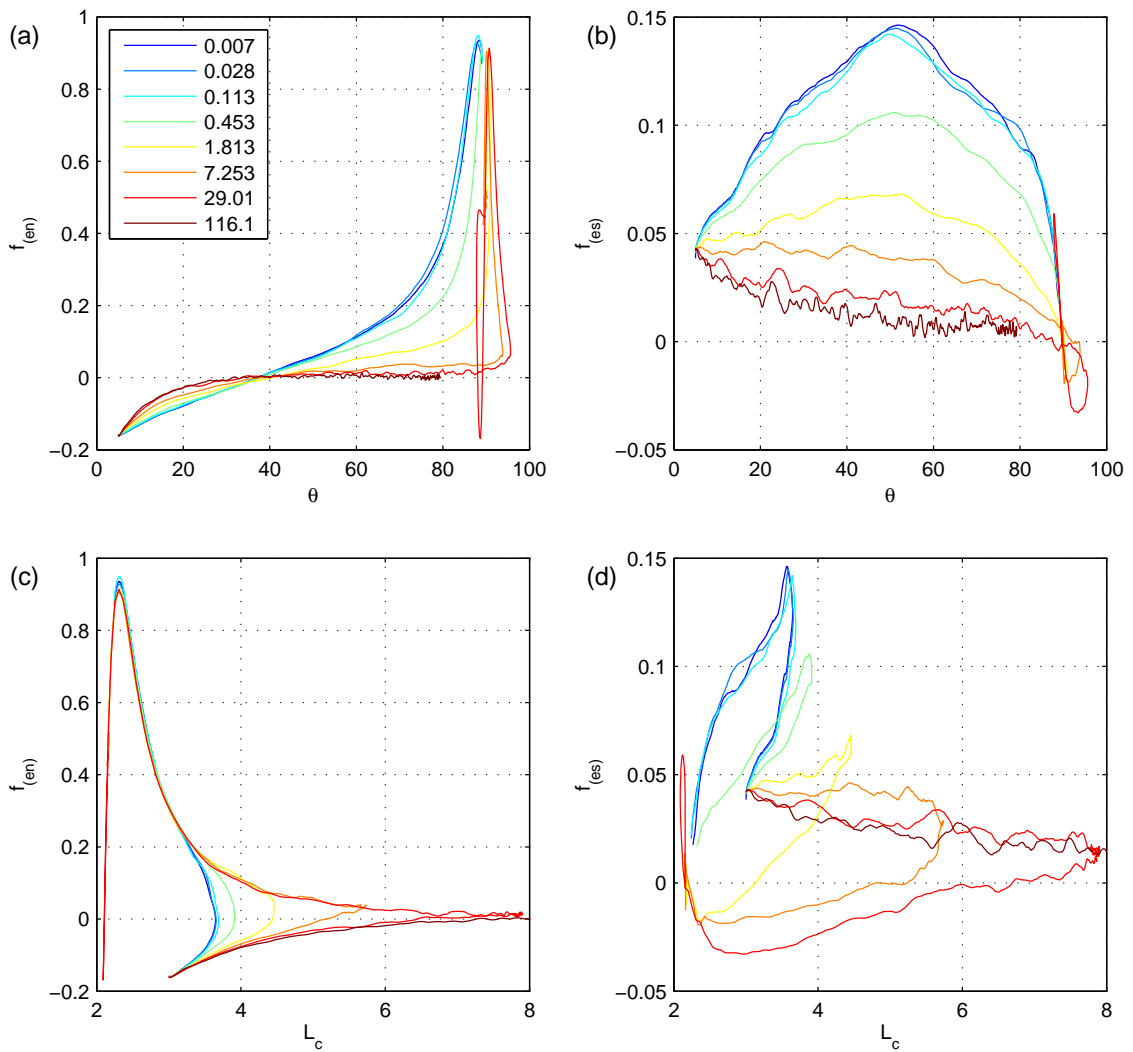


Figure 7.13: Center-to-center (a,c) and rotational (b,d) components of electric forces with respect to angle (a,b) and separation distance (c,d) for different Reynolds numbers at $\theta_i = 5^\circ$.

7.3.4 The effect of difference in permittivities

In this section, the effects of difference in permittivity between the discs is investigated. Both initial angles of 45 and 5 degrees are considered and Re is set 0.113. The number of particles discretizing the domain is identical to the values given in the previous section. The reasons behind changes in electrical properties may range from production defects to chaining of particles of different materials. To mimic such conditions, the permittivity of the second disc is changed while disc one remains identical between different cases, resulting in disc-to-disc permittivity ratios of $\mathcal{P}_r = 1, 0.975, 0.95, 0.9, 0.85, 0.8, 0.75, 0.5$ and 0.25 . All simulations are carried out until $\theta = 89^\circ$ and the corresponding dimensionless times for each case at 45° are 10.76, 11.05, 11.05, 11.33, 11.33, 11.61, 11.90, 13.03 and 16.71. For the starting angle of 5 degrees, the times of reaching $\theta = 89^\circ$ are 39.39, 39.39, 39.96, 41.10, 41.67, 42.80, 44.32, 48.76 and 57.27.

Figures 7.14 and 7.15 plot trajectories and center-to-center distance of the discs for cases starting from 45 and 5 degrees, respectively. The trajectories of the discs remain identical for $\mathcal{P}_r \geq 0.9$, especially for disc one. The differences in trajectory for $\theta_i = 45^\circ$ become more significant as \mathcal{P}_r decreases. For $\mathcal{P}_r \leq 0.5$, disc two starts to move toward the top electrode while disc one follows it and moves to align the center-to-center line with the electric field. This results in discs reaching the 89° mark at a position above the center of the computational domain and skewed toward the left. Despite this, the separation distance between the discs remains almost identical for all \mathcal{P}_r . This means that disc one travels larger distances after disc two to maintain the separation distance at smaller \mathcal{P}_r . Compared to the drastic changes in trajectory observed for $\theta_i = 45^\circ$, almost all cases with a starting angle of 5 degrees maintain the chaining position at the center of the computational domain. As \mathcal{P}_r decreases, disc one starts to take a longer route further away from the center of the computational domain while disc two takes shorter arcs that are closer to the center. The separation distance remains similar for all cases, except $\mathcal{P}_r = 0.25$, showing that the shorter and slower route taken by disc two is compensated by faster and longer route of disc one.

The reason behind the different routes taken by the discs is better explained in figures 7.16 and 7.17 where center-to-center and rotational components of the electrical forces are plotted. Since discs one and two experience different force magnitudes, both discs are shown in the figures. To differentiate between the discs, a negative $f_{(en)}$ shows attractive force for disc two while a negative $f_{(es)}$ causes clockwise rotation. The movement of the disc pair may be assessed based on the resultant force exerted on the discs. A general observation is that the forces see little change on disc one, which has identical properties across all test cases, while there is significant variation on forces exerted on disc two. The reason behind little change in disc one is that different permittivity values on disc two only affect the field lines passing in between the discs. This changes field intensity in the

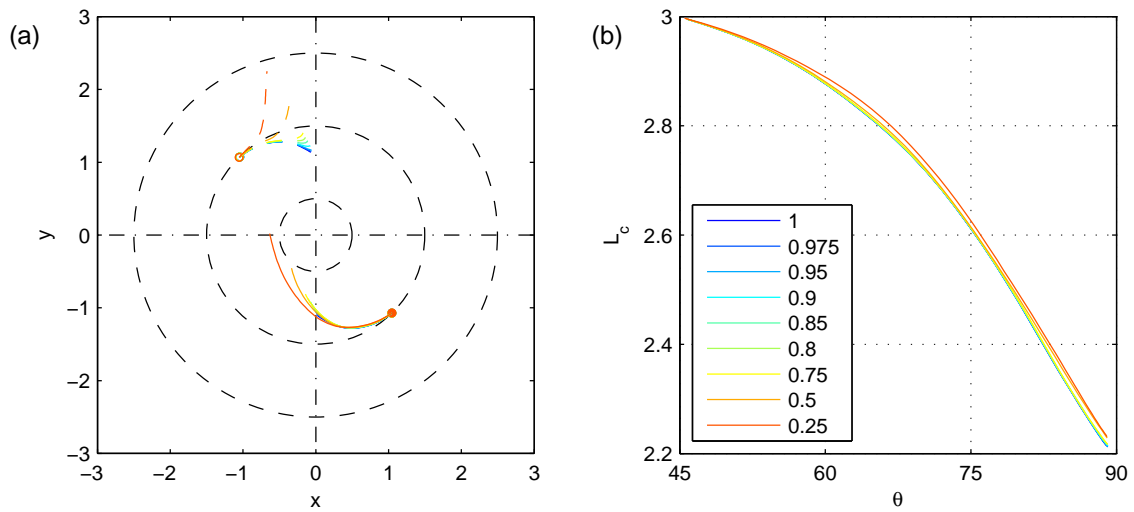


Figure 7.14: (a) Trajectory of disc one (continuous) and disc two (dashed) for $\theta_i = 45^\circ$ with different disc-to-disc permittivity ratios; (b) center-to-center separation distance with respect to angle.

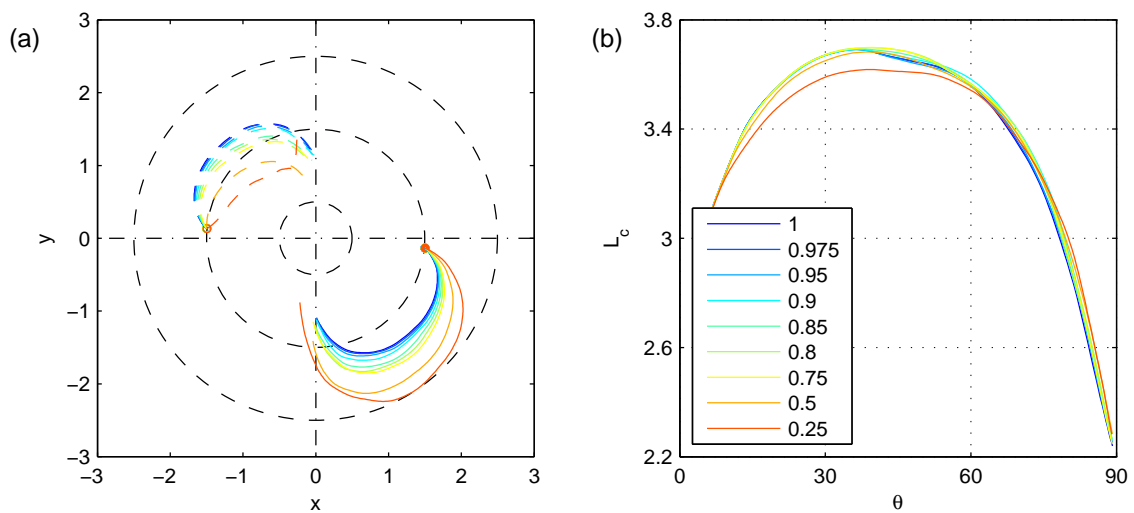


Figure 7.15: (a) Trajectory of disc one (continuous) and disc two (dashed) for $\theta_i = 5^\circ$ degrees starting angle with different disc-to-disc permittivity ratios; (b) center-to-center separation distance with respect to angle.

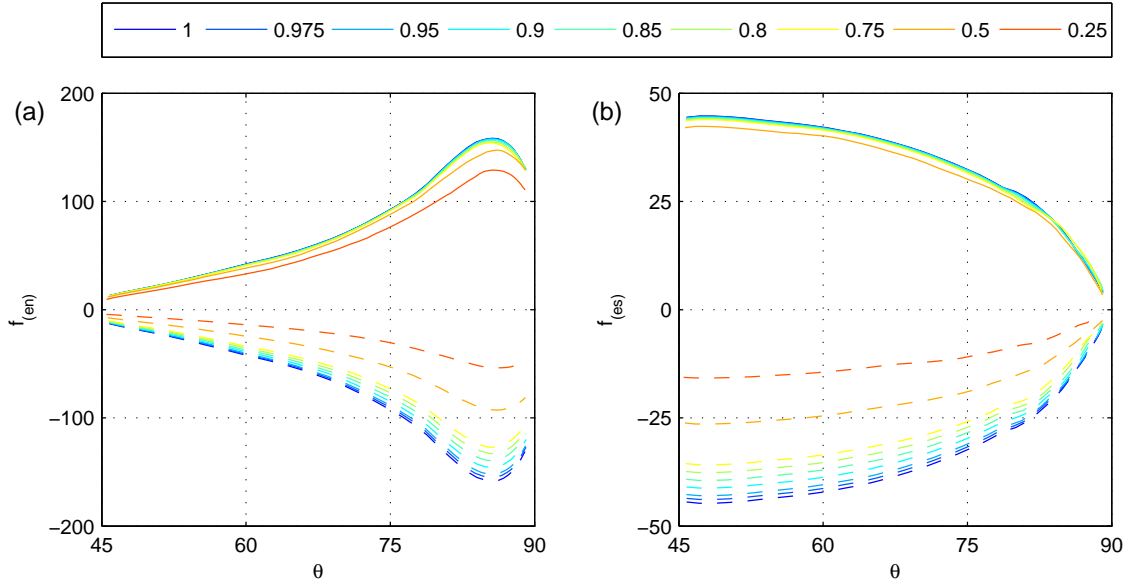


Figure 7.16: Center-to-center (a) and rotational (b) components of electric forces with respect to angle for different disc-to-disc permittivity ratios at $\theta_i = 45^\circ$.

vicinity of disc one, indirectly affecting it. On the other hand, disc two sees the combined effect of changing field intensity and reduction in permittivity gradient which ultimately reduces the magnitude of the forces exerted on it. Examining cases starting from an initial angle of 45 degrees in figure 7.16, it is evident that the resultant force at smaller \mathcal{P}_r points toward second quadrant of the computational domain which in turn causes the chaining point to skew upward and to the left of the center of the computational domain. On the other hand, the smaller force magnitude on disc two explains the shorter path taken by the disc. Similarly, the shorter path taken by disc two for cases starting at $\theta_i = 5^\circ$ is due to smaller magnitude of the force exerted on these discs. The reason for a more pronounced effect in the chaining position of 45° when compared to 5° lies in the angular span of the effective resultant force. Since discs at $\theta_i = 5^\circ$ pass the 45° mark at a larger separation, the resultant force is smaller for the majority of the angular span. The resultant force is only comparable to that of $\theta_i = 45^\circ$ in final stages of chaining. To quantify this observation, it is possible to calculate the work done by resultant forces on the middle point of the center-to-center line where chaining is supposed to happen. Case \mathcal{P}_r is used for comparison where both starting angles show some deviation from the center of the computational domain. The work done by x and y components of the resultant force and the total work for case $\theta_i = 45^\circ$ are 0.0921, 0.3815 and 0.4736 while the same components for case $\theta_i = 5^\circ$ are 0.0824, 0.3155 and 0.3979. While x components are relatively close, the difference between the y components shows that the resultant forces in case $\theta_i = 45^\circ$ is better inclined to carry the disc pair toward upper wall.

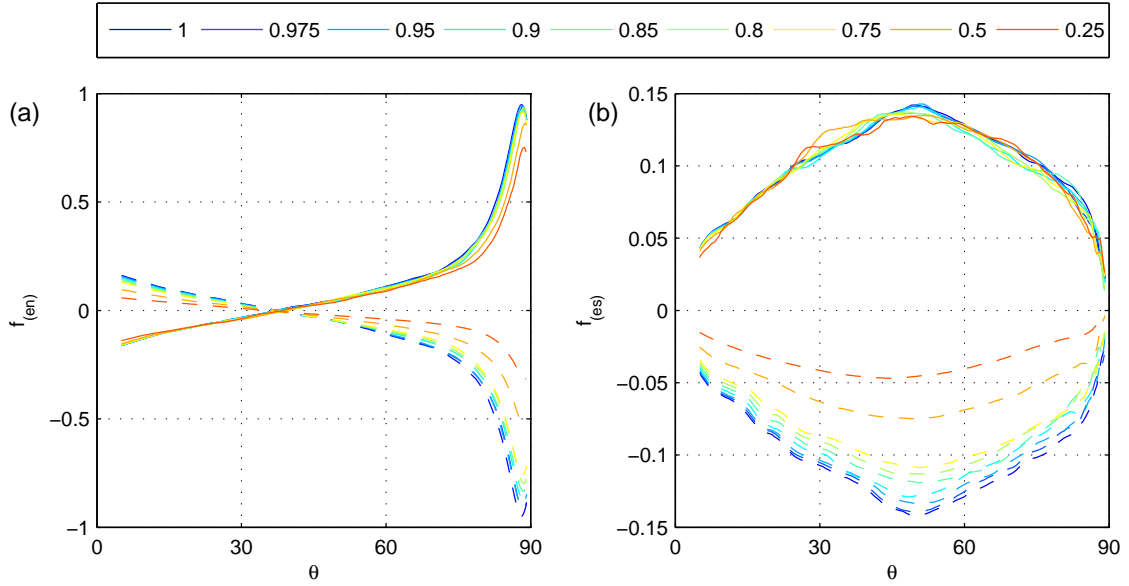


Figure 7.17: Center-to-center (a) and rotational (b) components of electric forces with respect to angle for different disc-to-disc permittivity ratios at $\theta_i = 5^\circ$.

7.3.5 The effect of difference in disc diameters

In this section, the interactions between discs of different sizes are investigated. The discs are arranged in both 45 and 5 degrees starting angles and Re and \mathcal{P} are set to 0.113 and 40, respectively while approximately 22500 particles are used to discretize the computational domain. To change the ratio of radii, the radius of disc two is increased such that $\mathcal{R}_r = 1.0, 1.5, 2.0, 2.5$ and 3.0 while the domain size and the radius of disc one are kept constant. Since the discs are positioned such that their surfaces have equal distance from the center of the computational domain, the center of disc two will be further away when compared to disc one. Since center-to-center separation will be different for each \mathcal{R}_r , the results are presented in terms of surface-to-surface separation L_s , when applicable. All simulations are carried out until $\theta = 89^\circ$ and the corresponding dimensionless times for each case at 45° are 10.77, 9.35, 8.21, 8.83 and 10.20. For the starting angle of 5 degrees, the times of reaching $\theta = 89^\circ$ are 39.39, 41.67, 24.64, 29.18, and 34.29.

Figures 7.18 and 7.19 plot the trajectory and surface-to-surface separation distance of the discs. When $\mathcal{R}_r \leq 1.5$, disc one turns toward the center of the computational domain as the discs approach for chaining. The chaining point is skewed toward the starting position of the larger disc. The surface-to-surface separation remains almost identical for $\theta_i = 45^\circ$ while it increases for larger \mathcal{R}_r when starting angle is set to 5 degrees. On the other hand, for $\mathcal{R}_r \geq 2.0$, the larger disc tends to move toward the upper wall and away from the smaller disc. Surface-to-surface separation decreases significantly for $\theta_i = 45^\circ$ after $\mathcal{R}_r = 2$, however, it remains almost constant for larger values. In the case of $\theta_i = 5^\circ$, a similar drop in L_s is observed, however, the maximum surface-to-surface

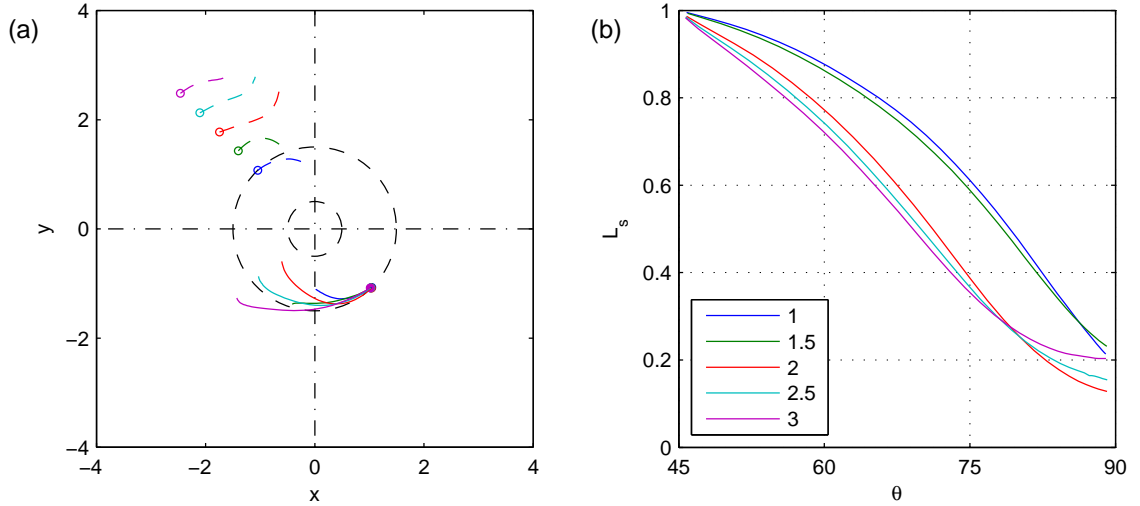


Figure 7.18: (a) Trajectory of disc one (continuous) and disc two (dashed) for $\theta_i = 45^\circ$ with different radii; (b) center-to-center separation distance with respect to angle.

separation increases as ratio of radii increases beyond $\mathcal{R}_r = 2$. In all cases, regardless of initial starting angle, the distance traveled by the smaller disc increases for larger \mathcal{R}_r .

Center-to-center and rotational components of the electric forces are shown in figures 7.20 and 7.21 for starting angles of 45 and 5 degrees, respectively. Both $f_{(en)}$ and $f_{(es)}$ show an increase for the smaller disc as the ratio of radii grows. This is in line with the observations made in [122] for AC electric fields and the results of [280] for DC electric fields. The transition in the behavior of the larger disc between $\mathcal{R}_r = 1.5$ and 2 is also visible here as the gap between the two cases does not follow the trend before and after $\mathcal{R}_r = 2$. The more interesting observation here is about the larger disc, *i.e.* disc two. The magnitude of both center-to-center and rotational components of the electric forces decrease as the radius of disc two increases. This could be expected since the figures are based on the volumetric force applied to particles. However, by accounting for the differences in the surface area between discs one and two, the forces applied to disc two are merely on the same order of magnitude as that exerted on disc one. In fact, the attractive forces on disc one become larger than that of disc two for $\mathcal{R}_r = 2$ causing the resultant force on the disc pair to point toward upper wall. The decrease in $f_{(en)}$ and $f_{(es)}$ applied to the larger disc may be attributed to the changes in the electric field distortion pattern. As the radius of disc two grows, its scale becomes comparable to that of the computational domain. This causes interaction with the walls as well as disc one. A larger radius means the ratio of disc two's surface facing disc one becomes smaller. This reduces the ratio of dielectrophoretic force to the surface area due to proximity with the smaller disc. On the other hand, if the larger disc is of comparable scale with the computational domain, the portion of the disc interacting with the wall remains constant regardless of its radius. This

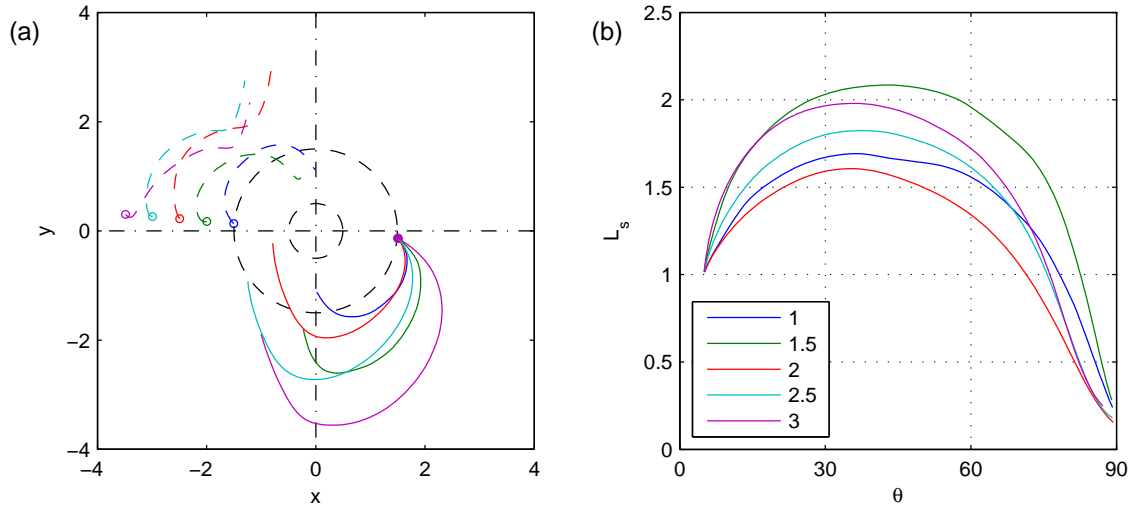


Figure 7.19: (a) Trajectory of disc one (continuous) and disc two (dashed) for $\theta_i = 5^\circ$ with different radii; (b) center-to-center separation distance with respect to angle.

means that a larger disc moves slower toward the wall. As a result, the disc pair is slower in moving toward the upper wall for larger ratios of radii after the transition in $\mathcal{R}_r = 2$ (figures 7.22 and 7.23). The difference in path length followed by each disc is also due to the similar magnitude of forces applied on discs of different sizes [122, 280].

7.4 Sedimentation of an elliptic disc in external electrical field

In this section, the sedimentation of an elliptic disc subject to an external electric field will be examined. The elliptic shape is of particular interest in biological systems. It is known that elliptic discs may exhibit complex motions while descending in quiescent fluid and interacting with bounding walls in the absence of an electric field [231]. The presence of the electric field may provide an additional parameter to influence the motion and possibly control it. To better understand the motion, a series of simulations are carried out here. First, the behavior of a neutrally buoyant ellipse in quiescent fluid is investigated. To enable longer simulations, the shifting boundary condition in the absence of the electric field is tested. Finally, the sedimentation of the ellipse with different electrical and boundary configurations is tested and the results are compared.

7.4.1 Ellipse Alignment in Electric Field

Alignment of elliptic particles with the external electric field is observed in experiments [257] and simulations [257, 281]. When left in quiescent fluid, the major axis of the ellipse becomes parallel to the external electric field. The schematic of the case is similar to the

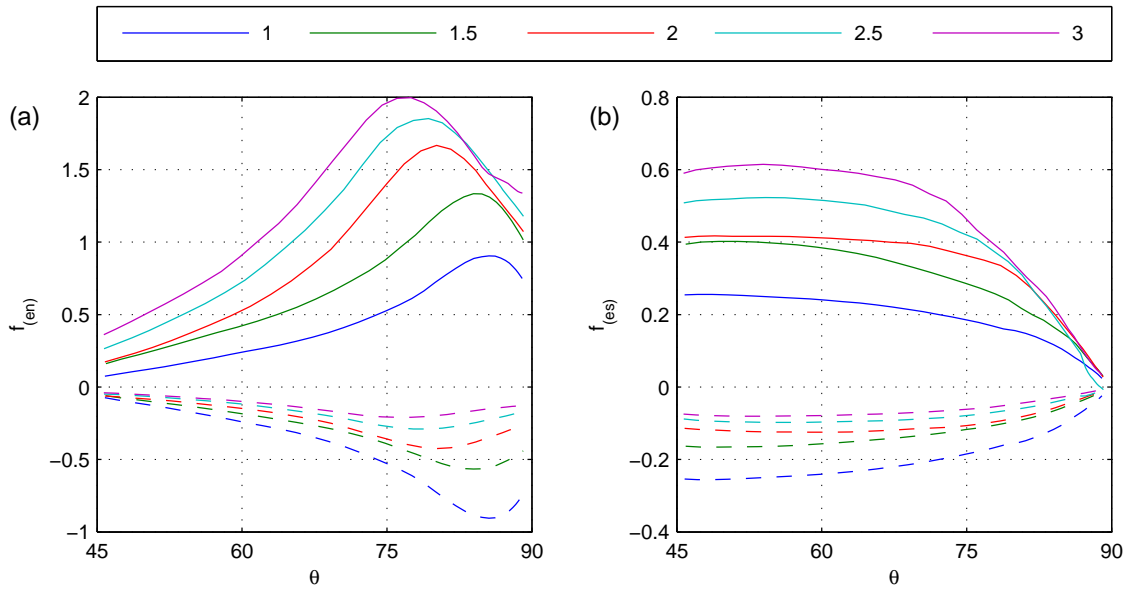


Figure 7.20: Center-to-center (a) and rotational (b) components of electric forces with respect to angle for different disc radii at $\theta_i = 45^\circ$.

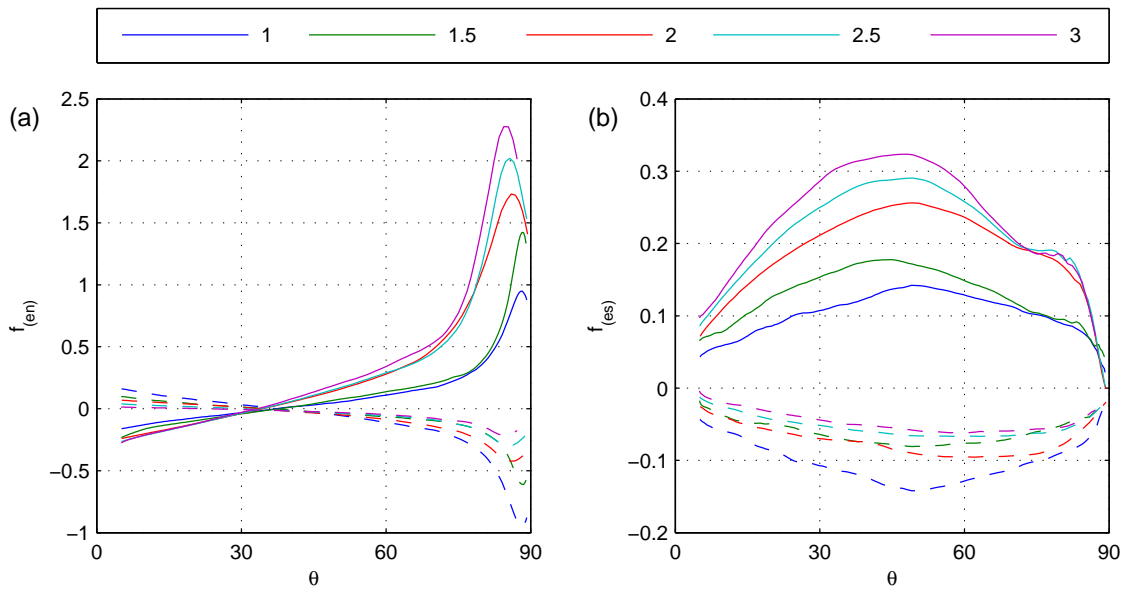


Figure 7.21: Center-to-center (a) and rotational (b) components of electric forces with respect to angle for different disc radii at $\theta_i = 5^\circ$.

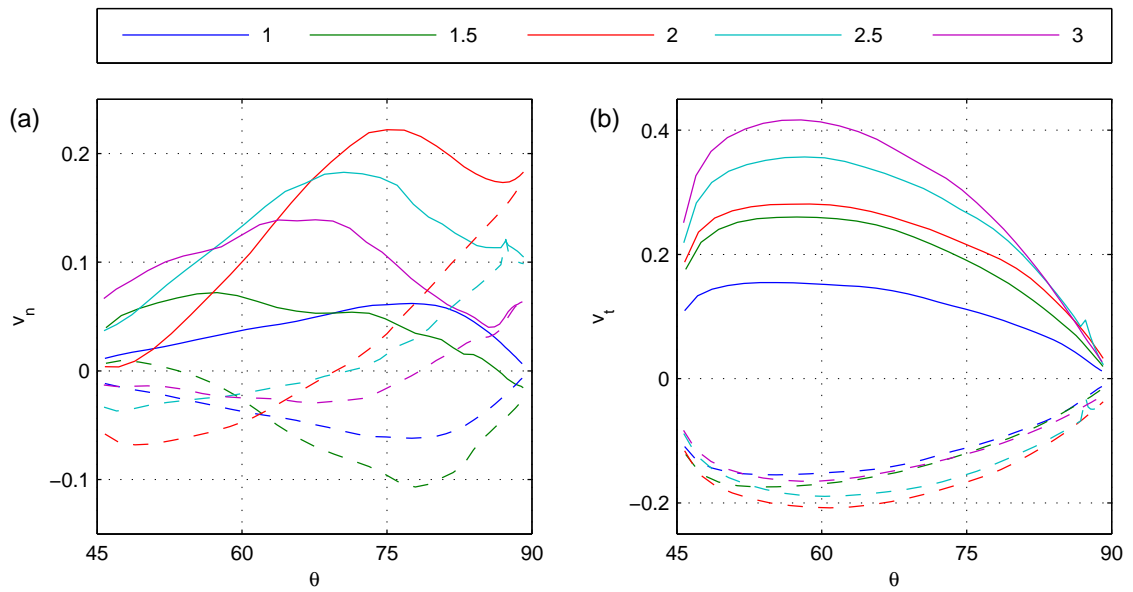


Figure 7.22: Center-to-center (a) and rotational (b) components of velocity with respect to angle for different disc radii at $\theta_i = 45^\circ$.

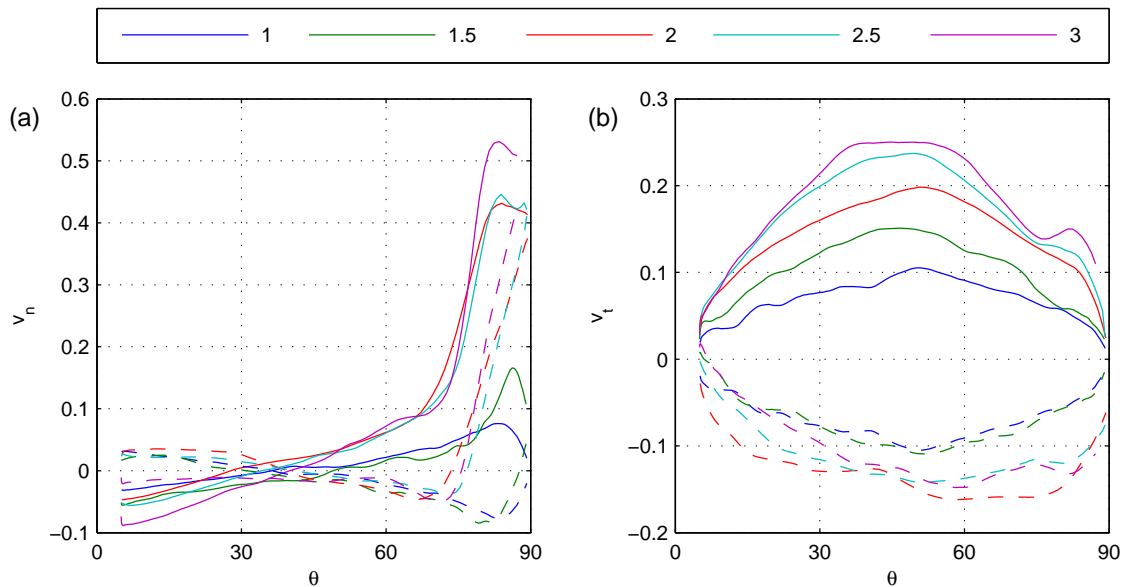


Figure 7.23: Center-to-center (a) and rotational (b) components of velocity with respect to angle for different disc radii at $\theta_i = 5^\circ$.

one provided in figure 6.1-e. To observe this effect, the elliptic particle is pinned at the middle of a rectangular box ($H = W$) with $H/a = 4$. Two sets of permittivity ratio and conductivity ratio pairs of (10, 20) and (20, 0.1) are used and will be referred to as cases S and U, respectively. The significance of the electrical parameters chosen is that the former has $\tau_s < \tau_f$ while the latter has $\tau_s > \tau_f$. Characteristic velocity of this case is $u_c = \varepsilon_f (E_\infty H)^2 / \mu_f a$ [108]. Reynolds and Electroinertial numbers are tied as $Ei = Re (H/a)^2$ and are set to 0.4 and 6.4, respectively.

This means that the electrical forces resist rotation for case S while the situation for case U is more complex.

Five initial orientations of 0° , 22.5° , 45° , 67.5° and 90° are simulated and the orientation of the ellipse with respect to time is plotted in figure 7.24. When released from rest, the ellipse starts to rotate in counterclockwise direction to align its major axis with the electric field. As the ellipse rotates, it passes the alignment angle at least once before returning to the 90° mark. Comparing the two sets of parameters, the ellipse remains stationary in case S after achieving the alignment while it continues to oscillate in case U even after the deviations become smaller than one degree. This is due to the electric force distribution across the surface of the ellipse. In case S, the distribution is such that the torque generated due to deviation from 90 degrees helps with the realignment of the ellipse. In case of U, there is a race between two opposing torques. The first component, mainly due to $\mathbf{f}_{(eq)}$, is applied to the tips and resists the alignment. The other component, mainly exerted by $\mathbf{f}_{(ep)}$, is applied to the sides of the ellipse and enforces the alignment. At exact alignment, no torque is applied to the ellipse. However, slight perturbations are inevitable and this results in the back and forth motion seen in case U which is caused by the interaction of the opposing torques. As expected, the ellipse at 90° which is already aligned with the electric field does not rotate in case S and merely oscillates in case U. The ellipse at 0° starts its rotation only after the other cases are aligned with the electric field. This is an expected behavior as the 0° is an unstable equilibrium position and a slight numerical asymmetry may disturb the balance, causing the ellipse to rotate. This behavior is also reported in BEM simulations [281]. It is notable that case U starts its rotation from the 0° starting angle before case S.

7.4.2 Validation of the shifting boundary condition

A sedimenting ellipse is likely to move in a periodic manner. However, the period of such motion may be very long and the effects of bounding walls may be substantial. As such, the long-term simulation of the sedimentation of the elliptic particle may be necessary for observing the periodic motion in some cases. There are two common methods for the long-term simulation of the sedimenting bodies in a confined computational domain. The first one is the moving reference frame method, where the reference frame is fixed to the

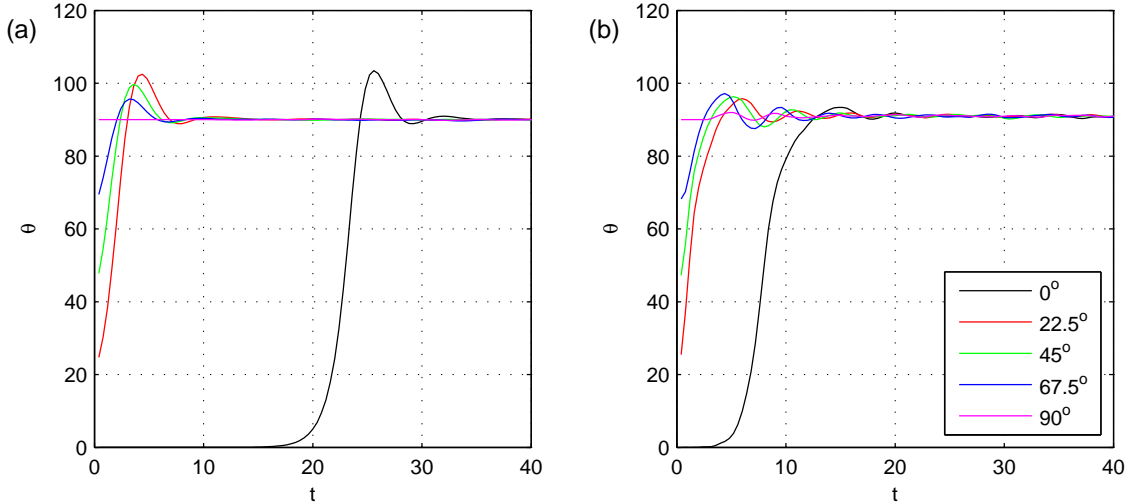


Figure 7.24: Orientation of the elliptic disc with different initial starting angles while aligning with the electric field for case S (a) and case U (b). The electric field is oriented at 90° (vertical).

Table 7.2: Configurations for testing the shifting boundary condition.

Case	A	B	C	D
Top and bottom	No-slip	Shifting	No-slip	Shifting
Side walls	No-slip	No-slip	Periodic	Periodic

moving body and momentum equations and domain boundaries are modified so that the computational domain is following the object. This method requires proper resolution of the bounding walls, prior estimate of the velocity of the rigid body and an accurate choice for the acceleration of the frame of reference. The second method is the shifting boundary condition proposed in section 3.4, which avoids the need for any *a priori* knowledge of the motion and is exceptionally suitable for particle methods. In order to facilitate the simulation of long term sedimentation and observing the periodic motion of the ellipse, the shifting boundary condition is used here.

Since the motion of the ellipse without electric field is well studied, the method is tested in the absence of an external electric field. The configuration is similar to the one given in section 6.3 with $\mathcal{D} = 1.1$, $\text{Re} = 58.8$, $a/b = 2$, $W/a = 4$, $h/d = 34$ and $\theta = \pi/4$. Computational domain is given in figure 6.1-e and is discretized by 80035 particles. The combination of the boundary conditions used here are given in table 7.2.

In most cases, the effects of top and bottom walls should not contaminate the results and the simulations are terminated before wall effects appear. However, the effects of side walls are unavoidable in sedimentation in confined domains and are sometimes studied deliberately [231]. In this sense configurations A-B and C-D are paired for comparison. It is expected that cases B and D behave similar to cases C and D as long as the ellipse is far from the bottom wall. Figure 7.25 plots the horizontal position and orientation of

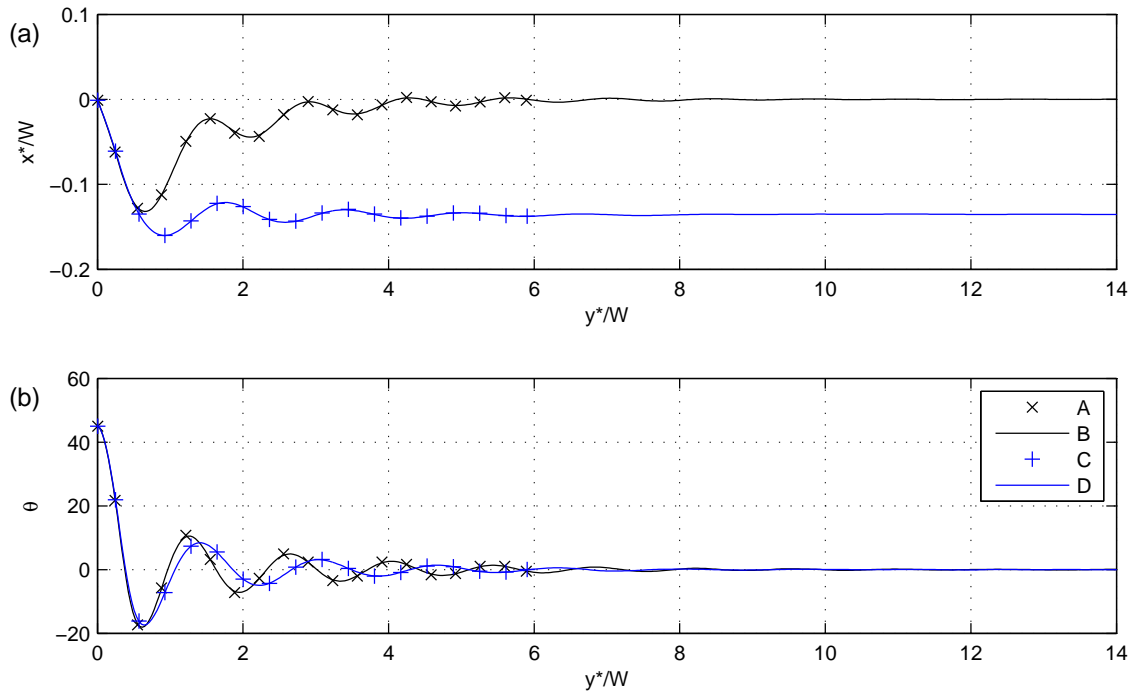


Figure 7.25: Horizontal position (a) and orientation (b) of the elliptic disc while sedimenting.

the particle with respect to its vertical position. Cases A and C reach the bottom wall at $y^*/W = 6$ while cases B and D may continue indefinitely. The agreement between A-B and C-D pairs is excellent and this means that from a hydrodynamic point of view, the implementation of the shifting boundary has no effect on the sedimentation. It is worth mentioning that in all cases, the ellipse comes to a horizontal orientation while its position is dependent on the side wall boundary condition. With a no-slip wall, the hydrodynamic forces move the ellipse toward the center of the domain while in periodic configuration, the ellipse is settle further away from its starting horizontal position. The Reynolds number based on terminal velocity, Re_t , is equal to 13.5 and 14.4 for A-B and C-D pairs, respectively. As expected, this shows that the ellipse descends slower in confined domain due to wall effects.

7.4.3 The effect of boundaries on the sedimentation of the elliptic particle subject to an external electric field

The introduction of the electrical field may significantly alter the behavior of the ellipse sedimenting in quiescent fluid. To test such effects, the parameter sets studied in section 7.4.1 are combined with the boundary configurations used in section 7.4.2. Additional boundary conditions are required to solve the electrical potential. A constant potential difference of $\Delta\phi$ is applied to the top and bottom walls for all configurations while the side walls have different boundaries depending on the hydrodynamic configuration. For

Table 7.3: Terminal Reynolds number Re_t for cases S and U for different boundary configurations. When no electric field is applied $Re_t = 13.5$ (cf. table 6.5).

Case	A	B	C	D
S	19.8	19.6	20.4	20.4
U	17.6	8.6	9.95	10.05

configurations A and B no field lines pass through the side walls while in configurations C and D, the side walls are periodic. Reynolds number is set to 58.8 while Electro-inertial, $Ei = \rho_f g d / \varepsilon_f E_\infty^2$, is equal to 27.7.

Figures 7.26 and 7.27 provide horizontal position and orientation of the ellipse versus its vertical position for electrical properties of S and U, respectively. For case S, the ellipse aligns itself with the electric field almost instantly, regardless of the boundary configuration, with cases A-B and C-D following the same trajectory. The alignment with the electric field is in line with the stable behavior observed in quiescent fluid in figure 7.24-a. When side walls are present, *i.e.* configurations A and B, the ellipse moves slowly toward the center of the computational domain whereas in configurations C and D, the ellipse remains to the right of its starting horizontal position. It is worth noting that the early horizontal deviation in electrified cases is in the opposite direction of the cases without the electric field. Unlike case S, case U shows remarkably different trajectories with different boundary configurations. While cases CU and DU behave similarly with a periodic motion, cases AU and BU are completely unrelated. This shows that the electrical boundaries have notable effects when there is a race between $\mathbf{f}_{(ep)}$ and $\mathbf{f}_{(eq)}$, as described in section 7.4.1. Cases CU and DU follow a periodic trajectory to the left of their starting position and rotate up to ten degrees around the flat orientation. Case BU follows a periodic motion of equal horizontal distance and angular span to that of CU and DU at a higher frequency in the center of the channel. Unlike others, case AU does not follow a periodic trajectory and stays mostly in an upright orientation. It moves back and forth near the left wall before changing direction in $y^*/W = 4$ and heading toward the right wall. Table 7.3 provides Re_t for all cases. For oscillating cases, the average vertical velocity is used instead of the terminal velocity in computation of Re_t . In agreement with the observations made above, cases AS-BS and CS-DS have similar terminal Reynolds numbers. For case U, the oscillatory motion reduces the descent velocity resulting in smaller Re_t . As expected, cases CU and DU have similar terminal Reynolds numbers while the largest Re_t belongs to AU which descends in a mostly upright orientation.

To explore the effects of the electrical forces on the motion of case S in more detail, figures 7.28 and 7.29 provide the torques and horizontal component of the forces applied to the ellipse during its descent. The electrical force and torque are computed directly from the electrical forces applied to particles of the solid phase. Since the FSI coupling technique used here does not provide an explicit interface for the solid body, the hydrody-

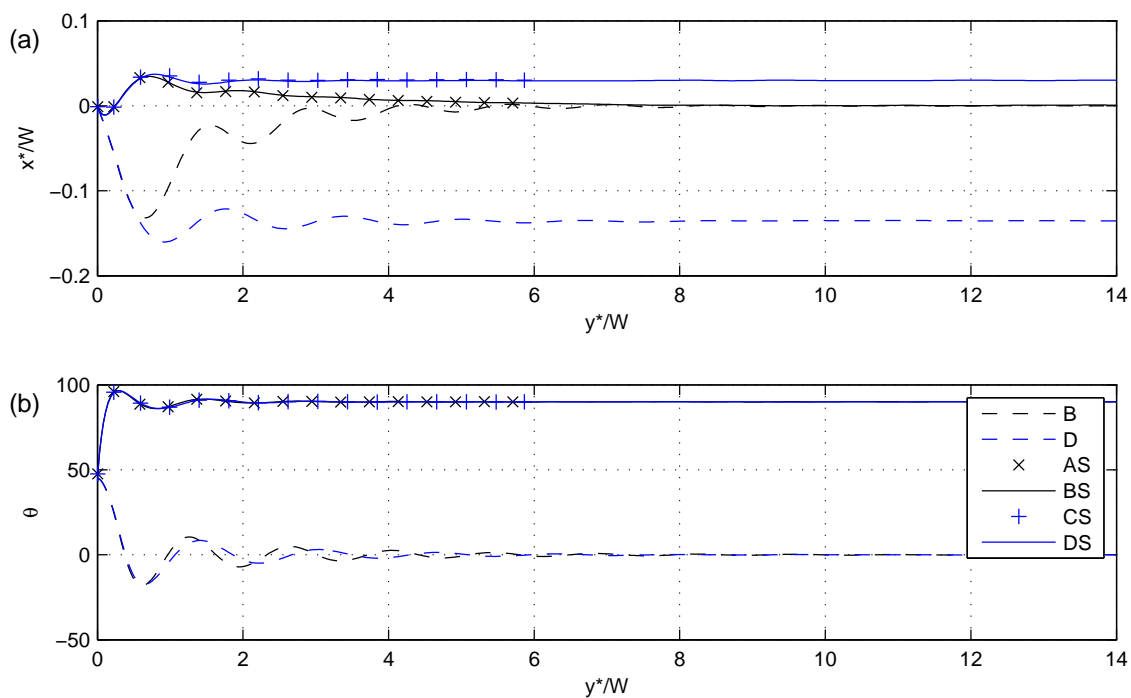


Figure 7.26: Horizontal position (a) and orientation (b) of the elliptic disc of case S while sedimenting in an external electric field.

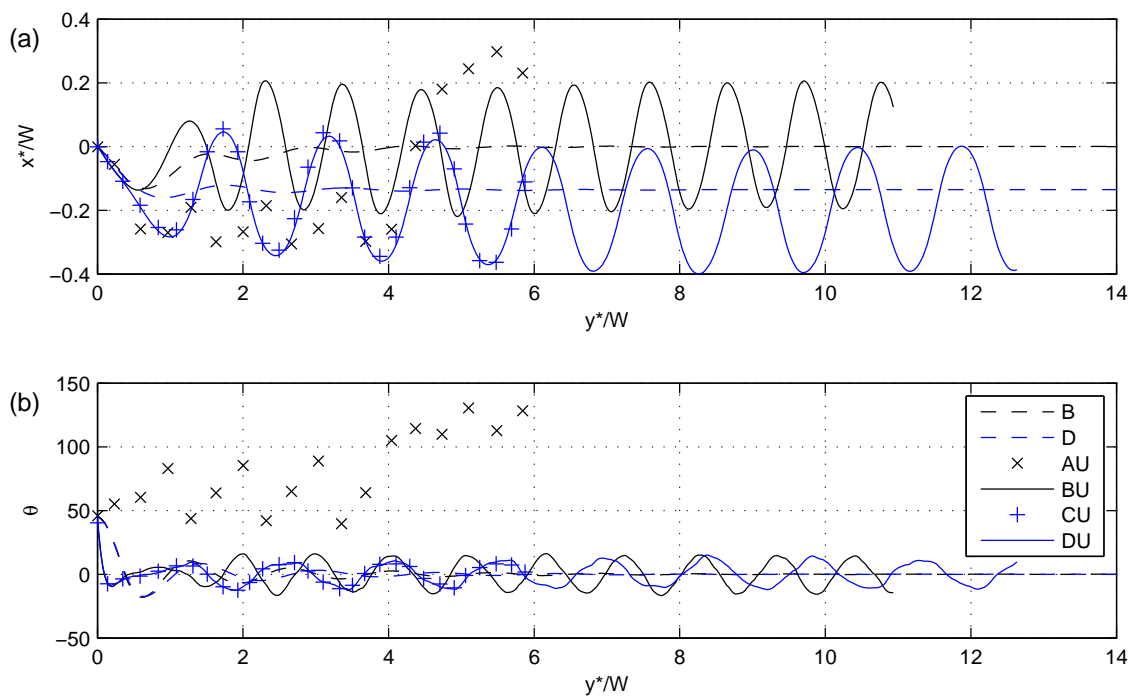


Figure 7.27: Horizontal position (a) and orientation (b) of the elliptic disc of case U while sedimenting in an external electric field.

namical parts are found by subtracting the electrical components from the resultant torque and force applied to the body. The resultant components are calculated using the position and orientation of the ellipse in time. The results are smoothed using a Gaussian filter to remove spurious oscillations.

The differences between case AU and other cases are apparent in both torque and forces exerted on it. Having both side and top boundaries in its vicinity, the ellipse behaves similar to case U of section 7.4.1. This means that the initial electrical torque turns the ellipse in counter-clockwise direction to align it with the electric field. The hydrodynamic torque is comparable but smaller than the electrical counterpart and the ellipse maintains its orientation. This causes it to approach the left wall where it is deflected due to electrical forces ($y^*/W \approx 0.75$). While descending near the wall from $y^*/W \approx 1$ to 4, the electric torque encourages a flat orientation whereas the hydrodynamic torque opposes it. The ellipse gets closer to the left wall progressively with each approach and this reduces the hydrodynamic forces pushing it toward the wall. At $y^*/W \approx 4$, the ellipse breaks off the left wall and heads toward the opposing wall. While passing the middle of the channel, the electrical and hydrodynamical forces become negligible. At this position, electrical torque encourages a counter-clockwise rotation while a slightly larger hydrodynamical torque resists it. After $y^*/W \approx 5$, the bottom wall affects the simulation.

Despite sharing the same side wall configuration with case AU, replacing top and bottom boundaries with shifting walls changes the electrical effects exerted on case BU significantly. Throughout its motion, the electrical torque remains the dominant term and dictates both rotation and horizontal position. Initially, the electrical torque turns the ellipse toward a flat position while the hydrodynamic torque resists it. The electrical torque is clockwise for positive angles and counter-clockwise for negative angles. Electrical and hydrodynamic forces are in agreement and act to move the ellipse away from the wall. The period of both forces are similar with electrical component lagging behind the hydrodynamical part.

Cases CU and DU act in a similar fashion. Since the ellipse lies at the proximity of only one set of electrical boundaries, the initial electrical response is similar to that of the case BU. The electrical and hydrodynamical torques alternate as the ellipse pivots around its flat orientation. The torques oppose each other with the electrical torque as the dominant component. On the other hand, the dominant force term is the hydrodynamic component. Although there are no side walls to induce electrical forces in the horizontal direction, the domain width is small enough for the periodic boundary to make an effect. The ellipse interacts with itself through the periodic boundary and as the symmetry breaks a horizontal force is exerted on the ellipse. The electrical force points in the negative direction for positive angles and in positive direction for negative angles. This means that the ellipse is electrically forced to the left for positive angles and to the right for negative angles, which is also in line with hydrodynamic tendency of the ellipse. As a result, electrical

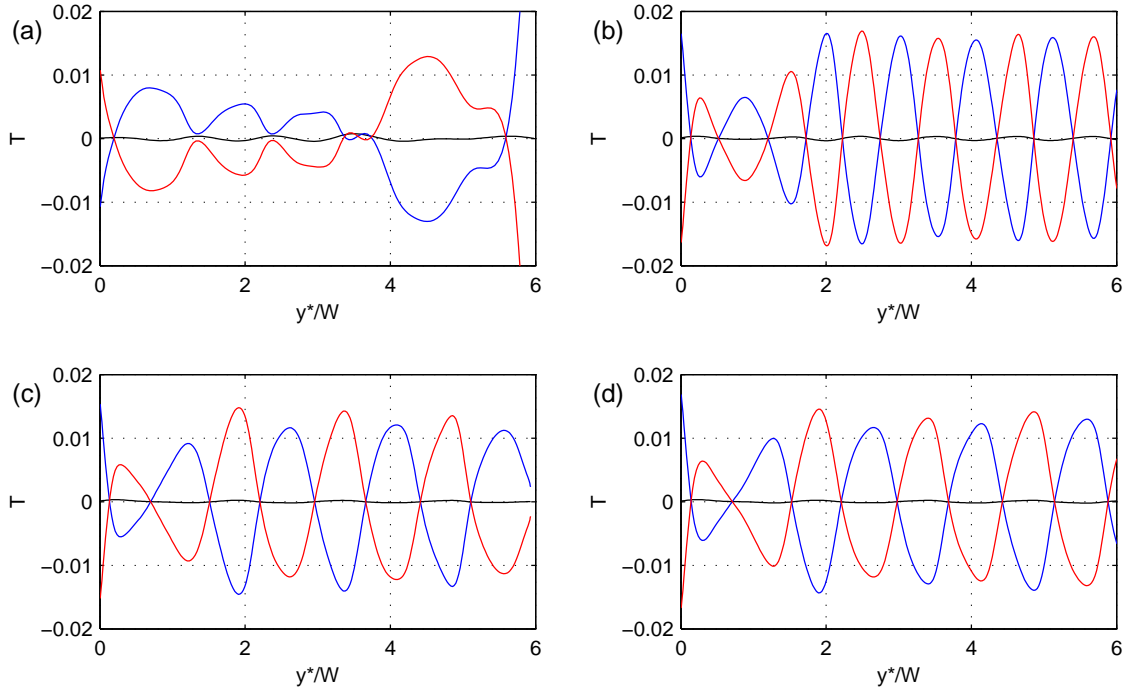


Figure 7.28: Hydrodynamic torque (blue), electric torque (red) and resultant torque applied to the ellipse of case U with boundary configurations of A (a), B (b), C (c) and D (d) while sedimenting in an external electric field. A positive value induces a counter-clockwise rotation.

and hydrodynamical forces have the same period with the electrical part slightly lagging behind.

7.5 Remarks

The individual elements of the scheme proposed and tested in previous chapters are combined together to investigate three different cases in electrostatic fluid-structure/solid interaction involving dielectrophoresis.

The first case shows the effects of electric field on the motion of a circular particle in proximity of the channel walls in simple shear. Depending on its electrical properties, the disc may approach the wall or channel center. This is in line with the relationship between electrical timescales of the background fluid and the disc.

The second case covers the interaction between two particles suspended in quiescent fluid. When subject to an external electric field, the particles align in the direction of the electric field while approaching each other. The effect of initial angle, electric field intensity, permittivity ratio and disc radii on the trajectories of the particles are investigated. The results are in qualitative agreement with those found in the literature.

The third case involves the sedimentation of an elliptic particle subject to different boundary conditions. The shifting boundary condition is tested for non-electrified sedi-

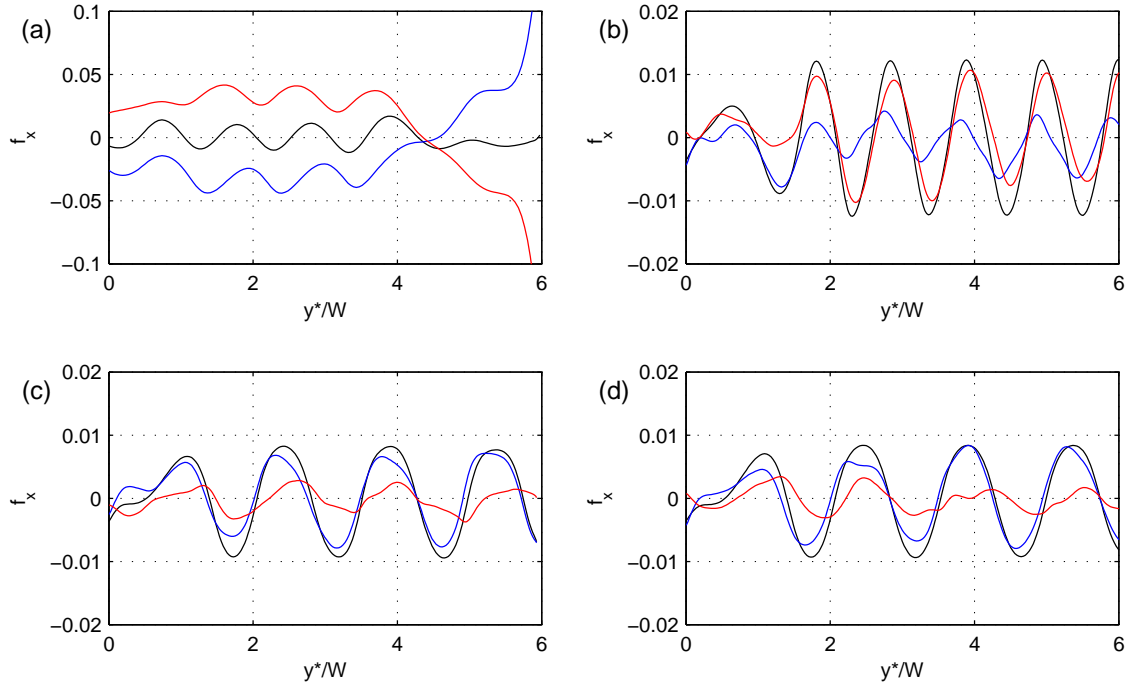


Figure 7.29: Horizontal component of hydrodynamic force (blue), electric force (red) and resultant force applied to the ellipse of case U with boundary configurations of A (a), B (b), C (c) and D (d) while sedimenting in an external electric field. A positive value moves the ellipse to the right.

mentation and it is shown that there are no effects on the hydrodynamic behavior of the elliptic disc due to the shifting boundary. Using the shifting boundary condition, long-term simulations of the sedimentation in finite computational domains becomes possible. The simulations in the presence of the electric field are carried out for two sets of electrical properties and four different boundary configurations. The results show that both electrical properties and the boundaries have significant effects on the trajectory of the sedimentation.

The cases considered in this chapter show the role of the electric field in controlling the motion of particles in fluids and the possibility of manipulating their motion through electrical properties. There are relatively few numerical studies dealing with such cases and those simulated using SPH are sparse. This chapter proves the capability of the proposed ISPH scheme in handling this class of phenomena and paves the way for its future use.

Chapter 8

Conclusion

An incompressible smoothed particle hydrodynamics method for modeling immiscible and isothermal flow of two- and three-phase Newtonian fluids has been developed. Surface tension coefficients are decomposed into phase specific coefficients and implemented in continuum surface force framework. Each phase is assigned to a unique color function which is then smoothed out to compute surface normals, curvature and surface tension as well as interpolating electrical and thermodynamic properties of the fluids. Perfect and leaky dielectric models are used to describe the electrical state of the system. A fluid-structure/solid interaction scheme based on viscous penalty method is coupled with rigidity constraints to simulate the motion of rigid particles submerged in Newtonian fluids.

The equations are discretized using SPH differential operators corrected for inconsistencies in particle distribution while the artificial particle displacement has been employed to ensure uniform spread of the particles throughout the computational domain. Linked list algorithm is used for establishing neighborhood relationship between the particles while ghost particle method is used to impose the boundary conditions. The projection method is used to advance the governing equations of the flow and electric field in time.

The multiphase component of the flow is tested by simulating the formation of a lens shape, levitation of a droplet as well as spreading of a droplet on a flat surface. The results show the importance of particle arrangement in certain test cases as well as the success of the proposed scheme in handling two- and three-phase flows. The multiphase treatment developed is used as a basis for the addition of the electrostatic and fluid-structure/solid interaction components.

The electrohydrodynamic component is used to simulate Rayleigh-Taylor instability as a basic test case combining capillary, viscous and gravitational forces. The fluids are assumed to be leaky dielectrics and the effects of electrical properties as well as electric field intensity on the evolution of the instability is investigated in detail.

The proposed fluid-structure/solid interaction component is tested for several configurations of moving rigid particles in Newtonian fluids. Translational motion, rotational motion and their combination are tested separately to fully address the suitability of the

method. The simulation results within the range of parameters used in this study are found to be in quantitative agreement with literature data.

The combination of the individual elements of the numerical method is used to simulate the motion of rigid particles submerged in Newtonian fluids subject to an external electric field. The behavior of the particles are found to be in agreement with experimental and numerical observations found in the literature. This shows the applicability of the proposed ISPH scheme in simulating such complex phenomena and paves the way for further investigation of this relatively unexplored field in computational fluid dynamics.

Bibliography

- [1] C. W. Hirt, B. D. Nichols, Volume of fluid (VOF) method for the dynamics of free boundaries, *J. Comput. Phys.* 39 (1981) 201–225.
- [2] J. Lopez, J. Hernandez, P. Gomez, F. Faura, An improved PLIC-VOF method for tracking thin fluid structures in incompressible two-phase flows, *J. Comput. Phys.* 208 (2005) 51–74.
- [3] E. G. Puckett, A. S. Almgren, J. B. Bell, D. L. Marcus, W. J. Rider, A high-order projection method for tracking fluid interfaces in variable density incompressible flows, *J. Comput. Phys.* 130 (1997) 269–282.
- [4] N. Ashgriz, J. Y. Poo, FLAIR - flux line-segment model for advection and interface reconstruction, *J. Comput. Phys.* 93 (1991) 449–468.
- [5] W. J. Rider, D. B. Kothe, Reconstructing volume tracking, *J. Comput. Phys.* 141 (1998) 112–152.
- [6] M. Rudman, Volume-tracking methods for interfacial flow calculations, *Int. J. Numer. Methods Fluids* 24 (1997) 671–691.
- [7] S. Sikalo, H. D. Wilhelm, I. V. Roisman, S. Jakirlic, C. Tropea, Dynamic contact angle of spreading droplets: Experiments and simulations, *Phys. Fluids* 17 (2005) 062103.
- [8] S. F. Lunkad, V. V. Buwa, K. D. P. Nigam, Numerical simulations of drop impact and spreading on horizontal and inclined surfaces, *Chem. Eng. Sci.* 62 (2007) 7214–7224.
- [9] G. Strotos, G. Aleksis, M. Gavaises, K.-S. Nikas, N. Nikolopoulos, A. Theodorakakos, Non-dimensionalisation parameters for predicting the cooling effectiveness of droplets impinging on moderate temperature solid surfaces, *Int. J. Therm. Sci.* 50 (2011) 698–711.
- [10] N. Nikolopoulos, A. Theodorakakos, G. Bergeles, A numerical investigation of the evaporation process of a liquid droplet impinging onto a hot substrate, *Int. J. Heat Mass Transfer* 50 (2007) 303–319.
- [11] P. R. Gunjal, V. V. Ranade, R. V. Chaudhari, Dynamics of drop impact on solid surface: Experiments and VOF simulations, *AIChE J.* 51 (2005) 59–78.
- [12] M. Bussmann, S. Chandra, J. Mostaghimi, Modeling the splash of a droplet impacting a solid surface, *Phys. Fluids* 12 (2000) 3121–3132.
- [13] I. V. Roisman, L. Opfer, C. Tropea, M. Raessi, J. Mostaghimi, S. Chandra, Drop impact onto a dry surface: Role of the dynamic contact angle, *Colloids Surf., A* 322 (2008) 183–191.
- [14] I. Malgarinos, N. Nikolopoulos, M. Gavaises, Coupling a local adaptive grid refinement technique with an interface sharpening scheme for the simulation of two-phase flow and free-surface flows using VOF methodology, *J. Comput. Phys.* 300 (2015) 732–753.

- [15] S. Osher, J. A. Sethian, Fronts propagating with curvature-dependent speed - algorithms based on Hamilton-Jacobi formulations, *J. Comput. Phys.* 79 (1988) 12–49.
- [16] K. Yokoi, D. Vadillo, J. Hinch, I. Hutchings, Numerical studies of the influence of the dynamic contact angle on a droplet impacting on a dry surface, *Phys. Fluids* 21 (2009) 072102.
- [17] E. Niemi, M. Lassas, A. Kallonen, L. Harhanen, K. Hamalainen, S. Siltanen, Dynamic multi-source X-ray tomography using a spacetime level set method, *J. Comput. Phys.* 291 (2015) 218–237.
- [18] S. Osher, R. P. Fedkiw, Level set methods: An overview and some recent results, *J. Comput. Phys.* 169 (2001) 463–502.
- [19] J. A. Sethian, Evolution, implementation, and application of level set and fast marching methods for advancing fronts, *J. Comput. Phys.* 169 (2001) 503–555.
- [20] Y. Wang, S. Simakhina, M. Sussman, A hybrid level set-volume constraint method for incompressible two-phase flow, *J. Comput. Phys.* 231 (2012) 6438–6471.
- [21] P. D. M. Spelt, A level-set approach for simulations of flows with multiple moving contact lines with hysteresis, *J. Comput. Phys.* 207 (2005) 389–404.
- [22] A. Smolianski, Numerical modeling of two-fluid interfacial flows, Ph.D. thesis, University of Jyväskylä, Finland, 2001.
- [23] M. Sussman, P. Smereka, S. Osher, A level set approach for computing solutions to incompressible two-phase flow, *J. Comput. Phys.* 114 (1994) 146–159.
- [24] Y. C. Chang, T. Y. Hou, B. Merriman, S. Osher, A level set formulation of eulerian interface capturing methods for incompressible fluid flows, *J. Comput. Phys.* 124 (1996) 449–464.
- [25] M. Sussman, P. Smereka, Axisymmetric free boundary problems, *J. Fluid Mech.* 341 (1997) 269–294.
- [26] H. Zhang, L. L. Zheng, Y. Prasad, T. Y. Hou, A curvilinear level set formulation for highly deformable free surface problems with application to solidification, *Numer. Heat Transf. B-Fundam.* 34 (1998) 1–20.
- [27] H. K. Zhao, B. Merriman, S. Osher, L. Wang, Capturing the behavior of bubbles and drops using the variational level set approach, *J. Comput. Phys.* 143 (1998) 495–518.
- [28] M. Sussman, A. S. Almgren, J. B. Bell, P. Colella, L. H. Howell, M. L. Welcome, An adaptive level set approach for incompressible two-phase flows, *J. Comput. Phys.* 148 (1999) 81–124.
- [29] A.-K. Tornberg, Interface tracking methods with application to multiphase flows, Ph.D. thesis, KTH Royal Institute of Technology, 2000.
- [30] D. Caviezel, C. Narayanan, D. Lakehal, Adherence and bouncing of liquid droplets impacting on dry surfaces, *Microfluid. Nanofluid.* 5 (2008) 469–478.
- [31] T. Abadie, J. Aubin, D. Legendre, On the combined effects of surface tension force calculation and interface advection on spurious currents within Volume of Fluid and Level Set frameworks, *J. Comput. Phys.* 297 (2015) 611–636.

- [32] M. Sussman, E. Fatemi, P. Smereka, S. Osher, An improved level set method for incompressible two-phase flows, *Comput. Fluids* 27 (1998) 663–680.
- [33] M. Herrmann, A balanced force refined level set grid method for two-phase flows on unstructured flow solver grids, *J. Comput. Phys.* 227 (2008) 2674–2706.
- [34] J. Glimm, J. Grove, B. Lindquist, O. McBryan, G. Tryggvason, The bifurcation of tracked scalar waves, *SIAM J. Sci. Stat. Comp.* 9 (1988) 61–79.
- [35] I. L. Chern, J. Glimm, O. McBryan, B. Plohr, S. Yaniv, Front tracking for gas-dynamics, *J. Comput. Phys.* 62 (1986) 83–110.
- [36] G. Moretti, Computation of flows with shocks, *Annu. Rev. Fluid Mech.* 19 (1987) 313–337.
- [37] A. Esmaeeli, G. Tryggvason, Direct numerical simulations of bubbly flows. Part 2. Moderate Reynolds number arrays, *J. Fluid Mech.* 385 (1999) 325–358.
- [38] A. Esmaeeli, G. Tryggvason, Direct numerical simulations of bubbly flows. Part 1. Low Reynolds number arrays, *J. Fluid Mech.* 377 (1998) 313–345.
- [39] S. O. Unverdi, G. Tryggvason, A front-tracking method for viscous, incompressible, multi-fluid flows, *J. Comput. Phys.* 100 (1992) 25–37.
- [40] M. T. Mehrabani, M. R. H. Nobari, G. Tryggvason, Accelerating Poisson solvers in front tracking method using parallel direct methods, *Comput. Fluids* 118 (2015) 101–113.
- [41] W. C. de Jesus, A. M. Roma, M. R. Pivello, M. M. Villar, A. da Silveira-Neto, A 3D front-tracking approach for simulation of a two-phase fluid with insoluble surfactant, *J. Comput. Phys.* 281 (2015) 403–420.
- [42] G. Tryggvason, S. Dabiri, B. Aboulhasanzadeh, J. Lu, Multiscale considerations in direct numerical simulations of multiphase flows, *Phys. Fluids* 25 (2013) 031302.
- [43] W. Dijkhuizen, I. Roghair, M. V. S. Annaland, J. A. M. Kuipers, DNS of gas bubbles behaviour using an improved 3D front tracking model-Drag force on isolated bubbles and comparison with experiments, *Chem. Eng. Sci.* 65 (2010) 1415–1426.
- [44] H. Terashima, G. Tryggvason, A front-tracking/ghost-fluid method for fluid interfaces in compressible flows, *J. Comput. Phys.* 228 (2009) 4012–4037.
- [45] X. Li, K. Sarkar, Front tracking simulation of deformation and buckling instability of a liquid capsule enclosed by an elastic membrane, *J. Comput. Phys.* 227 (2008) 4998–5018.
- [46] F. S. de Sousa, N. Mangiavacchi, L. G. Nonato, A. Castelo, M. F. Tome, V. G. Ferreira, J. A. Cuminato, S. McKee, A front-tracking/front-capturing method for the simulation of 3D multi-fluid flows with free surfaces, *J. Comput. Phys.* 198 (2004) 469–499.
- [47] C. W. Hirt, A. A. Amsden, J. L. Cook, An arbitrary Lagrangian-Eulerian computing method for all flow speeds, *J. Comput. Phys.* 14 (1974) 227–253.
- [48] C. W. Hirt, A. A. Amsden, J. L. Cook, An arbitrary Lagrangian-Eulerian computing method for all flow speeds (Reprinted from the *Journal of Computational Physics*, vol 14, pg 227-253, 1974), *J. Comput. Phys.* 135 (1997) 203–216.
- [49] M. Kucharik, M. Shashkov, Conservative multi-material remap for staggered multi-material Arbitrary Lagrangian-Eulerian methods, *J. Comput. Phys.* 258 (2014) 268–304.

- [50] P. Yue, J. J. Feng, C. A. Bertelo, H. H. Hu, An arbitrary Lagrangian-Eulerian method for simulating bubble growth in polymer foaming, *J. Comput. Phys.* 226 (2007) 2229–2249.
- [51] F. Montefusco, F. S. Sousa, G. C. Buscaglia, High-order ALE schemes for incompressible capillary flows, *J. Comput. Phys.* 278 (2014) 133–147.
- [52] D. C. Lo, D. L. Young, Arbitrary Lagrangian-Eulerian finite element analysis of free surface flow using a velocity-vorticity formulation, *J. Comput. Phys.* 195 (2004) 175–201.
- [53] T. J. R. Hughes, W. K. Liu, T. K. Zimmermann, Lagrangian-Eulerian finite-element formulation for incompressible viscous flows, *Comput. Meth. Appl. Mech. Eng.* 29 (1981) 329–349.
- [54] B. Ramaswamy, Numerical-simulation of unsteady viscous free-surface flow, *J. Comput. Phys.* 90 (1990) 396–430.
- [55] B. Ramaswamy, M. Kawahara, Arbitrary Lagrangian-Eulerian finite-element method for unsteady, convective, incompressible viscous free-surface fluid-flow, *Int. J. Numer. Methods Fluids* 7 (1987) 1053–1075.
- [56] R. Glowinski, T. W. Pan, A. J. Kearsley, J. Periaux, Numerical simulation and optimal shape for viscous flow by a fictitious domain method, *Int. J. Numer. Methods Fluids* 20 (1995) 695–711.
- [57] R. Glowinski, T. W. Pan, T. I. Hesla, D. D. Joseph, J. Periaux, A fictitious domain approach to the direct numerical simulation of incompressible viscous flow past moving rigid bodies: Application to particulate flow, *J. Comput. Phys.* 169 (2001) 363–426.
- [58] S. Vincent, T. N. Randrianarivelo, G. Pianet, J.-P. Caltagirone, Local penalty methods for flows interacting with moving solids at high Reynolds numbers, *Comput. Fluids* 36 (2007) 902–913.
- [59] S. Vincent, J. C. B. de Motta, A. Sarthou, J.-L. Estivalezes, O. Simonin, E. Climent, A Lagrangian VOF tensorial penalty method for the DNS of resolved particle-laden flows, *J. Comput. Phys.* 256 (2014) 582–614.
- [60] C. S. Peskin, Flow patterns around heart valves: A numerical method, *J. Comput. Phys.* 10 (1972) 252–271.
- [61] C. S. Peskin, The immersed boundary method, *Acta Numer.* 11 (2002) 479–517.
- [62] S. R. Idelsohn, E. Onate, F. Del Pin, The particle finite element method: a powerful tool to solve incompressible flows with free-surfaces and breaking waves, *Int. J. Numer. Methods Eng.* 61 (2004) 964–989.
- [63] F. Del Pin, S. Idelsohn, E. Onate, R. Aubry, The ALE/Lagrangian Particle Finite Element Method: A new approach to computation of free-surface flows and fluid-object interactions, *Comput. Fluids* 36 (2007) 27–38.
- [64] A. Larese, R. Rossi, E. Onate, S. R. Idelsohn, Validation of the particle finite element method (PFEM) for simulation of free surface flows, *Eng. Comput.* 25 (2008) 385–425.
- [65] M. Cremonesi, A. Frangi, U. Perego, A Lagrangian finite element approach for the simulation of water-waves induced by landslides, *Comput. Struct.* 89 (2011) 1086–1093.

- [66] B. Tang, J. F. Li, T. S. Wang, Some improvements on free surface simulation by the particle finite element method, *Int. J. Numer. Methods Fluids* 60 (2009) 1032–1054.
- [67] S. R. Idelsohn, J. Marti, P. Becker, E. Onate, Analysis of multifluid flows with large time steps using the particle finite element method, *Int. J. Numer. Methods Fluids* 75 (2014) 621–644.
- [68] T. S. Dang, G. Meschke, An ALE-PFEM method for the numerical simulation of two-phase mixture flow, *Comput. Meth. Appl. Mech. Eng.* 278 (2014) 599–620.
- [69] E. Onate, M. Angel Celigueta, S. R. Idelsohn, F. Salazar, B. Suarez, Possibilities of the particle finite element method for fluid-soil-structure interaction problems, *Comput. Mech.* 48 (2011) 307–318.
- [70] M. Zhu, M. H. Scott, Modeling fluid-structure interaction by the particle finite element method in OpenSees, *Comput. Struct.* 132 (2014) 12–21.
- [71] A. Franci, E. Onate, J. M. Carbonell, Unified Lagrangian formulation for solid and fluid mechanics and FSI problems, *Comput. Meth. Appl. Mech. Eng.* 298 (2016) 520–547.
- [72] S. Koshizuka, A. Nobe, Y. Oka, Numerical analysis of breaking waves using the moving particle semi-implicit method, *Int. J. Numer. Methods Fluids* 26 (1998) 751–769.
- [73] L. B. Lucy, A numerical approach to the testing of the fission hypothesis, *Astron. J.* 82 (1977) 1013–1024.
- [74] R. A. Gingold, J. J. Monaghan, Smoothed particle hydrodynamics: theory and application to non-spherical stars, *Mon. Not. R. Astron. Soc.* 181 (1977) 375–389.
- [75] J. J. Monaghan, Simulating free-surface flows with SPH, *J. Comput. Phys.* 110 (1994) 399–406.
- [76] A. J. Chorin, Numerical solution of the Navier-Stokes equations, *Math. Comput.* 22 (1968) 745–762.
- [77] S. J. Cummins, M. Rudman, An SPH projection method, *J. Comput. Phys.* 152 (1999) 584–607.
- [78] S. Cummins, Applications of projection techniques for incompressible flows, Ph.D. thesis, Monash University, Australia, 2000.
- [79] A. Souto-Iglesias, F. Macia, L. M. Gonzalez, J. L. Cercos-Pita, On the consistency of MPS, *Comput. Phys. Commun.* 184 (2013) 732–745.
- [80] A. Khayyer, H. Gotoh, Enhancement of stability and accuracy of the moving particle semi-implicit method, *J. Comput. Phys.* 230 (2011) 3093–3118.
- [81] A. Khayyer, H. Gotoh, Enhancement of performance and stability of MPS mesh-free particle method for multiphase flows characterized by high density ratios, *J. Comput. Phys.* 242 (2013) 211–233.
- [82] A. Souto-Iglesias, F. Macia, L. M. Gonzalez, J. L. Cercos-Pita, On the consistency of MPS (vol 184, pg 732, 2013), *Comput. Phys. Commun.* 185 (2014) 595–598.
- [83] H. Gotoh, T. Sakai, Lagrangian simulation of breaking waves using particle method, *Coastal Eng. J.* 41 (1999) 303–326.

- [84] H. Gotoh, T. Sakai, Key issues in the particle method for computation of wave breaking, *Coastal Eng.* 53 (2006) 171–179.
- [85] H. Gotoh, H. Ikari, T. Memita, T. Sakai, Lagrangian particle method for simulation of wave overtopping on a vertical seawall, *Coastal Eng. J.* 47 (2005) 157–181.
- [86] A. Khayyer, H. Gotoh, On particle-based simulation of a dam break over a wet bed, *J. Hydraul. Res.* 48 (2010) 238–249.
- [87] Z. Sun, G. Xi, X. Chen, Mechanism study of deformation and mass transfer for binary droplet collisions with particle method, *Phys. Fluids* 21 (2009) 032106.
- [88] A. Shakibaeinia, Y.-C. Jin, MPS mesh-free particle method for multiphase flows, *Comput. Meth. Appl. Mech. Eng.* 229 (2012) 13–26.
- [89] J. J. Monaghan, A. Kocharyan, SPH simulation of multiphase flow, *Comput. Phys. Commun.* 87 (1995) 225–235.
- [90] M. Landrini, A. Colagrossi, M. Greco, M. P. Tulin, Gridless simulations of splashing processes and near-shore bore propagation, *J. Fluid Mech.* 591 (2007) 183–213.
- [91] N. Grenier, M. Antuono, A. Colagrossi, D. Le Touze, B. Alessandrini, An Hamiltonian interface SPH formulation for multi-fluid and free surface flows, *J. Comput. Phys.* 228 (2009) 8380–8393.
- [92] K. Szewc, J. Pozorski, J. P. Minier, Simulations of single bubbles rising through viscous liquids using Smoothed Particle Hydrodynamics, *Int. J. Multiphase Flow* 50 (2013) 98–105.
- [93] X. Y. Hu, N. A. Adams, A multi-phase SPH method for macroscopic and mesoscopic flows, *J. Comput. Phys.* 213 (2006) 844–861.
- [94] J. J. Monaghan, R. A. F. Cas, A. M. Kos, M. Hallworth, Gravity currents descending a ramp in a stratified tank, *J. Fluid Mech.* 379 (1999) 39–70.
- [95] A. Ferrari, L. Fraccarollo, M. Dumbser, E. F. Toro, A. Armanini, Three-dimensional flow evolution after a dam break, *J. Fluid Mech.* 663 (2010) 456–477.
- [96] X. Xu, J. Ouyang, T. Jiang, Q. Li, Numerical simulation of 3D-unsteady viscoelastic free surface flows by improved smoothed particle hydrodynamics method, *J. Non-Newtonian Fluid Mech.* 177 (2012) 109–120.
- [97] M. Ozbulut, M. Yildiz, O. Goren, A numerical investigation into the correction algorithms for SPH method in modeling violent free surface flows, *Int. J. Mech. Sci.* 79 (2014) 56–65.
- [98] M. Bursik, B. Martinez-Hackert, H. Delgado, A. Gonzalez-Huesca, A smoothed-particle hydrodynamic automaton of landform degradation by overland flow, *Geomorphology* 53 (2003) 25–44.
- [99] Y. Zhu, P. J. Fox, Simulation of pore-scale dispersion in periodic porous media using smoothed particle hydrodynamics, *J. Comput. Phys.* 182 (2002) 622–645.
- [100] H. H. Bui, K. Sako, R. Fukagawa, Numerical simulation of soil-water interaction using smoothed particle hydrodynamics (SPH) method, *J. Terramech.* 44 (2007) 339–346.
- [101] A. Colagrossi, G. Colicchio, C. Lugni, M. Brocchini, A study of violent sloshing wave impacts using an improved SPH method, *J. Hydraul. Res.* 48 (2010) 94–104.

- [102] M. R. Hashemi, R. Fatehi, M. T. Manzari, A modified SPH method for simulating motion of rigid bodies in Newtonian fluid flows, *Int. J. Non-Linear Mech.* 47 (2012) 626–638.
- [103] G. Oger, M. Doring, B. Alessandrini, P. Ferrant, Two-dimensional SPH simulations of wedge water entries, *J. Comput. Phys.* 213 (2006) 803–822.
- [104] A. Skillen, S. Lind, P. K. Stansby, B. D. Rogers, Incompressible smoothed particle hydrodynamics (SPH) with reduced temporal noise and generalised Fickian smoothing applied to body-water slam and efficient wave-body interaction, *Comput. Meth. Appl. Mech. Eng.* 265 (2013) 163–173.
- [105] X. Liu, P. Lin, S. Shao, An ISPH simulation of coupled structure interaction with free surface flows, *J. Fluids Struct.* 48 (2014) 46–61.
- [106] C. Antoci, M. Gallati, S. Sibilla, Numerical simulation of fluid-structure interaction by SPH, *Comput. Struct.* 85 (2007) 879–890.
- [107] G. Taylor, Electrically driven jets, *Proc. R. Soc. London, Ser. A* 313 (1969) 453–475.
- [108] D. A. Saville, Electrohydrodynamics: The Taylor-Melcher leaky dielectric model, *Annu. Rev. Fluid Mech.* 29 (1997) 27–64.
- [109] Y. Tsori, F. Tournilhac, L. Leibler, Demixing in simple fluids induced by electric field gradients, *Nature* 430 (2004) 544–547.
- [110] S. M. Shin, I. S. Kang, Y. K. Cho, Mixing enhancement by using electrokinetic instability under time-periodic electric field, *J. Micromech. Microeng.* 15 (2005) 455–462.
- [111] J. Hua, L. K. Lim, C.-H. Wang, Numerical simulation of deformation/motion of a drop suspended in viscous liquids under influence of steady electric fields, *Phys. Fluids* 20 (2008) 113302.
- [112] G. Taylor, Disintegration of water drops in an electric field, *Proc. R. Soc. London, Ser. A* 280 (1964) 383–397.
- [113] J. D. Sherwood, Breakup of fluid droplets in electric and magnetic-fields, *J. Fluid Mech.* 188 (1988) 133–146.
- [114] J. W. Ha, S. M. Yang, Effect of nonionic surfactant on the deformation and breakup of a drop in an electric field, *J. Colloid Interface Sci.* 206 (1998) 195–204.
- [115] B. Bugarski, Q. Li, M. F. A. Goosen, D. Poncelet, R. J. Neufeld, G. Vunjak, Electrostatic droplet generation - mechanism of polymer droplet formation, *AIChE J.* 40 (1994) 1026–1031.
- [116] M. Sato, T. Hatori, M. Saito, Experimental investigation of droplet formation mechanisms by electrostatic dispersion in a liquid-liquid system, *IEEE Trans. Ind. Appl.* 33 (1997) 1527–1534.
- [117] V. Manojlovic, J. Djonlagic, B. Obradovic, V. Nedovic, B. Bugarski, Immobilization of cells by electrostatic droplet generation: a model system for potential application in medicine, *Int. J. Nanomed.* 1 (2006) 163–171.
- [118] J. Ogata, A. Yabe, Augmentation of boiling heat-transfer by utilizing the EHD effect - EHD behavior of boiling bubbles and heat-transfer characteristics, *Int. J. Heat Mass Transfer* 36 (1993) 783–791.

- [119] P. Di Marco, W. Grassi, G. Memoli, T. Takamasa, A. Tomiyama, S. Hosokawa, Influence of electric field on single gas-bubble growth and detachment in microgravity, *Int. J. Multiphase Flow* 29 (2003) 559–578.
- [120] F. J. Higuera, Injection of bubbles in a quiescent inviscid liquid under a uniform electric field, *J. Fluid Mech.* 568 (2006) 203–222.
- [121] Y. Ai, S. Qian, DC dielectrophoretic particle-particle interactions and their relative motions, *J. Colloid Interface Sci.* 346 (2010) 448–454.
- [122] Y. Ai, Z. Zeng, S. Qian, Direct numerical simulation of AC dielectrophoretic particle-particle interactive motions, *J. Colloid Interface Sci.* 417 (2014) 72–79.
- [123] O. D. Velev, K. H. Bhatt, On-chip micromanipulation and assembly of colloidal particles by electric fields, *Soft Matter* 2 (2006) 738–750.
- [124] S. Gangwal, O. J. Cayre, O. D. Velev, Dielectrophoretic Assembly of Metallodielectric Janus Particles in AC Electric Fields, *Langmuir* 24 (2008) 13312–13320.
- [125] S. Gangwal, A. Pawar, I. Kretzschmar, O. D. Velev, Programmed assembly of metallodielectric patchy particles in external AC electric fields, *Soft Matter* 6 (2010) 1413–1418.
- [126] K. D. Hermanson, S. O. Lumsdon, J. P. Williams, E. W. Kaler, O. D. Velev, Dielectrophoretic assembly of electrically functional microwires from nanoparticle suspensions, *Science* 294 (2001) 1082–1086.
- [127] D. J. Klingenberg, C. F. Zukoski, Studies on the steady-shear behavior of electrorheological suspensions, *Langmuir* 6 (1990) 15–24.
- [128] T. C. Halsey, Electrotheological fluids, *Science* 258 (1992) 761–766.
- [129] Y. G. Ko, U. S. Choi, Negative electrorheological fluids, *J. Rheol.* 57 (2013) 1655–1667.
- [130] U. Zimmermann, U. Friedrich, H. Mussauer, P. Gessner, K. Hamel, V. Sukhoruhov, Electromanipulation of mammalian cells: Fundamentals and application, *IEEE Trans. Plasma Sci.* 28 (2000) 72–82.
- [131] V. Brisson, R. D. Tilton, Self-assembly and two-dimensional patterning of cell arrays by electrophoretic deposition, *Biotechnol. Bioeng.* 77 (2002) 290–295.
- [132] M. Washizu, O. Kurosawa, I. Arai, S. Suzuki, N. Shimamoto, Applications of electrostatic stretch-and-positioning of DNA, *IEEE Trans. Ind. Appl.* 31 (1995) 447–456.
- [133] M. Washizu, Y. Nikaido, O. Kurosawa, H. Kabata, Stretching yeast chromosomes using electroosmotic flow, *J. Electrostat.* 57 (2003) 395–405.
- [134] Y. Huang, K. L. Ewalt, M. Tirado, T. R. Haigis, A. Forster, D. Ackley, M. J. Heller, J. P. O’Connell, M. Krihak, Electric manipulation of bioparticles and macromolecules on microfabricated electrodes, *Anal. Chem.* 73 (2001) 1549–1559.
- [135] L. F. Zheng, S. D. Li, J. P. Brody, P. J. Burke, Manipulating nanoparticles in solution with electrically contacted nanotubes using dielectrophoresis, *Langmuir* 20 (2004) 8612–8619.
- [136] S. Gupta, R. G. Alargova, P. K. Kilpatrick, O. D. Velev, On-chip electric field driven assembly of biocomposites from live cells and functionalized particles, *Soft Matter* 4 (2008) 726–730.

- [137] O. D. Velev, S. Gangwal, D. N. Petsev, Particle-localized ac and dc manipulation and electrokinetics, *Annu. Rep. Prog. Chem., Sect. C: Phys. Chem.* 105 (2009) 213–246.
- [138] G. Taylor, Studies in electrohydrodynamics. I. The circulation produced in a drop by an electric field, *Proc. R. Soc. London, Ser. A* 291 (1966) 159–166.
- [139] J. R. Melcher, G. I. Taylor, Electrohydrodynamics: A review of role of interfacial shear stresses, *Annu. Rev. Fluid Mech.* 1 (1969) 111–146.
- [140] P. Gambhire, R. M. Thaokar, Electrohydrodynamic instabilities at interfaces subjected to alternating electric field, *Phys. Fluids* 22 (2010) 064103.
- [141] G. K. Batchelor, *An introduction to fluid dynamics*, Cambridge University Press, 1973.
- [142] S. Chandrashekar, *Hydrodynamic and Hydromagnetic Stability*, Dover Publications, New York, 1981.
- [143] J. U. Brackbill, D. B. Kothe, C. Zemach, A continuum method for modeling surface-tension, *J. Comput. Phys.* 100 (1992) 335–354.
- [144] B. Lafaurie, C. Nardone, R. Scardovelli, S. Zaleski, G. Zanetti, Modeling merging and fragmentation in multiphase flows with SURFER, *J. Comput. Phys.* 113 (1994) 134–147.
- [145] C. Albert, H. Raach, D. Bothe, Influence of surface tension models on the hydrodynamics of wavy laminar falling films in Volume of Fluid-simulations, *Int. J. Multiphase Flow* 43 (2012) 66–71.
- [146] K. A. Smith, F. J. Solis, D. L. Chopp, A projection method for motion of triple junctions by level sets, *Interface Free Bound.* 4 (2002) 263–276.
- [147] J. P. Morris, Simulating surface tension with smoothed particle hydrodynamics, *Int. J. Numer. Methods Fluids* 33 (2000) 333–353.
- [148] A. Zainali, N. Tofighi, M. S. Shadloo, M. Yildiz, Numerical investigation of Newtonian and non-Newtonian multiphase flows using ISPH method, *Comput. Meth. Appl. Mech. Eng.* 254 (2013) 99–113.
- [149] G. Tomar, D. Gerlach, G. Biswas, N. Alleborn, A. Sharma, F. Durst, S. W. J. Welch, A. Delgado, Two-phase electrohydrodynamic simulations using a volume-of-fluid approach, *J. Comput. Phys.* 227 (2007) 1267–1285.
- [150] J. R. Melcher, C. V. Smith, Electrohydrodynamic charge relaxation and interfacial perpendicular-field instability, *Phys. Fluids* 12 (1969) 778–790.
- [151] A. C. Eringen, M. G. A., *Electrodynamics of continua II: Fluids and complex media*, Springer-Verlag, 1990.
- [152] K. Suzuki, T. Inamuro, Effect of internal mass in the simulation of a moving body by the immersed boundary method, *Comput. Fluids* 49 (2011) 173–187.
- [153] J. B. Ritz, J. P. Caltagirone, A numerical continuous model for the hydrodynamics of fluid particle systems, *Int. J. Numer. Methods Fluids* 30 (1999) 1067–1090.
- [154] S. Shao, Incompressible SPH simulation of water entry of a free-falling object, *Int. J. Numer. Methods Fluids* 59 (2009) 91–115.

- [155] G. R. Liu, M. B. Liu, *Smoothed particle hydrodynamics: a meshfree particle method*, World Scientific, 2003.
- [156] D. J. Price, *Smoothed particle hydrodynamics and magnetohydrodynamics*, *J. Comput. Phys.* 231 (2012) 759–794.
- [157] W. Dehnen, H. Aly, *Improving convergence in smoothed particle hydrodynamics simulations without pairing instability*, *Mon. Not. R. Astron. Soc.* 425 (2012) 1068–1082.
- [158] R. A. Dalrymple, B. D. Rogers, *Numerical modeling of water waves with the SPH method*, *Coastal Eng.* 53 (2006) 141–147.
- [159] J. J. Monaghan, J. C. Lattanzio, *A refined particle method for astrophysical problems*, *Astron. Astrophys.* 149 (1985) 135–143.
- [160] J. P. Morris, *A study of the stability properties of smooth particle hydrodynamics*, *Publ. Astron. Soc. Aust.* 13 (1996) 97–102.
- [161] S. Li, W. K. Liu, *Meshfree and particle methods and their applications*, *Appl. Mech. Rev.* 55 (2002) 1–34.
- [162] T. Belytschko, Y. Krongauz, J. Dolbow, C. Gerlach, *On the completeness of meshfree particle methods*, *Int. J. Numer. Methods Eng.* 43 (1998) 785–819.
- [163] N. R. Aluru, *A point collocation method based on reproducing kernel approximations*, *Int. J. Numer. Methods Eng.* 47 (2000) 1083–1121.
- [164] J. J. Monaghan, *Smoothed particle hydrodynamics*, *Annu. Rev. Astron. Astrophys.* 30 (1992) 543–574.
- [165] J. Bonet, S. Kulasegaram, *Correction and stabilization of smooth particle hydrodynamics methods with applications in metal forming simulations*, *Int. J. Numer. Methods Eng.* 47 (2000) 1189–1214.
- [166] P. W. Randles, L. D. Libersky, *Smoothed particle hydrodynamics: Some recent improvements and applications*, *Comput. Meth. Appl. Mech. Eng.* 139 (1996) 375–408.
- [167] G. R. Johnson, S. R. Beissel, *Normalized smoothing functions for SPH impact computations*, *Int. J. Numer. Methods Eng.* 39 (1996) 2725–2741.
- [168] J. K. Chen, J. E. Beraun, T. C. Carney, *A corrective smoothed particle method for boundary value problems in heat conduction*, *Int. J. Numer. Methods Eng.* 46 (1999) 231–252.
- [169] J. K. Chen, J. E. Beraun, *A generalized smoothed particle hydrodynamics method for non-linear dynamic problems*, *Comput. Meth. Appl. Mech. Eng.* 190 (2000) 225–239.
- [170] J. J. Monaghan, *An introduction to SPH*, *Comput. Phys. Commun.* 48 (1988) 89–96.
- [171] G. Oger, M. Doring, B. Alessandrini, P. Ferrant, *An improved SPH method: Towards higher order convergence*, *J. Comput. Phys.* 225 (2007) 1472–1492.
- [172] M. Yildiz, R. A. Rook, A. Suleman, *SPH with the multiple boundary tangent method*, *Int. J. Numer. Methods Eng.* 77 (2009) 1416–1438.
- [173] J. J. Monaghan, *Smoothed Particle Hydrodynamics and Its Diverse Applications*, *Annu. Rev. Fluid Mech.* 44 (2012) 323–346.

- [174] R. Xu, P. Stansby, D. Laurence, Accuracy and stability in incompressible SPH (ISPH) based on the projection method and a new approach, *J. Comput. Phys.* 228 (2009) 6703–6725.
- [175] M. S. Shadloo, A. Zainali, S. H. Sadek, M. Yildiz, Improved Incompressible Smoothed Particle Hydrodynamics method for simulating flow around bluff bodies, *Comput. Meth. Appl. Mech. Eng.* 200 (2011) 1008–1020.
- [176] N. Tofighi, M. Yildiz, Numerical simulation of single droplet dynamics in three-phase flows using ISPH, *Comput. Math. Appl.* 66 (2013) 525–536.
- [177] A. Colagrossi, B. Bouscasse, M. Antuono, S. Marrone, Particle packing algorithm for SPH schemes, *Comput. Phys. Commun.* 183 (2012) 1641–1653.
- [178] S. D. Shao, E. Y. M. Lo, Incompressible SPH method for simulating Newtonian and non-Newtonian flows with a free surface, *Adv. Water Resour.* 26 (2003) 787–800.
- [179] D. Gueyffier, J. Li, A. Nadim, R. Scardovelli, S. Zaleski, Volume-of-fluid interface tracking with smoothed surface stress methods for three-dimensional flows, *J. Comput. Phys.* 152 (1999) 423–456.
- [180] D. Gao, N. B. Morley, V. Dhir, Numerical simulation of wavy falling film flow using VOF method, *J. Comput. Phys.* 192 (2003) 624–642.
- [181] J. A. Sethian, P. Smereka, Level set methods for fluid interfaces, *Annu. Rev. Fluid Mech.* 35 (2003) 341–372.
- [182] R. Chella, J. Vinals, Mixing of a two-phase fluid by cavity flow, *Phys. Rev. E* 53 (1996) 3832–3840.
- [183] V. E. Badalassi, H. D. Ceniceros, S. Banerjee, Computation of multiphase systems with phase field models, *J. Comput. Phys.* 190 (2003) 371–397.
- [184] G. Tryggvason, B. Bunner, A. Esmaeeli, D. Juric, N. Al-Rawahi, W. Tauber, J. Han, S. Nas, Y. J. Jan, A front-tracking method for the computations of multiphase flow, *J. Comput. Phys.* 169 (2001) 708–759.
- [185] B. Merriman, J. K. Bence, S. J. Osher, Motion of multiple junctions: A level set approach, *J. Comput. Phys.* 112 (1994) 334–363.
- [186] M. Zhang, Simulation of surface tension in 2D and 3D with smoothed particle hydrodynamics method, *J. Comput. Phys.* 229 (2010) 7238–7259.
- [187] M. Muradoglu, S. Tasoglu, A front-tracking method for computational modeling of impact and spreading of viscous droplets on solid walls, *Comput. Fluids* 39 (2010) 615–625.
- [188] F. Boyer, C. Lapuerta, Study of a three component Cahn-Hilliard flow model, *ESAIM-Math. Model. Numer. Anal.-Model. Math. Anal. Numer.* 40 (2006) 653–687.
- [189] J. Kim, Phase field computations for ternary fluid flows, *Comput. Meth. Appl. Mech. Eng.* 196 (2007) 4779–4788.
- [190] J. Kim, Phase-field models for multi-component fluid flows, *Commun. Comput. Phys.* 12 (2012) 613–661.
- [191] J. R. Melcher, W. J. Schwarz, Interfacial relaxation overstability in a tangential electric field, *Phys. Fluids* 11 (1968) 2604–2616.

- [192] X. P. Chen, L. B. Jia, X. Z. Yin, J. S. Cheng, J. Lu, Spraying modes in coaxial jet electrospray with outer driving liquid, *Phys. Fluids* 17 (2005) 032101.
- [193] F. J. Higuera, Stationary coaxial electrified jet of a dielectric liquid surrounded by a conductive liquid, *Phys. Fluids* 19 (2007) 012102.
- [194] G. Li, X. Luo, T. Si, R. X. Xu, Temporal instability of coflowing liquid-gas jets under an electric field, *Phys. Fluids* 26 (2014) 054101.
- [195] F. J. Higuera, Electrodispersion of a liquid of finite electrical conductivity in an immiscible dielectric liquid, *Phys. Fluids* 22 (2010) 112107.
- [196] M. H. Oddy, J. G. Santiago, J. C. Mikkelsen, Electrokinetic instability micromixing, *Anal. Chem.* 73 (2001) 5822–5832.
- [197] A. O. El Moctar, N. Aubry, J. Batton, Electro-hydrodynamic micro-fluidic mixer, *Lab. Chip* 3 (2003) 273–280.
- [198] R. Cimpeanu, D. T. Papageorgiou, P. G. Petropoulos, On the control and suppression of the Rayleigh-Taylor instability using electric fields, *Phys. Fluids* 26 (2014) 022105.
- [199] M. R. E. Warner, R. V. Craster, O. K. Matar, Pattern formation in thin liquid films with charged surfactants, *J. Colloid Interface Sci.* 268 (2003) 448–463.
- [200] R. V. Craster, O. K. Matar, Electrically induced pattern formation in thin leaky dielectric films, *Phys. Fluids* 17 (2005) 032104.
- [201] L. F. Pease, W. B. Russel, Electrostatically induced submicron patterning of thin perfect and leaky dielectric films: A generalized linear stability analysis, *J. Chem. Phys.* 118 (2003) 3790–3803.
- [202] V. Shankar, A. Sharma, Instability of the interface between thin fluid films subjected to electric fields, *J. Colloid Interface Sci.* 274 (2004) 294–308.
- [203] B. S. Tilley, P. G. Petropoulos, D. T. Papageorgiou, Dynamics and rupture of planar electrified liquid sheets, *Phys. Fluids* 13 (2001) 3547–3563.
- [204] D. T. Papageorgiou, J. M. Vanden-Broeck, Large-amplitude capillary waves in electrified fluid sheets, *J. Fluid Mech.* 508 (2004) 71–88.
- [205] A. K. Uguz, N. Aubry, Quantifying the linear stability of a flowing electrified two-fluid layer in a channel for fast electric times for normal and parallel electric fields, *Phys. Fluids* 20 (2008) 092103.
- [206] L. Rayleigh, Investigation of the character of the equilibrium of an incompressible heavy fluid of variable density, *Proc. London Math. Soc.* s1-14 (1882) 170–177.
- [207] G. Taylor, The instability of liquid surfaces when accelerated in a direction perpendicular to their planes. I, *Proc. R. Soc. Lon. Ser. A* 201 (1950) 192–196.
- [208] A. E. M. A. Mohamed, E. S. F. E. Shehawy, Nonlinear electrohydrodynamic Rayleigh-Taylor instability. Part 1. A perpendicular field in the absence of surface charges, *J. Fluid Mech.* 129 (1983) 473–494.
- [209] A. E. M. A. Mohamed, E. S. F. El Shehawy, Nonlinear electrohydrodynamic Rayleigh-Taylor instability. II. A perpendicular field producing surface charge, *Phys. Fluid* 26 (1983) 1724–1730.

- [210] N. T. Eldabe, Effect of a tangential electric-field on Rayleigh-Taylor instability, *J. Phys. Soc. Jpn.* 58 (1989) 115–120.
- [211] A. Joshi, M. C. Radhakrishna, N. Rudraiah, Rayleigh-Taylor instability in dielectric fluids, *Phys. Fluids* 22 (2010) 064102.
- [212] L. L. Barannyk, D. T. Papageorgiou, P. G. Petropoulos, Suppression of Rayleigh-Taylor instability using electric fields, *Math. Comput. Simul.* 82 (2012) 1008–1016.
- [213] L. F. Pease, W. B. Russel, Linear stability analysis of thin leaky dielectric films subjected to electric fields, *J. Non-Newton. Fluid Mech.* 102 (2002) 233–250.
- [214] R. M. Thaokar, V. Kumaran, Electrohydrodynamic instability of the interface between two fluids confined in a channel, *Phys. Fluids* 17 (2005) 084104.
- [215] M. S. Shadloo, A. Zainali, M. Yildiz, Simulation of single mode Rayleigh-Taylor instability by SPH method, *Comput. Mech.* 51 (2013) 699–715.
- [216] M. S. Shadloo, A. Rahmat, M. Yildiz, A smoothed particle hydrodynamics study on the electrohydrodynamic deformation of a droplet suspended in a neutrally buoyant Newtonian fluid, *Comput. Mech.* 52 (2013) 693–707.
- [217] IEEE-DEIS-EHD Tech. Comm., Recommended international standard for dimensionless parameters used in electrohydrodynamics, *IEEE Trns. Dielectr. Electr. Insul.* 10 (2003) 3–6.
- [218] C. Dopazo, A. Lozano, F. Barreras, Vorticity constraints on a fluid/fluid interface, *Phys. Fluids* 12 (2000) 1928–1931.
- [219] J. Z. Wu, A theory of three-dimensional interfacial vorticity dynamics, *Phys. Fluids* 7 (1995) 2375–2395.
- [220] E. H. Dowell, K. C. Hall, Modeling of fluid-structure interaction, *Annu. Rev. Fluid Mech.* 33 (2001) 445–490.
- [221] Z. S. Yu, A DLM/FD method for fluid/flexible-body interactions, *J. Comput. Phys.* 207 (2005) 1–27.
- [222] A. A. Shirgaonkar, M. A. Maclver, N. A. Patankar, A new mathematical formulation and fast algorithm for fully resolved simulation of self-propulsion, *J. Comput. Phys.* 228 (2009) 2366–2390.
- [223] J. Feng, H. H. Hu, D. D. Joseph, Direct simulation of initial-value problems for the motion of solid bodies in a Newtonian fluid .2. Couette and Poiseuille flows, *J. Fluid Mech.* 277 (1994) 271–301.
- [224] K. Sugiyama, S. Ii, S. Takeuchi, S. Takagi, Y. Matsumoto, A full Eulerian finite difference approach for solving fluid-structure coupling problems, *J. Comput. Phys.* 230 (2011) 596–627.
- [225] C. D. Eggleton, A. S. Popel, Large deformation of red blood cell ghosts in a simple shear flow, *Phys. Fluids* 10 (1998) 1834–1845.
- [226] C. Pozrikidis, Axisymmetric motion of a file of red blood cells through capillaries, *Phys. Fluids* 17 (2005) 031503.

- [227] H. Kamada, Y. Imai, M. Nakamura, T. Ishikawa, T. Yamaguchi, Computational study on thrombus formation regulated by platelet glycoprotein and blood flow shear, *Microvasc. Res.* 89 (2013) 95–106.
- [228] H. Watanabe, S. Sugiura, H. Kafuku, T. Hisada, Multiphysics simulation of left ventricular filling dynamics using fluid-structure interaction finite element method, *Biophys. J.* 87 (2004) 2074–2085.
- [229] D. Liu, P. Lin, A numerical study of three-dimensional liquid sloshing in tanks, *J. Comput. Phys.* 227 (2008) 3921–3939.
- [230] T. N. Randrianarivelo, G. Pianet, S. Vincent, J. P. Caltagirone, Numerical modelling of solid particle motion using a new penalty method, *Int. J. Numer. Methods Fluids* 47 (2005) 1245–1251.
- [231] Z. Xia, K. W. Connington, S. Rapaka, P. Yue, J. J. Feng, S. Chen, Flow patterns in the sedimentation of an elliptical particle, *J. Fluid Mech.* 625 (2009) 249–272.
- [232] E. J. Ding, C. K. Aidun, The dynamics and scaling law for particles suspended in shear flow with inertia, *J. Fluid Mech.* 423 (2000) 317–344.
- [233] K. Stein, R. Benney, T. Tezduyar, J. Potvin, Fluid-structure interactions of a cross parachute: numerical simulation, *Comput. Meth. Appl. Mech. Eng.* 191 (2001) 673–687.
- [234] M. Uhlmann, An immersed boundary method with direct forcing for the simulation of particulate flows, *J. Comput. Phys.* 209 (2005) 448–476.
- [235] J. Yang, F. Stern, Sharp interface immersed-boundary/level-set method for wave-body interactions, *J. Comput. Phys.* 228 (2009) 6590–6616.
- [236] R. Mittal, G. Iaccarino, Immersed boundary methods, *Annu. Rev. Fluid Mech.* 37 (2005) 239–261.
- [237] N. A. Patankar, P. Singh, D. D. Joseph, R. Glowinski, T. W. Pan, A new formulation of the distributed Lagrange multiplier/fictitious domain method for particulate flows, *Int. J. Multiphase Flow* 26 (2000) 1509–1524.
- [238] T.-W. Pan, S.-L. Huang, S.-D. Chen, C.-C. Chu, C.-C. Chang, A numerical study of the motion of a neutrally buoyant cylinder in two dimensional shear flow, *Comput. Fluids* 87 (2013) 57–66.
- [239] A. Sarthou, S. Vincent, J. P. Caltagirone, P. Angot, Eulerian-Lagrangian grid coupling and penalty methods for the simulation of multiphase flows interacting with complex objects, *Int. J. Numer. Methods Fluids* 56 (2008) 1093–1099.
- [240] P. Angot, C. H. Bruneau, P. Fabrie, A penalization method to take into account obstacles in incompressible viscous flows, *Numer. Math.* 81 (1999) 497–520.
- [241] K. Khadra, P. Angot, S. Parneix, J. P. Caltagirone, Fictitious domain approach for numerical modelling of Navier-Stokes equations, *Int. J. Numer. Methods Fluids* 34 (2000) 651–684.
- [242] M. B. Liu, G. R. Liu, Smoothed Particle Hydrodynamics (SPH): an Overview and Recent Developments, *Arch. Comput. Method Eng.* 17 (2010) 25–76.
- [243] P. Koumoutsakos, Multiscale flow simulations using particles, *Annu. Rev. Fluid Mech.* 37 (2005) 457–487.

- [244] J. Feng, H. H. Hu, D. D. Joseph, Direct simulation of initial-value problems for the motion of solid bodies in a Newtonian fluid .1. Sedimentation, *J. Fluid Mech.* 261 (1994) 95–134.
- [245] A. J. C. Ladd, Numerical simulations of particulate suspensions via a discretized Boltzmann-equation .2. Numerical results, *J. Fluid Mech.* 271 (1994) 311–339.
- [246] Z. G. Feng, E. E. Michaelides, The immersed boundary-lattice Boltzmann method for solving fluid-particles interaction problems, *J. Comput. Phys.* 195 (2004) 602–628.
- [247] M. Coquerelle, G. H. Cottet, A vortex level set method for the two-way coupling of an incompressible fluid with colliding rigid bodies, *J. Comput. Phys.* 227 (2008) 9121–9137.
- [248] Z. Zhang, A. Prosperetti, A method for particle simulation, *J. Appl. Mech.-T. ASME* 70 (2003) 64–74.
- [249] Y. Yan, J. F. Morris, J. Koplik, Hydrodynamic interaction of two particles in confined linear shear flow at finite Reynolds number, *Phys. Fluids* 19 (2007) 113305.
- [250] S. Bottin, O. Dauchot, F. Daviaud, P. Manneville, Experimental evidence of streamwise vortices as finite amplitude solutions in transitional plane Couette flow, *Phys. Fluids* 10 (1998) 2597–2607.
- [251] J. P. Matas, J. F. Morris, E. Guazzelli, Transition to turbulence in particulate pipe flow, *Phys. Rev. Lett.* 90 (2003) 014501.
- [252] C. A. Kossack, A. Acrivos, Steady simple shear flow past a circular cylinder at moderate reynolds numbers: a numerical solution, *J. Fluid Mech.* 66 (1974) 353–376.
- [253] C. M. Zettner, M. Yoda, The circular cylinder in simple shear at moderate Reynolds numbers: An experimental study, *Exp. Fluids* 30 (2001) 346–353.
- [254] G. G. Poe, A. Acrivos, Closed-streamline flows past rotating single cylinders and spheres: Inertia effects, *J. Fluid Mech.* 72 (1975) 605–623.
- [255] A. P. S. Bhalla, R. Bale, B. E. Griffith, N. A. Patankar, Fully resolved immersed electrohydrodynamics for particle motion, electrolocation, and self-propulsion, *J. Comput. Phys.* 256 (2014) 88–108.
- [256] M. R. Hossan, R. Dillon, A. K. Roy, P. Dutta, Modeling and simulation of dielectrophoretic particle-particle interactions and assembly, *J. Colloid Interface Sci.* 394 (2013) 619–629.
- [257] Y. Ai, A. Beskok, D. T. Gauthier, S. W. Joo, S. Qian, DC electrokinetic transport of cylindrical cells in straight microchannels, *Biomicrofluidics* 3 (2009) 044110.
- [258] N. Aubry, P. Singh, M. Janjua, S. Nudurupati, Micro- and nanoparticles self-assembly for virtually defect-free, adjustable monolayers, *Proc. Natl. Acad. Sci. U.S.A.* 105 (2008) 3711–3714.
- [259] X. Xiong, A. Busnaina, S. Selvarasah, S. Somu, M. Wei, J. Mead, C.-L. Chen, J. Aceros, P. Makaram, M. R. Dokmeci, Directed assembly of gold nanoparticle nanowires and networks for nanodevices, *Appl. Phys. Lett.* 91 (2007) 063101.
- [260] L. M. Ying, S. S. White, A. Bruckbauer, L. Meadows, Y. E. Korchev, D. Klenerman, Frequency and voltage dependence of the dielectrophoretic trapping of short lengths of DNA and dCTP in a nanopipette, *Biophys. J.* 86 (2004) 1018–1027.

- [261] S. Tuukkanen, A. Kuzyk, J. J. Toppari, H. Hakkinen, V. P. Hytonen, E. Niskanen, M. Rinkio, P. Torma, Trapping of 27 bp-8 kbp DNA and immobilization of thiol-modified DNA using dielectrophoresis, *Nanotechnology* 18 (2007) 295204.
- [262] S. Park, M. Koklu, A. Beskok, Particle trapping in high-conductivity media with electrothermally enhanced negative dielectrophoresis, *Anal. Chem.* 81 (2009) 2303–2310.
- [263] J.-R. Du, Y.-J. Juang, J.-T. Wu, H.-H. Wei, Long-range and superfast trapping of DNA molecules in an ac electrokinetic funnel, *Biomicrofluidics* 2 (2008) 044103.
- [264] I.-F. Cheng, H.-C. Chang, D. Hou, H.-C. Chang, An integrated dielectrophoretic chip for continuous bioparticle filtering, focusing, sorting, trapping, and detecting, *Biomicrofluidics* 1 (2007) 021503.
- [265] K. H. Kang, X. C. Xuan, Y. J. Kang, D. Q. Li, Effects of dc-dielectrophoretic force on particle trajectories in microchannels, *J. Appl. Phys.* 99 (2006) 064702.
- [266] H. Morgan, M. P. Hughes, N. G. Green, Separation of submicron bioparticles by dielectrophoresis, *Biophys. J.* 77 (1999) 516–525.
- [267] P. R. C. Gascoyne, J. Vykoukal, Particle separation by dielectrophoresis, *Electrophoresis* 23 (2002) 1973–1983.
- [268] B. Cetin, Y. Kang, Z. Wu, D. Li, Continuous particle separation by size via AC-dielectrophoresis using a lab-on-a-chip device with 3-D electrodes, *Electrophoresis* 30 (2009) 766–772.
- [269] Y. Kang, B. Cetin, Z. Wu, D. Li, Continuous particle separation with localized AC-dielectrophoresis using embedded electrodes and an insulating hurdle, *Electrochim. Acta* 54 (2009) 1715–1720.
- [270] N. Lewpiriyawong, C. Yang, Y. C. Lam, Dielectrophoretic manipulation of particles in a modified microfluidic H filter with multi-insulating blocks, *Biomicrofluidics* 2 (2008) 034105.
- [271] G. O. F. Parikesit, A. P. Markesteyn, O. M. Piciu, A. Bossche, J. Westerweel, I. T. Young, Y. Garini, Size-dependent trajectories of DNA macromolecules due to insulative dielectrophoresis in submicrometer-deep fluidic channels, *Biomicrofluidics* 2 (2008) 024103.
- [272] J. Zhu, X. Xuan, Dielectrophoretic focusing of particles in a microchannel constriction using DC-biased AC electric fields, *Electrophoresis* 30 (2009) 2668–2675.
- [273] J. Zhu, T.-R. J. Tzeng, G. Hu, X. Xuan, DC dielectrophoretic focusing of particles in a serpentine microchannel, *Microfluid. Nanofluid.* 7 (2009) 751–756.
- [274] S. O. Lumsdon, E. W. Kaler, O. D. Velev, Two-dimensional crystallization of microspheres by a coplanar AC electric field, *Langmuir* 20 (2004) 2108–2116.
- [275] O. D. Velev, E. W. Kaler, In situ assembly of colloidal particles into miniaturized biosensors, *Langmuir* 15 (1999) 3693–3698.
- [276] G. H. Markx, L. Carney, M. Littlefair, A. Sebastian, A.-M. Buckle, Recreating the hematopoietic stem cell niche: microfabrication of artificial haematopoietic stem cell niches in vitro using dielectrophoresis, *Biomed. Microdevices* 11 (2009) 143–150.

- [277] N. Aubry, P. Singh, Influence of particle-particle interactions and particles rotational motion in traveling wave dielectrophoresis, *Electrophoresis* 27 (2006) 703–715.
- [278] M. R. Hossan, R. Dillonc, P. Duttaa, Hybrid immersed interface-immersed boundary methods for AC dielectrophoresis, *J. Comput. Phys.* 270 (2014) 640–659.
- [279] S. Kang, Dielectrophoretic motion of two particles with diverse sets of the electric conductivity under a uniform electric field, *Comput. Fluids* 105 (2014) 231–243.
- [280] C. Xie, B. Chen, C.-O. Ng, X. Zhou, J. Wu, Numerical study of interactive motion of dielectrophoretic particles, *Eur. J. Mech. B. Fluids* 49 (2015) 208–216.
- [281] D. L. House, H. Luo, S. Chang, Numerical study on dielectrophoretic chaining of two ellipsoidal particles, *J. Colloid Interface Sci.* 374 (2012) 141–149.
- [282] D. Das, D. Saintillan, Electrohydrodynamic interaction of spherical particles under Quincke rotation, *Phys. Rev. E* 87 (2013) 043014.
- [283] G. Quincke, Ueber rotationen im constanten electrischen felde, *Ann. Phys.* 295 (1896) 417–486.
- [284] C. Boissy, P. Atten, J. N. Foulc, On a negative electrorheological effect, *J. Electrostat.* 35 (1995) 13–20.
- [285] H. Hwang, J.-J. Kim, J.-K. Park, Experimental investigation of electrostatic particle-particle interactions in optoelectronic tweezers, *J. Phys. Chem. B* 112 (2008) 9903–9908.